

HARVARD UNIVERSITY  
Graduate School of Arts and Sciences



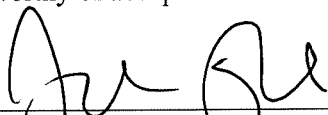
DISSERTATION ACCEPTANCE CERTIFICATE

The undersigned, appointed by the  
Department of Physics  
have examined a dissertation entitled

Engineered Collisions, Molecular Qubits, and Laser Cooling of Asymmetric  
Top Molecules

presented by Sean Burchesky

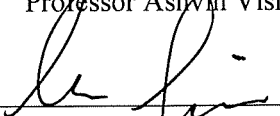
candidate for the degree of Doctor of Philosophy and hereby  
certify that it is worthy of acceptance.

Signature  \_\_\_\_\_

Typed name: Professor John Doyle, Chair

Signature  \_\_\_\_\_

Typed name: Professor Ashwin Vishwanath

Signature  \_\_\_\_\_

Typed name: Professor Markus Greiner

Date: April 27, 2023

# Engineered Collisions, Molecular Qubits, and Laser Cooling of Asymmetric Top Molecules

A DISSERTATION PRESENTED  
BY  
SEAN BURCHESKY  
TO  
THE DEPARTMENT OF PHYSICS

IN PARTIAL FULFILLMENT OF THE REQUIREMENTS  
FOR THE DEGREE OF  
DOCTOR OF PHILOSOPHY  
IN THE SUBJECT OF  
PHYSICS

HARVARD UNIVERSITY  
CAMBRIDGE, MASSACHUSETTS  
APRIL 2023

©2023 – SEAN BURCHESKY  
ALL RIGHTS RESERVED.

# Engineered Collisions, Molecular Qubits, and Laser Cooling of Asymmetric Top Molecules

## ABSTRACT

In this dissertation, I present studies of molecules for uses in quantum science ranging from quantum computing and ultracold collisions to controlling organic-inspired molecular species. Starting with a diatomic molecule, calcium monofluoride, we developed an optical tweezer platform for use in quantum computing and demonstrated rotational coherence times significantly longer than measured dipole-enabled gate times. Using the Tweezer platform, we studied ultracold collisions of exactly two molecules and exerted full quantum control over the internal structure of the molecules. The collisions resulted in a rapid loss from the tweezers, leading us to develop a microwave shield to prevent these lossy collisions. The shielding scheme enhanced the rate of elastic collisions enabling the demonstration of forced evaporative cooling.

To explore the possible use of larger molecules for quantum science, we studied the rotational structure of an asymmetric top and aromatic molecule, calcium monophenoxide, with the intent of identifying a path toward laser cooling and trapping. We cycled several photons, but theory predicted many more. After eliminating several decay paths, the key loss remained unknown. Applying the same methods to  $\text{CaNH}_2$ ,

Thesis advisor: Professor John Doyle

Sean Burchesky

a smaller asymmetric top molecule with similar spatial symmetry, we performed laser cooling. Using  $\text{CaNH}_2$ , we demonstrated photon cycling, and then observed Sisyphus cooling and heating features for the first time using an asymmetric top molecule. This work lays the foundation for future laser-cooling of organic-inspired molecules in an optical tweezer array for applications ranging from quantum computing to quantum chemistry, and precision measurement.

# Contents

Title Page . . . . .	i
Copyright Notice . . . . .	ii
Abstract . . . . .	iii
Table of Contents . . . . .	v
List of Figures . . . . .	viii
Dedication . . . . .	xi
Previously Published Works . . . . .	xii
Acknowledgments . . . . .	xiv
<b>1 INTRODUCTION</b>	<b>1</b>
1.1 Why ultracold? . . . . .	1
1.2 Research Directions . . . . .	3
1.3 Anatomy of a Buffer Gas Source . . . . .	7
1.4 Future Directions . . . . .	10
1.5 This Thesis . . . . .	12
<b>2 TRAPPING AND COOLING A SINGLE MOLECULE</b>	<b>15</b>
2.1 Optical Dipole Traps . . . . .	17
2.2 Sub-Doppler Cooling . . . . .	21
2.3 Optical Tweezers . . . . .	30
2.4 Light Assisted Collisions . . . . .	39
2.5 Ground State Collisions Part 1 . . . . .	43
<b>3 COLLISIONS OF EXACTLY TWO MOLECULES</b>	<b>47</b>
3.1 Why study collisions? . . . . .	47
3.2 Merging Tweezers . . . . .	49
3.3 Coherent Control of Molecules . . . . .	52
3.4 Collisions . . . . .	59
3.5 What is happening to the molecules? . . . . .	69
<b>4 ENGINEERING MOLECULAR COLLISIONS</b>	<b>71</b>
4.1 How does Microwave Shielding work? . . . . .	73
4.2 Polarization . . . . .	76
4.3 Loss Processes . . . . .	78
4.4 Building the Microwave System . . . . .	80

4.5	Polarization . . . . .	83
4.6	Measuring Polarization . . . . .	86
4.7	Adjusting the Polarization in the Chamber . . . . .	88
4.8	Dressed State Preparation . . . . .	97
4.9	Microwave Phase Noise . . . . .	102
4.10	Picking a microwave source with low phase noise . . . . .	105
4.11	Shielding . . . . .	108
4.12	Shielding Outlook . . . . .	118
<b>5</b>	<b>EVAPORATIVE COOLING OF SHIELDED MOLECULES</b>	<b>119</b>
5.1	Parameter Space for Evaporative Cooling . . . . .	121
5.2	Estimating the Elastic Rate . . . . .	121
5.3	Trap Transfer and Optimizing Density . . . . .	124
5.4	Bulk gas shielding . . . . .	132
5.5	Evaporative Cooling . . . . .	138
5.6	Elastic Collision Rate . . . . .	141
5.7	Summary . . . . .	143
5.8	Prospectives on Evaporative Cooling of CaF . . . . .	145
<b>6</b>	<b>THE MAKING OF A MOLECULAR QUBIT</b>	<b>146</b>
6.1	Considerations . . . . .	148
6.2	Light Shifts in an Optical Tweezer . . . . .	148
6.3	State Selection . . . . .	151
6.4	Experimental Sequence . . . . .	154
6.5	Stabilizing the Lab Environment . . . . .	155
6.6	Ramsey Spectroscopy and Microwave System Performance . . . . .	158
6.7	The Qubit States in an Optical Field . . . . .	161
6.8	“Magic” Conditions in the Experiment . . . . .	165
6.9	What limits the Ramsey Coherence Time? . . . . .	170
6.10	Loose Ends . . . . .	173
6.11	Future outlook . . . . .	175
<b>7</b>	<b>AROMATIC MOLECULES FOR LASER COOLING</b>	<b>177</b>
7.1	Collecting our bearings . . . . .	177
7.2	Phenol Derived Molecules . . . . .	181
7.3	Producing the Phenol Derivatives . . . . .	185
7.4	Structure of Asymmetric Top Molecules . . . . .	195
7.5	High Resolution Spectroscopy . . . . .	197
7.6	Laser Induced-Flourescence . . . . .	199
7.7	Initial attempts to Photon Cycle . . . . .	207
7.8	Flourescence Imaging . . . . .	210

7.9	Repump Transition . . . . .	216
7.10	Pump and Repump Measurement . . . . .	221
7.11	Assesing the Situation . . . . .	223
<b>8</b>	<b>LASER COOLING OF AN ASYMMETRIC TOP MOLECULE</b>	<b>226</b>
8.1	A simpler Asymmetric Top . . . . .	226
8.2	Production . . . . .	227
8.3	Vibrational Structure . . . . .	229
8.4	CaNH <sub>2</sub> Spectroscopy . . . . .	229
8.5	Vibrational Repump Transitions . . . . .	232
8.6	Photon Cycling and Rotational Leakage . . . . .	235
8.7	Rotational Leakage . . . . .	236
8.8	Fluorescence Streak Imaging . . . . .	242
8.9	Deflection . . . . .	248
8.10	Sisyphus Heating and Cooling . . . . .	251
8.11	Summary . . . . .	258
<b>9</b>	<b>CONCLUSION</b>	<b>259</b>
	<b>REFERENCES</b>	<b>278</b>

# Listing of figures

1.1	Research directions for cold and ultracold molecules . . . . .	4
1.2	Schematic drawing of the CaF experiment . . . . .	8
1.3	iPhone image of a CaF MOT . . . . .	10
1.4	molecular species studied in this thesis . . . . .	11
2.1	Optical trapping potential . . . . .	20
2.2	Gray molasses cooling . . . . .	23
2.3	Lambda-enhanced gray molasses cooling . . . . .	26
2.4	Loading the optical dipole trap . . . . .	28
2.5	Microscope objective used to project the optical tweezer . . . . .	31
2.6	Single molecule loading . . . . .	33
2.7	Imaging fidelity . . . . .	35
2.8	Characterizing the optical tweezer . . . . .	38
2.9	Optical tweezer array . . . . .	40
2.10	Light-assisted inelastic collisions . . . . .	42
2.11	Ground state inelastic collisions . . . . .	44
3.1	Optical tweezer merging . . . . .	50
3.2	Optical pumping . . . . .	53
3.3	Microwave state transfer . . . . .	55
3.4	Landau-Zener sweeps . . . . .	57
3.5	Sample density . . . . .	61
3.6	Van-der Waals interaction potentials . . . . .	63
3.7	Ground state inelastic collision loss rate . . . . .	67
3.8	State dependent inelastic loss rates . . . . .	68
3.9	Summary of inelastic loss rates . . . . .	69
4.1	Microwave shielding interaction schematic . . . . .	74
4.2	Coupled channel inelastic loss rate calculations . . . . .	80
4.3	Helical microwave antenna array . . . . .	82
4.4	Microwave system schematic . . . . .	83
4.5	In-situ microwave polarization measurement . . . . .	86
4.6	Microwave field components . . . . .	87
4.7	Rabi frequency optimization . . . . .	89
4.8	Imaging the antenna radiation pattern . . . . .	90

4.9	Mounted antenna assembly . . . . .	91
4.10	Antenna position with microwave absorbers . . . . .	93
4.11	Microwave polarization simulation inside the MOT chamber . . . . .	95
4.12	Dressed state preparation error . . . . .	98
4.13	Adiabatic preparation of the dressed states . . . . .	100
4.14	Microwave phase noise limits on dressed state lifetime . . . . .	103
4.15	Phase noise from microwave sources . . . . .	106
4.16	Density of molecules in the tweezer . . . . .	109
4.17	Shielding vs. anti-shielding . . . . .	111
4.18	Shielding magnetic field dependance . . . . .	112
4.19	Effect of the tensor Stark shift . . . . .	114
4.20	Shielding microwave power dependance . . . . .	115
4.21	Shielding polarization dependance . . . . .	117
5.1	Elastic collision rate predictions . . . . .	123
5.2	Light-assisted collision rate in the ODT . . . . .	126
5.3	Density characterization . . . . .	129
5.4	Molecule number calibration . . . . .	130
5.5	Two-body inelastic lifetime ground state . . . . .	131
5.6	Two-body inelastic lifetime with shielding in bulk gas . . . . .	133
5.7	Microwave spectroscopy Tensor Stark shifts . . . . .	134
5.8	Bulk gas shielding . . . . .	136
5.9	Trap ramp sequence for evaporative cooling . . . . .	137
5.10	Evaporative cooling. . . . .	139
5.11	Measurement of elastic collision rate . . . . .	142
6.1	Qubit states . . . . .	149
6.2	Tensor Stark shifts . . . . .	152
6.3	External decoherence sources in the lab . . . . .	156
6.4	Ramsey pulse sequence . . . . .	160
6.5	Hyperpolarizability of the CaF qubit states . . . . .	162
6.6	Coherence time . . . . .	164
6.7	Scan of the magic angle condition . . . . .	166
6.8	Spin-echo coherence time . . . . .	169
6.9	Dynamical decoupling pulse sequences . . . . .	170
6.10	Decoherence rate vs. temperature . . . . .	172
6.11	Optical tweezer polarization gradients . . . . .	174
7.1	CaOPh Structure . . . . .	180
7.2	CaOPh dispersed laser-induced fluorescence . . . . .	184
7.3	Heated fill line . . . . .	186

7.4	Beambox with heated fill line installed . . . . .	187
7.5	Heated fill line details . . . . .	189
7.6	Atmpshere-side heated fill line plumbing . . . . .	190
7.7	CaOPh beam vs. CaOPh-345F production . . . . .	192
7.8	Chemical production enhancement . . . . .	194
7.9	Phenol deposits in buffer gas cell . . . . .	195
7.10	Temperature dependence of the CaOPh spectrum . . . . .	200
7.11	Pattern fitting, recognizable rotational lines . . . . .	202
7.12	Optical-optical double resonance spectroscopy setup . . . . .	203
7.13	Mainline power saturation . . . . .	204
7.14	Optical-optical double resonance spectroscopy . . . . .	205
7.15	High resolution spectroscopy of the $\tilde{B}^2B_1-\tilde{X}^2A_1$ transition and $\tilde{A}^2B_2-\tilde{X}^2A_1$ transition . . . . .	206
7.16	Molecular constants . . . . .	208
7.17	Photon cycling on the $\tilde{A}^2B_2-\tilde{X}^2A_1$ transition . . . . .	209
7.18	Fluorescence streak imaging of CaOH . . . . .	211
7.19	Buffer gas beam forward velocity measurements . . . . .	212
7.20	Fluorescence streak imaging of a CaOPh beam . . . . .	214
7.21	CaOPh photon scattering rate calibration . . . . .	215
7.22	Spectroscopy apparatus . . . . .	217
7.23	Pump-repump spectroscopy configuration . . . . .	218
7.24	High-resolution spectroscopy of the V=1 repump transition . . . . .	219
7.25	Characterizing the repump transition . . . . .	221
7.26	Pump-repump efficiency measurement . . . . .	222
8.1	CaNH <sub>2</sub> Dispersed laser-induced fluorescence . . . . .	230
8.2	Pump-repump-detect measurements . . . . .	232
8.3	High resolution spectroscopy of the V = 1 repump transition . . . . .	233
8.4	Vibrational repump transitions . . . . .	234
8.5	Spin-rotation structure . . . . .	236
8.6	Rotational leakage channels . . . . .	237
8.7	Rotational leakage check . . . . .	239
8.8	Opposite parity decays . . . . .	241
8.9	Scattering rate . . . . .	243
8.10	Photon scattering with the vibrational repumpers . . . . .	245
8.11	Excitation and scattering rates . . . . .	247
8.12	Photon scattering with the V=2 Repump . . . . .	249
8.13	Molecular beam deflection from photon scattering recoil . . . . .	250
8.14	Schematic overview of the laser cooling setup . . . . .	253
8.15	Doppler Cooling . . . . .	256
8.16	Sisyphus heating and cooling . . . . .	257

TO MY FAMILY FOR THEIR SUPPORT.

# Previously Published Works

Parts of this dissertation have been previously reported in the following publications.

B. L. Augenbraun, S. Burchesky, A. Winnicki, and J. M. Doyle, “High-Resolution Laser Spectroscopy of a Functionalized Aromatic Molecule”, *J. Phys. Chem. Lett.*, **13**, 46, (2022)

S. Burchesky, L. Anderegg, Y. Bao, S. S. Yu, E. Chae, W. Ketterle, KK. Ni, and J. M. Doyle, “Rotational Coherence Times of Polar Molecules in Optical Tweezers”, *Phys. Rev. Lett.* **127**, 123202 (2021)

L. Anderegg, S. Burchesky, Y. Bao, S. S. Yu, T. Karman, E. Chae, KK. Ni, W. Ketterle, and J. M. Doyle, “Observation of microwave shielding of ultracold molecules”, *Science*, **373**, 6556 (2021)

L.W. Cheuk, L. Anderegg, Y. Bao, S. Burchesky, S. S. Yu, W. Ketterle, KK. Ni, and J. M. Doyle, “Observation of Collisions between Two Ultracold Ground-State CaF Molecules”, *Phys. Rev. Lett.* **125**, 043401 (2020)

L. Anderegg, B. L. Augenbraun, Y. Bao, S. Burchesky, L. W. Cheuk, W. Ketterle and J. M. Doyle, “An optical tweezer array of ultracold molecules”, *Science* 365, 6458 (2019)

L. W. Cheuk, L. Anderegg, B. L. Augenbraun, Y. Bao, S. Burchesky, W. Ketterle, and J. M. Doyle, “ $\Lambda$ -Enhanced Imaging of Molecules in an Optical Trap”, *Phys. Rev. Lett.* 121, 083201 (2018)

L. Anderegg, B. L. Augenbraun, Y. Bao, S. Burchesky, L. W. Cheuk, W. Ketterle and J. M. Doyle, “Laser cooling of optically trapped molecules”, *Nature Phys* 14, 890-893 (2018)

# Acknowledgments

Many people helped me during my Ph.D. journey. First and foremost, my advisor John Doyle provided invaluable guidance and mentorship. His curiosity and willingness to take risks in order to push the field forward carried me down pathways I couldn't have foreseen at the beginning of my Ph.D. I moved from working on atoms as an undergraduate to diatomic molecules after joining John's group and then transferred to organic-inspired polyatomic molecules. Each new project was a step into the unknown, further away from my previous experience but towards what we think will be the future of our field. John's extensive technical knowledge cut weeks of troubleshooting and redesigning by steering us around potential pitfalls.

John's "can do" mentality came through as bright as ever during the pandemic. He guided our group to develop new expertise through a series of projects to help hospital workers safely reuse masks, write a master plan to reoccupy our own labs, test the effectiveness of masks and invent a "Chiron" shield to improve the quality of life of the Harvard undergraduates. It was a pleasure to work on the lab re-entry plan, the mask testing, and most of all, the Chiron shield. Much of what I learned from John will help me in my next career in the Space Industry. He served as an excellent group leader, a great advisor, and an admirable mentor. It has been an honor to work with him.

I owe a big thank you to Wolfgang Ketterle. We met during my freshman year of undergraduate studies at MIT. I had seen a PBS NOVA show many years before coming to MIT about Bose-Einstein condensates featuring Wolfgang and I was thrilled to be taking my first physics class from him at MIT. I went to his office hours and asked him many questions. I later had the audacity to ask him for old equipment for a hobby project I was working on and he politely turned me down but then asked if I would like to work on cutting-edge research in his lab. I accepted and joined the BEC II lab in the Fall of 2013, where I worked for nearly four years. We discovered a new phase of matter, the supersolid, but more importantly, I discovered my interest in physics research. As I applied for graduate school programs, Wolfgang directed me toward John Doyle's group. Upon joining the CaF experiment in John's group, it was a pleasant surprise to have Wolfgang as a collaborator on the project. This collaboration amounted to another four years of working with Wolfgang. Wolfgang inspired my interest in AMO physics, mentored me as a young student, shared his remarkably insightful way of understanding the physical world with me, and steered me toward a Ph.D. project that was a perfect match for me.

The Doyle group was a rewarding place to work for five and a half years. The group culture is friendly and welcoming. I began working on the CaF team with Loic Anderegg, Lawrence Chuek, Yicheng Bao, and Scarlett Yu who joined a few years after. In the early days, Loic and Lawrence provided excellent leadership on the experiment and thought me how to run an AMO experiment with more responsibilities and how to run

at a breakneck pace without working extremely long hours. Lawrence soon found a professorship at Princeton and moved on but his sharpness left a long-lasting positive impact on the experiment.

Loic and I had the pleasure of working through the pandemic together on the microwave shielding project. We managed to make progress while working non-overlapping shifts in the lab during the summer and fall of 2020. Loic's technical skills and rapid troubleshooting abilities were extremely useful for the microwave shielding project. We worked together on the coherence time project and finally on the evaporative cooling project before we both moved on to different polyatomic molecules.

Yicheng Bao and I have been working in the high bay since my first day at Harvard. Yicheng's technical abilities and work ethic are unmatched. Working with him is a pleasure; we are productive and have fun the whole time. I still very much enjoy chatting with Yicheng about technical problems I've overcome or issues I'm stuck on even after he moved to the other side of the high bay to build the second-generation CaF experiment. I wish him well moving forward with his academic career. CaF Gen 2 will be left in the capable hand of Scarlett after Yicheng graduates.

The Asymmetric tops team consisted of Ben Augnebraun, Andrew Winnicki, Grace Kehui Li, and Derick Gonzalez-Acevedo. I recall meeting Ben when I visited Harvard as a prospective graduate student in 2017 at the open house. He was working on CaF at the time and his sharpness stood out to me. Years later we joined forces to work on asymmetric top molecules. Ben's dedication to understanding complex molecules

made him an excellent colleague and I wish him well with his new faculty position at William's College. Andrew joined our experiment one year ago as an undergraduate and it was rewarding to watch him grow as a researcher as he prepares for graduate school. Grace worked with us for a year before joining the SrOH experiment, where I wish her continued success.

I owe a thank you to the first lab I worked in as an undergraduate, BEC II at MIT. The experiment was led by Junru Li and Boris Shteynas. They both served as excellent mentors to me and inspired me to pursue my Ph.D. I hope I've returned the same favor to Andrew while we worked together on the asymmetric tops experiment.

Over the course of the CaF experiment, I worked with several collaborators. First and foremost, Wolfgang Ketterle and Kang-Kuen Ni from the Harvard Chemistry Department. Doyle group alumna, Eunmi Chae from Korea University later joined the CaF collaboration. Finally, Tijs Karman (Radboud University) provided theory support for the collisions and shielding experiments. Tijs and I exchanged many long emails and worked out the intricacies of implementing shielding with CaF as well as its limitations.

Many other people in the physics department deserve recognition too. The machine shop staff were invaluable. Stan Cotreau taught me how to machine and weld as a G1, Steve Sansone's patience and persistence made the waterjet a well-used luxury, and Alejandro Lopez runs the student machine shop. Jim MacArthur in the electronics shop helped repair microwave amplifiers during the shielding project and provided good advice saving considerable time. Erica Mantone is the hardworking, ever-organized

driving force behind the Doyle Group's functionality and she does a fantastic job administering the group. Jacob Barandes taught me how to teach during the graduate teaching seminar and was always there to help me navigate the difficulties of graduate school. Lisa Cacciabauda deserves a special thank you for being a long-running part of my Harvard physics experience from the open house she organized through planning my thesis defense.

Finally, my family and friends supported me and kept me busy outside the lab.

# 1

## Introduction

### 1.1 WHY ULTRACOLD?

A long-standing frontier in physics is to understand fragile interacting quantum systems in unprecedented levels of detail by producing them in pristine and manipulable laboratory environments. The promise of quantum technology to deliver meaningful benefits, whether it is a digital quantum computer or new tools for designing materials

with exotic properties, rests with understanding interacting systems in nearly perfect isolation. In this thesis, I will present a new quantum science platform based on arrays of single-trapped ultracold diatomic molecules and initial work towards extending the platform to include larger organic-inspired molecules. Our work is motivated by the prospects of introducing a competitive new molecular platform for quantum computing that addresses some of the challenges facing quantum technology on an implementation level including isolation, long-lived coherences, ease of measurement, individual addressability, and system scalability.

Trapped ultracold atom and molecular systems provide opportunities to observe complicated quantum systems in an environment completely free of impurities and with unique access to some physical observables that are oftentimes unavailable in solid-state systems. The process of preparing an ultracold sample of molecules using laser cooling in particular will be described in great detail throughout this thesis. Laser cooling processes require manipulating the molecule's internal and motional degrees of freedom through highly controlled interactions with optical fields by scattering thousands of photons. The first and most critical step is selecting a molecular species.<sup>131,17,142,5,39</sup>

An extraordinary number of permutations of atoms on the periodic table give rise to chemically bonded molecules. Only a handful of atom arrangements produce structures that lend themselves to laser cooling. In order for laser cooling to work, a molecule must absorb photons and then emit a photon, returning to exactly the same quantum state it came from before the excitation. This sounds simple but the vast majority of

molecules will decay to a large number of different vibrational states after absorbing and emitting several photons.

A general class of molecules has been identified with the property that after photoexcitation, the molecules return to the same rovibrational state with a very high probability.<sup>120,117,80,79</sup> When it decays elsewhere, the number of possible states in which the molecule could branch is small enough to directly address all of these states with a set of repumping lasers tuned for each vibrational level requiring repumping. In the case of calcium monofluoride, which we will use extensively in this thesis, nearly  $10^5$  photons can be scattered using only one mainline laser and three repump lasers.

## 1.2 RESEARCH DIRECTIONS

The effort of trapping ultracold molecules must be commensurate with the research prospects. There are several promising directions including quantum computing,<sup>44,160,76,108,21</sup> quantum chemistry,<sup>86,13</sup> and precision measurement<sup>1,72,90,82,30</sup> for which laser cooled molecules are uniquely suited offering several distinct advantages over competing platforms. Figure 1.1 outlines some of the uses for cold and ultracold molecules.

### 1.2.1 QUANTUM COMPUTING WITH ULTRACOLD MOLECULES

Quantum computing with ultracold molecules is one of the directions most closely linked to the work in this thesis. We imagine using the strong electric dipolar inter-

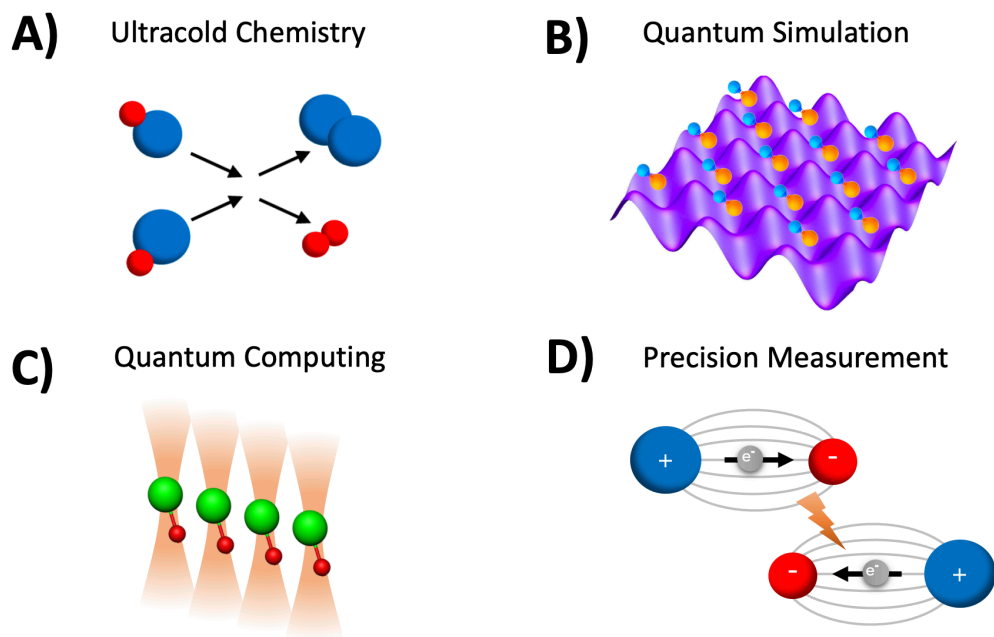


**Figure 1.1:** Pallet of applications for cold and ultracold molecules. Figure A shows a chemical reaction between two diatomic molecules which can be studied in great detail using optical tweezers to trap and react a pair of molecules. Figure B shows ultracold CaF (or similar) molecules in an optical lattice potential. Strong electric dipole interactions between molecules can be used to generate rich Hamiltonians for molecules in an optical lattice, simulating condensed matter systems. Figure C shows CaF molecules in an array of optical tweezers. Similar to the lattice, dipolar interactions can couple neighboring molecules but, in contrast, there is no tunneling between tweezers therefore the molecules remain perfectly isolated. Each tweezer is individually controllable, making this platform ideal for quantum computing. Figure D shows an electron electric dipole moment measurement using the strong effective internal electric field present in ThO molecules. Currently, these measurements are made using beams of cold ThO molecules but in the near future, a large sample of laser-cooled and trapped SrOH molecules could provide a significantly tighter bound on the electron electric dipole moment.

actions between nearby molecules to selectively couple qubits in an array of optical tweezers<sup>44,160,76,108,21,32,124</sup>. In contrast to competing platforms such as optical tweezer arrays of Rydberg atoms, the excited rotational states in molecules we use have natural lifetimes long exceeding the duration of the experiment, which is a key attribute. Long lifetimes and strong dipolar interactions are also useful for analog quantum simulations.<sup>99,26,118</sup>

Several architectures using polar molecules for quantum computing have been proposed but we will focus on the use of optical tweezer arrays.<sup>48,16,6,93</sup> We will develop the optical tweezer platform in this thesis and demonstrate its initial capabilities including scalability, rearrangement, quantum control, and long coherence times. The second generation CaF experiment was able to further the platform, demonstrating larger tweezer arrays, electric dipole coupling between neighboring molecules, and entanglement between molecules in different optical tweezers.

### 1.2.2 QUANTUM CHEMISTRY

Understanding how chemical reactions take place in a highly controlled environment between constituent molecules in pure quantum states is another active research avenue.<sup>87,31,43,11</sup> Calculating potential energy surfaces for colliding and reacting diatomic molecules remains a formidable task for the theory community, thus the predictions need to be informed by experimental input. Studying reactions at the single-molecule scale might inform important innovations in the chemical sciences since ultracold-trapped

molecules provide an unparalleled level of control and access. While the work presented in this thesis does not directly aim to explore these possibilities, our study of molecular collision dynamics already provides some information about the reaction processes of exactly two colliding CaF-CaF molecules in a variety of quantum states in a way that has never been studied.

### 1.2.3 PRECISION MEASUREMENT

The structure of heavy molecules, in particular, provides benchtop scale measurement sensitivity to important quantities in high-energy physics.<sup>1,72,90,82,30</sup> Molecules such as YbOH and SrOH have large effective internal electric fields, augmented by the presence of a heavy nucleus. This internal field provides a way to measure the asymmetry of the electron if it exists, by polarizing the electron leading to a small but potentially measurable splitting. Experiments using beams of ThO molecules, which are not laser-coolable, have placed the tightest bound on the electron electric dipole moment (EDM) of any experiment, including accelerators and colliders.<sup>1</sup> The next generation of molecule-based EDM experiments will make use of a large number of optically trapped laser-cooled molecules where the distinct advantages will include a smaller volume to control systematic effects and a long interrogation lifetime offered by a trapped sample. In addition to EDM measurements, some polyatomic molecules such as SrOH have nearly degenerate vibrational modes which provide sensitivity to some forms of dark matter.<sup>82</sup>

### 1.3 ANATOMY OF A BUFFER GAS SOURCE

The molecular species that support photon cycling and the previously outlined research agenda are all radicals with a single optically active valence electron. This means they are highly reactive species that cannot be stored easily. We generate the molecular species by way of a chemical reaction in a comparatively low-density buffer gas cell where the only matter the radical molecules contact is cold helium with which there are no chemical reactions. The chemical reactions all proceed in a similar fashion: a warm gas containing the ligand of interest flows into the buffer gas cell where cold helium provides suspension for the reactant gases. The other component of the molecule we want to make is a metal atom (either calcium, strontium, or Ytterbium) which we vaporize off a solid metal target using a pulsed-YAG laser. The initially hot molecules form in the bath of cold helium within the buffer gas cell which cools the rotational degree of freedom to a few Kelvin. Within several milliseconds, the newly formed molecules exit the buffer gas cell entrained in a beam of cold, slow helium atoms. The molecular beam exits the cryogenic beambox source and propagates into a room-temperature vacuum chamber where the rest of the experiment takes place. We'll start by describing how the CaF experiment proceeds from this point. Figure 1.2 gives a pictorial overview.

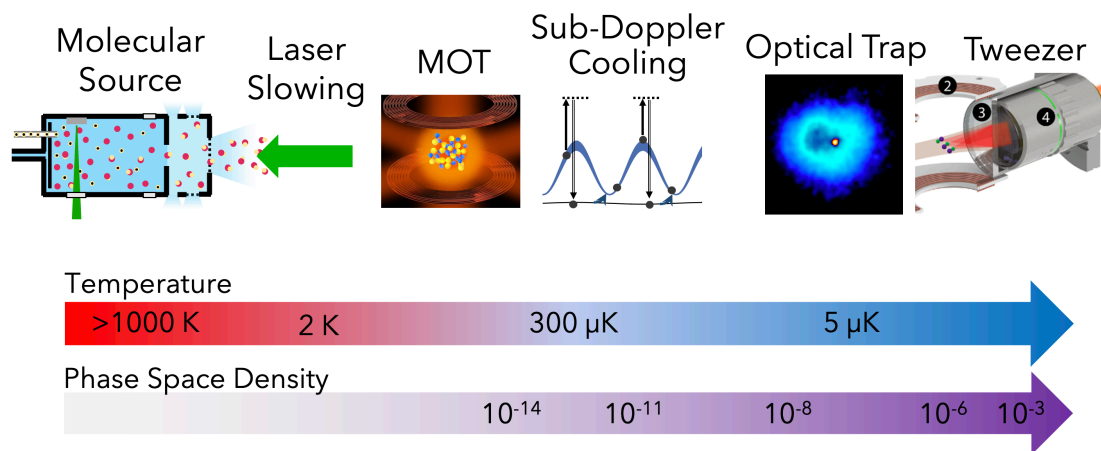


**Figure 1.2:** Schematic drawing of the CaF experiment. CaF molecules are generated in a buffer gas cell at 2 K and then exit as a molecular beam. A counter-propagating laser beam slows the molecules to a few meters per second, at which point they are moving sufficiently slowly to be captured in the MOT. Molecular MOTs act as a reservoir but a conservative trap is needed for the quantum state-controlled experiments described in this thesis. We use a sub-doppler cooling method called lambda-enhanced grey molasses to further cool and load the molecules into the optical dipole trap immediately after switching off the MOT. Finally, the molecules are transferred from the optical dipole trap to the optical tweezer where the experiments described in this thesis take place.

### 1.3.1 CaF LASER COOLING EXPERIMENT

The immediate goal of the CaF experiment is to trap the molecules at ultracold temperatures. As the beam exits the cell, the molecules move at nearly 160 m/s. We use a counter-propagating laser beam to slow the molecules to a near standstill. The slowing happens when molecules absorb photons from the laser beam and then scatter them in a random direction, which provides an average of one photon recoil worth of momentum per photon scattered against the direction of motion of the molecular beam. Repeating this several thousand times is enough to bring the molecules nearly to rest. The difficult part of the process is arranging for the laser light to be in resonance with the molecules despite the Doppler shift. There are several ways to match the frequency, but we will opt to chirp the frequency of the laser beam to match the deceleration profile of the molecular beam.

Once the molecules have been slowed, they must be trapped otherwise they fall to the bottom of the vacuum chamber. This is the job of the molecular magneto-optical trap (MOT). Molecular MOTs are more complicated than their atomic counterparts due in part to the rotational angular momentum structure of the molecule, which atoms lack. The additional challenges for molecular MOTs are highlighted extensively in these references.<sup>17,112,142,5,39</sup> To further emphasize the difficulty, magneto-optical trapping of atoms has been around since 1985<sup>100</sup> whereas the first molecular MOT was realized in 2014.<sup>17</sup> The only molecular species that have been loaded into MOTs are SrF, CaF, YO,

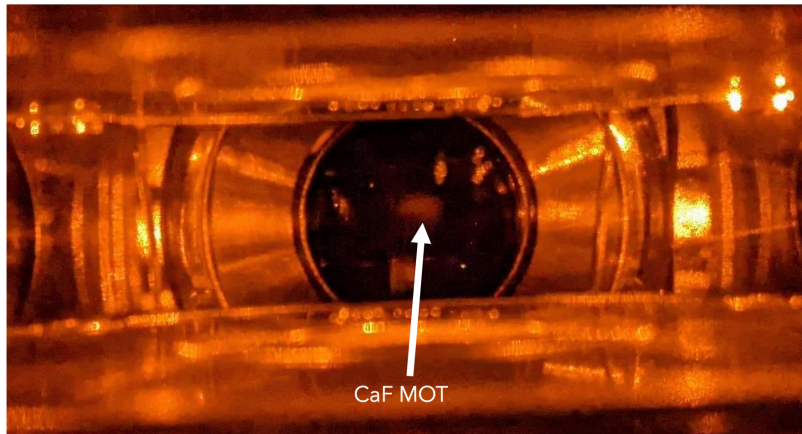


**Figure 1.3:** An iPhone 10 image of the CaF MOT produced in the second generation CaF experiment taken by Yicheng Bao. The MOT is plainly visible without visual aids or filtering. This is the first time a molecular MOT has ever been seen by the unaided eye.

and CaOH.<sup>17,142,39,101</sup>

The CaF MOT in the second generation Doyle group apparatus, led by Yicheng Bao and Scarlett Yu captured nearly  $10^6$  molecules but for most other molecular MOTs,  $10^5$  molecules is a realistic loading number. See figure 1.3 for an image of a molecular MOT. For the purpose of this thesis, the MOT serves as the initial reservoir of molecules for lambda cooling and optical dipole trap loading which we will describe in Chapter 2.

#### 1.4 FUTURE DIRECTIONS

One upcoming frontier in the field is gaining control over large organic-inspired molecules for uses in quantum computing, quantum chemistry, and precision measurement<sup>84,69,83,162</sup>. These molecules are generally asymmetric tops, meaning they have three distinct principal axes with different moments of inertia around each axis.<sup>9,68,46,47</sup> The challenges we

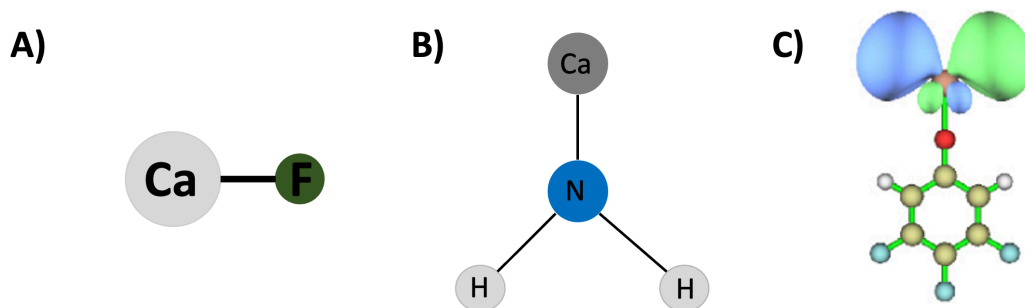


**Figure 1.4:** Schematic drawing of the three molecular species studied in this thesis. Molecule A is CaF, which is a laser-coolable diatomic radical with excellent photon cycling properties. We use this molecule in the optical tweezer experiment for our controlled collision study and rotational coherence time measurements. Molecule B is CaNH<sub>2</sub>, which is a polyatomic radical with reduced spatial symmetry. This molecule belongs to a class of molecules known as asymmetric tops and it is the lowest general symmetry class, where all three principal axes of rotation have different moments of inertia. We demonstrated photon cycling and laser cooling of this molecule. Molecule C is calcium monophenoxide (CaOPh), which is also an asymmetric top with similar spatial symmetry to CaNH<sub>2</sub>. This organic-inspired functionalized radical molecule appeared to be a favorable laser-cooling candidate. We investigated photon cycling and potential laser cooling pathways for this molecule, yet could not identify an unknown loss channel preventing further progress.

will explore in this thesis with these molecules are related to the size and complexity as well as the reduced spatial symmetry. Assuming we can trap these species at ultracold temperatures, the additional structure will offer abundant opportunities to study chemical reactions of organically relevant species and do quantum computing with large qudit (quantum “bits” with more than two levels involved) systems. Small asymmetric top molecules such as SrSH might offer higher sensitivity to high-energy physics phenomena which can be measured spectroscopically. Figure 1.4 gives an overview of the species studied in this thesis.

## 1.5 THIS THESIS

In this thesis, I'll cover experiments on ultracold CaF molecules in optical traps and on polyatomic molecules with reduced spatial symmetry for future use in laser cooling experiments. Chapter 2 gives a broad overview of the work we did to optically trap and laser cool CaF molecules. We demonstrated lambda-enhanced grey molasses cooling which we immediately used to cool molecules into a conservative optical trap and eventually image them with high fidelity. Loading CaF molecules into conservative traps, especially optical traps, was the key step for the CaF experiments outlined in this thesis.<sup>149,97,3,34</sup> We took the optical trapping approach a step further to make an optical tweezer array by compressing the trap volume to a regime where only a single molecule remains in the trap after the loading process.<sup>6,128,155,77,111,41,123</sup> The array of optical tweezers was generated by diffracting a laser beam opto-electronically giving us the ability to move the traps around in real-time. In Chapter 3, we utilize our dynamical controls over the optical tweezer array to do a carefully controlled study of collisions between exactly two molecules. We simultaneously implemented microwave state control allowing us to prepare the molecular sample in an internal state of our choosing. Ground state molecules underwent rapid collisional loss, as did all other internal state configurations we tested. In Chapter 4, we developed a microwave shielding scheme that creates a long-range repulsive barrier around the molecules to prevent them from coming sufficiently close to undergo chemical reactions or other related loss processes.

The microwave shield suppressed the collisional loss rate by a factor of 6 while enhancing the rate of elastic collisions.<sup>51,119,50,74</sup> In Chapter 5, we take advantage of the elastic collision rate to demonstrate forced evaporative cooling. The microwave shielding is necessary to see the effect however our small sample size and limited lifetime hampered our efforts to obtain a molecular Bose-Einstein condensate through evaporative cooling. In Chapter 6 we explore the optical tweezer array potential as a quantum computing platform by measuring the rotational coherence time. This key property indicates how long the qubits will maintain memory, either of how they were programmed or the result of a computation. The 100 ms coherence time we observed was made possible by a variety of control tactics including active feedback of noise sources from the lab environment and optical tweezer control<sup>121,78</sup>.

Chapter 7 represents a major change in direction. Diatomic molecules such as CaF offer advantages over atomic systems due in part to the additional rotational structure of a molecule. Generally, a system with more structure will have the potential to be more useful, as long as the structure can be controlled. In that spirit, we initiated a study of calcium mono-phenoide (CaOPh) molecules in an effort to identify a laser cooling path for a large molecule with significantly reduced spatial symmetry.<sup>9,68,46,47</sup> We upgraded our apparatus to produce these organic-inspired molecules, studied the rotational spectrum at high resolution, identified the transitions needed for optical cycling and vibrational repumping, and then carried out provisional experiments where we observed photon cycling. The results were unexpected; a slow scattering rate and unknown

loss channels limited the number of photons scattered. In Chapter 8, we switched to a smaller molecule,  $\text{CaNH}_2$  which has similar spatial symmetry to  $\text{CaOPh}$ . Our goal was to laser cool  $\text{CaNH}_2$  and understand the role of reduced symmetry in photon cycling which we can then apply to  $\text{CaOPh}$ . We observed photon cycling on  $\text{CaNH}_2$  and then successfully implemented Sisyphus cooling and heating processes. Similar to  $\text{CaOPh}$ , we ran into unknown loss channels in  $\text{CaNH}_2$ .

# 2

## Trapping and Cooling a Single Molecule

Isolating and containing samples of atoms and molecules in a pristine environment is a key enabler for modern AMO studies. The ideal means would allow a pure, controllable sample to be trapped in a pristine environment for a long period of time. While a bottle of gas satisfies the purity and lifetime requirements in most cases, the level of single-molecule control over the sample and isolation from the environment is insufficient. The

pristine isolation we desire requires a vacuum environment and non-solid confinement, which is very hard in practice.

For some experiments, forgoing confinement is an acceptable concession. This brings molecular beams into the picture. Beams are very useful as they allow single particle control in dilute, pure samples with excellent isolation from the lab environment. The last two chapters of this thesis will deal entirely with a beam-delivered source, however, for all of our results on the CaF molecule, we require long experimental lifetimes, extremely tight confinement, and an exquisite level of control not available in a beam.

This is the role of optical trapping in our experiment, and it is accomplished in the form of an optical dipole trap (ODT) and an optical tweezer. The ODT is formed from a tightly focused laser beam where the molecules are attracted to the region of highest light intensity at the focus. In contrast to other types of traps (magneto-optical traps and magnetic traps), single quantum state control is available because the trapping characteristics are nearly independent of the molecule's internal state and ODTs are conservative traps.<sup>150,98,17,112,136,143,5</sup> Optical dipole traps of assembled bi-alkali molecules have been realized<sup>140,106</sup> before but we seek to trap laser-cooled molecules with an optically active valence electron, a completely new class. Taking advantage of this control we will explore two major research directions in the next few chapters: collisions of two molecules and the coherence properties of trapped molecules for quantum computing applications<sup>118,44,160,99,30,152,114</sup>.

## 2.1 OPTICAL DIPOLE TRAPS

An optical dipole trap (ODT) is a tightly focused laser beam, usually red-detuned from resonance. The AC Stark shift, given by  $I\alpha/\Delta$  describes how the energy levels shift when the molecules are illuminated by light with detuning  $\Delta$  and intensity  $I$ . The polarizability,  $\alpha$ , is wavelength dependent and carries the information about the structure of the atom or molecule. For red-detuned light, the sign of the AC-Stark shift is negative so the ground state energy of the molecule is lowered by moving to a region with higher light intensity. Blue detuned light has the opposite effect. The spatial part of the trapping force comes from the spatial gradient of the light intensity, pulling the molecules to the center of the trap. For CaF, we use a 1064 nm optical trapping beam, which is far red-detuned from the X-A transition. One distinct advantage of using far-detuned wavelengths is that the off-resonant scattering rate scales as  $1/\Delta^2$  whereas the trapping depth only decreases as  $1/\Delta$ . Our trap consists of a 13 Watt beam focused to 30  $\mu\text{m}$  at the location of the molecules. This provides a trap depth of 380  $\mu\text{K}$  and an off-resonant scattering rate less than 1 Hz.

### 2.1.1 TRAPPING CHARACTERISTICS OF A GAUSSIAN BEAM

The geometry of the trapping environment is defined by the intensity profile of a focused Gaussian beam and it is the same for both an optical dipole trap and an optical tweezer. The intensity profile of a focused gaussian beam is

$$I(r, z) = I_0 \left( \frac{\sigma_0}{\sigma(z)} \right)^2 e^{-2r^2/\sigma^2(z)} \quad (2.1)$$

where  $\sigma(z) = \sigma_0 \sqrt{1 + (z/z_r)^2}$  and  $\sigma_0$  is the beam waist at the focal plane. The quantity  $z_r = \pi\sigma_0^2/\lambda_{trap}$  is called the Rayleigh range and it is the length scale along the axial direction of the beam (along the k-vector).

The radial trapping force is relatively strong because the tight beam waist  $\sigma_0$  sets the curvature of the trap. For small displacements in the focal plane ( $z=0$ ) the trap looks nearly harmonic and we can approximate it as:

$$U(r) \approx \frac{2}{\sigma_0^2} \frac{\alpha I_0}{\Delta} r^2 \quad (2.2)$$

The harmonic expansion describes some of the behavior of a cold, trapped gas but it misses finite depth effects which are always relevant to the loading and loss processes. The main utility of the harmonic expansion is that it allows for an easy way to characterize the trapping potential. Molecules moving in the trap oscillate in the radial direction with a frequency of approximately 2.5 kHz, which will be measured later.

If we do the same analysis along the z-direction, we can write the trapping potential as follows:

$$U(z) \approx \frac{\alpha I_0}{\Delta} \frac{z^2}{z_r^2} \quad (2.3)$$

Along the axial direction, a focused Gaussian beam has an intensity profile that is much less steep than the radial direction. We can see this from the expression for the Rayleigh range, by factoring it as  $z_r = \pi w_0(w_0/\lambda)$ . Diffraction of the beam implies  $w_0 > \lambda$  therefore the Rayleigh range will always be a softer trapping potential than the radial direction. In the case of our ODT, the Rayleigh range is an enormous 2.6 mm in comparison to the radial dimension of 30  $\mu\text{m}$ . CaF molecules moving harmonically along the axial direction will oscillate with a frequency of 20 Hz.

In the context of the harmonic approximations, we've assumed the molecules are deep in the trap. The parameter  $\eta = U_0/T$  is a useful way to characterize the sample since this quantity appears in the statistical mechanics analysis of a classical thermal gas in a trap. The molecules in our experiment are cooled to about 30  $\mu\text{K}$  (we will discuss cooling in the next section), resulting in  $\eta \approx 12$ . For  $\eta = 10$ , the trap potential is very harmonic with the molecule bound to  $\delta r \approx \sqrt{1/\eta} \approx 10 \mu\text{m}$ . At smaller values of  $\eta$ , molecules are energetically allowed to occupy the wings of the trap which have much softer curvature than the center regions resulting in slower, non-harmonic motion.

### 2.1.2 LOADING THE OPTICAL DIPOLE TRAP

Getting the molecules into the trap is not a simple endeavor. Unlike the MOT, an optical dipole trap on its own is conservative therefore no cooling processes are naturally present. Any molecule that traverses the trap will have enough energy to escape the trap when it re-emerges on the other side. If we imagine loading the trap from a cloud

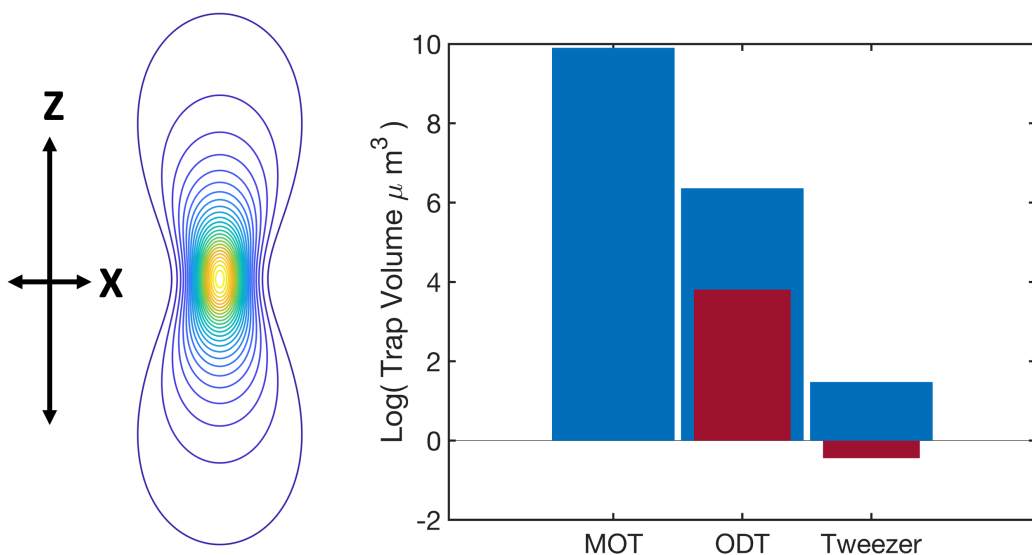


**Figure 2.1:** Left is an equipotential contour plot of the optical trapping potential produced by a focused beam. The ODT and the tweezer have similar contours, with different aspect ratios. Note the softening of the potential along the axial (z) direction. To the right is a size comparison of the three traps we use in the experiment. The MOT volume is based on the temperature and compression of the molecules. The blue bars showing ODT and tweezer trap volumes are calculated geometrically from the trapping beam properties and the red bars show the cloud size in the trap, considering the temperature. For ODT loading, the blue MOT bar and blue ODT bar are the relevant comparisons. This indicates the importance of cooling during loading, as these traps do not have good spatial mode overlap. For tweezer loading, compare the red ODT bar to the blue tweezer bar. This once again shows how the large cloud of molecules in the ODT needs to be cooled and compressed to effectively load the tweezer. Finally, the red tweezer bar indicates the volume a single molecule at  $40 \mu\text{K}$  explores in the tweezer.

of cold molecules (let's not worry about the origin of this cloud yet) we might first try adiabatically ramping the depth up from zero to full depth. That would capture the molecules spatially overlapped with the trap but it would create a sample with a temperature roughly equal to the trap depth. In other words, most of the molecules would have energies barely below the top of the trap. It would also require long loading times to maintain adiabaticity.

Alternatively, we could add a cooling process as we ramp the trap up. The effect of this is twofold; first, it would cool the molecules already in the trap volume much lower into the trap resulting in a colder sample. Secondly, molecules originating from outside the trapping volume that happen to cross the trap while the cooling light is on will be cooled into the trap and captured. See figure 2.1 for a loading schematic comparison.

## 2.2 SUB-DOPPLER COOLING

The dissipative mechanism needed to load the traps comes from laser cooling. Before we consider trap loading and other trap-induced effects, let's get a handle on how the cooling mechanism works in free space. There are several similar cooling schemes that achieve base temperatures below the Doppler limit ( $250 \mu\text{K}$  for CaF). In the case of systems with inverted angular momentum structures (higher angular momentum in the electronic ground state than the electronically excited state) such as molecules or alkali-atoms on the D1 line, the schemes require modification but the basic physics is still the

same<sup>56,132,45,143</sup>.

The laser cooling scheme, commonly referred to as grey molasses cooling, creates a motional damping force capable of cooling molecules well below the Doppler limit<sup>143,4</sup>. Grey molasses cooling relies on the interplay of bright states, dark states, and non-adiabatic coupling between them. In the next section, we'll discuss an additional cooling feature called Lambda-Enhanced grey molasses that significantly improves the robustness of the dark states, leading to a lower temperature floor.

### 2.2.1 GREY MOLASSES COOLING

The sub-doppler cooling scheme is the next step from the MOT towards significantly lower temperatures and loading of conservative ODTs.<sup>143,4</sup> The cooling beams come from all 3 directions and are retro-reflected back on themselves. Furthermore, each beam is circularly polarized creating a 3D polarization gradient at the location of the molecules. This polarization gradient is responsible for creating dark states. Our system has higher angular momentum in the ground state than the excited state, guaranteeing the existence of dark states that do not couple to the light field. The bright states, by contrast, feel a strong AC-Stark shift as the molecule moves through the polarization gradient formed by counter-propagating circularly polarized laser beams. This polarization gradient is generated by the same beams that form the MOT. To transition to the sub-doppler cooling step, we quench the MOT magnetic field and jump the detuning with the beams briefly switched off during the transition.

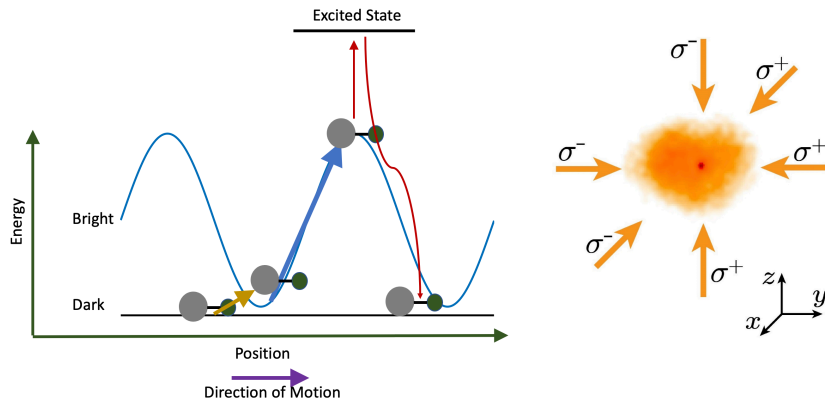


**Figure 2.2:** Left is a schematic of the laser cooling process. A molecule traveling from left to right, initially in the dark state will non-adiabatically couple into the bright state near the minimum (gold arrow). The molecule in the bright state moves up AC-Stark shift potential hill until it nears resonance with the optical pumping light at the top of the potential (straight red arrow). The molecule scatters photons until it is pumped into the dark state (curved red arrow) and then the cycle repeats. The image on the right is a fluorescence image of molecules loading into the ODT from the molasses cloud. The arrows indicate the direction of the 3D retro-reflected cooling beams with their polarizations noted.

Molecules in the bright state moving through the standing wave will climb the potential hill and lose kinetic energy<sup>56,132,45</sup>. At the top of the hill, the light intensity is brightest and the molecule has a higher chance of being excited by a photon which can result in a decay to a dark state via spontaneous emission, as shown in Figure 2.2. In this way, the molecule was lowered down the potential hill by the photon so it arrives in the dark state at the bottom of the hill without regaining any of the kinetic energy lost while rolling up the AC Stark shifted potential hill. The photon emitted carries away the energy and the molecule is cooled.

The key to repeating this cycle is to have a way to couple the dark states slowly back into the bright state manifold. This is accomplished non-adiabatically. As the molecule

moves, there is a small Doppler shift that destabilizes the dark states. Ideally, the non-adiabatic passage between bright and dark states happens at the base of the AC Stark shift potential hill so that maximum kinetic energy can be removed each cycle. The transition rate is maximized at the base of the hill, owing to the fact that the energy gap is smallest here.

The detuning of the molasses light controls whether the bright states are above or below the dark state. In the case of red detuning, the non-adiabatic coupling happens at the top of the hill and the optical pumping happens at the bottom. This results in heating since kinetic energy is added to the system every cycle. Blue detuning (which is what we use, of course) flips the AC Stark shift of the bright states and creates the cooling environment that we desire.

The cooling process is very sensitive to magnetic fields. The dark state is defined by laser polarization and consists of different magnetic sub-levels in a careful superposition. Magnetic fields will mix the bright and dark states, but not in the spatially selective way the motional non-adiabatic coupling does. The mixing from the magnetic field is independent of motion and position in the light field thus it interrupts the cooling significantly. We find we have to cancel the earth's magnetic field to better than 50 mG to reach our base temperature of  $50 \mu\text{K}$  in free space.

### 2.2.2 LAMBDA-ENHANCED COOLING

The performance of the grey molasses cooling is inherently limited by the “darkness” of the dark states. A better version of the same cooling mechanism can be realized with more robust dark states<sup>55</sup>. These dark states are not simply states that remain uncoupled by the polarization, but they are coherent dark states generated by two detuned laser beams, creating a lambda system. See Figure 2.3. We will refer to this cooling process as Lambda cooling which works in combination with the grey molasses. The grey molasses cooling sub-doppler mechanism remains the same as I just described but now the lambda system dark states will safeguard the cold molecules from heating processes by keeping them dark, resulting in much colder temperatures than grey molasses alone<sup>55,25,132,40</sup>.

This set of dark states lends itself to a cooling process known as Velocity Selective Coherent Population Trapping (VSCPT) where molecules at rest remain (ideally) perfectly dark whereas molecules in motion continue to see the grey molasses cooling effects until they scatter into the coherent dark states. Finding the coherent dark states is a diffusive process but once the molecules enter the dark state, there are generally 3 ways to exit. One way is, again, the Doppler shift  $\delta = kv$  where  $k$  is the wave vector of the cooling light and  $v$  is the velocity of the molecule. As the molecules get colder, they remain dark for longer<sup>7,88,89</sup>. This is inherently part of the cooling process and we won't consider it to be a problem, as long as the sample is initially cold enough to be within

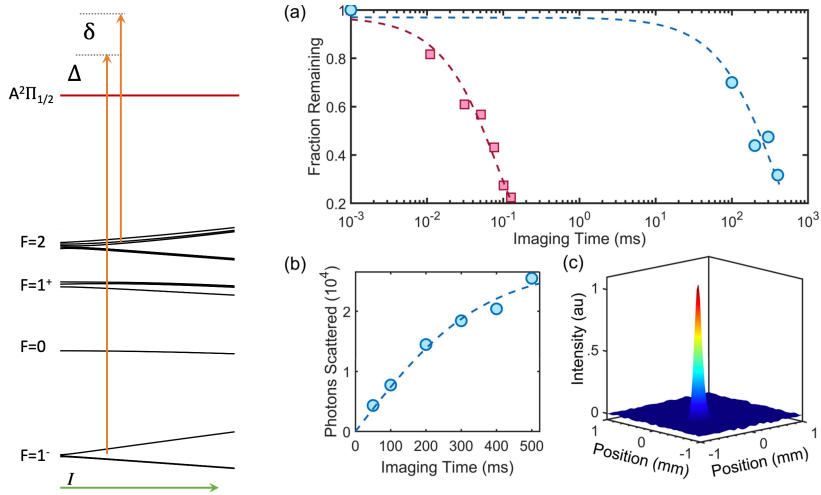


**Figure 2.3:** Left: The level diagram of the  $N=1$  ground state manifold in the presence of a strong far-detuned optical field with linear polarization. The two orange beams indicate the two legs of the VSCPT scheme with two-photon detuning  $\delta$  and single photon detuning  $\Delta$ . The single-photon detuning,  $\delta$  plays the same role as the grey molasses detuning and the two-photon detuning  $\Delta$  plays a key role in establishing the VSCPT dark states. To the right is a demonstration of the imaging performance. Figure a shows the survivability vs imaging time for lambda imaging vs resonant imaging. Box b shows the number of photons scattered during lambda imaging. We can scatter 200 times more photons during lambda imaging than resonant imaging. Box c is an image of the ODT taken with lambda imaging, demonstrating the excellent signal-to-noise ratio.

the capture range. This is always the case for us.

Another way to escape the dark state is through external field remixing, similar to the grey molasses dark states in the presence of the magnetic field. The VSCPT dark states are also combinations of magnetic sublevels with different magnetic field sensitivity. This causes the VSCPT dark states to precess and become bright again. We cancel the Earth's magnetic field to the 0.01 Gauss level, enough to ensure magnetic fields are not the temperature floor limitation.

The third way molecules exit the dark state is by off-resonant scattering of the cooling light. This is our major limitation in free space. The lambda cooling light requires two beams, which address the  $F = 1^-$  and  $F = 2$  levels. Due to the relatively tight spacing of the hyperfine levels, the lambda cooling beams are never far detuned from the other hyperfine levels that nominally don't participate in the cooling process. This is where the off-resonant scattering has the largest impact on our temperature, limiting us to  $5 \mu\text{K}$  in free space.

### 2.2.3 COOLING INTO AND IMAGING IN OPTICAL TRAPS

We've built an understanding of the cooling mechanisms in free space for the explicit purpose of using lambda-enhanced grey molasses to load optical traps and to image the molecules. The optical traps cause new issues for the cooling processes as well as add richness since we will be forced to understand the interplay of trap motion and cooling.

Unfortunately in the optical trap environment, we cannot cancel every effect that

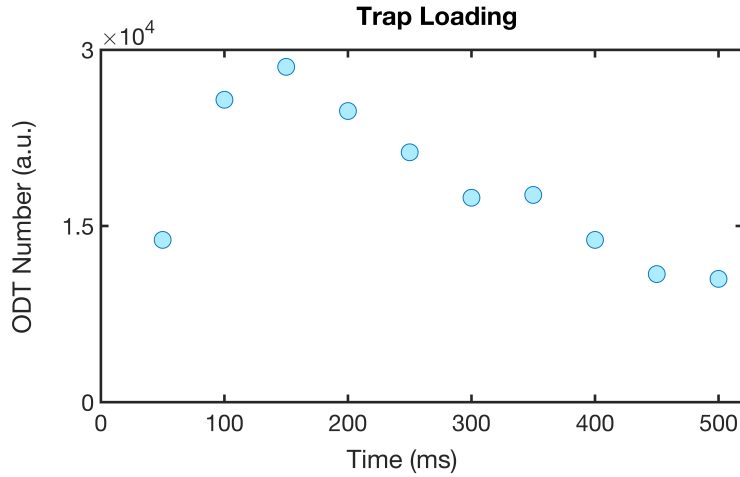


**Figure 2.4:** This plot shows the number of molecules loaded into the 1064 nm ODT as a function of overlap time with the lambda cooling light. The optimal loading time at 100 ms corresponds roughly to the amount of time it takes a molecule to traverse the trap volume. Beyond 150 ms, the molasses cloud density drops significantly and the loss rate out of the ODT is faster than the loading rate from the now dilute molasses cloud.

causes mixing of the dark states with the bright states as we did with stray magnetic fields in free space. In the presence of far-detuned linearly polarized light, like in the ODT, the molecules experience an anisotropic and state-dependent interaction with the laser light. We will describe the nature of this interaction in much more detail later but for now, all we need to know is that the ODT light will split the magnetic sub-levels similarly to a DC electric field. This interrupts the dark states in the same way as a stray magnetic field however there's no simple way to counteract it.

The effect of the light shifts from the ODT is twofold. The detuning of the sub-doppler light shifts slightly to accommodate the scalar shift from the trap. The secondary effect is that the base temperature comes up to  $20 \mu\text{K}$  when the cooling light is fully optimized.

While it is possible to do clever things to mitigate the effect of the light shifts on the cooling performance, this operating temperature is more than sufficient to load the ODT from the molasses cloud.

The cooling process is fairly fast with a time scale of 100 ms, as seen in Figure 2.4. It is important to load the ODT as fast as possible because the molecules in the molasses cloud are not trapped; they are frozen in place but still diffuse around due to the recoils from the optical pumping photons. Density is quickly lost as a result. We find the optimal loading time is about the amount of time it takes a molecule to cross the ODT trapping volume at the rms velocity of 2 cm/s corresponding to the 20  $\mu\text{K}$  sample temperature. Any loading after this point is diminishing returns due to the expansion of the molasses cloud and loss processes in the trap.

While we need the lambda cooling light to load the trap and produce the coldest sample, we take advantage of its dual purpose to scatter photons and cool as a way to enhance our imaging, non-destructively<sup>48,16,20</sup>. Similar techniques have been used for quantum gas microscope experiments with atoms<sup>12,130,59,36,116</sup>. Since the beams provide cooling while scattering photons, many many photons can be scattered from the system before the molecules are lost. Compared to resonant scattering, lambda-enhanced cooling produces about 200 times as many photons despite the significantly slower scattering rate of the cooling light. This is because of the extremely long imaging lifetime of the molecules in the large 1064 nm ODT. In the optical dipole trap the imaging lifetime was 370 ms before the molecules were lost. By comparison, the vacuum

lifetime is 700 ms, limited by background gas collisions with stray Helium atoms. The resonant imaging lifetime is around 10 ms since the molecules are heated continuously during the imaging process. We will revisit imaging shortly, however, I'll mention now the use of lambda cooling light for imaging purposes is what made single molecule detection possible in the optical tweezers.

### 2.3 OPTICAL TWEEZERS

The optical tweezer is nothing but a very tight optical dipole trap capable of holding exactly one molecule<sup>128,126</sup>. However, this is potentially part of an extremely powerful platform for quantum computation<sup>44,160,76,108,21</sup>, simulation<sup>99,26,118</sup>, studying ultracold chemistry<sup>86,13</sup> and even performing searches for beyond-the-standard-model physics<sup>157</sup>.

For now, assume the single-molecule nature of the tweezer loading and we will revisit this in detail later in this chapter<sup>128,155,77,111,41</sup>. The optical tweezer is generated by sending a 780 nm laser beam through an acousto-optical deflector and then through a 0.29 numerical aperture commercial microscope objective, pictured in Figure 2.5. The tweezer beam is nearly diffraction limited, producing a trap with a beam waist of 1.8  $\mu\text{m}$ , much smaller than our optical dipole trap.

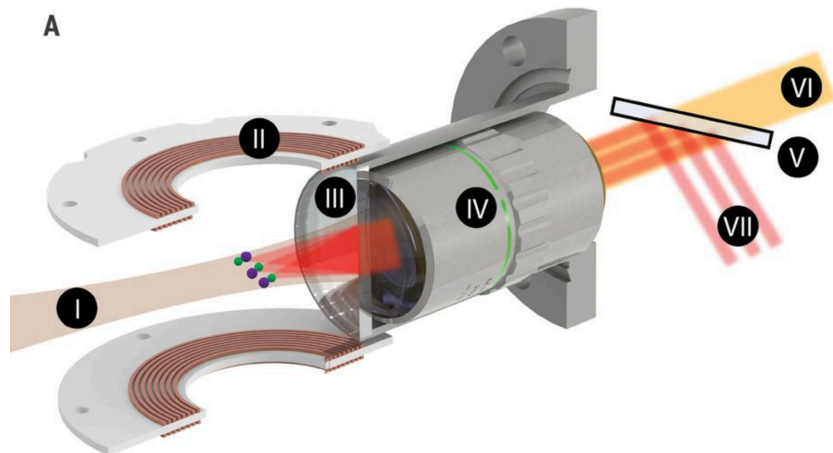


**Figure 2.5:** Schematic of the optical tweezer layout. A 0.29 numerical aperture objective (IV) from Mitutoyo fits tightly in a re-entrant window positioned as close as possible to the edge of the MOT coils (II) to accommodate the objective working distance of 3 cm. The beam labeled (I) is the 1064 nm ODT, propagating from the left to the right. The window (III) is coated to reflect the 1064 nm light. Beam VII is the tweezer light after the AOD. Three optical tweezers are generated by putting 3 closely spaced RF tones into the AOD. VI indicates the imaging beam path through the same objective that projects the tweezers. Dichroic V reflects the 780 nm tweezer light but passes the 606 nm fluorescence light to the EMCCD camera (not shown).

### 2.3.1 LOADING THE TWEEZERS

Due to the small size of the tweezer, we employ the 1064 nm ODT to provide a sufficient reservoir of molecules at a higher density than the background molasses cloud. The relative trap volumes and trap density comparison in figure 4.16 illustrates the need for a density “stepping stone”.<sup>127,156</sup> Loading the tweezer from the molasses results in a few percent loading of the tweezers with a molecule, whereas loading from the high-density ODT can saturate the theoretical loading rate of the tweezers (50%). The 1064 nm ODT and the tweezer are aligned coaxially, which relaxes the z-axis alignment. In fact, we see tweezer loading for a wide range of focal plane positions of the 1064 ODT. The

transverse alignment is very sensitive and occasionally drifts but was otherwise stable using nothing more than radiant dye double spring optics mounts.

During the transfer between the 1064 ODT and the tweezer, we adiabatically ramp up the tweezer light while applying our lambda cooling beams. The lambda cooling beams require slightly different detunings in the tweezer to compensate for the higher intensity and the polarizability difference between 1064 nm and 780 nm traps.

### 2.3.2 SINGLE MOLECULE LOADING

The key capability of the optical tweezer is that it reliably loads single molecules. However, proving single-molecule loading can be challenging. Making a histogram of the fluorescence is a very useful way to look at the tweezer data. The histogram is produced by taking many images, counting the fluorescence brightness in the region of interest, and then plotting the occurrence probability vs brightness. The shape of the histogram is a signature of single-molecule loading. When the molecules are imaged, they are significantly brighter than the background which, on the histogram, appears as a peak separated by a well-defined valley from the peak corresponding to the background (unloaded tweezer) image counts. Figure 2.6 shows a resolved histogram where the background camera counts and camera counts accumulated during the imaging of a tweezer loaded with a molecule are well separated.

Initially, we used this as a diagnostic to prove single molecule loading. By lowering the density in the transfer ODT, we observed a fluorescence peak in the histogram that

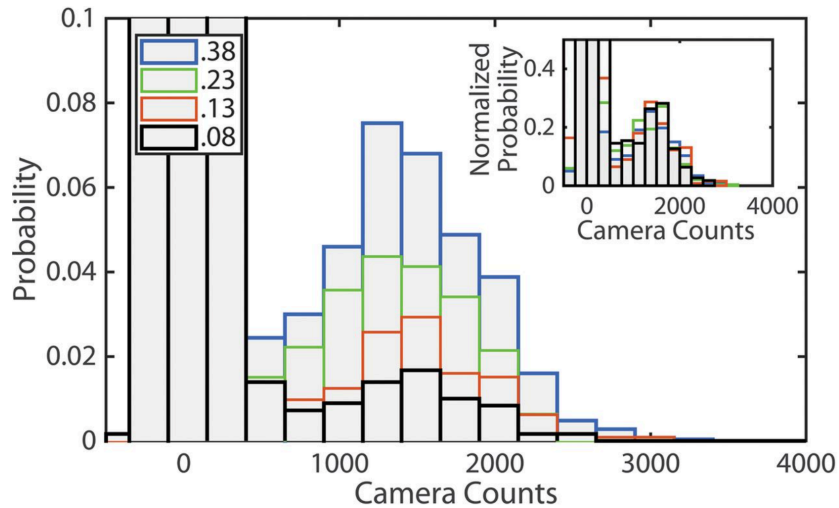


**Figure 2.6:** This figure shows histograms of the imaging fluorescence for variable loading rates. We adjusted the loading rate by reducing the number of molecules in the 1064 nm ODT. The fluorescence histogram shape remains the same, indicating that with a reduced loading fraction the fluorescence doesn't become dimmer in an individual shot. This is the signature of single molecule loading in the tweezer.

did not change shape but simply scaled down. Maintaining the shape indicates the source of the fluorescence (a single molecule) is unaffected by the change in density of the transfer ODT. Had it been multiple molecules, the fluorescence peak would have become dimmer and narrower in response to lowering the density. Instead what we see is that the fluorescence peak looks the same however the tweezer is loaded less often due to the lower density in the transfer ODT. This is an unambiguous signal of single molecule loading in the optical tweezer.

For the platform to be useful, single-shot high-fidelity detection is imperative, and improving this fidelity was the next key step. Without the ability to identify single molecules in a single shot, we lose the ability to make defect-free arrays which would

prevent us from using this as a quantum computing platform. Behind the scenes, a lot of work went into mitigating background laser scatter and optimizing the lambda imaging parameters to generate the most photons. The goal is to create as large a separation as possible between the background light peak and the single-molecule fluorescence peak in the histogram.

We can use the histogram to set the threshold distinguishing a loaded tweezer from background light and to calculate the imaging fidelity based on this threshold. For unloaded tweezers, there is always some scattered light background with a characteristic width. In the single shot resolved regime, the histogram will be strongly bimodal where the fluorescence peak associated with a loaded tweezer is much brighter and well separated from the background peak. The separation of the two determines the imaging fidelity or the error rate to misidentify an empty trap as a loaded trap. This is a particularly bad type of error and we seek to avoid it.

### 2.3.3 IMAGING THE TWEEZER

Avoiding loaded versus unloaded tweezer misidentification errors requires excellent imaging and our lambda cooling scheme is the key to making this platform usable. Imaging through the same objective used to project the tweezer, we collect about 1% of the fluorescence light given off by the molecules on the camera. The lambda cooling light is extremely useful for imaging because it actively cools the molecules while producing fluorescence, leading to an imaging lifetime exceeding 150 ms, over which many photons

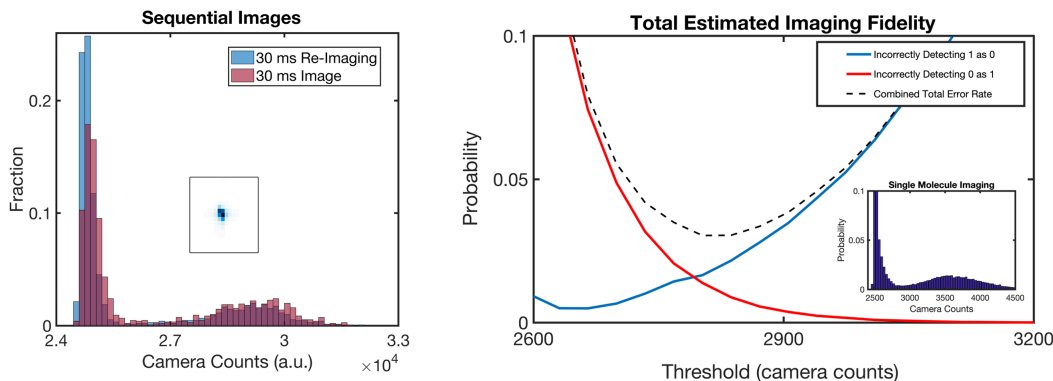


**Figure 2.7:** On the left is a histogram of the tweezer image fluorescence. The general shape of the histogram is the result of two processes; the first large peak shows the background and the second smaller bump to the right is the fluorescence yield of a single molecule in the tweezer. The red bars indicate the fluorescence captured during an initial 30 ms exposure. The blue bars indicate the fluorescence captured in a second consecutive image of the same molecule. Our ability to re-image is critical to the utility of the platform since the first image is needed to identify loaded traps and the second image is measuring the experimental result, always as a surviving fraction. On the right, we characterize the imaging fidelity by considering where to set the threshold to discriminate between background light vs loaded molecules. The two kinds of errors are 1) misidentifying a loaded trap as empty and 2) misidentifying an empty trap as loaded. The second type of error is very bad, the first type only reduces our data rate. The plot on the right characterizes the type 1, type 2, and overall error rates as a function of the threshold value.

can be integrated by the EM CCD camera. We optimized the imaging parameters to maximize the product of the lifetime and the scattering rate, i.e. produce the most photons while maintaining a high survival probability. Due to the stochastic loading of the optical tweezers, it is necessary to image twice during the experiment. The first image identifies loaded tweezers prior to initiating the “experimental” step of the sequence. The second image taken after the experiment runs is simply a readout shot.

For the first image, survival is just as important as fidelity. We image for 30 ms with a scattering rate of approximately 50 kHz, resulting in the scattering of 1500 photons. We can distinguish a loaded tweezer from an empty tweezer with a fidelity exceeding

97%, as shown in Figure 2.7. Furthermore, about 90% of the molecules remain in the trap after imaging. For the second image, survival is not important at all and we image for at least 60 ms to collect as many photons as possible from each molecule before it is lost.

The mechanism for the imaging loss isn't particularly well understood however we believe the molecules are random-walking out of the trap. In the regime where the scattering rate is higher than the trap frequency, molecules on the edges of the trap can randomly walk out as they scatter light in the molasses (lambda cooling) beams. The loss rate depends on the scattering rate and on the geometric size of the trap. The optical tweezer imaging lifetime is about 4 times shorter than the ODT. This is not proof, but it is consistent with a random walking diffusive model.

#### 2.3.4 CHARACTERIZING THE TWEEZER

In contrast to the larger 1064 nm optical dipole trap, we seek to have a much better understanding of the optical tweezer trap potential. The easiest trap parameter for us to measure is the trapping frequency. We do this by applying a shallow sinusoidal modulation to the trap light. The equation of motion of a molecule in a trap undergoing amplitude modulation is  $\ddot{X} + \Omega(1 + \epsilon \sin(\omega t))X = 0$  where  $\Omega$  is the trap frequency and  $\omega$  is the frequency of the weak modulation,  $\epsilon$ . Driving this system at  $\omega = 2\Omega$  results in a growing amplitude (parametric resonance). Experimentally, we would drive the tweezer intensity at about 5 – 10% modulation depth for roughly 200-500 cycles. As we

scanned the drive frequency looking for decreased survival corresponding to the parametric heating resonance, we were careful to hold the number of cycles constant. This was important to produce loss curves without a global slope. Matching the measured trapping frequencies to the input power through the objective, we backed out the tweezer beam waist by comparing it to a Monte Carlo code simulating the classical motion of the molecules.

The second important property is the sample temperature. To be precise, an optical tweezer only contains one molecule therefore the temperature I'm referring to is the average per particle energy of an ensemble of tweezer traps represented by a single tweezer re-loaded every experimental cycle. We measure the temperature using the "release and recapture" method which involves rapidly shutting off the trap for a variable period of time and then suddenly turning the trap back on to recapture any molecules that remain in the trap volume. We can extract the temperature by fitting the data to the results of a Monte Carlo simulation seeded at a known temperature. We find this way of measuring temperature fast and experimentally reliable however there could be systematic issues with how the tweezer trap is modeled. Figure 2.8 shows the temperature and trap frequency measurements.

During a later project, we measured the temperature using the time of flight expansion of a single molecule in the tweezer. The data rate was very slow, however, with  $10^5$  shots taken, we fit a temperature that was in agreement with the release and recapture measurements.

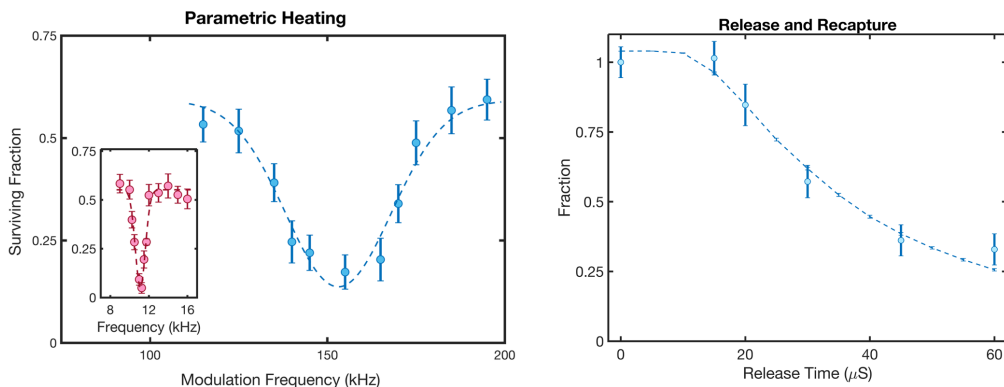


**Figure 2.8:** Left is a measure of the trap frequency using the parametric heating method. The amplitude of the trap is modulated, resulting in resonant heating when the modulation frequency is twice the frequency of harmonic motion. Due to the aspect ratio of a tightly focused Gaussian beam, the axial trap frequency (in red) is much slower than the radial frequency (in blue). The trap is axially symmetric within our measurement resolution. The plot on the right shows a release and recapture temperature measurement. The trap is rapidly switched off for a variable drop time, then turned back on to recapture molecules remaining in the trap volume. The dashed line is a Monte Carlo fit based on the trap geometry. This particular release and recapture curve fits to about  $35 \mu\text{K}$ .

### 2.3.5 SPATIALLY MANIPULATING THE OPTICAL TWEEZER

The tweezer light passes through a 100 MHz acousto-optic deflector (AOD) allowing us to control the tweezer light spatially. The AOD has a diffraction angle that depends linearly on the frequency of the RF drive. We can generate multiple traps by sending in multi-tone RF signals to the 5 Watt amplifier driving the AOD. For our optics, a 100 MHz vs a 101 MHz RF tone would produce tweezer traps separated by about  $10 \mu\text{m}$ . Figure 2.9 shows an optical tweezer array with 5 loaded traps.

Furthermore, we can move the traps around by chirping the drive frequency<sup>21</sup>. In practice, we are able to adiabatically move tweezers with loaded molecules without losses

until the tweezers get too close. At that point, there is an intensity beat note resulting from the near-detuning of neighboring traps and the overlapping light. This will be an issue later, but for now, it means that we keep the tweezer about 2 beam waists apart on the closest approach.

Re-arrangement capabilities are needed for a quantum computing platform. Since tweezer loading is stochastic, the probability of randomly loading a perfect defect-free array is unacceptably small ( $1/2^N$ , where  $N$  is the number of tweezers in the array). We are forced to turn off vacant traps and shift loaded traps to form a perfect array. We demonstrated this capability, however, never fully used it in our experiment. We did, however, find a way to merge tweezers for collision studies to be described in the next few chapters.

## 2.4 LIGHT ASSISTED COLLISIONS

Light-assisted collisions are exactly what the name implies; inelastic collision rates between molecules are enhanced in the presence of light<sup>128,126</sup>. Let's build a simple semi-classical model first assuming red detuned light. When two molecules are near each other and one becomes electronically excited by absorbing a photon, a strong dipolar interaction exists. When the photon field is red-detuned, the molecule dipole moments oscillate in-phase and dressed-state potential is attractive and temporary, as the dipolar potential disappears when the excited molecule emits a photon. Due to the strength of

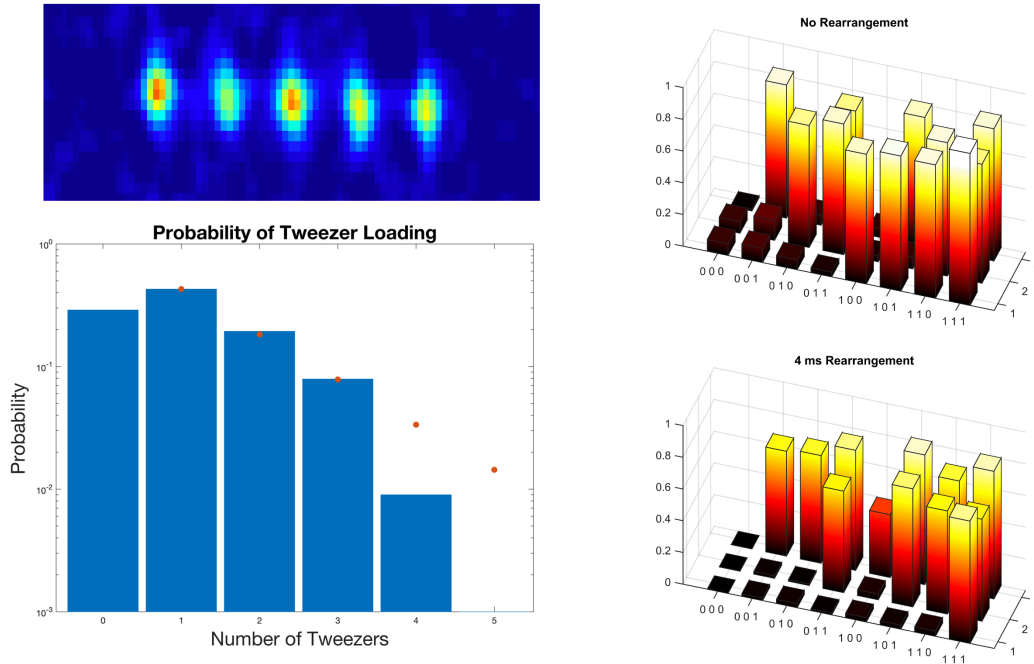


**Figure 2.9:** On the top left is an averaged image of the 5 tweezer array. Below is a bar plot showing the probability of loading  $N/5$  total traps in a single image. The loading fraction is relatively low, making the probability of loading more than 3 traps simultaneously extremely low. The orange dots are the expected loading probabilities based on a uniform loading rate. The tweezers loaded somewhat uniformly, however, the difference in brightness in the averaged image is a reflection of the loading probability, not the fluorescence yield in the different traps. The figures on the right-hand side show the rearrangement process for an array of 3 tweezers. The “configuration” axis is the occupation number of each tweezer, either 0 or 1. The adjacent axis labeled 1,2,3 indicates the tweezer number in the array. The rearrangement process shifts the loaded tweezers towards tweezer number 3. For example, look at the row labeled (101). The initial configuration is an array with tweezers 1 and 3 loaded with the middle tweezer empty. We shut off the middle tweezer and shift tweezer 1 to the location of tweezer 2 with a 4 ms long RF sweep feeding to the AOD. The result is an array of two tweezers next to each other and aligned right. This rearrangement capability will be important for quantum computing and simulation but we do not further utilize it in our experiments.

the interaction potential, a lot of kinetic energy can be gained during the short radiative lifetime of the excitation. In practice, this causes loss since the colliding molecules often have kinetic energies far exceeding the trap depth<sup>128,126</sup>.

Due to the strength of the attractive potential between an excited and ground state molecule, the collision cross-section is much larger than the cross-section for ground state-ground state Van der Waals-driven collisions. As a result, light-assisted collisions will occur on the experimental time scale at lower densities than ground state collisions making them the first type of collision that we have the density to observe in our traps. In order to be observable in our experiment, the characteristic collision time scale given semi-classically by  $n\sigma v$  where  $n$  is the density,  $\sigma$  is the cross-section and  $v$  is the mean velocity, must be faster than 100 ms. It is usually convenient to combine the velocity and cross-section into a quantity called the two-body rate constant,  $\beta$  which has units of  $\text{cm}^3/\text{s}$ . Typically the first collisional process that occurs at low density is two body collisions, followed by 3 body collisions at significantly higher density. At 20  $\mu\text{K}$  the density in the 1064 ODT would require a minimum two-body rate of  $1 \times 10^{-9} \text{ cm}^3/\text{s}$  to be observed. We do not see light-assisted collisions in the ODT. However, in the optical tweezer the density is  $1 \times 10^{11} \text{ cm}^3$ , requiring a two-body rate greater than  $1 \times 10^{-7} \text{ cm}^3/\text{s}$ . Indeed light assisted collisions to happen faster than this time scale and thus are extremely important in the loading of the tweezer trap. Figure 2.10 shows measurements of the light-assisted inelastic collision rates under a variety of conditions.

The importance of light-assisted collisions is what distinguishes the tweezer from

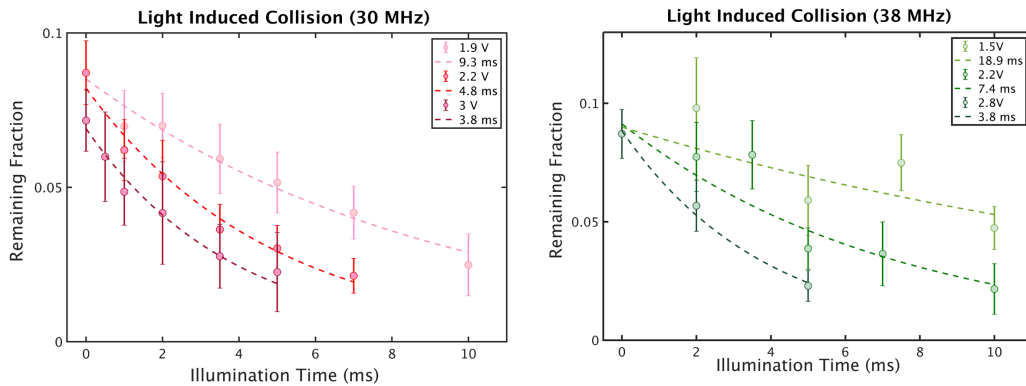


**Figure 2.10:** These plots show the single photon detuning and intensity dependence of the light-assisted collision rate. The light-assisted collisions get slower as the light is more detuned and the intensity lowers. This is explained by our simple model which requires one molecule to be excited during the collision. The light-assisted collision rates are slower than the cooling time scale, therefore all of the collisions are happening in thermal equilibrium. This data was taken by merging optical tweezers and looking at pair-wise decays, an experimental technique we’ll discuss thoroughly in the next chapter.

the ODT in the atomic and molecular physics community. Two body collisional processes enforce “parity projection” where molecules collide pairwise to leave either 0 or 1 molecules remaining at the end of the collisional process depending on whether the initial number of molecules in the tweezer was even or odd. This implies that 50% loading fraction is a fundamental limitation to the tweezer loading efficiency and the tweezer platform is manifestly stochastic. There is one caveat to consider; it is not necessarily true that the collision removes both molecules from the trap.<sup>24</sup>

The processes at hand in our experiment are slightly less simple, as we are driving light-assisted collisions with the lambda cooling light. There are two frequency components, one is blue detuned relative to all of the hyperfine levels while the other beam is red detuned relative to some levels. Red detuned light creates an attractive potential

however blue detuned light creates a repulsive potential. The advantage of the repulsive potential is that much less kinetic energy is transferred to the molecules during the collisions since the potential softens as the molecules accelerate away from each other. The potential is highly detuning dependent and has been shown in experiments with atoms to be tunable such that only one particle escapes the trap at a time. That would imply 100% loading fractions are possible.

We conducted a brief study of light-assisted collisions in the optical tweezer by slightly expanding the trap volume to give ourselves time to observe the collisions before the losses set in. Scanning the sub-doppler detuning, the two-photon detuning, and the intensity of the light, we never observed “enhanced” loading fractions greater than 50% in the CaF experiment. This is potentially because the upper leg of our lambda cooling beams is between two closely spaced hyperfine levels which means not all transitions are blue-detuned. Beyond enhancing the trap loading, we were not interested in studying light-assisted collisions.

## 2.5 GROUND STATE COLLISIONS PART 1

While excited electronic state collisions are not terribly interesting due to their transient nature, ground state collisions are. Primarily, we want to know if high-density gases of molecules are collisionally stable or if fast loss processes will set in. Some of these properties can be calculated theoretically however the two-body rate constants cannot

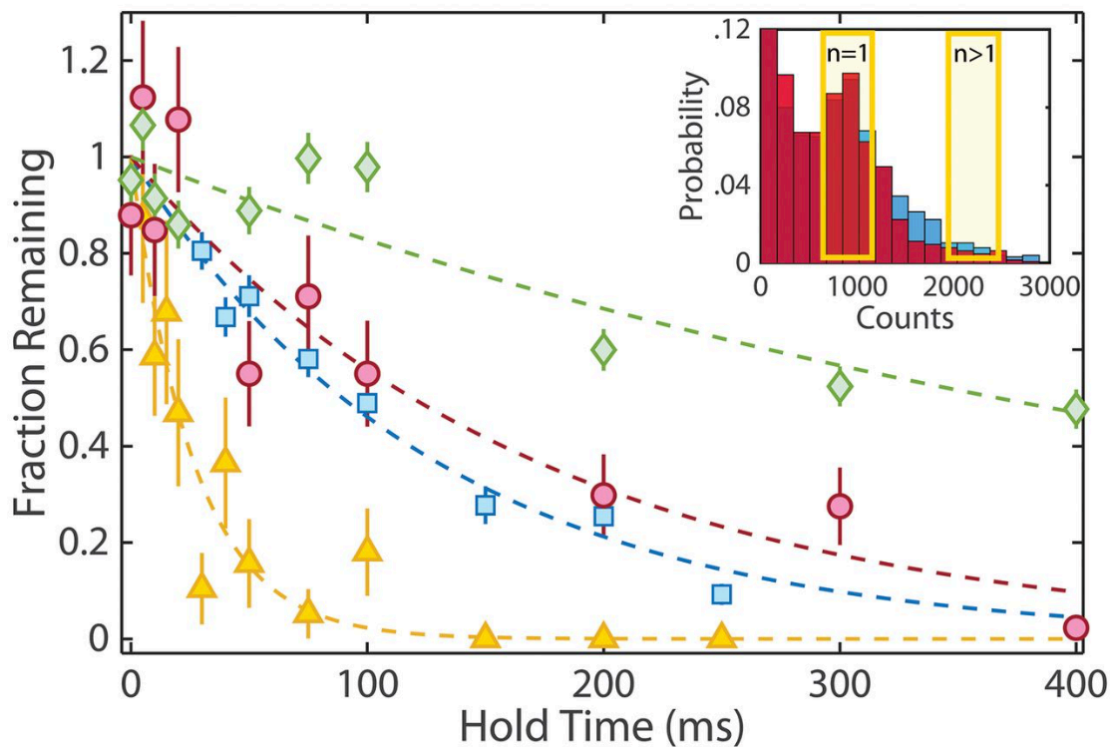


**Figure 2.11:** The green trace is the survival of single molecules in the optical tweezer, with a vacuum hold lifetime of 500 ms. The red trace shows the survival of two molecules decaying in 180 ms, indicating collisional losses. The blue and yellow traces show the survival of singles and doubles, respectively, in the presence of the lambda cooling light. The single molecules imaging lifetime is reduced in the optical tweezer compared to the 1064 nm ODT (130 ms vs 500 ms in the 1064 nm ODT). We observe rapid light-assisted collisions with pairs decaying in 26 ms. This is consistent with light-assisted collisions driving parity projection during the tweezer loading. The survivability plot was taken from the integrated counts in the two marked regions of the histogram. The  $n=1$  region is where we expect single molecule fluorescence to appear with a very high probability. In the  $n>2$  region, it's extremely unlikely that a single molecule could produce that much fluorescence, leading us to interpret this region of the histogram as the "multiples" region. This is where we calculate the decay rates of pairs.

be predicted well enough to make strategic experimental decisions, so we set out to make an initial measurement of the electronic ground state loss rate.

At this point in the experiment, we don't have the ability to merge the tweezers yet. However, we can reuse the same trick by slightly expanding the trap to a beam waist of  $8\mu\text{m}$  in order to load multiple molecules. We see the multiple molecules as an elongated tail in the fluorescence histograms, indicating fluorescence coming from several emitters in the same trap. See Figure 2.11. We can estimate the electronic ground state (the molecules are still in the  $N=1$  manifold) collision rate by watching the decay of the fluorescence tail vs hold time in the tweezers with the cooling light off. Knowing the fluorescence yield of a single trapped molecule, we can bound the region of the histogram tail where the doubly occupied tweezers are expected to be. We see the fluorescence in the histogram tail decaying in 180 ms.

The lifetime of the doubly occupied tweezer can be converted into a useful two-body loss rate only if the density of the gas is known. We measured the temperature using the release and recapture method while the trap frequencies are measured using the parametric resonance method and found the density to be  $5 \times 10^7 \text{ cm}^3$ . That implies a 2-body loss rate of  $4 \times 10^{-9} \text{ cm}^3/\text{s}$ , consistent with a "universal" loss rate model where colliding molecules are lost with 100% probability once they come close enough.

This initial measurement of the ground state collisional loss rate will serve as the starting point for the next chapter where we implement the merging of optical tweezers to deterministically prepare two molecules in the same trap. We also implement

microwave state control to create samples where both molecules are in a single internal quantum state of our choosing. This study will carefully assess the stability of a high-density CaF gas, inform theory calculations, and inspire a collisional engineering project described in the following chapter.

# 3

## Collisions of Exactly two Molecules

### 3.1 WHY STUDY COLLISIONS?

Understanding what happens when two molecules collide in the ultracold regime is an important aspect of molecular physics that needs to be understood in order to stabilize high-density gases.

Collisional loss rates have been measured in several bi-alkali molecules, either in the  $^1\Sigma$

ground state or the metastable  $^3\Sigma$  state, including  $^{40}\text{K}^{87}\text{Rb}$  <sup>107</sup>,  $^{23}\text{Na}^{40}\text{K}$  <sup>115</sup>,  $^6\text{Li}^{23}\text{Na}$  <sup>122</sup>,  $^{23}\text{Na}^{87}\text{Rb}$  <sup>159</sup>, and  $^{87}\text{Rb}^{133}\text{Cs}$  <sup>141,52,53</sup>. Our study is the first to measure the collisional properties of  $^2\Sigma$  laser-cooled molecules <sup>5,149,97,3,34,6</sup>.

It is very important to know whether high-density gases of ultracold CaF molecules are collisionally stable, where stability means that collisional processes at play are dominated by elastic collisions. Any inelastic collisions where, for example, the molecules stick together, undergo chemical reactions, interact with the trap light, or emerge in different rotational or hyperfine states, will lead to loss and/or heating. Most of these loss processes happen when the molecules are very close together. Modeling two molecules interacting strongly at close range is difficult. Although the current state-of-the-art theory predictions are getting better, they of course do not supersede measurements.

To motivate why we care at all about high-density bulk gases when we have a functioning optical tweezer platform for CaF molecules, let's recall how the field of atomic physics became what it is today through the discovery of Bose-Einstein condensates (BEC). While laser cooling was the workhorse in the early 1990s, it was insufficient to reach condensate temperatures. The same is true for the molecules experiments of today. The breakthrough enabling cooling to BEC was evaporative cooling, which relies on a high ratio of elastic collisions to inelastic collisions <sup>137,134</sup>. Evaporative cooling of molecules is a project we will work on later in this thesis but for now, we seek to understand the basic collisional properties of ultracold CaF molecules.

Our study of collisions is somewhat paradoxical, starting with single molecules in

optical tweezers. By merging pairs of loaded tweezers, we can study the collisions of exactly two molecules in an ultra-controllable environment<sup>151,94,133,61</sup>. Adding microwave state control allows us to prepare the molecules in any internal hyperfine state of our choosing with very high fidelity. The experiment answers the question “how long do pairs of molecules survive when they share a tightly confined trapping environment”?

## 3.2 MERGING TWEEZERS

In the previous chapter, we developed the optical tweezer platform for CaF molecules and mentioned in passing the active capabilities of the AOD. Here we will fully utilize the dynamic capability of the AOD to move and merge the optical tweezer<sup>6</sup>.

### 3.2.1 DYNAMIC AND STATIC TWEEZERS

The AOD generates the tweezers using different RF tones to produce slightly different diffraction angles of the light. We can move the tweezers 10  $\mu\text{m}$  for every 1 MHz deviation from the center drive frequency of 100 MHz. Merging the tweezers involves sweeping the RF frequency and then switching off one of the traps after the merger. We can infer an immediate problem with the direct merging of tweezers: As we sweep the frequency of one tweezer to match its neighbor there will be a very large amplitude beat note on the light as the traps merge. This beat note will sweep through the parametric heating resonance and cause rapid loss. Indeed this is what happened as we merged the

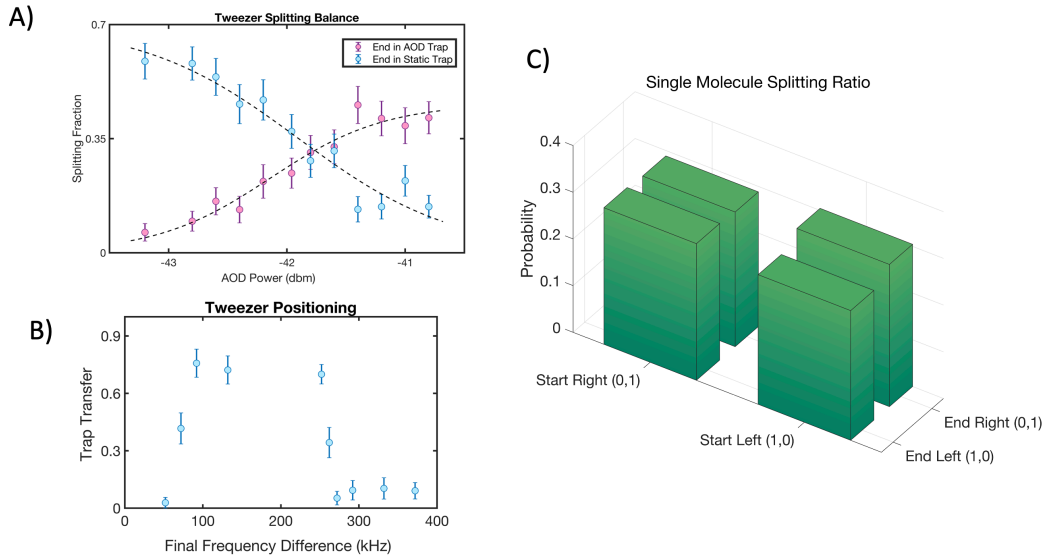


**Figure 3.1:** Merging the tweezers is a delicate balance requiring fine-tuning of the power and frequency. Box A) depicts an experiment where we merge the dynamic (AOD) and the static tweezers, hold for a short time, and then reseparate. The tendency of the molecule to switch traps or remain in the same trap depends sensitively on the trap depths, where the AOD trap depth is tunable via RF drive power shown on the x-axis. Box B) shows the sensitivity of the spatial overlap for a molecule to be transferred between tweezers. The AOD tweezer was swept to a final frequency (shown on the x-axis) and then switched off. Molecules that are transferred to the static tweezer survive. In real space, the AOD tweezer translates  $10 \mu\text{m}/\text{MHz}$ . The width of the transfer feature ( $3 \mu\text{m}$ ) is almost exactly double the beam waist. Box C) is what we monitor during the collision experiment to ensure tweezer splitting is done symmetrically. It maps the probability of a single molecule starting in either of the two traps to swap traps or remaining after the merger. All four of the possibilities should have the same probability when the splitting is optimized to be as symmetric as possible.

traps directly and we never saw any transfer.

The simple fix is to have one stationary tweezer and one dynamic tweezer produced by the AOD. The stationary tweezer was split off and recombined with the AOD light using a polarizing beam splitter. This method provides two layers of beat note protection. First, the AOD is 100 MHz shifted relative to the stationary tweezer; a frequency far too high to have any motional coupling effects. Second, the polarizations of the two

tweezers are crossed on the cube, preventing beating altogether.

Positioning the tweezers turns out to not be difficult as they only need to be overlapped better than a beam waist. Once the tweezers are merged, we hold the molecules together for a variable amount of time during which collisions occur and molecules can be lost from the trap. After the collision time is over, we measure how many molecule pairs survive the encounter.

### 3.2.2 SPLITTING

Unfortunately, due to light-assisted collisions, we cannot image two molecules together in the same tweezer, so we elect to separate the tweezers. The splitting process requires the depths of the two tweezers to be very well matched, otherwise, both molecules end up in the same trap. The tolerance is roughly set by the temperature of the molecules and any differences in trap geometry between the static and dynamic traps. Trap depth matching needs to be done on the few percent level to be effective. We do this by fine-tuning the RF power going to the AOD, observing which trap the molecule ends up in after the splitting, and then iterating to make it as even as possible. In practice, this effort takes a few tens of minutes. Figure 3.1 shows the merging process and splitting efficiency.

While the splitting procedure works well, it is subject to slow drifts throughout the day which can bias the apparent survival fraction of pairs. Fortunately, our experiment is self-calibrating in real-time and we always have a monitor of the splitting ratio interwoven

between data points. The tweezers load approximately 50% of the time, which means only 25% of the time both contain a molecule. For the 50% of occurrences where only one tweezer is loaded, we perform the merging experiment and then map out the probability of the single molecule returning to the same trap or switch traps after splitting. The same data set also provides a check on the single molecule survival rate during the collision hold time; a quantity that should (and does) remain perfectly constant.

### 3.3 COHERENT CONTROL OF MOLECULES

The second aspect of this experiment is control over the internal state of the molecule<sup>7</sup>. The previous collision rate we measured in the last chapter involved molecules in a statistical mixture of hyperfine levels belonging to the  $N=1$  rotational manifold<sup>6</sup>. With the addition of optical pumping and microwave transfer, we can prepare high-purity samples of molecules in any internal quantum state we desire.

#### 3.3.1 OPTICAL PUMPING

The “purification” of the quantum state is a two-step process. After the lambda cooling, the molecular population is distributed over the four hyperfine levels in the  $N=1$  rotational manifold. The first step is to use optical pumping to move as much population as possible to one of the hyperfine levels. Optical pumping is the energy and entropy dissipating step in the state preparation process. Fortunately in CaF, the  $N=1$  rotational

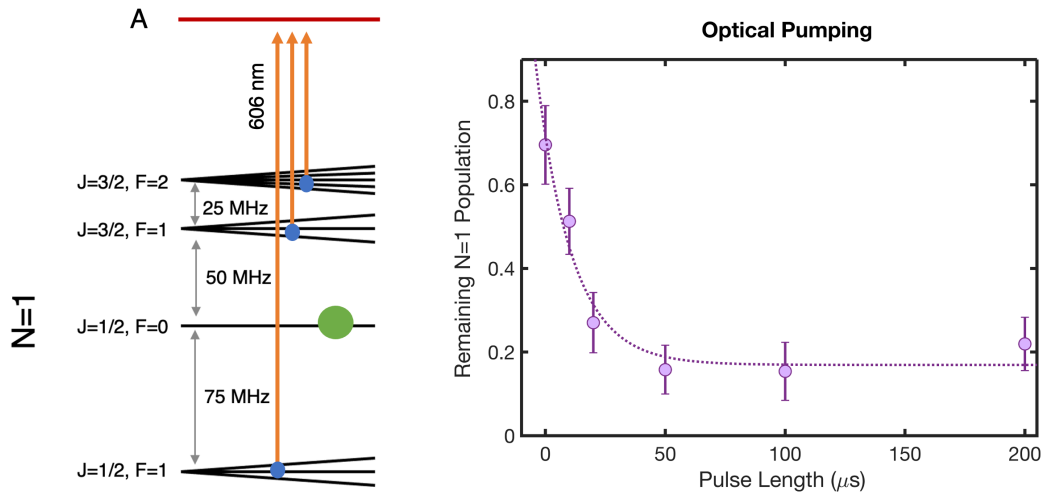


**Figure 3.2:** We optically pump the  $N=1$  population to the  $|N=1, F=0, m_f=0\rangle$  hyperfine level using low-intensity light with resonant frequency components indicated in the figure on the left. Some residue remains in the other states due to off-resonant scattering which pumps the population out of the desired state. On the right is a plot showing the optical pumping rate. Molecules pumped into  $|N=1, F=0, m_f=0\rangle$  were transferred to the  $N=0$  manifold via a microwave pulse where they are dark to the imaging light. We imaged the remaining molecules in all hyperfine levels in the  $N=1$  manifold and found after  $50 \mu\text{s}$  of optical pumping, 20% of the population was either in an  $N=1$  hyperfine level at was not  $|N=1, F=0, m_f=0\rangle$ , or the microwave pulse left a residue in  $|N=1, F=0, m_f=0\rangle$ . In this sense, the measurement is a lower bound on the optical pumping efficiency.

manifold has a well-isolated  $F=0$  state which is perfect for optical pumping because it is a single state.

The optical pumping beams are low-intensity beams resonant with the  $F=1^-$ ,  $F=1^+$ , and  $F=2$  hyperfine levels, seen in Figure 3.2. The population cycles until a spontaneous decay takes it to the  $F=0$  level which is dark by construction. A  $50 \mu\text{s}$  optical pumping pulse is sufficient to pump about 80% of the  $N=1$  population into  $F=0$ . The limiting factor is the energy spacing between  $F=1^+$  and  $F=0$  which is only about 2.5 linewidths therefore the  $F=1^+$  beam is off-resonantly driving the  $F=0$  population.

### 3.3.2 MICROWAVE TRANSITIONS

With a substantial population fraction in the  $|N = 1, F = 0\rangle$  state, we can now focus on driving between  $N=1$  and  $N=0$  manifolds with a microwave transition. The gap is roughly  $2B \approx 20.5$  GHz and the transition is very strong since the coupling is provided by the rotational dipole moment (3.07 Debye for CaF).

The microwave system for this application consists of a few components. We use a low-power K-band microwave source with a 5 watt amplifier followed by two stacked switches to feed a microwave horn antenna. Our microwave source is tied to a 100 MHz oven-stabilized reference. The antenna is outside of the vacuum chamber and couples in through a viewport. Due to the strong nature of rotational transitions, electric fields on the order of 1 V/cm are sufficient to drive MHz scale Rabi oscillations (coherent driving between rotational levels).

To find the rotational transitions, we expose the molecules to a several-millisecond-long high-power microwave pulse. When the pulse is on resonance, it drives Rabi oscillations for several cycles until it decoheres and spreads the population into a 50 : 50 statistical mixture between the upper and lower states. We observe this as a dip in molecular fluorescence, as seen in Figure 3.3. The width of the transition is due to pure power broadening and the transitions can be located to the kHz scale by lowering the microwave power.

To measure the Rabi frequency, we tune the microwave frequency to resonance and

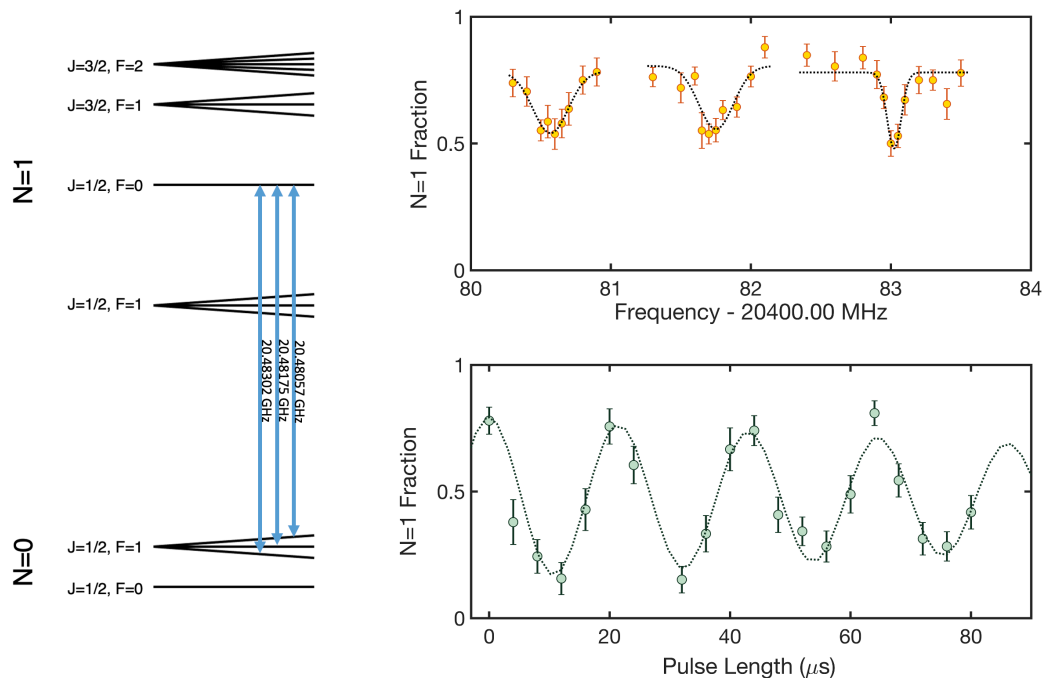


**Figure 3.3:** On the left is a level diagram with the relevant states. The blue arrows correspond to the microwave transitions we observed on the top right plot, where the  $m_f$  levels were resolved by applying a 1 Gauss magnetic field. The spectrum was obtained using a 2 ms long microwave pulse, long enough for the Rabi oscillations to decohere. On the bottom right is a sample Rabi oscillation on the  $|N = 1, F = 0, m_f = 0\rangle \leftrightarrow |N = 0, F = 1, m_f = 0\rangle$  transition. It was driven at very low microwave power, resulting in a slow Rabi oscillation, where only the molecules remaining in the  $N=1$  manifold are detected by the lambda imaging process.

then rapidly switch on the microwaves. The microwaves drive the system coherently for a variable amount of time before we rapidly switch it off. The switch-off leaves the molecules in a superposition of  $N=0$  and  $N=1$  which we measure projectively by lambda imaging the population in the  $N=1$  manifold. Rabi frequencies of 1 MHz are sufficient for our experiment. Our primary interest is to tune the microwave pulse length to the  $\pi$  time, which provides the maximum population transfer to the ground state.

We first characterized the  $|N = 1, F = 0, m_f = 0\rangle \rightarrow |N = 0, F = 1, m_f = 0, \pm 1\rangle$  transitions. Nominally the three  $|N = 0, F = 1, m_f = 0, \pm 1\rangle$  projection states are degenerate but we apply a roughly 2 Gauss magnetic field to split them sufficiently to resolve the three components. The Rabi frequency of the three possible transitions in this manifold provides information about the polarization of the microwave field relative to the quantization axis set by the magnetic field. No special consideration was given to driving any particular polarization and our data show the microwaves are more or less completely unpolarized despite the antenna generating mostly linear polarization.

Once the Rabi frequency is known, the population can be transferred by exposing the molecules to the microwaves for half a period ( $\pi$ -pulse time), resulting in most of the population being projected into the  $N=0$  level when the microwaves switch off. The final step to preparing a very clean system is to remove any remaining population in the  $N=1$  manifold with a resonant heating pulse. We tune the lambda cooling light to resonance and expose the molecules for 5 ms, more than enough to heat any remaining  $N=1$  molecules out of the tweezer.

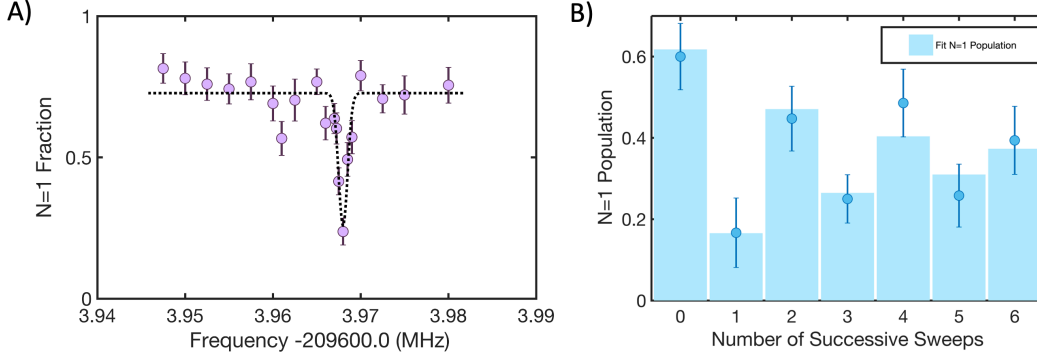


**Figure 3.4:** On the left is a spectroscopic scan showing the location of the nominally forbidden  $|N = 1, F = 0, m_f = 0\rangle \longleftrightarrow |N = 0, F = 0, m_f = 0\rangle$  transition. The 3.5 Gauss magnetic field makes the transition weakly allowed by mixing in nearby hyperfine levels. Due to the narrow nature of the transition, we opted to use a Landau-Zener pulse to transfer the population. On the right, we estimate the transfer efficiency of the Landau-Zener sweep by fitting the population measured in  $N=1$  after a sequence of  $n$  Landau-Zener sweeps. An odd number of sweeps moves the population to  $|N = 0, F = 0, m_f = 0\rangle$  where it is dark to the imaging light. An even number of sweeps brings the population back to  $|N = 1, F = 0, m_f = 0\rangle$ , where it is bright. The solid bars are a calculated from a decaying sinusoid model, indicating a Landau-Zener transfer efficiency of 74%

### 3.3.3 DRIVING TO GROUND STATE

The optical pumping into  $|N = 1, F = 0, m_f = 0\rangle$  creates an issue for transferring the population to the absolute ground state  $|N = 0, F = 0, m_f = 0\rangle$  because this transition is not dipole allowed. However in the presence of a weak magnetic field, the  $|N = 1, F = 0, m_f = 0\rangle$  state mixes primarily with  $|N = 1, F = 1^+, m_f = 0\rangle$  and gains a transition dipole moment coupling to  $|N = 0, F = 0, m_f = 0\rangle$ . The effective Rabi frequency is  $\Omega_{eff} = (\mu_B B / \Delta) \Omega_{N=1, F=1^+}$ . In practice, the Rabi frequency is a few kHz which is enough to find the transition however directly driving Rabi cycles is somewhat hard due to the transition frequency drifting on the kHz scale for any number of reasons.

### 3.3.4 LANDAU-ZENER TRANSFER

The best way to handle population transfer for narrow transitions is to use a Landau-Zener sweep. This is an adiabatic passage technique that sweeps the population coherently from the upper state to the lower state by dressing the system with a detuned microwave field and then sweeping the frequency across resonance to invert the dressed state. We do the Landau-Zener sweep by hold the microwave frequency constant and sweeping a magnetic field from 5 Gauss to 2.5 Gauss in 20 ms, shown in Figure 3.4. The microwave frequency is resonant with the transition when the magnetic field is at 3.5 Gauss. As the microwaves switch on at a magnetic field of 5 Gauss, the population projects into a dressed state basis that looks like  $|N = 1, F = 0, m_f = 0\rangle + \frac{\Omega}{\Delta}|N = 0, F = 0, m_f = 0\rangle$  where  $\frac{\Omega}{\Delta}$  is smaller than  $3 \times 10^{-4}$ .

The sweep rate is set fast enough to minimize dephasing while the microwaves are on, yet slow enough to limit non-adiabatic transfer as the sweep cross the narrowest gap on resonance. The slew rate needs to be slow relative to our  $2\pi \times 2$  kHz Rabi frequency to avoid Landau Zener tunneling which scales as  $e^{-2\pi \frac{\Omega^2}{d\Delta/dt}}$ . We determined experimentally that sweeping from 5 Gauss to 2.5 Gauss in 20 ms is optimal.

After the sweep, the ending dressed state,  $(|N = 0, F = 0, m_f = 0\rangle - \frac{\Omega}{\Delta}|N = 1, F = 0, m_f = 0\rangle)$  is mostly the bare  $|N = 0, F = 0, m_f = 0\rangle$  level and is projected onto the absolute ground state when the microwaves switch off, resulting in population transfer. We estimated the transfer fraction by doing several Landau-Zener sweeps while removing

the non-transferred molecules. The data fit to a single sweep transfer efficiency of 74%, good enough for preparing molecules for a collision study.

### 3.4 COLLISIONS

The collision data we have access to is how long pairs of molecules survive in the trap. It doesn't necessarily tell us what happened when we observe losses of pairs however by utilizing our careful state preparation process we can create samples with different possible loss mechanisms and observe the loss rates. We measure the loss rates as a time decay of two-particle survival. This needs to be converted to a 2-body loss rate or a cross-section, corresponding to  $\gamma = n\sigma v$  where the loss rate  $\gamma$  is what we measure,  $n$  is the sample density measured separately,  $\sigma$  is the collision cross section containing all of the interaction physics and  $v$  is the average relative velocity set by the temperature of the sample. Another useful quantity is the two-body rate given by  $\gamma = \beta n$  ( $\beta = \sigma v$ ).

#### 3.4.1 EXTRACTING THE 2-BODY RATES

Measuring the density can be difficult. It is based on the confinement of the trap that we estimate by measuring the trap frequencies and the temperature of the molecule. The trap frequency measurements are the same as described in the last chapter. To ascertain the temperature, we rely on three different measurements which all turn out to be mutually consistent. The first technique, release and recapture, works as described

in the last chapter and gives a temperature of  $52 \mu\text{K}$ . This measurement is based on modeling the trap and is sensitive to the shape of the trap<sup>6</sup>.

We measured the temperature using an adiabatic ramp down. As the trap decreases in depth, some of the motional states become unbounded and couple to free particle states, resulting in loss. We used a Monte Carlo simulation to model this process, however, like the release and recapture, it is assuming a Gaussian model for the trap shape. The measurement returned a sample temperature of  $24 \mu\text{K}$ .

The third and most robust temperature measurement is time of flight. For single molecules, this is very time-consuming to see the expansion with enough signal-to-noise to fit it however there is no modeling required at all making this a very robust measurement. We used resonant light to image the molecules for  $10 \mu\text{s}$ , scattering an average of 100 photons per molecule. Tens of thousands of averages were needed to produce the measurement and the result was  $42 \mu\text{K}$  which we use as the temperature we used to calculate the 2-body loss rates.

Exactly as described in the last chapter, we use parametric heating to measure the trap frequencies of  $\omega_{x,y} = 2\pi \times 77 \text{ kHz}$  and  $\omega_z = 2\pi \times 5.5 \text{ kHz}$ . From the trap frequencies and temperature, we can calculate the density for a harmonic trap:

$$\rho = \frac{\omega_x \omega_y \omega_z}{8\pi^{3/2} (k_b T / m)^{3/2}} \quad (3.1)$$

This harmonic approximation works well at our trap depth of  $1400 \mu\text{K}$  and tempera-

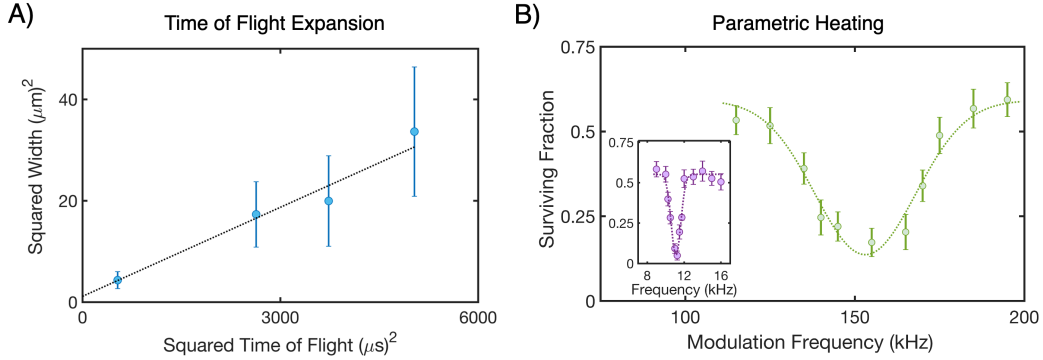


**Figure 3.5:** Accurately estimating the single molecule density in the optical tweezer is the key to converting the loss rates we measure into useful 2-body rates and cross sections. In panel a, we use a time of flight expansion to measure the temperature in the optical tweezer. Fitting the square of the time of flight vs the square of the cloud size produces a linear function where the slope is the temperature. We extracted a temperature of  $41 \pm 12 \mu\text{K}$ , consistent with the release and recapture data. In panel B, we measure the trap frequencies ( $2\omega$ ) using parametric heating. Both radial trap frequencies fit to 77 kHz and the axial frequency is 5.5 kHz. Our measurements predict a density of  $5 \times 10^{11}/\text{cm}^3$

ture of  $42 \mu\text{K}$ . An  $\eta$  value of 33 indicates the trap is very harmonic. The single molecule density in the optical tweezer is  $4 \times 10^{11}/\text{cm}^3$ . The measurements used to obtain this value are shown in Figure 4.16.

### 3.4.2 INTERACTION POTENTIAL

The mechanics of the collisions can be described semi-classically. The interaction potential is based on the attractive Van der Waals interaction characterized by  $C_6$ , and the repulsive centrifugal barrier.

$$U(r) = -C_6/R^6 + L(L+1)/(mR^2) \quad (3.2)$$

The centrifugal barrier depends strongly on the relative angular momentum between the colliding pair, which defines the symmetry of the 2-particle wavefunction when both molecules are in the same internal state. CaF is a Boson requiring the total wavefunction  $|\psi\rangle = |N, F, m_f\rangle_1 \otimes |N, F, m_f\rangle_2 \otimes |L, m_l\rangle$  to be symmetric under the exchange of particles 1 and 2. For the 2-particle states of this form, only even partial wave components contribute.

The  $L = 0$  (S-wave) collisions have no angular momentum and no centrifugal barrier needs to be overcome. These collisions are purely attractive and it's easy for the molecules to reach short range. The next lowest even partial wave, the D-wave component, has two quanta of angular momentum and an associated potential barrier of height  $110 \mu\text{K}$ . The D-wave collision channel is not a major contributor to the total collision rate.

The next task is to calculate the  $C_6$  coefficient in units of the Bohr radius and Hartree energy by summing the dipole transition moments between the ground and excited states.

$$\left(\frac{1}{4\pi\epsilon_0}\right)^2 \sum_i d_i^4 / 6\Delta_i = -2.25 \times 10^5 a_0^6 E_h \quad (3.3)$$

The  $N=0$  hyperfine states as well as  $N = 1, F = 0$  have isotropic  $C_6$  coefficients whereas all the other hyperfine levels in  $N = 1$  and beyond have the typical D-wave characteristic of a dipolar system. Figure 3.6 shows the  $C_6$  coefficients for all the hyperfine levels in

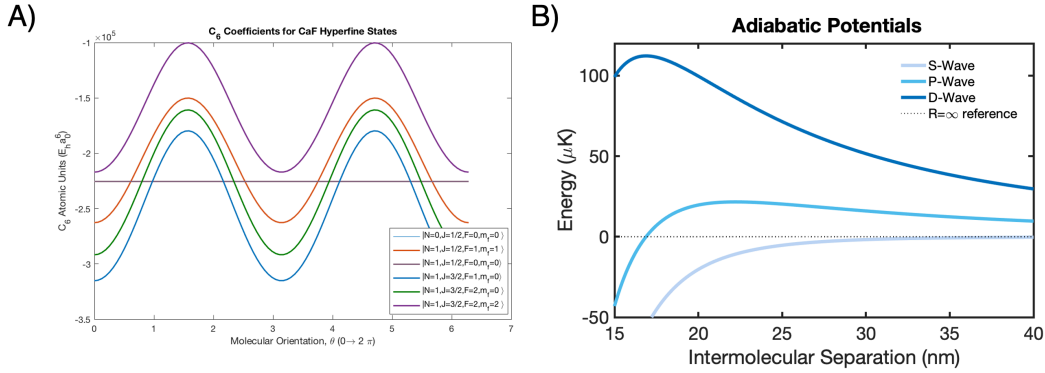


**Figure 3.6:** For molecules in the absence of a polarizing external field, the interaction potential at long range is well described by the Van der Waals interaction. Molecules in the  $N=1$  rotational state have an anisotropic interaction except for the  $|N=1, F=0, m_f=0\rangle$  state, which is isotropic like the  $N=0$  states. Using the calculated Van der Waals interaction strength from plot A), in plot B) we add the centrifugal term to get the interaction potential. For two molecules in the same internal state, only even partial waves preserve the Bosonic exchange symmetry of the wave function. The S-wave potential has no barrier and is the dominant interaction. The P-wave term is not allowed and the next lowest partial wave (D-wave) only contributes slightly due to the activation barrier being above the sample temperature.

$N=1$  and shows the interaction potential for S, P and D-wave components for the isotropic  $N=1, F=0$  Van der Waals interaction potential. This simple model helps us to estimate the capture range below which more complicated things happen such as inelastic processes.

### 3.4.3 SHORT RANGE INTERACTIONS

The length scale we are calling short-range needs to be quantified. It is the length scale associated with the Van der Waals interaction and it's given by

$$l_{vdw} = \frac{2\pi}{\Gamma(1/4)^2} \left( \frac{mC_6}{h^2} \right)^{1/4} \quad (3.4)$$

which is approximately  $200a_0$  for CaF.

At the short-range length scale, the interactions are no longer strictly Van der Waals and much more complicated things can happen involving the mixing of the molecular states and eventually changes in the relative position of the bonded atoms, leading to a chemical reaction. These processes are much harder to calculate, however, we can make progress by assuming a black box below  $l_{VDW}$  and only asking the following question: What collision cross section do we expect if the processes below  $l_{VDW}$  have loss probability  $p$ ? Let's assume  $p = 1$ , or equivalently we'll call it universal loss<sup>65,49</sup>. From this model, we estimated a loss rate of  $3 \times 10^{-10}$  cm<sup>3</sup>/s, which we will use as our comparison point from now on.

#### 3.4.4 WHAT HAPPENS AT SHORT RANGE?

Comparing our measured 2-body loss rates to the universal rate, we can attempt to draw conclusions about the loss probability at short-range. While the universal loss model makes no assumptions about what happens at short range, there are a few possibilities. CaF molecules in the absolute ground state have possible chemical reaction pathways. The highly exothermic  $2\text{CaF} \rightarrow \text{Ca} + \text{CaF}_2$  reaction does not have an activation barrier meaning this reaction will happen all the way down to absolute zero. No products of this reaction will remain in the trap due to the high energy released.

The other loss possibility stems from a process called sticky collisions<sup>96,95</sup>. This happens when colliding molecules form a long-lived collisional complex. When the

molecules come close together, on the order of the bond length, the interactions become very strong, and complicated dynamics ensue. There are many many quantum states for the system to explore, however, no energy has been conferred to the system. Non-reacting ground state molecules, for example, can only exit the complex in the same state they entered. There is only one channel and the lifetime of the complex is determined by how long it takes the system to find the exit channel. Typical complex dynamics happen on the vibrational period time scale (picoseconds) however the complex lifetime can be hundreds of nanoseconds due to the enormous density of states and the length of time it takes to explore that state space to find the exit channel.

The lifetime of the complex can be estimated statistically using RRKM theory (Rice-Ramsperger-Kassel-Marcus) and is given by  $\Gamma_{RRKM} = N_0/(2\pi\rho)$  where  $N_0$  is the number of open scattering channels (order unity) and  $\rho$  is the density of states, which is relatively large. In practice, estimating the density of states can be challenging, leading to a wide range of predicted complex lifetimes<sup>37</sup>. Our experiment isn't particularly well suited to measure the lifetime of a complex; however, a subsequent bi-alkali experiment recently reported measurements of collision complex lifetimes significantly longer than the RRKM predictions<sup>110</sup>.

Nominally, the complex formation could be elastic since the molecules separate in the same states they entered, however, several bad things can happen to the complex. First, low-probability chemical reactions have a much longer time to occur when the molecules are stuck in a collisional complex. Another loss mechanism, relevant to non-reactive

species in optical traps, is where a trap light photon excites the complex, resulting in heating and subsequent loss. While CaF is reactive, other non-reactive species see rapid losses in optical traps and this light-induced collisional complex loss model is the leading explanation<sup>38</sup>.

### 3.4.5 GROUND STATE COLLISIONS

Studying the ground state collisional loss rate is a good starting point because it eliminates any possible single-molecule state-changing effects during the collisions since there are no lower single-molecule states to which the system can relax. The remaining loss processes can only be chemical reactions or “sticky collisions” that result in loss.

The barrier-less chemical reactivity is enough to suggest that ground-state CaF molecules will be lost with unit probability when they collide at short-range. We find the ground state molecules are lost at a rate of  $\beta_{gs} = 1.5(1) \times 10^{-10} \text{cm}^3/\text{s}$ , slightly below but not significantly inconsistent with universal loss. Our result, shown in figure 3.7, is very similar to recent bi-alkali experiments<sup>53</sup>.

### 3.4.6 SPIN-STRETCHED STATE

It’s potentially disappointing to see universal loss for ground-state molecules, however, there are more quantum states with different natures. The lower-most spin stretched state (nuclear and electronic spins aligned),  $|N = 0, F = 1, m_f = -1\rangle$  is one. The triplet nature of the interaction potential means there is a substantial barrier to the  $2\text{CaF} \rightarrow$

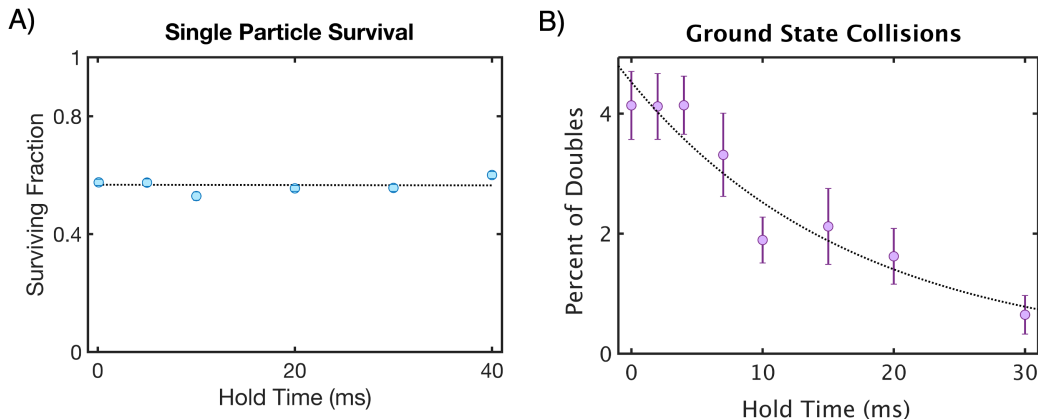


**Figure 3.7:** The plot on the left shows the survival of single molecules vs hold time during the collision measurement sequence. Each time a single tweezer is loaded, the sequence proceeds as if collision data is being taken which serves as a self-calibration for the survival of single molecules. The lifetime is consistent with no single molecule lifetime issues, indicating all hold time-related loss processes are collisional in origin. Panel B shows the survival probability of pairs of ground-state molecules as a function of merging time. The pairs are lost with an exponential time constant of 16 ms. One subtlety is that the lifetime should be fit by an exponential, not the usual density-dependant 2-body algebraic decay rate because the density does not decay during the collisional process.

Ca + CaF<sub>2</sub> reaction and it might be suppressed as a result. We did not measure any suppression in the experiment, however. The measured rate was  $\beta_{stretched} = 2.5(1) \times 10^{-10} \text{cm}^3/\text{s}$ , which is also fully consistent with universal loss.

One of the potential pitfalls is ensuring spin-polarization is maintained at all times throughout the collision. We split the  $N = 0, F = 1$  sublevels with a 10 gauss magnetic field and it's possible the spin polarization is not maintained during the collisional process due to the relatively small gap between the  $m_f$  levels. Once it's lost, the spin-singlet reaction channel is available once again. Larger magnetic fields would make the spin polarization more robust, but we didn't have the means during this experiment to go much higher than several Gauss.

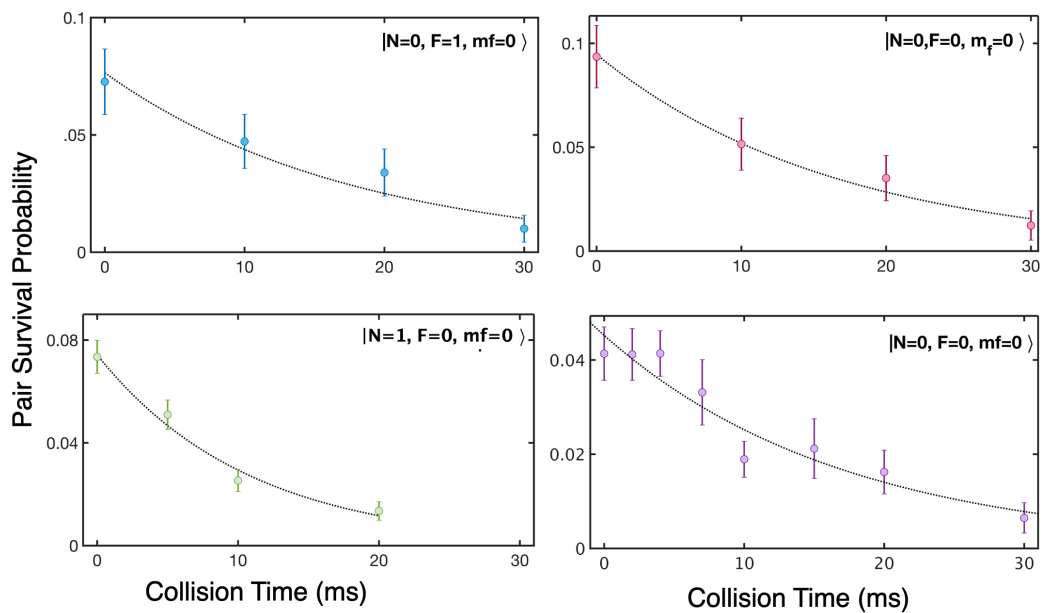


**Figure 3.8:** The plots above depict the survival probability of pairs of molecules prepared in the labeled quantum state as a function of hold time. All pairs decay exponentially with similar time scales. The density is the same for all 4 iterations of the experiment, and we can read off similar 2-body rates due to the similarity between all 4 exponential time scales.

State	$N=1, F=0, m_f=0$	$N=0, F=0, m_f=0$	$N=0, F=1, m_f=0$	$N=0, F=1, m_f=1$
Two-body rate ( $\text{cm}^3/\text{s}$ )	$1.5 (0.5) \times 10^{-10}$	$1.5 (1.0) \times 10^{-10}$	$2.0 (1.0) \times 10^{-10}$	$2.5 (1.0) \times 10^{-10}$

**Figure 3.9:** Two-body loss rates for all the states measured in this study. The universal loss rate is  $3 \times 10^{-10} \text{ cm}^3/\text{s}$

### 3.4.7 ROTATIONALLY EXCITED MOLECULES

We also studied collisions of molecules in  $N = 1, F = 0, m_f = 0$ . This system can have both hyperfine and rotational relaxation in addition to possible chemical reactions and complex formation/destruction. We observed  $\beta_{N=1} = 1.5(0.50) \times 10^{-10} \text{ cm}^3/\text{s}$ , once again slightly below the universal loss rate but still un-informative about which loss process is occurring. Figure 3.8 summarizes the measured two-body inelastic lifetimes for all the states we prepared.

## 3.5 WHAT IS HAPPENING TO THE MOLECULES?

For every configuration with potentially different behavior, we observe two-body loss rates consistent with universal loss (comparison in Figure 3.9). While the concrete conclusion is during a short-range collision, no outward molecular flux is generated, it doesn't definitively indicate what is the loss process. In principle, one could detect the free Ca atom produced in the  $2\text{CaF} \rightarrow \text{Ca} + \text{CaF}_2$  chemical reaction however this is beyond the technical scope of our experiment.

While trap light-induced losses could be destroying collisional complexes, we are inclined to conclude the barrier-less chemical reaction will proceed anyway resulting in

universal loss regardless of the radiative lifetime of the collisional complex.

It is abundantly clear that ultracold, high-density gases of CaF molecules are not collisionally stable, which is a serious issue for the implementation of evaporative cooling. There are some ways to engineer interactions that prevent short-range losses and we will spend substantial efforts investigating one of these schemes in the next chapter <sup>51,119,50,74</sup>

# 4

## Engineering Molecular Collisions

We looked to nature to provide us with a collisionally stable high-density gas of ultracold CaF based solely on the intrinsic properties of the molecule but found universal losses occurring in every configuration we tried. This is not unexpected considering nearly every ultracold molecular collision experiment sees universal losses<sup>158,53,62,35</sup>. Evidently, we will not get good collisional properties for free, so we have to be creative and engineer

a way around the collisional loss processes. The end goal is to have control over the collisions such that we can implement evaporative cooling and have a long-lived high-density ultracold gas<sup>145,135</sup>.

The problem is navigable because the loss processes seem to only be active when the molecules are very close together<sup>14,139,71,105</sup>. This is the motivation to engineer a repulsive long-range barrier around each molecule to keep them from coming close enough together for a chemical reaction or sticky collision to occur. The idea is not to remove collisions altogether from the system but to create a situation where the molecules collide elastically and bounce off each other without changing state.

We have not yet taken advantage of the full structure of polar molecules and the collisional processes we have studied so far are dominated by the Van der Waals interaction. By virtue of the large permanent electric dipole moment of the molecules, we can polarize them in external fields and realize strong and long-range dipolar interactions. Of course, these interactions can be attractive or repulsive, depending on the relative orientations of the molecules. The trick to building a shield is to somehow orient any pair of colliding molecules in the repulsive direction of the dipole-dipole interaction<sup>51,119,50,74,75,73</sup>. We will accomplish this by using microwaves to program the molecules to repel when they cross paths with one another.

## 4.1 HOW DOES MICROWAVE SHIELDING WORK?

Engineering an interaction that guarantees repulsive behavior is not easy. There are two regimes we have to control: the separated regime where the molecules are far apart, unable to feel the presence of the other molecules, and the collision regime where all the two-particle dynamics happen.

Beginning with the separated regime, we prepare single-particle microwave field-dressed states by exposing the molecules to a carefully designed microwave field. Throughout the experiment, the microwave drive is continuously running, generating the dressed state. Molecules prepared in the upper dressed state (higher energy dressed state) rotate with their dipole moments perfectly out of phase with the microwave field, in contrast to molecules in the lower dressed state which follow in phase<sup>154</sup>. All other orientations of the molecule dipole moment and the nearly resonant microwave field are described by linear combinations of the two dressed states. As we will explain momentarily, the upper dressed state is relevant to collisional shielding and the lower dressed state enhances the loss rates (anti-shielding). When the molecules are very far apart, we want them to remain coherently driven by the microwaves in the upper-dressed state and that's the full extent of the separated regime control we must exercise over the system.

During a collision, the interaction becomes much more complicated. The molecules have a 3.07 Debye permanent dipole moment that generates a molecule-frame dipolar electric field given below:

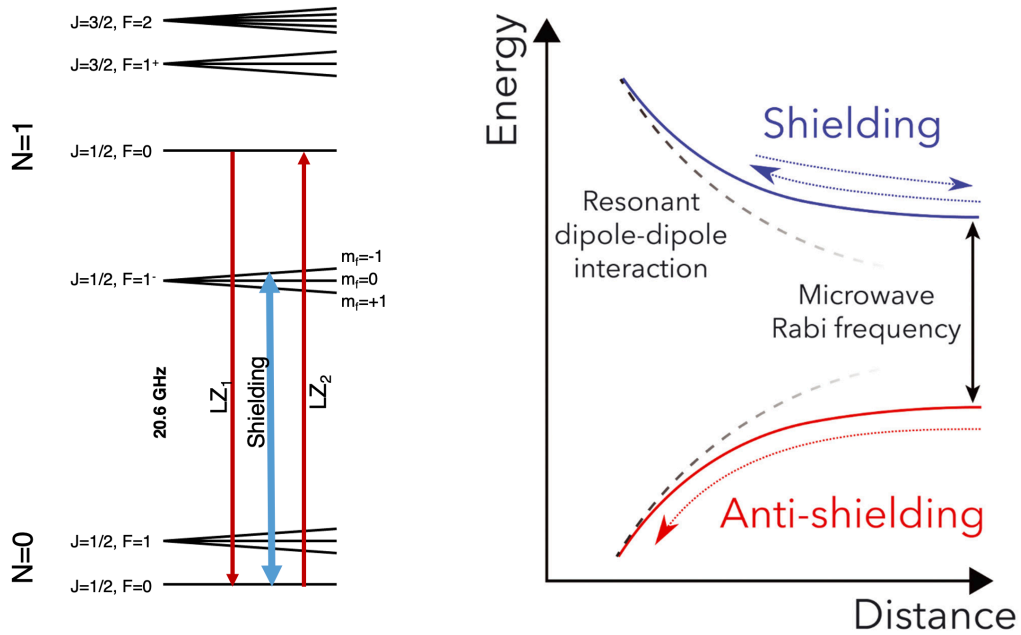


**Figure 4.1:** On the left is a level diagram showing all the hyperfine states in the  $N=0$  and  $N=1$  rotational manifolds. We optically pump all the population to the  $|N=1, F=0, m_f=0\rangle$  state. The red arrows indicate the direction of the Landau-Zener transfers,  $LZ_1$  and  $LZ_2$ .  $LZ_1$  moves the population to the absolute ground state, after which an optical pulse resonant with all 4 hyperfine levels in  $N=1$  heats away any remaining population. The thick blue arrow indicates the transition we drive during the shielding process. The  $LZ_2$ , at the very end of the experiment, brings the population back into the  $N=1$  manifold for imaging after the collision time. On the right is a cartoon showing the potential. The upper dressed state adiabatically connects to the repulsive branch, resulting in a classical turning point at around  $1000 a_0$ , long range compared to  $l_{V,dW}$ . The lower dressed state or anti-shielding state converts to the strongly attractive side of the potential resulting in enhanced loss rates compared to the ground state. The Rabi frequency is responsible for maintaining the gap that protects against Landau-Zener tunneling between the dressed states.

$$U(r, \theta) = \frac{d^2(1 - 3\cos^2(\theta))}{r^3} \quad (4.1)$$

When the molecules are close to each other, this field becomes the dominant interaction. In the case of collisions in the absence of an external field, there is nothing generating an orientation for the dipoles. During a series of collisions, the dipolar effects average out and the only remaining interaction is the dipole-induced-dipole interaction otherwise known as the Van der Waals interaction.

However, with the addition of microwaves, direct dipolar interactions become relevant because the external microwave field generates a global polarization of the dipole moments. As the molecules approach, there is a cross-over region (Condon point) where the dipolar interaction becomes stronger than the microwave driving<sup>51,50,74,75,73</sup>. Within this regime, there are two branches of dipolar interaction; one where the potential is attractive and one where it is repulsive. Since the manifold is smooth, the two free space-dressed states connect to the two branches of the dipolar interaction. The upper-dressed state maps to the repulsive branch during the collision, clearly where we want to be. The key to shielding is to cross this Condon point adiabatically connecting the upper dressed state to the repulsive branch. This results in a classical turning point at long-range compared to the Van der Waals length, below which universal loss is known to take place<sup>74,75</sup>. This turning point is illustrated semi-classically in Figure 4.1.

How does this create a repulsive dipole-dipole interaction for all orientations of collid-

ing molecules? The answer is it doesn't, however, it creates a situation whereby dressing the single molecules at large separations, we are programming the dipoles to anti-align with the electric field of the microwaves. During the collisions, the molecules are still programmed to be anti-aligned with an electric field provided that the anti-alignment adiabatically converts from the microwave electric field to the electric field of the colliding partner molecule's dipole moment. In this way, we always anti-align the dipole moments for maximum repulsion. Anti-shielding is possible too by preparing the lower dressed state and generating a situation where the dipoles auto-align to be strongly attractive<sup>154</sup>.

The key to this scheme working is to maintain adiabaticity during the collision and for many collisions thereafter. Maintaining adiabaticity requires a large gap between the dressed states which translates to high Rabi frequencies and a lot of microwave power<sup>74,75</sup>. In our case, we need to drive the molecules with 10's of MHz of Rabi frequency. This is the initial engineering challenge, to build a high-power K-band microwave source, however, there is a direct corollary with regard to the polarization.

## 4.2 POLARIZATION

Maintaining a large enough gap at the Condon point to ensure adiabaticity puts a constraint on the polarization of the microwaves, as we will see momentarily. The size of the gap is sensitive to the relative orientations of the microwave polarization to the

axis connecting two molecules during the collision, which is described by the following matrix element<sup>164</sup>

$$\begin{pmatrix} J' & 1 & J \\ m+q & -q & m \end{pmatrix} \quad (4.2)$$

For linear microwave polarization ( $q = 0$ ) and for molecules approaching along the polarization vector ( $m = 0$ ), the Q-branch of this matrix element ( $\Delta J = 0$ ) vanishes. For this configuration, the far field-dressed states cross over to the dipole-dipole-dominated regime with zero coupling and no energy gap, thus it is a real level crossing and non-adiabatic conversion between the dressed states cannot be avoided. In simple terms, for linear polarization, there is a hole in the shield at the North and South poles through which rapid losses can occur<sup>164</sup>. In the case of pure circular polarization, the matrix elements are always non-zero, leading to an avoided crossing at the Condon point with a gap sensitive to the Rabi frequency.

Elliptical polarizations can still be problematic, with the linear component able to create a hole in the shield. From the theory calculations, microwave shielding requires highly circular polarizations in order to have a loss rate below the universal ground state loss rate, measured in the previous chapter. We are targeting a 10 : 1 polarization cleanliness ratio, which corresponds to increasing the power of the circular polarization component by 20 dB above the other two polarization components.

### 4.3 LOSS PROCESSES

There are many ways shielding can fail and cause losses substantially faster than the bare Van der Waals-based universal loss rates we previously observed.

The first consideration is maintaining the dressed state while the molecules are not colliding since this is the state of the system for the vast majority of the time. Maintaining coherent microwave-molecule driving when the molecules are not colliding is critical since it defines the upper dressed state. The robustness and lifetime of the dressed state depend critically on the quality of the microwave drive in terms of the source phase noise, which we will characterize in great detail. As the coherence is lost, the population becomes a statistical mixture of both upper and lower dressed-states resulting in inelastic collisional losses.

When collisions occur, an obvious failure mode for shielding is not maintaining adiabaticity and unintentionally converting to the lower-dressed state/ attractive dipole-dipole interaction. This is the result of Landau-Zener tunneling, which we suppress with high Rabi frequency and circular polarization. The high Rabi frequency itself causes problems in the form of microwave-driven losses where the hyperfine levels become shifted during the collision process and can be driven directly by the microwaves<sup>74,75</sup>. This results in heating and the potential for lossy collisions when other hyperfine states become involved. Microwave-induced loss is the main limitation to shielding in free space and is heavily influenced by the structure of the molecule. We choose our shield-

ing states with this in mind.

### 4.3.1 STATE SELECTION

Having established microwave-induced loss as the primary loss channel, the success of the project relies on picking the most optimal sets of states to use for shielding. Using a coupled-channel calculation run by Tijds Karman (Figure 4.2), we settled on using the absolute ground state  $|N = 0, F = 0, m_f = 0\rangle$  and the  $|N = 1, J = 1/2, F = 1^-, m_f = -1\rangle$  state as the bare states that we want to dress for the shielding experiment. The intuition, which happens to be somewhat accurate, suggests these states should suffer the least from microwave-induced losses because both the upper and lower states in the transition are the “ground states” of their respective rotational manifolds. This eliminates hyperfine loss channels within the same rotational manifold driven by level crossings that happen during collisions, however, there is probably no way to get around hyperfine state-changing loss channels between the rotational manifolds coupled directly by the microwaves as the energy levels shift during a collision.

The only downside to our choice of states is with regard to how we populate the shielding states. Since the optical pumping step is ideal for single quantum states, we elect to pump all the population into  $|N = 1, F = 0, m_f = 0\rangle$ . This requires us to use the same Landau-Zener transfer mechanism from the last chapter to move the population into the absolute ground internal state,  $|N = 0, F = 0, m_f = 0\rangle$ . From here, we jump the microwave frequency to be nearly on resonance with the  $|N = 0, F = 0, m_f = 0\rangle \longleftrightarrow$

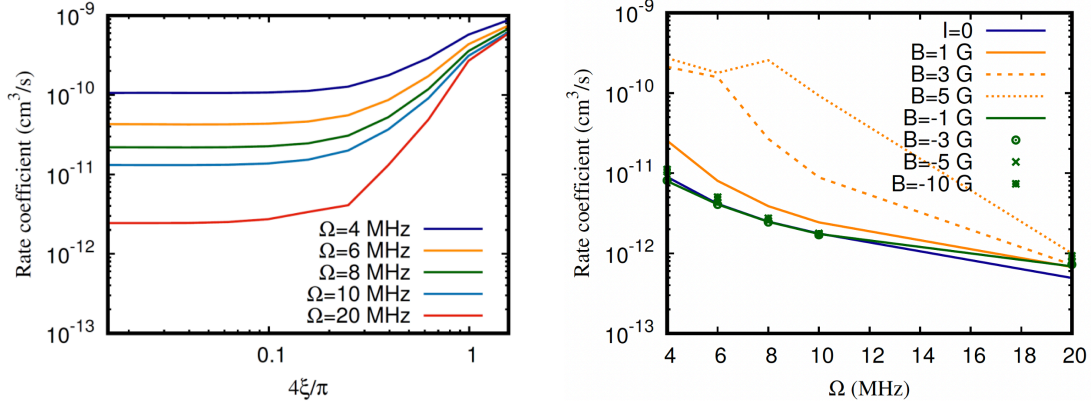


**Figure 4.2:** Coupled channel inelastic loss rate calculations produced by Tijs Karman. On the left is a plot of two-body loss rate vs microwave polarization ellipticity for several different Rabi frequencies. The ground state loss rate is  $1.4 \times 10^{-10} \text{ cm}^3/\text{s}$  which restricts the parameter space for the Rabi frequency and microwave polarization cleanliness if we seek to suppress the loss rates below the bare ground state. This calculation does not include the effects of the trap light, which we will add later in the chapter. The plot on the right shows the loss rates at different magnetic fields. The negative magnetic fields correspond to driving to the  $|N = 1, F = 1^-, m_f = -1\rangle$  excited state level. It was not clear to us why the calculations indicate the  $|N = 1, F = 1^-, m_f = -1\rangle$  state is better than  $|N = 1, F = 1^-, m_f = +1\rangle$ .

$|N = 1, J = 1/2, F = 1^-, m_f = -1\rangle$  transitions, for preparing the dressed states. The multi-step preparation process significantly reduces our data rate due to the multiplicative losses for each step of the process.

#### 4.4 BUILDING THE MICROWAVE SYSTEM

Our experiment will use the same tweezer merging architecture from the previous study but now with the addition of a much more sophisticated microwave system and quantum state engineering. The microwave system's technical requirements for power, frequency, polarization control, polarization cleanliness, and phase noise will require considerable

innovation to meet. We will also find the quantum state engineering for microwave shielding has its own set of challenges.

The first objective is to settle on an antenna architecture that can produce circularly polarized microwaves at 20.5 GHz. We opted to build a  $2 \times 2$  array of helical antennas<sup>85</sup>. The circumference of the helix is the wavelength and the spacing between wraps should be  $\lambda/4$ . The directional gain of the antenna is set by the total number of windings. Our 20.5 GHz antenna was 5 mm in diameter and had 8 windings, giving it a height of 3 cm. The copper wire was bound to a 3D-printed (ABS) helical form to ensure uniformity and ease of construction and an individual SMA connector was soldered onto each arm of the antenna to feed power. Figure 4.3 depicts the antenna. The 4-antenna array, with each antenna rotated sequentially by 90 degrees produces a very clean circular polarization in free space. We impedance-matched the antenna by minimizing back reflected microwave power at 20.5 GHz, monitored on a spectrum analyzer. The tuning was done by dropping little pieces of molten solder on the fixture to influence the capacitance. We found this method wasn't particularly controllable but it eventually yielded an antenna with less than  $-12$  dB of back reflected power at 20.5 GHz

The helical antennas operate in axial mode creating circular polarization around the z-axis of the MOT coils. The array has a copper back plate with a hole for the z-beam MOT light to pass through. A 90% transparency copper mesh covers this hole to allow light to pass through, but reflect microwaves. The antenna array is mounted inside of a re-entrant window tube just above the upper, in-vacuum, MOT coil with the tip of the

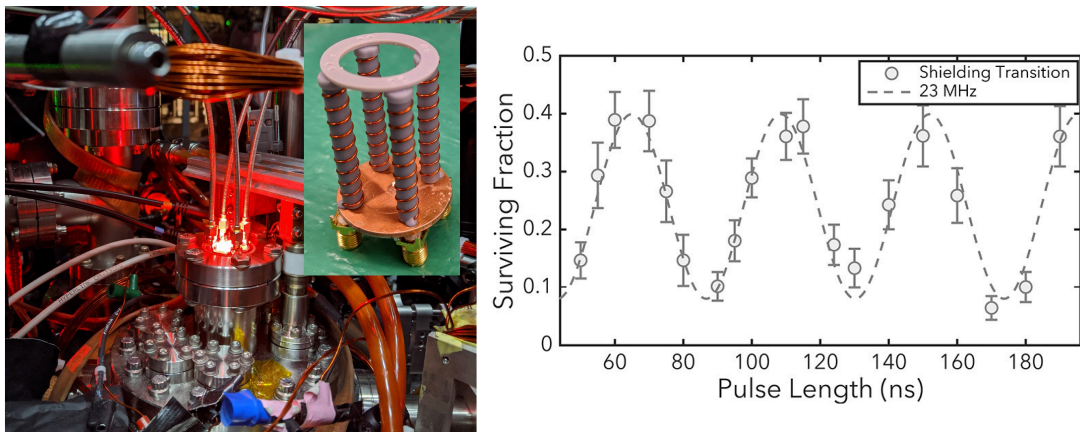


**Figure 4.3:** On the left is a picture of the helical antenna array and the antenna mounting configuration in the MOT chamber. The antenna array assembly (green background) sits in the re-entrant window with the SMA connectors facing upwards. Just out of frame at the top of the MOT chamber image are the 4 amplifiers, phase shifters, and phase-stabilized cables on each of the 4 antenna arms. On the right is a measure of the Rabi frequency on the shielding transition. This corresponds to a circularly polarized electric field of 27 V/cm at 20.5 GHz.

antenna a few centimeters away from the molecules in order to maximize the microwave electric field at the tweezer location.

The antenna is fed with microwaves generated by mixing an 18.5 GHz (Keysight E8257D) source with a 2 GHz source (Windfreak SynthHD Pro locked to a 100 MHz low-phase noise oscillator). Following the mixer, a bandpass filter selects the 20.5 GHz signal which is then amplified, as seen in Figure 4.4. Next, the signal is split into four paths, each with an individually adjustable phase shifter and a high-power amplifier (TGA4548-SM) producing about 5 Watts each.

This setup is capable of producing 30 V/cm electric fields at 20.5 GHz based on the combined power of the amplifiers and the expected directional gain of the antenna array.

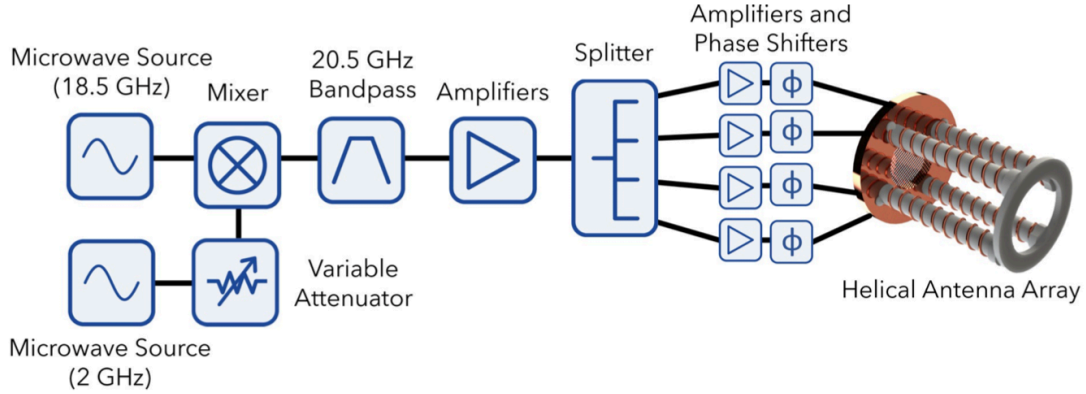


**Figure 4.4:** Microwave system used for shielding. Our method of state preparation for shielding requires amplitude control of the microwaves which we achieve using a voltage variable attenuator on the 2 GHz arm. Several microwave elements are not shown. We used stacked switches (2 switches, each with 60dB isolation) to prevent low-level microwave leakage from driving unwanted rotational transitions. Also not pictured on the 2 GHz arm is the second microwave source coupled in on a switch. We use this source for a Landau-Zener frequency sweep during the state preparation steps, but then the switches close, and the Windfreak provides the CW microwave source for shielding. Every component after the 4-way power splitter is phase-stabilized and carefully tested on the vector network analyzer for phase stability.

The next challenge is to optimize the polarization of the field in the vacuum chamber environment, with uncontrolled reflections coming from the metal chamber itself as well as metallic fixtures for the MOT coils.

#### 4.5 POLARIZATION

The coupled channel theory calculations indicating that driving the  $|N = 0, F = 0, m_f = 0\rangle$  to  $|N = 1, F = 1^-, m_f = -1\rangle$  transition is optimal for shielding. This implies that we want the antenna to drive the  $\epsilon_-$  polarization, relative to the molecule's reference frame. The helical antenna array produces microwaves with a handedness set by the coil windings of the antennas however we can orient the molecules using the directionality of the  $z$ -axis

magnetic field. Swapping the direction of the magnetic field also swaps the labeling of the  $m_f$  states, or the assignments of the  $\sigma_{+,-}$  transitions while in the lab frame, the helicity of the microwaves never changes.

In order to optimize the  $\epsilon_-$  polarization experimentally, we need to be precise about what specifically matters. The shielding is sensitive to polarization ellipticity relative to the local k-vector axis of the microwave field. However, our fixed orientation experiment gives us measurement access to the polarization of the field projected onto a quantization axis that we define in the lab frame. The tricky aspect is that in order to optimize the polarization by measuring it directly with the molecules we need a single measurement that captures the polarization state. In practice, we do this by applying a bias magnetic field along the z-direction, co-axial to the propagation direction of the microwave beam. This works because the microwaves are nominally traveling along the z-axis and their polarization should lie in the x-y plane only. This indicates the  $\pi$  polarization should be almost non-existent by construction which reduces the degrees of freedom making it possible to optimize the  $\epsilon_-$  polarization by only looking at the  $\sigma_-$  transition Rabi frequency.

While we want to optimize the  $\epsilon_-$  polarization, we still need to fully characterize the microwave electric field. We measure the polarization directly by driving three sets of microwave transitions in the molecule, each one sensitive to the  $\sigma_+$ ,  $\sigma_-$ , and  $\pi$  projections of the microwave polarization on the quantization axis defined by our applied magnetic field. We used the following “test” transitions to characterize the 20.5 GHz

electric field.

$$\sigma_- \text{ Transition } |N = 1, F = 0, m_f = 0\rangle \longleftrightarrow |N = 0, F = 1, m_f = +1\rangle \quad (4.3)$$

$$\pi \text{ Transition } |N = 1, F = 0, m_f = 0\rangle \longleftrightarrow |N = 0, F = 1, m_f = 0\rangle \quad (4.4)$$

$$\sigma_+ \text{ Transition } |N = 1, F = 0, m_f = 0\rangle \longleftrightarrow |N = 0, F = 1, m_f = -1\rangle \quad (4.5)$$

Each of these transitions corresponds to a component of the polarization written in the basis  $\vec{E} = E_+ \hat{\epsilon}_+ + E_- \hat{\epsilon}_- + E_z \hat{z}$ , where  $\hat{\epsilon}_{+,-}$  is  $\hat{x} \pm i\hat{y}$ . This basis is complete and carries the same information as the usual cartesian basis, however, it's written in a natural form for the angular momentum description of the field. The test transition Rabi frequencies are sufficient to characterize the full field, requiring only the matrix element associated with the dipole transition moment as a conversion factor to electric field strength. The matrix elements enter in the following way:

$$\Omega_{rabi} = d \times E_{+,-,z} d \langle N = 1, F = 0, m_f = 0 | \epsilon_{+,-,z} | N = 0, F = 1, m_f = -1 \rangle \quad (4.6)$$

Based on the nature of the hyperfine couplings between the electron spin and nuclear spin, the test transition matrix elements are very sensitive to magnetic fields. In Figure 4.5 we calculate the matrix elements for the test transition as well as the shielding

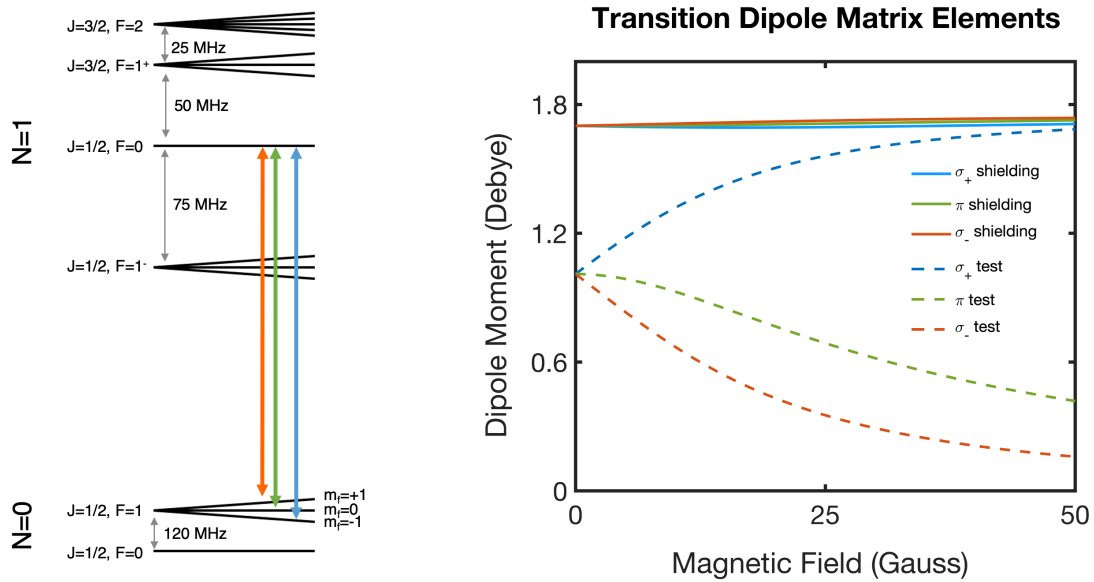


**Figure 4.5:** Left: Color-coded arrows indicate the test transitions we used to measure the microwave polarization. The arrow color coding corresponds with the color coding of the dotted lines in the calculation of the transition dipole moment on the right. The test transition is very sensitive to magnetic fields because it requires driving a spin-flip that is only allowed because of the mixing from the hyperfine interaction. The shielding transition has little sensitivity because it does not rely on any internal couplings to drive the transition. The value of these matrix elements is used to calculate the electric field polarization from the measurements of the Rabi frequencies on the same transitions in the presence of a 13 Gauss magnetic field.

transition as a function of the magnetic field.

#### 4.6 MEASURING POLARIZATION

The “test” transitions we used to measure the polarization are not the same as the shielding transitions. This is a matter of convenience, as the additional Landau-Zener sweep required to access the shielding states reduces our data rate. The width of the test transitions is set entirely by microwave power broadening. Splitting the  $m_f$  projections by applying a 13 Gauss magnetic field is sufficient to spectroscopically resolve all three

<b>Transition Type</b>	<b><math>\Omega</math> “Test”</b>	<b>Dipole (Test)</b>	<b><math>\Omega</math> Shielding</b>	<b>Electric Field</b>
$\sigma_+$	1.6 MHz	1.4 D	1.9 MHz	2.4 V/cm
$\pi$	2 MHz	0.98 D	3.4 MHz	4.0 V/cm
$\sigma_-$	7.7 MHz	0.6 D	22 MHz	26 V/cm

**Figure 4.6:** This chart indicates typical properties of our microwave electric field. The test transition Rabi frequencies are given after optimization and the matrix elements for the test transition are calculated for a 13 Gauss magnetic field. From the matrix elements, we can back out the electric field components, plotted on the far right. The equivalent Rabi frequencies for the shielding transition for the same microwave polarization pattern are also given (calculated in this case). We measured the ratios of the Rabi frequencies on the shielding and test transitions separately and the ratios match the matrix elements extremely well.

transitions. The matrix elements show a significant magnetic field dependence because a spin flip is required to drive the  $\pi$  and  $\sigma_+$  components of the transition. Table 4.6 below summarizes typical values for the field and the rabi frequencies.

We also compared the polarization on the shielding transition to the test transition to check the ratios of the Rabi frequencies. The test transition is about 60 MHz lower in frequency than the shielding transition, which should not cause much of a change in polarization due to antenna geometry. The polarization measured on the test vs shielding transitions confirmed the matrix elements are correct and the polarization produced by the antenna is the same at both frequencies. This validates our use of the “test” transition to quickly diagnose and optimize the polarization.

## 4.7 ADJUSTING THE POLARIZATION IN THE CHAMBER

Each of the 4 helical antennas in the array has an independently adjustable phase that can be tuned to optimize the polarization. The phase is adjusted using differential path length mechanical phase shifters, actuated manually. The phase tuning primarily steers the beam, however, steering the beam also changes the polarization pattern of the emission as well as the electric field structure in the vacuum chamber due to the reflections. It is important to note that we were only aiming to optimize the polarization over a very small volume, one optical tweezer. Our beam steering and polarization optimization controls do not necessarily guarantee that optimal Rabi frequency and polarization cleanliness can be simultaneously achieved, and sometimes times we found that was not the case.

We were able to do an initial alignment of the microwave phases by aiming the free space beam at a microwave-absorbing material and imaging the spot with a thermal camera (see figure 4.8). This worked courtesy of the relatively high power we had available. Using this technique, we adjusted the phases of the antennas to make the spot as symmetrical as possible and we found with a reasonably high correlation, this condition was not too far from optimal once the antenna was installed in the re-entrant window on the experiment.

The process of optimizing the polarization was time-consuming at best. We optimize the polarization by adjusting the phase shifters to maximize the Rabi frequency of the

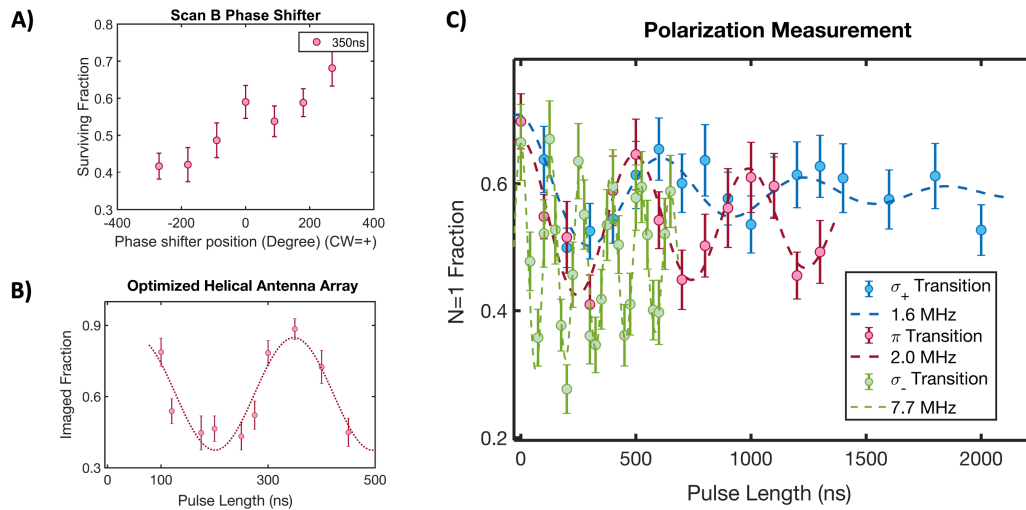


**Figure 4.7:** The polarization was optimized by setting the pulse length to a time that was mid-way up the rising slope of a Rabi oscillation driving the  $\sigma_-$  transition. Plot A shows the phase of “arm A” on the helical antenna array and the resulting effect on the N=1 surviving population. As the Rabi frequency increases, the oscillation phase shifts such that more population remains in N=1 for the same pulse length of 350 ns. As the surviving fraction approaches the full survivability of the experiment, we shorten the time. This process is iterated until the global maximum is reached. Optimizing the power in the most strongly driven polarization component had the corresponding effect of reducing the power in the other two polarizations, as seen in part C. Due to the matrix elements in figure 4.5, the electric field components are actually more favorable than the Rabi frequencies indicate.  $\epsilon_{\sigma_+} = 2.4$  V/cm,  $\epsilon_{\sigma_-} = 26$  V/cm and  $\epsilon_{\pi} = 4$  V/cm; corresponding to a 31:1 power extinction ratio in this particular case.

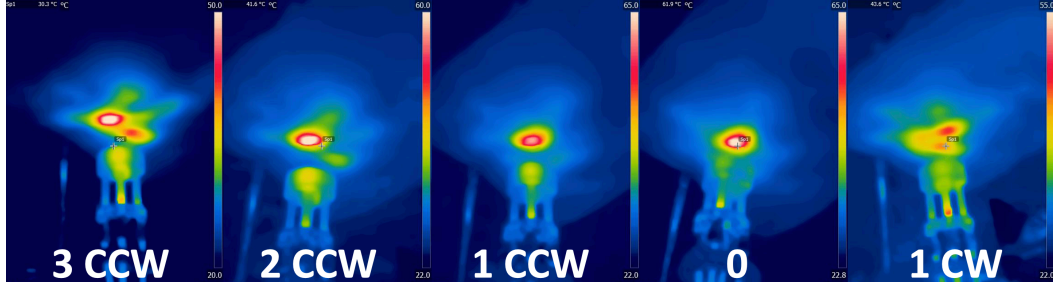


**Figure 4.8:** Thermal images of a microwave absorbing material being heated by the microwave beam. The labels indicate the number of turns ( $60^\circ/\text{turn}$ ) of the phase shifter on one arm of the array. Note the beam shape becomes very irregular. We optimized the phases to make the beam as circular as possible in free space before installing the antenna into the MOT chamber. This was a sufficiently good starting point from which we often found the optimal polarization in the MOT chamber could be achieved within 1 turn of tunability on each arm. We later substituted a microwave power meter on the floor to measure the power of the beam as it exits the MOT chamber through the lower z-MOT beam window. Optimizing the power on the floor seemed to have the same effect as circularizing the beam on a microwave absorber outside of the chamber.

transition driven by the  $\sigma_-$  component of the field. The process involves measuring the initial Rabi frequency, parking on the falling edge of the first period by setting the microwave pulse time to roughly  $\pi/2$ , and then slowly walking the phase, one antenna at a time, to minimize the probability of a molecule remaining in  $N=1$ . This indicates an increase in Rabi frequency, as the Rabi oscillations speed up the  $\pi/2$  pulse eventually becomes a  $\pi$  pulse. Once we are near the minimum, we cut the pulse time further and continue optimizing. We only adjust 3 of the 4 antenna phases, leaving one stationary as the global phase reference. We then try moving the pulse length out past several Rabi cycles to increase the sensitivity to the phase shifts and then repeat the optimization process. At this point, the typical phase increment is about  $5^\circ$  per tuning step and several minutes' worth of data is needed to have sufficient statistics for each point. Figure 4.19 depicts the process.

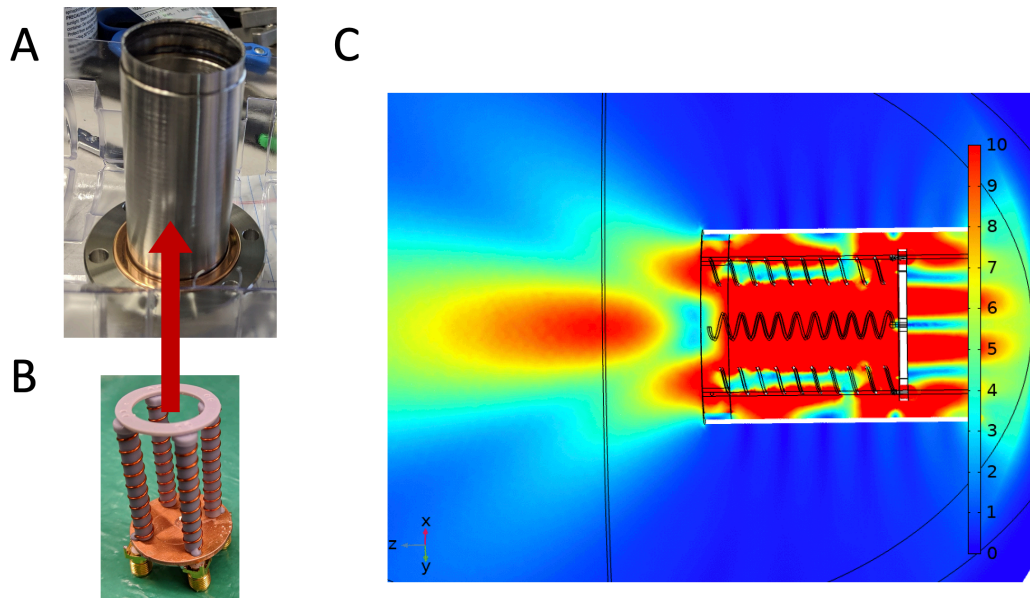


**Figure 4.9:** Images A and B show the re-entrant window tube and antenna assembly, respectively. The antenna slides into the re-entrant tube, indicated by the red arrow. The assembly mounts in the vacuum chamber with the window tube ending a few millimeters above the top MOT coil. Figure C is a simulation of the electric field intensity generated by the antenna in the re-entrant tube. The conductive boundary condition greatly impacts the radiation pattern. Fortunately, the location of the optical tweezer is in the high-power region, about 2 cm below the antenna. This simulation doesn't take into account the rest of the MOT chamber geometry.

Maximizing the Rabi frequency in the  $\sigma_-$  component appears to produce a local maximum in the power extinction ratio  $\epsilon_+^2/(\epsilon_-^2 + \epsilon_z^2)$ , however, it is not guaranteed to find the global maximum. We found we had to move the microwave antenna in the re-entrant window when after optimizing the microwave phases the resulting polarization was not clean enough. Moving the antenna involved sliding it up and down which changed the mode structure slightly in the chamber and changed the structure of the side lobes of the radiation pattern produced by the antenna.

We supplemented our system with various microwave absorbers and reflector plates. Our simulations showed the stainless steel walls of our re-entrant window tube in close proximity to the antenna array significantly changed the radiation pattern and polarization cleanliness (Figure 4.9 and Figure 4.10). We changed the boundary condition by adding a microwave-absorbing material layer between the helical array and chamber walls. This seemed to improve the polarization cleanliness at the cost of Rabi frequency.

]

We also attempted to modify the lower window on the vacuum chamber in the direction the microwave beam propagates. First, we replaced the small 2.75" z-MOT beam viewport with the largest viewport the chamber could accommodate (6" CF) to minimize the cross-section of the reflecting plane directly below the helical antenna. We placed an absorbing microwave meta-material sheet with a small hole for the MOT beam right under the window. This did not seem effective. We then turned the sheet over and used the metallic backside as a reflector. Adjusting the angle and position of

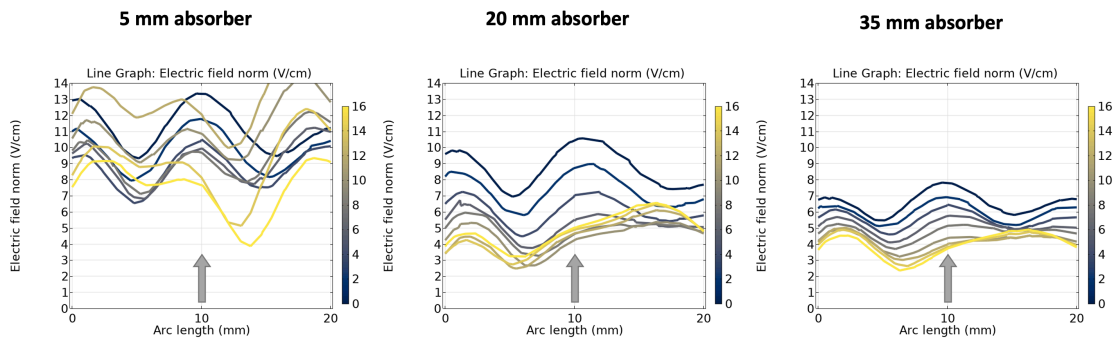


**Figure 4.10:** Adding an absorbing material to the edge of the antenna array in the re-entrant window has a dramatic effect on the microwave field. While the absorber made the polarization cleaner by removing interference effects from reflected sidelobes in the re-entrant tube, it came at a steep cost in power coupled into the chamber. Evidently, near-field effects around the antenna are critical for delivering power in a beam. The x-axis indicates the position below the bottom of the antenna array along the symmetry axis and the arrow marks the position of the optical tweezer. The different curves on each plot indicate different antenna insertion heights in the re-entrant tube. Typically the further the antenna goes down the re-entrant tube, the better.

the reflector increased the Rabi frequency slightly but did not help substantially with the polarization. We ultimately left the reflective side facing up but tilted the plane to  $45^\circ$  to better outcouple the microwaves and reduce any unwanted reflections coming from the reflector plate.

The polarization felt by the molecules is largely dominated by the reflections in the chamber, as indicated by the simulations shown in Figure 4.11. This is probably the reason why adjusting the phases on the 4 antennas had such a dramatic effect. Nominally the phase shifters steer the microwave beam which doesn't change the polarization so dramatically in free space. In our quasi-cavity vacuum chamber, small direction changes in the beam have dramatically different reflective consequences for polarization. The most basic way to see this is to understand that in the chamber vs. free space, the

microwave k-vector is no longer axially oriented so there will automatically be substantial 3D polarization effects in the chamber. This leads to a stronger-than-desired  $\pi$  polarization component which we found was difficult to tune out.

We often found the ratio of  $\sigma_-$  to  $\sigma_+$  polarization was easily adjustable using our phase shifters however the  $\pi$  polarization was not. It was, by construction, supposed to be very weak given the microwave beam should propagate along the z-direction parallel to the magnetic field. We found different positions of absorbers in the re-entrant window sometimes made this polarization stronger. We think this has to do with the side lobes of the radiation pattern becoming attenuated. This probably steers the beam off-axis, contributing to the large  $\pi$  projection of the microwave electric field onto the quantization axis. When the antenna was in a favorable position that was inspired by simulation but found via trial and error, the  $\pi$  projection was very small indicating the plane containing the microwave polarization was nearly perfectly perpendicular to the direction of our bias magnetic field.

Once we secured the antenna in a favorable position and optimized the phases through several iterations of adjustment, we measured all three Rabi frequencies on the test transitions. From the measurements, we calculated the polarization ellipticity angle in the plane containing the electric field vector by first estimating the angle between the polarization plane and the z-axis magnetic field using the formula:

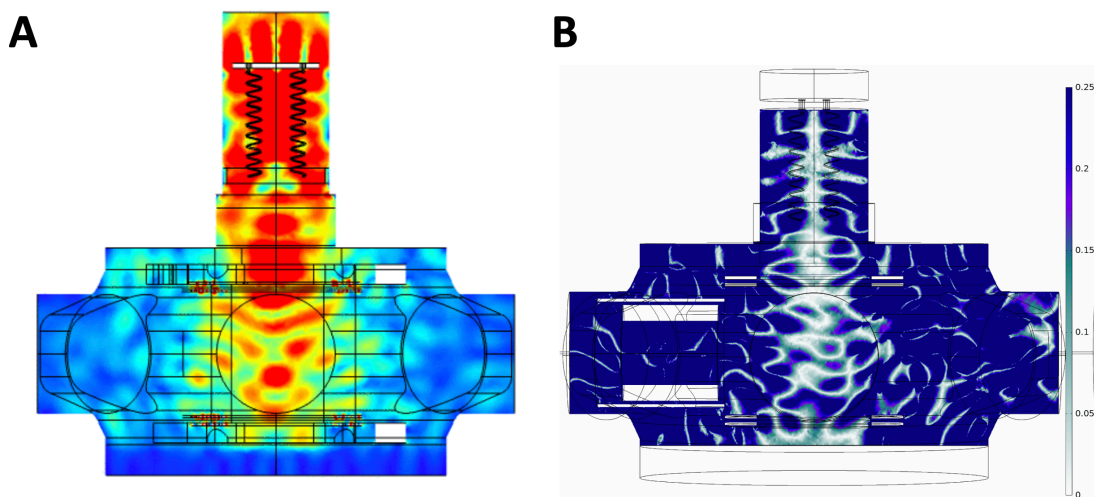


**Figure 4.11:** Figure A is a simulation showing the microwave power in the chamber. The nodal pattern is mostly set by the reflection of microwaves in the chamber. We have a limited capacity to move the nodes by raising and lowering the antenna in the re-entrant tube. This is indicated both experimentally and in the numerical model. We found forcing the antenna to the bottom of the re-entrant tube was always ideal. The molecules are located at the center of the chamber in a volume that is many orders of magnitude smaller than the length scale of the structures we see in the chamber. Figure B shows the polarization cleanliness of the microwave field. The color scale indicates the ellipticity of the microwaves ( $\zeta$ ) where small values of  $\zeta$  indicate a high degree of circular polarization. The central region where the microwave beam propagates is relatively clean whereas off-axis regions are dominated by reflections that tend to randomize the polarization.

$$\theta = \tan^{-1}\left(\frac{\epsilon_{\pi}}{\epsilon_{\sigma_{+}} + \epsilon_{\sigma_{-}}}\right) \quad (4.7)$$

The tilt angle is very small,  $5 - 10^{\circ}$  but not negligible considering the high extinction required by shielding. Correcting for the tilt angle, we can estimate the polarization ellipticity angle in the tilted plane containing the polarization ellipse from the  $\sigma_{+,-}$  field components, defined as:

$$\vec{E} = \epsilon_{\sigma_{-}} \cos(\zeta) - \epsilon_{\sigma_{+}} \sin(\zeta) \quad (4.8)$$

The ellipticity  $\zeta$  can be as good as 0.1 for our best optimization. This is excellent, considering the chamber is full of uncontrolled reflections coming from non-planar surfaces. During a collision, the microwave electric field independent of its projection onto our applied quantization axis is what the molecules are sensitive to, so a full field reconstruction is necessary. The agnosticism towards the lab magnetic field is because the relevant quantization axis during the collision is the vector between the two colliding molecules, which we have no control over in the lab frame.

#### 4.7.1 MICROWAVE ANECDOTES

Early in the experiment, we struggled with phase/polarization stability, finding the polarization cleanliness would drift day to day. We later discovered the power-stabilized SMA cables we used are not phase-stabilized cables. Non-phase stabilized cables have

some insidious characteristics. Checking the cables with a vector network analyzer, we realized they are very stress-sensitive, and moving the cables by the amount we did to adjust the antenna height can change the phase by 10's degrees. That's enough to completely alter the polarization patterns and it's probably the reason why we thought rotating the antenna in the re-entrant window was a useful tuning degree of freedom despite the axial symmetry of the MOT chamber. Upon adding the phase-stabilized SMA cables, we saw no effects from rotating the antenna assembly or from bumping and slightly stressing cables.

The second thing ordinary SMA cables with PTFE dielectrics do is undergo a phase transition right around room temperature<sup>42</sup>. PTFE undergoes a structural change in the  $20^\circ - 30^\circ$  C range, perfectly overlapped with the lab temperature. This phase transition called the PTFE knee, can cause phase shifts when the cables are heated by the touch of a hand. We promptly replaced all the cables after the 4-way splitter with phase-stabilized SMA cables and the polarization stability issues disappeared completely from the experiment. One lesson to learn is that power-stabilized cables are often not phase-stabilized cables and vice versa.

## 4.8 DRESSED STATE PREPARATION

Shielding requires us to adiabatically prepare the upper dressed state. There are several ways to prepare dressed states including frequency sweeps and power ramps. We opted

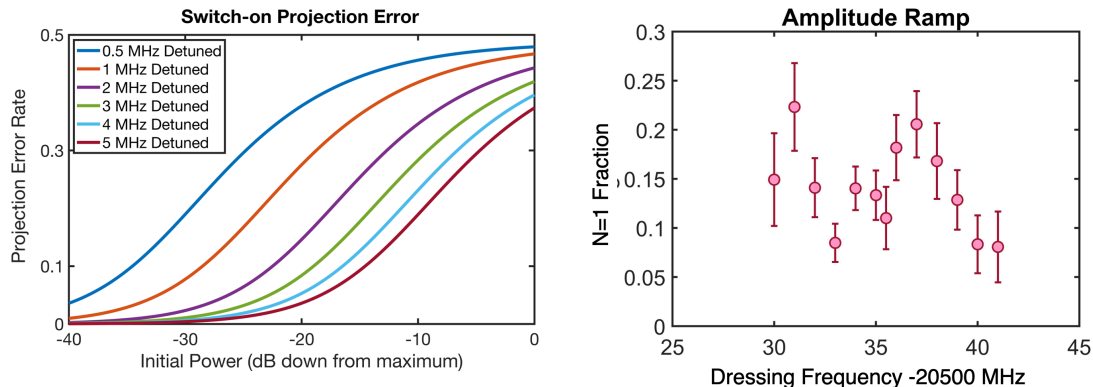


**Figure 4.12:** On the left is a calculation of the “switch on” projection error in our state preparation. A finite amount of microwave power leaking through the voltage variable attenuator goes to the antenna the moment our fast switches open. The x-axis is the amount by which the leakage is suppressed relative to the full power value (20 MHz, in Rabi frequency units measured at the molecules on the shielding transition). The projection error is sensitive to the detuning of microwaves. On the right, we use this projective error measurement to do spectroscopy. While we already know where the states are, this technique produces a measure of dressed state preparation fidelity as a function of detuning from the resonance. It serves as a reference for how close to resonance we should set the fixed detuning for well-constructed dressed states leading to optimal shielding

to keep the detuning fixed and ramp the microwave power using the voltage variable attenuators on the 2 GHz arm. We generated the ramp using a programmable and triggerable DDS system to output the ramp profile to the variable attenuator. Meanwhile, the detuning was held constant, typically around 2 MHz. At this detuning, we are able to ramp the microwave power extremely fast without projecting into the wrong dressed state. This implies that most of our state preparation error is switch-on generated error (projection error that occurs due to having finite microwave power when we open the fast microwave switches calculated in Figure 4.12), and not due to the adiabaticity of the power ramp.

While the ramp rate doesn’t have a strong impact, the detuning offset does. We

devised a spectroscopic way to set the detuning and measure the population in the correct dressed state. When we prepare the dressed states, we start with all of the population in the bare ground state. If we adiabatically dress the state by ramping on the microwave power and then adiabatically convert back to the bare ground state by ramping down the microwave power, we should find no population was transferred to the  $N=1$  manifold. This measure doesn't guarantee that we've prepared the correct dressed state but it is a measure of reversibility and preparation fidelity. We went about setting the detuning by ramping the dressing microwaves up, holding for 5 ms, ramping down, and then imaging the  $N=1$  manifold. When the detuning is too close to resonance there is a large switch-on projection error and we see population transferred to the  $N=1$  manifold. We picked the smallest detuning where no population was accidentally transferred to the  $N=1$  manifold, typically 2 MHz. Again, this is probably set by the switch-on power however there's no need to reduce the projection error since a 2 MHz detuning on a 20 MHz Rabi frequency drive works well for shielding, according to the coupled-channel calculations.

While our method for preparing the dressed state is simple, there are a few complexities to consider when we want to prepare the lower dressed state for anti-shielding as we will do later. In the case of the upper dressed state, we started with the microwave detuning set 2 MHz to the blue and then ramped the power up. This dressed state goes up in energy as the microwave power increases, away from the other  $m_f$  levels below and as a result, it never has any avoided crossings and remains what we will

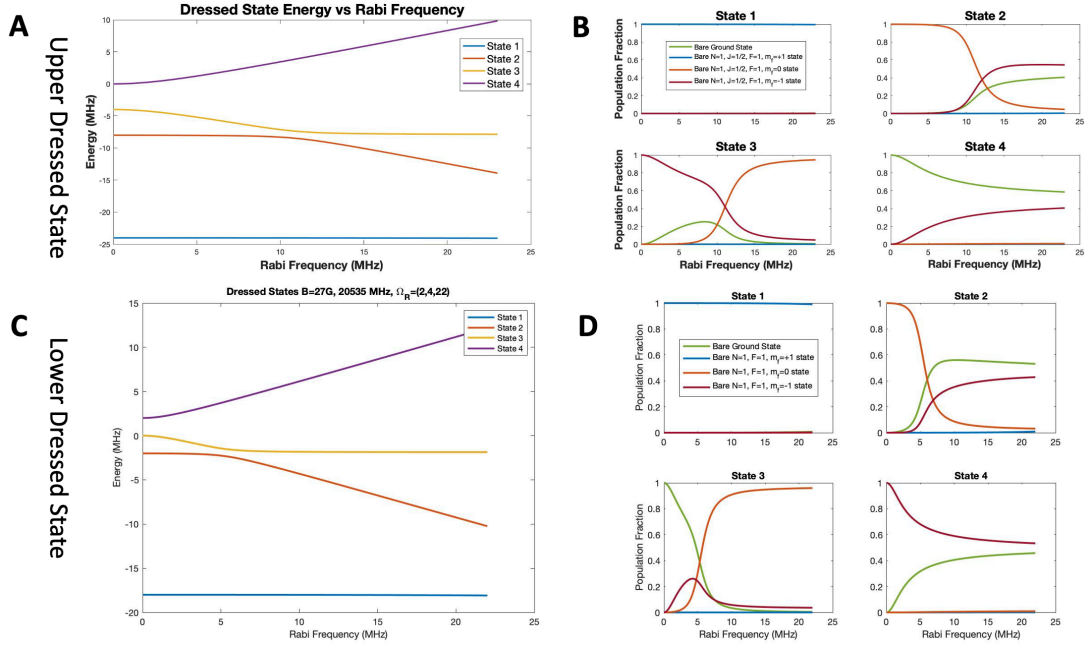


**Figure 4.13:** Simulation results showing the composition of the dressed states as the microwave power ramps up. The splittings of the  $m_f$  levels in the  $N=1$  manifold are set by the bias magnetic field (27 Gauss), and the light shifts from the trap. The microwaves predominantly drive the shielding transition,  $\pm 2$  MHz blue/red detuned of resonance and the polarization of the microwave field is incorporated by including the off-resonant driving of  $\sigma_+$  and  $\pi$  transitions with a coupling strength given by the ratios of the resonant Rabi frequencies (we measured these directly in the experiment). In the calculation, the ratio of the coupling strengths (microwave polarization) is held constant as the power ramps up.

Panels A and B show the state preparation for the shielding configuration. Panel A shows how the dressed states shift as a function of microwave power. State number 4 is the one we are interested in, the upper dressed state. Panel B shows the bare state composition of the same states 1-4 from panel A as a function of Rabi frequency measured on the strong polarization component. We can see that state 4 begins as the pure ground state (this is where the population sits after the first Landau-Zener sweep) and becomes nearly a 50 : 50 mixture of the bare ground state and the bare  $|N = 1, F = 1^-, m_f = -1\rangle$  state. Panels C and D show what happens if we try to prepare the lower dressed state in the same way, doing nothing other than setting the detuning to -2 MHz. Now we are interested in state 3 (again this is where the population enters from the bare ground state), which moves down in energy as the rabi frequency increases. It eventually runs into state 2. Panel D shows the population adiabatically transfers to  $|N = 1, F = 1^-, m_f = 0\rangle$ , which is not what we want. This is the reason why we have to prepare the lower dressed state by flipping the magnetic field direction and then tune the microwaves red of  $|N = 1, F = 1^-, m_f = -1\rangle$ . That process is the mirror image of panels A and B, where the lower dressed state moves down and away from all other states as the power ramps up.

call an uncontaminated dressed state comprising of increasingly equal mixtures of the bare ground state and the bare upper state  $|N = 1, J = 1/2, F = 1^-, m_f = -1\rangle$ . Note the  $|N = 1, J = 1/2, F = 1^-, m_f = 0\rangle$  manifold has a negative g-factor so the  $m_f = -1$  projection is actually the highest energy state in the presence of a small magnetic field. This is an ideal situation, however, to prepare the lower dressed state, we set the detuning to be -2 MHz below the  $|N = 0, F = 0, m_f = 0\rangle \longleftrightarrow |N = 1, J = 1/2, F = 1^-, m_f = -1\rangle$  transition. As the microwave power increases the lower dressed state moves down and has an avoided crossing with the  $|N = 1, J = 1/2, F = 1^-, m_f = 0\rangle$  state, adiabatically converting the population we prepared into a hybrid state with a substantial admixture of  $|N = 1, J = 1/2, F = 1^-, m_f = 0\rangle$ . We did not simulate hybrid dressed states in the coupled channel calculations, nor do we have good reason to think that  $m_f = 0$  states contribute strongly to the shielding performance.

In order to prepare the lower-dressed state properly, we opted to flip the entire system over to make a mirror image of the upper-dressed state. In principle, setting the detuning 2 MHz below the  $|N = 0, F = 0, m_f = 0\rangle \longleftrightarrow |N = 1, J = 1/2, F = 1^-, m_f = +1\rangle$  transition would produce a lower dressed state, but we wouldn't be driving this transition with the strongly circularly polarized microwaves because the handedness is wrong. A simple fix is to flip the direction of the magnetic field to reverse the handedness of the microwaves in the molecule's frame. The lower dressed state moves down and away from all other states as the power is ramped up. This is symmetrical to the process of creating the upper dressed state. Figure 4.13 summarizes the evolution of the states during the state

preparation microwave power ramp.

#### 4.9 MICROWAVE PHASE NOISE

A secondary, but no less important, microwave control problem surfaced when we tried to prepare long-lived dressed states. The dressed state relies on a coherent interaction between the molecular system and the microwave field. Instabilities in the microwave power or fluctuations in the frequency (equivalent to phase noise or phase jitter) could upset the dressed state, depending on the time scale of the fluctuations. The dressed state dynamical sensitivity is centered around the gap frequency; the Rabi frequency of the drive field. Slower fluctuations won't impact the dressed state populations because the state vector can follow adiabatically. Fast fluctuations will average out and also have minimal impact, however, fluctuations at the Rabi frequency can have severe consequences because they will scramble the relative phase between the microwave field and the oscillating dipole moment of the molecule. After some time this will result in a 50 : 50 statistical mixture of the dressed states. In other words, the molecule will, on average, not be oriented relative to the microwave field. Phase diffusion-driven loss of coherence is not specific to the upper dressed state; the lower dressed state will have the same sensitivity and will undergo phase diffusion in exactly the same way.

We will model the problem by assuming the phase noise on the microwaves is Gaussian and then calculating how the phase of the dressed state we prepared diffuses in the

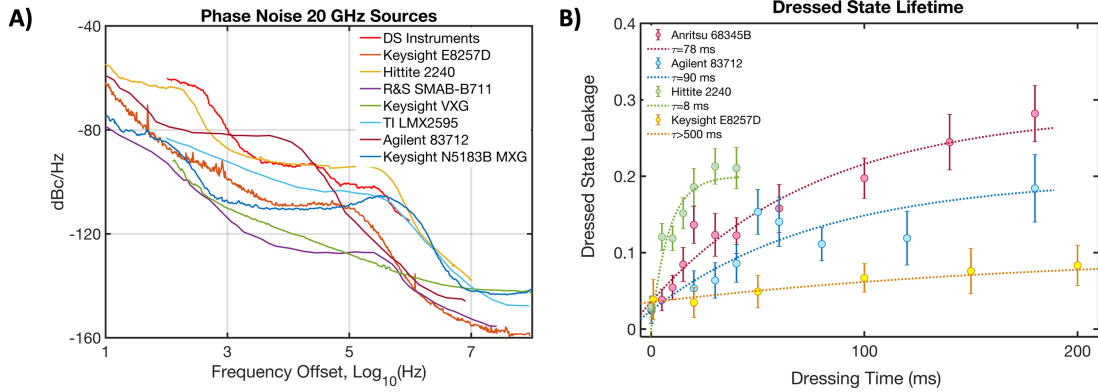


**Figure 4.14:** Side A shows the measured phase noise of every 20 GHz microwave source we had available to us. The all-important measure is the phase noise at the Rabi frequency, 23 MHz from the carrier. The sources show a large variability in phase noise. In Figure B, we measure the lifetime of the dressed state using several different microwave sources to generate the dressing. The lifetime of the dressed state matches the measured phase noise in exactly the way we predicted, with no free parameters in our model.

presence of Gaussian-distributed phase noise with frequency components near the Rabi frequency.

The first thing we need to know is how the dressed states overlap as a function of the phase angle on the equator of the Bloch sphere. Ordinarily, the upper and lower dressed states are orthogonal (ie  $\phi = 0$ ) however in our phase diffusion model,  $\phi = 0$  will diffuse to a non-zero value. Starting in one dressed state (either  $|\pm_x\rangle$  x basis), an accumulated phase  $\phi$  will produce overlap with the other dressed state in the following way

$$|\pm_x, \phi\rangle = \frac{1}{\sqrt{2}}(|\uparrow\rangle \pm e^{i\phi}|\downarrow\rangle) \rightarrow (\langle \mp_x | \pm_x, \phi \rangle)^2 = \sin^2\left(\frac{\phi}{2}\right) \quad (4.9)$$

So far we've treated this problem coherently with  $\phi$  representing a rotation angle of one of the dressed states on the Bloch sphere equator. Next, we'll add a statistical

treatment by averaging  $\phi$  over a distribution of angles characterized by a variance  $(\Delta\phi)^2$  which captures the phase noise originating from the microwave source. The averaging is done by integrating:

$$P_{\text{wrong dressed state}}(t) = \frac{1}{\sqrt{2\pi\Delta\phi^2(t)}} \int_{-\infty}^{\infty} \sin^2\left(\frac{\phi}{2}\right) \exp\left(-\frac{\phi^2}{2\Delta\phi^2(t)}\right) d\phi \quad (4.10)$$

This integral can be done analytically, but first, let's be explicit about  $\Delta\phi^2(t)$ , since our goal is to calculate a decay time constant in the time domain.

This is a diffusive process with frequency sensitivity centered at  $\Omega_R$ . We can write  $\Delta\phi$  in the time domain using the knowledge that we only care about driving at the Rabi frequency, leading us to write down the formula<sup>33</sup>:

$$(\Delta\phi)^2 = \frac{1}{4}(2\pi\Omega_R)^2 S_\phi(\Omega_R)t \quad (4.11)$$

where  $S_\phi(\omega)$  is the single-side band phase noise spectral power density. The variance grows linearly in time and is only sensitive to the amount of power at the Rabi frequency, which we capture statistically using the power spectral density to characterize the noise. A more rigorous treatment can be done by using transfer matrices to describe the dynamics. The transfer matrices produce frequency response profiles which become delta functions centered at the Rabi frequency for interaction times substantially longer than the Rabi period. Details on that treatment can be found in this reference<sup>33</sup>. The power spectral density is the quantity we measure in the lab for various microwave

sources using a spectrum analyzer. Putting it all together, we can compute the integral and substitute our expression for the variance:

$$P_{\text{wrong dressed state}}(t) = \frac{1}{2} \left[ 1 - \exp \left( -\frac{\pi^2}{2} \Omega_R^2 \mathcal{S}_\phi(\Omega_R) t \right) \right] \quad (4.12)$$

It asymptotes to 1/2 with an exponential decay rate  $\gamma = \frac{\pi^2}{2} \Omega_R^2 \mathcal{S}_\phi(\Omega_R)$ , characteristic of a system driven towards a maximum entropy statistical mixture by a gaussian noise source. This decay rate gives us the lifetime of the dressed states based on a phase noise phase-diffusion model.

#### 4.10 PICKING A MICROWAVE SOURCE WITH LOW PHASE NOISE

We characterized all the microwave sources we could find in the lab by measuring both the lifetime of the dressed state and the phase noise on a high-sensitivity spectrum analyzer. The calculation in the previous section matches very well with what we looked at experimentally: the dressed state we prepared leaked into the wrong dressed state as a function of time. Based on the way we prepared the states, the leaking population can be observed directly in the lambda image by disabling the second Landau-Zener sweep. This would leave the molecules ending in the correct dressed state in the N=0 manifold after the dressing time but the other dressed state population would adiabatically connect to the N=1 manifold and become bright to the imaging light. We fit this function with the result of the equation 4.10 and extracted the single-sideband phase

Source	Measured $\tau$ (ms)	Fit $S_{\phi}$ (20 MHz)
Hittite 2240	8 ms	-132 dBc/Hz
Anritsu	78 ms	-142 dBc/Hz
Agilent 83712	90 ms	-142.5 dBc/Hz
Keysight E8257D	600 ms	-151 dBc/Hz

**Figure 4.15:** This chart shows the measured dressed state lifetime when driven by the respective microwave source at 20.5 GHz with a Rabi frequency of 20 MHz for all sources used. The phase noise is calculated from the observed lifetime. The calculated phase noise agrees to within 1-5 dB of the phase noise measured on our spectrum analyzer, indicating the validity of our model and that phase noise is the sole limitation to the dressed state lifetime.

noise from the fit of the lifetime. Figure 4.14 shows the phase noise of the sources and demonstrates exceptionally good agreement with the fit values from the experimentally measured dressed state lifetime. This strongly indicates our phase diffusion model is correct and all of the lifetime issues with the dressed state originate from a single source: microwave phase noise.

The part of the spectrum where we are sensitive to phase noise is roughly 20 MHz from the carrier frequency. While phase noise generally drops further from the carrier, it is sometimes non-monotonic and usually has features depending on the specific microwave source and on the internal phase locking loop. In our system, two microwave sources, one at 2 GHz and one at 18.5 GHz, are mixed to generate the microwaves. The 2 GHz source (Windfreak SynthHD Pro locked to a 100 MHz low phase noise oscillator), owing to its lower frequency, has a phase noise of  $-160$  dBc/Hz at 20 MHz (160 dB suppressed

relative to the carrier height). The limiting phase noise was always coming from the 18.5 GHz arm. Figures 4.14 and 4.15 show the lifetime of the dressed state and the phase noise comparison measured on the spectrum analyzer.

One other aspect worth mentioning is the effect of high-power amplifiers on phase noise. They have a noise figure of 3 dB, which turns out to be irrelevant here because the noise figure does not necessarily add to the noise floor, rather it is a comparison of signal-to-noise degradation of the amplifier compared to an ideal amplifier with thermal noise at 290 K (roughly room temperature). The thermal noise of the amplifier is  $k_B T \Delta\omega$  where  $k_B$  is the Boltzmann constant,  $T$  is the temperature and  $\Delta\omega$  is the bandwidth. At 290 K, the thermal noise per 1 Hz bandwidth is  $-174$  dBm. This implies the amplifiers do not contribute to the phase noise until the source phase noise is below  $-170$  dBc/Hz.

We did not implement any active or passive phase noise compensation techniques. Our best source, the Keysight E8257D, had low enough phase noise for the dressed state to not limit the shielding lifetime we observed in the experiment. If we didn't have this source, there are ways to suppress the phase noise using high-Q cavities. The cavity can be tuned to support the carrier frequency while suppressing phase noise at 20 MHz. Getting a high Q-factor for this type of microwave cavity is fairly easy as we could mount it to the 77 K cryogenic shields inside the beambox. We opted not to go this route because a passive high-Q cavity will not allow frequency tuning which we often did during the experiment. For the future implementation of microwave shielding, a phase noise-suppressing cavity would be a worthwhile addition.

#### 4.11 SHIELDING

Finally, we have everything in place to try shielding. The collision aspect of the experiment was done in exactly the same manner as the ground-state collision described in the previous chapter, up to the additional state preparation challenges<sup>35</sup>. We prepared the dressed states before the tweezers merged, to prevent losses due to unshielded collisions during the several milliseconds-long merging and separating process.

The molecules sit in the merged traps, dressed states intact, for a variable amount of time after which we ramp down the dressing microwaves and separate the tweezer traps. The ramping down of the shielding microwaves adiabatically converts the upper dressed state to the bare ground state of the system, and the second Landau-Zener sweep transfers the surviving molecules back to the  $N=1$  manifold for imaging. The long series of state preparation steps and tweezer merging steps led to an extremely slow data rate. At best, we would have a surviving pair of molecules (for short collision hold times) once in every 50-100 shots.

We compared all of the shielding lifetimes directly to the ground state lifetime to extract the shielding ratio (direct ratio of the pair lifetimes) and the two-body loss rates. This comparison requires the density to be the same for the ground state and the dressed states, despite any possible state dependence on the trap depth. We calculated the AC stark shift for the dressed state to be within 1% of the bare state and we measured the trap frequency for the bare ground state and dressed states to be the same. The

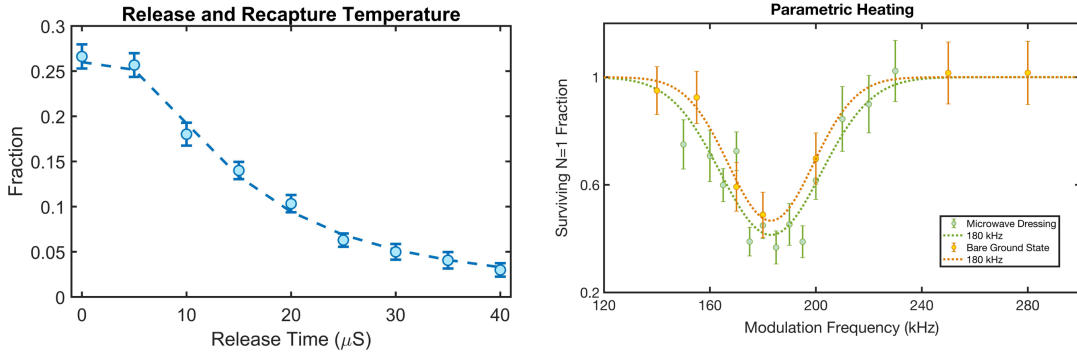


**Figure 4.16:** We measured the temperature and trap frequency for the bare ground state and for the dressed state to ensure the density is the same, implying the shielding factor is directly comparable to the exponential time scales we measured and fit. The radial trap frequency is  $2\pi \times 90$  kHz for both states and the temperature is similar within the fitting error. The temperature was measured using the release and recapture method and fit  $T = 95 \mu\text{K}$ .

temperature of the ground state and dressed state samples were also identical. This is sufficient to conclude that the exponential lifetimes we measure are a direct comparison for 2-body rates because the density of the two samples is identical.

#### 4.11.1 SHIELDING RESULTS

At a density of  $2.4 \times 10^{11} \text{ cm}^{-3}$  (see Figure 4.16 for measurements), the ground state lifetime was 10.8 ms. Our best blue shielding lifetime was 64 ms, a shielding ratio of 6, with a corresponding two-body rate of  $7.2 (2.0) \times 10^{-11} \text{ cm}^3/\text{s}$ , shown in Figure 4.17. This was with 23 MHz Rabi frequency, 2 MHz blue detuning from the resonance, 27 Gauss magnetic field, and polarization ellipticity angle  $\zeta = 0.1$ . An additional comparison we did was to prepare the anti-shielding lower-dressed state. Everything is the same as shielding, except the lower-dressed state couples onto the attractive branch of the

dipole-dipole interaction, leading to rapid losses. We prepared the lower dressed state by reversing the direction of the bias magnetic field and flipping the detuning to be 2 MHz red of the  $m_f = -1$  transition, now the lowest energy projection of the  $F = 1^-$  manifold. We observed a 2.7 ms lifetime, corresponding to  $\beta = 1.7(0.5) \times 10^{-9} \text{cm}^3/\text{s}$ , or a factor of 4 faster than the bare ground state loss rate. By changing the sign of the detuning and the branch of the dipolar-interaction potential, we can tune the collisional loss rate by a factor of 25.

#### 4.11.2 MAGNETIC FIELD DEPENDENCE

We set out to characterize what conditions lend themselves to optimal shielding. We first found the shielding factor was largely insensitive to the magnetic field. Using the MOT coils, connected to a switchable H-bridge to convert the anti-Helmholtz MOT configuration to a Helmholtz configuration, we applied magnetic fields ranging from 10 Gauss to 54 Gauss, with almost no variation in the shielding factor. This indifference is also captured by the coupled channel calculations, shown in Figure 4.18.

#### 4.11.3 POLARIZATION DEPENDENCE

More surprising, at least initially, was the lack of polarization dependence. Our best shielding was taken with  $\zeta = 0.1$ , corresponding to a 100:1 power extinction ratio, however with degraded polarization  $\zeta = 0.4$  (power extinction ratio of 10:1) the shielding factor was similar. The original coupled channel calculations did not include the effects

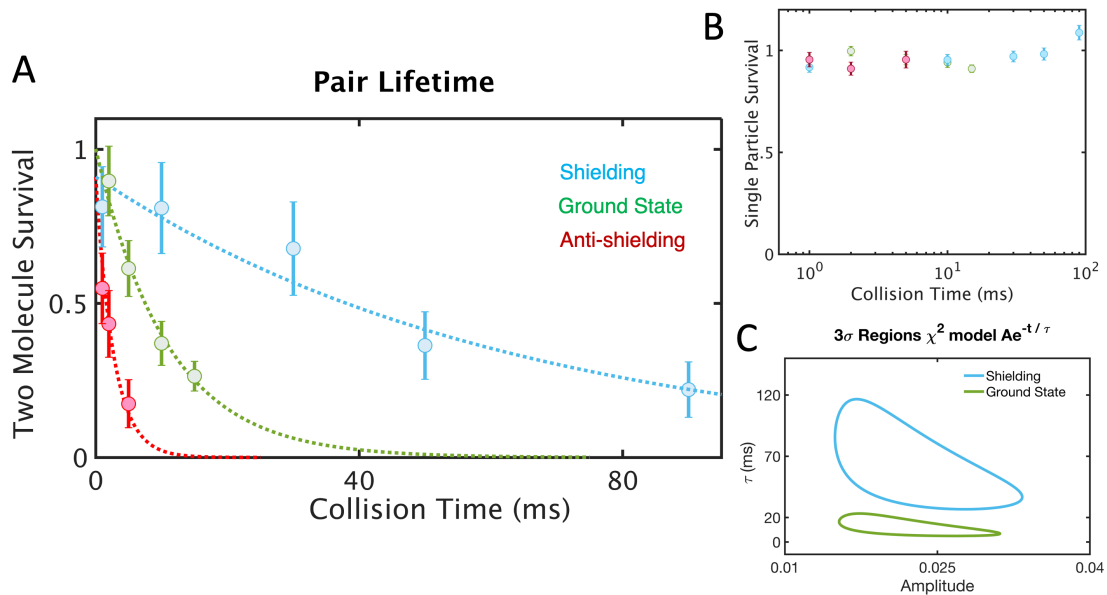


**Figure 4.17:** Figure A shows the survival of the molecule pairs in the merged optical tweezer trap. The lifetime is a single exponential decay because the density remains constant during the collision. The shielded time scale is 64 ms, the ground state time scale is 10.8 ms and the anti-shielding is 2.5 ms. Figure B shows the survival of single molecules during the same merging sequence used for the collision data. These data were taken in between loaded pairs and served as a real-time self-calibration of the experimental stability. Figure C shows a  $3\sigma$  parameter exclusion plot based on a  $\chi^2$  statistical test of an exponential fitting model. The y-axis is the all-important lifetime fitting parameter and the x-axis (amplitude) is the zero-hold time survivability of the pairs. Notice this value is only around 2.5% of pairs surviving. The many steps involved in state preparation, tweezer merging, separating and imaging take a heavy toll on the data rate. While the shielding results are easily discernable in Figure A, these data represent tens of thousands of experimental iterations. During the optimization part of the experiment, the  $\chi^2$  exclusion plots were a useful statistical tool for low signal-to-noise data sets.

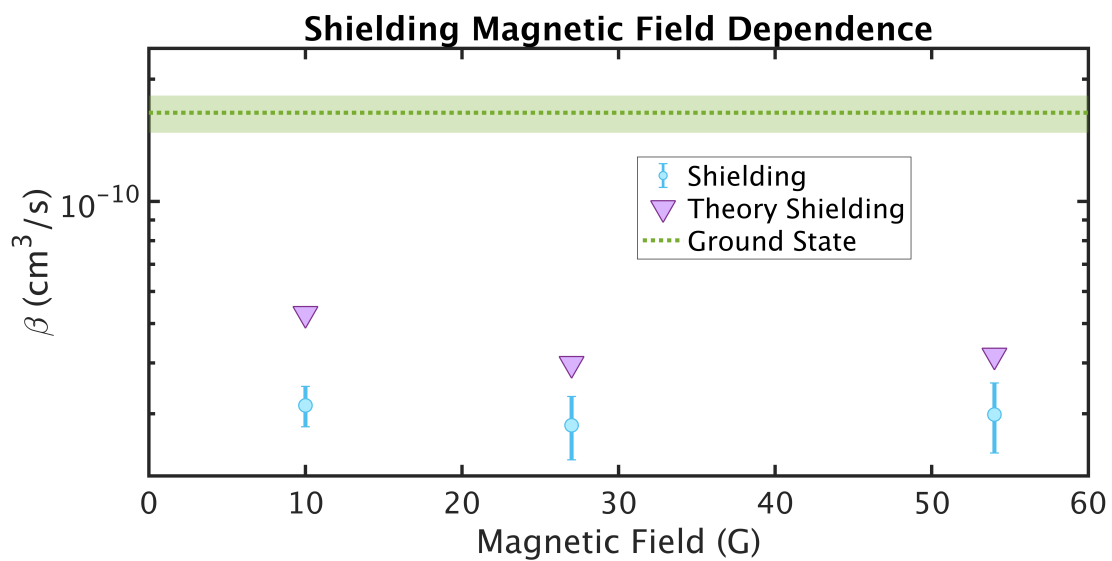


**Figure 4.18:** We measured the two-body loss rate for shielded collisions at several different magnetic fields. The coupled channel collision theory predicts (purple diamonds) low sensitivity to the magnetic field and reflects the dependence measured experimentally. For large magnetic fields, beyond our capability, the coupled channel calculation predicts the shielding eventually fails. The green line and green shaded region indicate the ground state 2-body loss rate and 1-sigma standard statistical error bar on the loss rate, respectively.

of the trapping light, known as the tensor shift, which turns out to have a substantial effect on the polarization sensitivity. We will describe the tensor shift in much more detail in the rotational coherence time chapter but for now, the important thing to know is that the anisotropic nature of the molecules creates an interaction with the linear polarization of the tweezer light. This interaction has a time-reversal symmetry therefore it cannot distinguish  $\pm m_f$  states so the splittings look reminiscent of a DC-Stark shift. The spatial representation of the tensor light shift is described by the following Hamiltonian.

$$H_{Tensor} = -I(x,y,z)\alpha_2 P_2 \cos(\theta) \quad (4.13)$$

$I(x,y,z)$  is the tweezer light intensity and  $\alpha_2$  is the tensor polarizability. For the conditions of the shielding experiment, we measured  $I_{max}\alpha_2 = 17$  MHz. The impact of the anisotropic tensor shift on the shielding is that the tweezer polarization generates some amount of orientation during the collisions, or in other words, it is a strongly competing quantization axis that behaves like another electric field. This interrupts the shielding mechanism because the axis connecting the colliding molecules should be the only quantization axis during the collisions but the lab-frame orientation generated by the Stark shift competes to align the molecules leading to increased loss rates compared to the original coupled channel theory calculations. The electric field-like behavior of the AC-Stark shift reduces the sensitivity to the polarization enough to wash out the

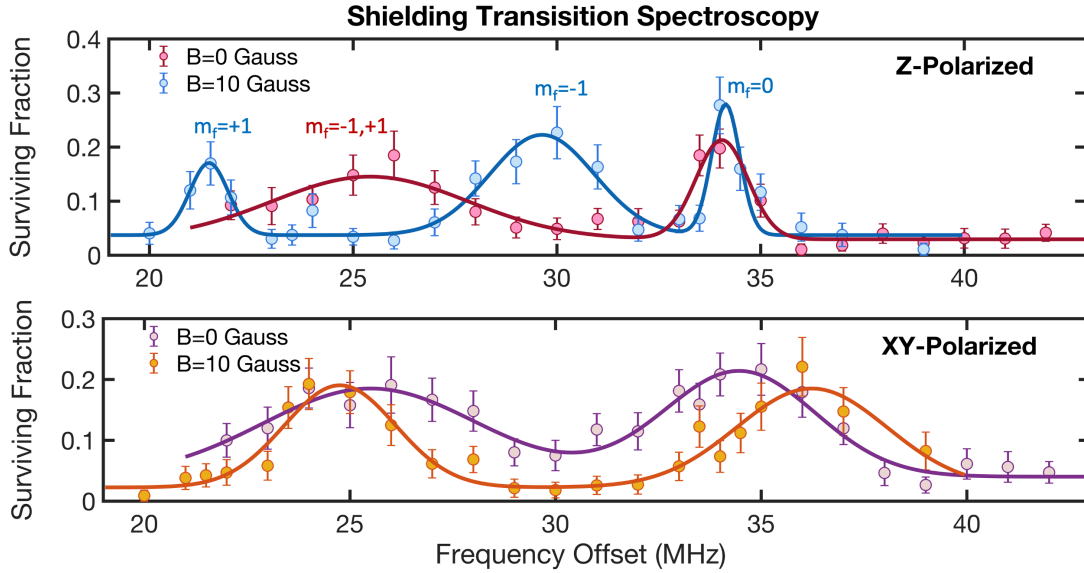


**Figure 4.19:** Microwave spectroscopy of the three  $|N = 1, F = 1^-, m_f\rangle$  to  $|N = 0, F = 0, m_f = 0\rangle$  transitions. The z-polarized configuration has the tweezer polarization and bias magnetic field in parallel orientations. The 780 nm tweezer is 1400  $\mu\text{K}$  deep with a waist of 1.4  $\mu\text{m}$ , corresponding to a tensor light shift strength  $I\alpha_2 = 17$  MHz, fit from the data. At zero magnetic field, the  $m_f = \pm 1$  states are degenerate (centered around 26 MHz). These levels are split when the magnetic field is ramped up to 10 Gauss. The  $m_f$  states are ordered  $+1, -1, 0$  in increasing energy for this particular combination of light intensity and magnetic field. At 27 Gauss where we did the shielding experiment, the ordering becomes  $+1, 0, -1$ ; the normal ordering for Zeeman splittings with a negative g-factor. The widths of the features indicate the ratios of the rabi frequency and microwave polarization, taken at reduced power and therefore un-optimized polarizations. The X-Y polarized configuration orients the tweezer polarization perpendicular to the bias magnetic field. In this case, the Tensor light shift is dominant and the 10 Gauss magnetic field is not sufficient to split the  $m_f = \pm 1$  levels. We used the z-polarized configuration for shielding.

difference between 100 : 1 and 10 : 1 power extinction ratios in our experimental data.

The data is shown in Figure 4.19.

There are several ways to deal with the tensor shift. Lowering the trap depth to reduce the magnitude of the tensor shift is not an option since we require the deepest tweezer possible to generate tight confinement, leading to high-density samples. Without the density, the collisions would happen too slowly to observe within our experimental

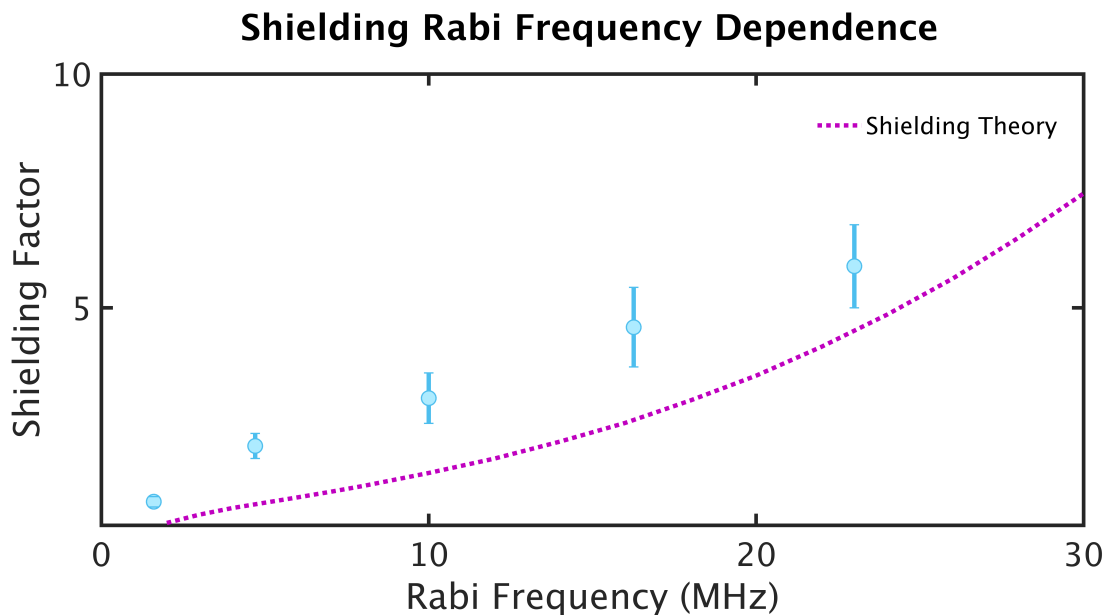


**Figure 4.20:** The shielding factor (ratio of the shielded lifetime to ground state lifetime) was measured for several different rabi frequencies. The Rabi frequency was set by the choice of attenuators used to lower the power while maintaining the microwave phase stability and polarization stability. We found qualitative agreement with the coupled channel theory, which does not predict a saturation in shielding performance up to 30 MHz and possibly well beyond.

window. Another option is to use a different set of states. This could be explored theoretically; we understood the impact of the tensor shifts at a late stage in the experiment, making it highly impractical to switch states. A third option is to use a large optical dipole trap with many molecules. In that case, the density can come from a large number of molecules in a less confining trap, with correspondingly smaller tensor stark shifts. We'll go in this direction in the next chapter.

#### 4.11.4 RABI FREQUENCY DEPENDENCE

The final parameter we scanned was the dressing Rabi frequency. Our simple shielding model indicates that adiabaticity near the Condon point relies on having high Rabi frequencies. A slightly more sophisticated model suggests that low Rabi frequency might be worse than the bare ground state because it will increase the collision cross-section in the same way the high power microwaves will, however, there is insufficient protection at the Condon point and rapid losses occur. Lowering the Rabi frequency turned out to not be straightforward due to phase shifts in the 4-high power amplifiers at different operating powers. The polarization of the microwaves shifted significantly when the power of the sources was lowered. We countered this issue by optimizing the polarization at high power and then installing attenuators with a known phase shift that we measured on the vector network analyzer. The attenuator stack went on each individual arm of the antenna array, after the high-power amplifiers. This way of reducing the power maintained the phase stability of the array after the microwave splitter and the polarization in the chamber. In our experiment, due to the way we prepare the dressed state with a roughly 2 MHz finite detuning, it wasn't prudent to reduce the Rabi frequency much below 2 MHz, however, we saw a clear dependence on the Rabi frequency, resembling the predictions of the coupled channel theory model in Figure 4.20.

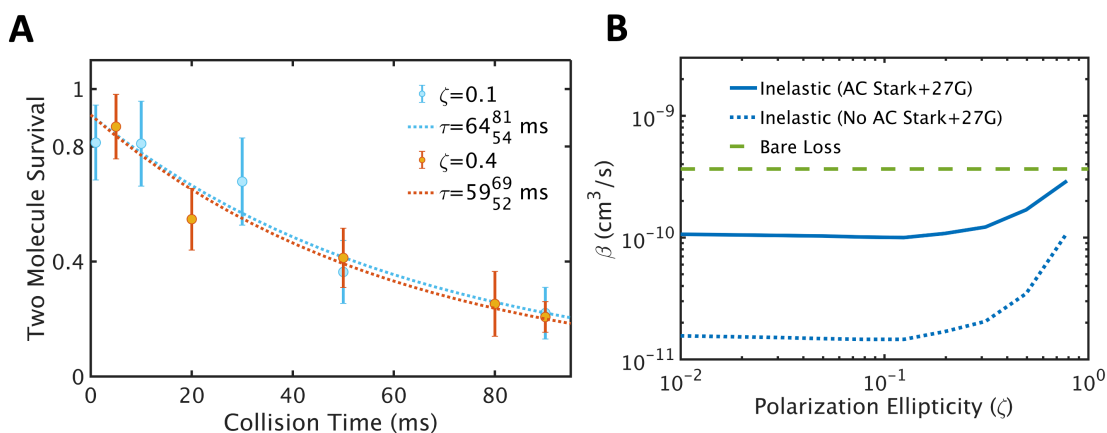


**Figure 4.21:** The final parameter we explored was polarization dependence. The initial coupled channel calculations, which did not include trap light shifts predicted a strong dependence on the polarization. On the left, the blue trace was taken with 16 MHz Rabi frequency and a polarization ellipticity  $\zeta = 0.1$ . The orange curve was also taken at 16 MHz driving the shielding transition but with an ellipticity of  $\zeta = 0.4$ . The fit decay times have significantly overlapped error bars, indicating no detectable polarization dependence. In practice, this is hard to measure because we must hold the Rabi frequency constant on the shielding transition but a less elliptical microwave field with the same Rabi frequency in one polarization implies the other two transitions become more strongly driven. This is captured in the couple channel calculation but it makes a direct comparison difficult. On the right, the solid blue and dotted blue curves are the predicted loss rates at 27 Gauss including and excluding the effect of the tensor light shift, respectively. The green is the measured ground state loss rate.

#### 4.12 SHIELDING OUTLOOK

We demonstrated a highly controllable ability to engineer the collisional process at play between two trapped ultracold molecules. Our motivation was to demonstrate a way to suppress the lossy collisions we saw in the previous study. Long collisional lifetimes are a necessity for the evaporative cooling scheme we will attempt in the next chapter. The success of evaporative cooling relies on the reduction of inelastic losses by means of shielding and, a yet unmeasured quantity, the rate of elastic collisions which are needed to thermalize the sample. Collisional shielding-enabled evaporative cooling has the potential to be an instrumental new tool for reaching temperatures unachievable by laser cooling alone.

# 5

## Evaporative Cooling of Shielded Molecules

Evaporative cooling can be a powerful tool for cooling bulk gas samples far below the photon recoil limit of laser cooling if the collisional properties are favorable. Evaporative cooling works by selectively removing the hottest molecules from the sample while elastic

collisions rethermalize the remaining molecules resulting in the cooling of the gas. The key property required for evaporative cooling is a high ratio of elastic collisions to inelastic collisions. Elastic collisions are needed to thermalize the population while inelastic collisions do not contribute to the cooling process, and almost always heat the sample. Some atomic species have ratios of elastic to inelastic collision rates exceeding several thousand. This is generally not the case for molecules<sup>158,53,62,35</sup>. However, some molecules have been evaporatively cooled. These experiments took advantage of spin polarization and Fermi statistics to reduce the loss rate enough to observe evaporative cooling of ultracold alkali molecules<sup>145,135</sup>. Another experiment observed evaporative cooling of OH radicals<sup>138</sup> but no one up to this point has observed evaporative cooling of laser-cooled molecules. Since we published the microwave shielding result a group at MPQ in Germany, inspired by our success, demonstrated microwave shielding and evaporative cooling of ultracold NaK alkali Fermions<sup>125</sup>.

Our microwave shielding scheme suppresses the inelastic collision channels while activating strong dipolar interactions that lead to a large elastic rate<sup>51,50,74,75,73</sup>. Without microwave shielding, the ratio of elastic to inelastic is order unity for molecules such as CaF. For every collision, the chance of an inelastic process is very high, prohibitive for evaporative cooling. Gaining control over this ratio was the primary motivation for the microwave shielding project. Also, previously we only made a direct measurement of the loss rates, not the elastic rate. We will measure the elastic collision rate in the bulk gas setting and demonstrate forced evaporative cooling.

## 5.1 PARAMETER SPACE FOR EVAPORATIVE COOLING

The demonstration of microwave shielding on its own isn't enough to guarantee evaporative cooling will work. Our experiment has two severe limitations which set a narrow window for us to observe evaporation. The vacuum lifetime of a single molecule in the tweezer is only about 1 second due to helium released from the buffer gas cell and the total number of molecules we can load into the 1064 nm ODT is around 2000. The combination of short vacuum lifetime and low number puts us at odds with evaporation initialization and optimization: If the number of molecules is low, one has the choice to evaporate efficiently but at the cost of time<sup>113</sup>. Slower evaporation is more efficient because it allows us to remove fewer but higher energy molecules resulting in more energy removed per molecule lost. Due to the limited vacuum lifetime, we are forced to evaporate quickly at the cost of molecule numbers<sup>113</sup>.

## 5.2 ESTIMATING THE ELASTIC RATE

In the absence of external fields, the elastic rate is set by the strength of the Van der Waals interaction which scales as  $-C_6/R^6$ . Focusing only on the ground state, which is spherically symmetric, we can calculate the scattering phase using the semi-classical WKB approximation and then back out a cross-section. The spherical symmetry makes the calculation simpler because it will not mix particle waves, therefore we can focus on the s-wave scattering properties for our estimate. Following reference<sup>54</sup>, we first

calculate the scattering length:

$$a_s = \bar{a} \left( 1 - \tan\left(\phi - \frac{\pi}{8}\right) \right) \quad (5.1)$$

where

$$\bar{a} = \frac{\pi}{8} \left( \frac{2\pi m C_6}{h} \right)^{1/4} = \frac{\Gamma(1/4)^2}{16} L_{VdW} \quad (5.2)$$

$L_{VdW}$  is the familiar Van Der Waals length and  $\phi$  is the WKB phase accumulated over the potential traverse from infinity up to the classical turning point.

$$\phi = \frac{2\pi}{h} \int_R^\infty \sqrt{mC_6/r^6} dr \quad (5.3)$$

That calculation gives us an estimate of the s-wave scattering length from which we get the cross-section  $\sigma = 4\pi a_s = 1.8 \times 10^{-11} \text{ cm}^2$  and then the two-body loss rate by multiplying by the average thermal velocity of the molecules. The estimate gives a 2-body rate of  $\gamma_{ground\ state} = 2 \times 10^{-10} \text{ cm}^3/\text{s}$  which indicates the ratio of elastic to inelastic loss rates is roughly 1 at 100  $\mu\text{K}$ .

When we add microwave shielding, the interaction potential is very different due to the polarization of the dipole moments from the microwave driving. Tijs Karman calculated the elastic rate with all of our shielding parameters included, predicting an elastic rate of  $\gamma_{shielded} = 6 \times 10^{-9} \text{ cm}^3/\text{s}$ . The measured shielding loss rate of  $\beta_{shielding} =$

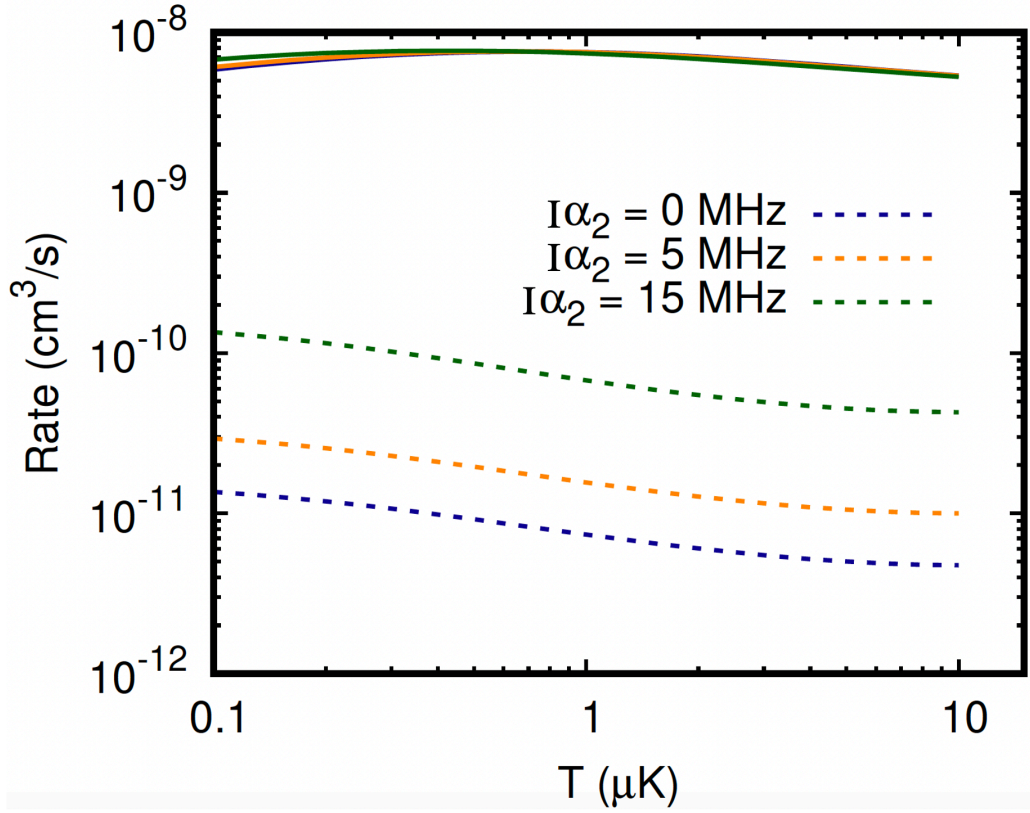


**Figure 5.1:** Coupled channel two-body loss rate calculations for microwave shielding in a variety of traps. The three dotted traces labeled  $\alpha = I\alpha_2$  refer to the strength of the tensor light shift in the trap, where  $\alpha_2$  is the constant tensor polarizability and  $I$  is the trap light intensity. The shielding two-body loss rates have a slight temperature dependence. The solid curves are the corresponding elastic two-body rates. The elastic rate is sensitive to neither the temperature (for  $T > T_{dipolar} = 70$  nK) nor the tensor shifts in the trap. Below  $T_{dipolar}$ , the Wigner threshold scaling law for S-wave colliding Bosons indicates the two-body rate drops as  $\sqrt{T}$ . The inelastic two-body loss rate becomes a constant in the Wigner regime<sup>58</sup>. Understanding the behavior of the collision rates as the gas cools is important for evaporative cooling.

$7.2 \times 10^{-11} \text{ cm}^3/\text{s}$  indicates a ratio of elastic to inelastic of nearly 100, at a temperature of  $100 \mu\text{K}$ .

The ratio of elastic to inelastic rates is temperature dependent. There is a general formalism that produces the Wigner threshold scaling laws, which work in the regime where the temperature is below the characteristic temperature of the interaction potential<sup>58</sup>. In the case of microwave shielding, the dipolar interaction is responsible for the elastic rate and also for setting the temperature scale, which is  $T_{dipolar} = 70 \text{ nK}$ . Our experiment is well outside the Wigner scaling regime and therefore we will rely on thermally averaged coupled channel calculations in figure 7.25, however, the Wigner threshold scaling is still useful in the case of deep evaporative cooling.

In the Wigner regime, the inelastic two-body rate approaches a constant as  $T \rightarrow 0$  and the elastic cross section approaches a constant as  $T \rightarrow 0$ . The two-body rate is related to the cross-section  $\beta = v\sigma$  where  $v$  is the average differential velocity. The velocity goes to zero as  $T \rightarrow 0$  which implies in the Wigner regime the ratio of elastic to inelastic ( $\Gamma$ ) scales<sup>58</sup> as  $v\sigma_{elastic}/\beta_{inelastic} \propto \sqrt{T}$ . As the temperature lowers deeper into the Wigner scaling regime, the collision rates become less favorable for cooling.

### 5.3 TRAP TRANSFER AND OPTIMIZING DENSITY

We initially hoped to do the evaporative cooling experiment in the 1064 nm ODT, skipping the transfer step to the 780 nm trap, however, the maximum density in the

1064 nm trap is around  $1 \times 10^8 \text{ cm}^{-3}$ . At this density, we observed light-assisted collisions but the time scale for ground state collisions was over 1 second at full trap depth making evaporation far too slow.

Shrinking the 1064 ODT is possible, however, shrinking the 1064 nm ODT reduces the spatial overlap with the molasses cloud from which the trap loads. A smaller ODT would load considerably fewer molecules. The next option is to leave the 1064 nm ODT alone but expand the 780 nm tweezer out of the collisional blockade regime to a volume large enough to hold hundreds of molecules at a high density. We are once again forced to use the 1064 nm ODT as a molecule reservoir and perform a transfer step.

This requires an efficient transfer between traps, an aspect that gets overshadowed by the parity projection process during tweezer loading. The 780 nm trap can be loaded directly from the molasses, however, we find twice as many molecules can be loaded simply by overlapping the 1064 nm and 780 nm traps and then subsequently switching off the 1064 nm ODT. We can do even better by adiabatically ramping off the 1064 nm light in a smooth 20 ms ramp down with the lambda cooling light on. This transfers roughly 30% of molecules to the 780 nm trap.

Due to the density in the 780 nm trap, the light-assisted collision two-body lifetime was on the several millisecond time scale, as seen in 5.2. This is just long enough for a short lambda cooling pulse to cool the transferred molecules in the 780 nm ODT, however, it is far too short for high-fidelity imaging. We opted to not image the molecules in that trap, rather we would image the molecules in the 1064 nm ODT prior to the

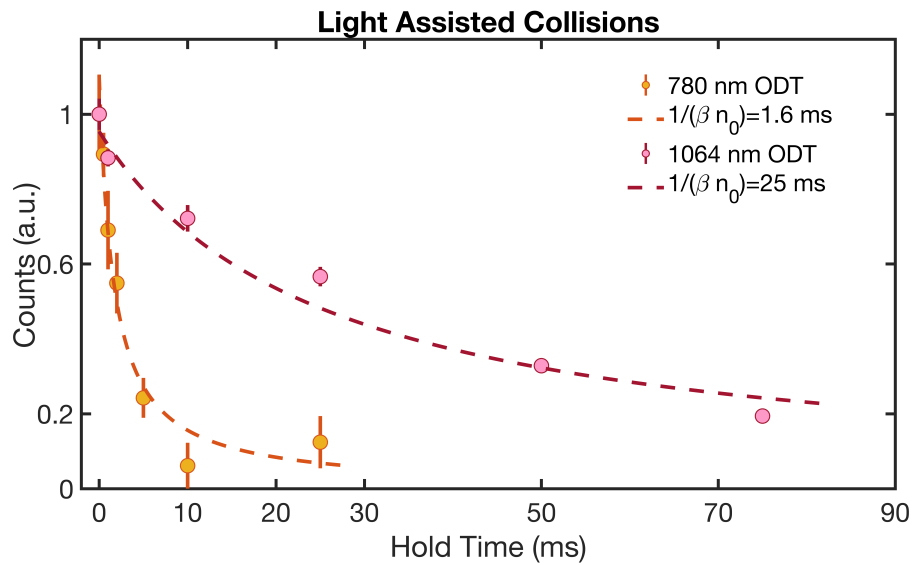


**Figure 5.2:** Light-assisted collision rate for the same set of lambda imaging parameters in both the 1064 nm ODT and the now-expanded 780 nm ODT. The imaging parameters are similar in both cases with the single-photon detuning set to 30 MHz and the two-photon detuning set to 200 kHz. The light intensity is approximately 1 W/cm<sup>2</sup> with a total power of 10 mW per beam. The factor of 15 in two-body lifetime indicates a significant difference in density between the two traps. It is for this reason we opt to load the 1064 nm ODT and then transfer the population into the more tightly confined 780 nm ODT where collisions happen on a faster, more experimentally favorable, timescale.

transfer, then after the experiment transfer back to the 1064 nm ODT to image the remaining molecules.

### 5.3.1 SETTING THE 780 NM ODT SIZE

We need to set the trap size to have a reasonable density where the collisional lifetime is long enough for the cooling to work, yet the elastic rate is high enough to do forced evaporation faster than the 1-second vacuum lifetime. Fortunately, we can easily control the size of the 780 nm trap by resizing the input beam to the objective. Filling any less than the full input aperture of the objective results in a larger beam spot size in the focal plane. We adjust the input beam with a zoom collimator on the delivery fiber. This method of adjusting the beam spot size at constant laser power results in a dramatically steep scaling law for the density dependence, assuming the temperature remains reasonably constant.

Let's estimate the beam waist dependence on the density of molecules in a (harmonically approximated) optical trap. The density is:

$$n = N \left( \frac{m(\omega_x \omega_y \omega_z)^{2/3}}{2\pi k_B T} \right)^{3/2} \quad (5.4)$$

where the trap frequencies can be written in the following way:

$$\omega_x = \omega_y = \sqrt{\frac{4U}{m\sigma^2}} \text{ and } \omega_z = \sqrt{\frac{2U}{mz_r^2}} \quad (5.5)$$

and now substituting  $z_r = \pi\sigma^2/\lambda$  and  $U = \alpha I_{\text{gaussian}} = \alpha(2P/\pi\sigma^2)$  where  $\alpha$  is the polarizability of the molecule at 780 nm,  $I$  is the peak intensity of a gaussian beam and  $P$  is the total laser power, we finally, we arrive at:

$$n = N \frac{8}{\pi^4 \sqrt{2}} \sqrt{m} \lambda \frac{1}{\sigma^7} \left( \frac{\alpha P}{k_b T} \right)^{3/2} \quad (5.6)$$

which scales extremely fast with respect to the beam waist  $\sigma$ . The density optimization also relies on the number of loaded molecules, in contrast to the tweezer experiment.

There are two ways we can characterize the density in the expanded 780 nm ODT. We can measure the temperature, trap frequencies, and molecule numbers to calculate the density. The other avenue is to measure the two-body loss rate for ground-state molecules and then compute the density from our previously measured two-body loss rates.

### 5.3.2 DENSITY CHARACTERIZATION: METHOD 1

Knowing the number of molecules and the density per molecule as separate numbers is important because evaporative cooling relies on having high enough density for rapid elastic collisions and having sufficient molecule numbers to lose a large fraction during the cooling process. Simply knowing the density doesn't distinguish between having a high number of molecules with reasonable density per molecule due to the trap confinement vs having very few molecules in a tightly confined trap. Given the  $1/\sigma^7$  scaling of

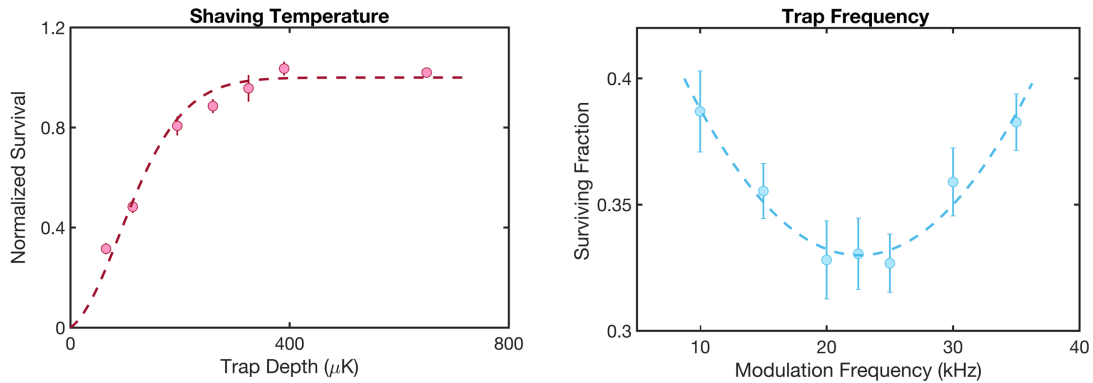


**Figure 5.3:** We characterize the per-particle density in the 780 nm optical trap, similar to the optical tweezer with a temperature and trap frequency measurement. This trap has a beam waist of  $8.5 \mu\text{m}$  and a depth of  $650 \mu\text{K}$ . The temperature is measured by rapidly cutting the trap depth, holding for 30 ms, and then imaging the surviving molecules. The model fits a temperature of  $60 \mu\text{K}$ . On the right is a parametric heating measurement of the trap frequency. The trap frequency is  $\omega_r = 2\pi \times 11\text{kHz}$ . The per-particle density in this trap is  $3 \times 10^8 \text{cm}^{-3}$ ,

the density, this is a sensitive optimization.

We characterize the number of molecules in the trap by measuring the fluorescence and calibrating the scattering rate. To measure the scattering rate, we switch off the pumpers and measure the exponential decay of the fluorescence when the molecules are illuminated by the  $V = 0$  light only. From the Frank-Condon factors for CaF (97% probability to return to  $V=0$  on the A-X decay), The  $1/e$  decay time of the fluorescence corresponds to scattering about 30 photons, implying the scattering rate is 30 times the exponential decay rate 5.4. Factoring in transmission losses and the collection efficiency of our objective, we collect about 1% of the total light. From the scattering rate, camera calibration, and brightness of the ODT image, we estimated a total of 2000 molecules in the 1064 nm ODT and 200 molecules transferred into the 780 nm ODT. This is a

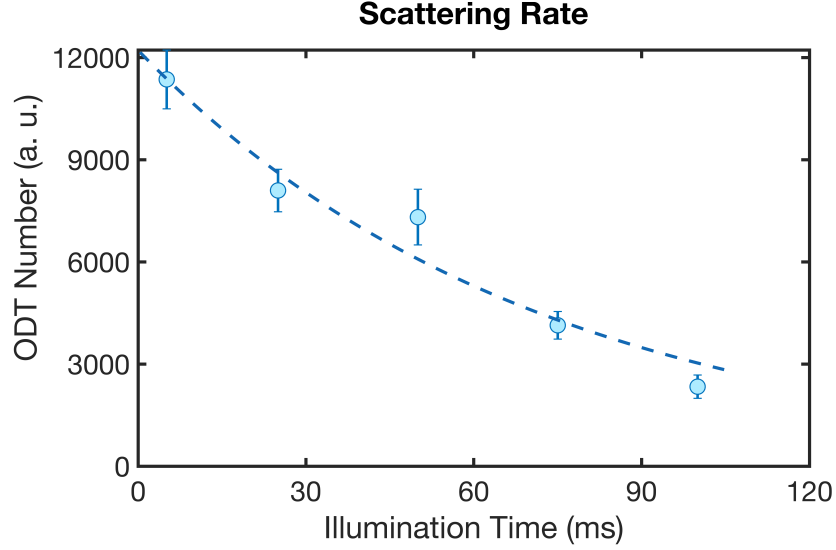


**Figure 5.4:** In order to calibrate the number of molecules in the ODT, we measure the decay time scale of the fluorescence during a lambda image by switching off the repump light. Based on the Frank-Condon factor for CaF (99% X-A) and the 70 ms measured decay, we estimate a 20 kHz scattering rate.

small number for an evaporative cooling experiment, but evaporative cooling has been demonstrated on similar-sized samples<sup>23</sup>.

To calculate the molecular density, we use the same approach as the tweezer experiment, which requires measuring the temperature and trap frequency. We measured the temperature to be  $50 \mu\text{K}$  and the radial trap frequency was  $\omega_r = 2\pi \times 11 \text{ kHz}$ . With 1.4 Watts of laser power going into the trap and a beam waist of  $8.5 \mu\text{m}$ , the trap depth is  $650 \mu\text{K}$ . We did not measure the trap frequency along the Rayleigh range directly, however, in the Gaussian-harmonic approximation,  $\omega_z = \frac{\lambda}{\pi\sigma_0} \omega_r$  which in our case is  $\omega_z = 2\pi \times 300 \text{ Hz}$ . From the trap frequencies and the temperature, the per particle density is  $3 \times 10^8 \text{ cm}^{-3}$  and from the scattering rate calibration, we have 200 molecules

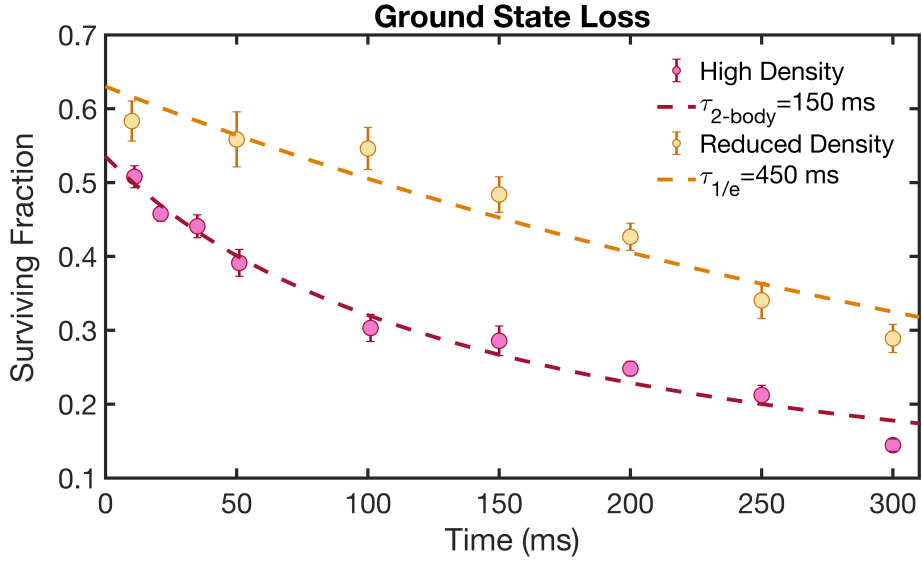


**Figure 5.5:** The two-body inelastic lifetime depends on the number density of molecules in the 780 nm ODT. We test that collisions are happening as expected by reducing the density and observing a subsequent reduction in the inelastic loss rate. The ground state loss rate shows clear density dependence indicating the loss is collisional in nature.

in the 780 nm ODT, yielding a density of  $5.5 \times 10^{10} \text{ cm}^{-3}$ . Data can be seen in figure 5.3.

### 5.3.3 DENSITY CHARACTERIZATION: METHOD 2

Next, we measured the ground state collision rate in the 780 nm ODT. In contrast to the tweezer collision experiments, the density does change throughout the collision time as molecules are lost from the trap. The density of the bulk gas is described by the following differential equation

$$\frac{d}{dt}n(t) = -\gamma n(t) - \beta n^2(t) \quad (5.7)$$

with the solution:

$$n(t) = \frac{n_0}{e^{\gamma t}(R+1) - R}; \quad \text{where } R = \frac{\beta n_0}{\gamma} \quad (5.8)$$

The single molecule vacuum lifetime ( $\gamma$ ) is 900 ms, measured at low density to avoid confusion with CaF-CaF collisional losses. That leaves  $\frac{1}{\beta n_0}$  as the fit parameter, characterizing the inelastic loss decay time scale. At full trap depth, we measured the survival vs time of the molecules and fit the two-body lifetime to 150 ms. Using the two-body loss rate of  $\beta_{ground\ state} = 1.4 \times 10^{-10} \text{ cm}^3/\text{s}$ , we get a total density of  $5 \times 10^{10} \text{ cm}^{-3}$ . Dividing the total density by the per-particle density we calculated earlier ( $3 \times 10^8 \text{ cm}^{-3}$ ), implies we have about 170 molecules in the 780 nm ODT for evaporation. This estimate is very close to the carefully calibrated density and loss rate using the previous method. Measuring and fitting the two-body lifetime is quick and easy compared to measuring three parameters in the other method. We will rely on the measurements of the two-body loss rate to extract the density from now on.

#### 5.4 BULK GAS SHIELDING

The next step is to bring back the shielding and implement it in a bulk gas setting. There are two significant differences now: the tensor shifts are smaller due to the reduced intensity of the large trap 780 nm and the second difference is that three-body processes could occur now that we have many molecules vs exactly two molecules in the tweezer.

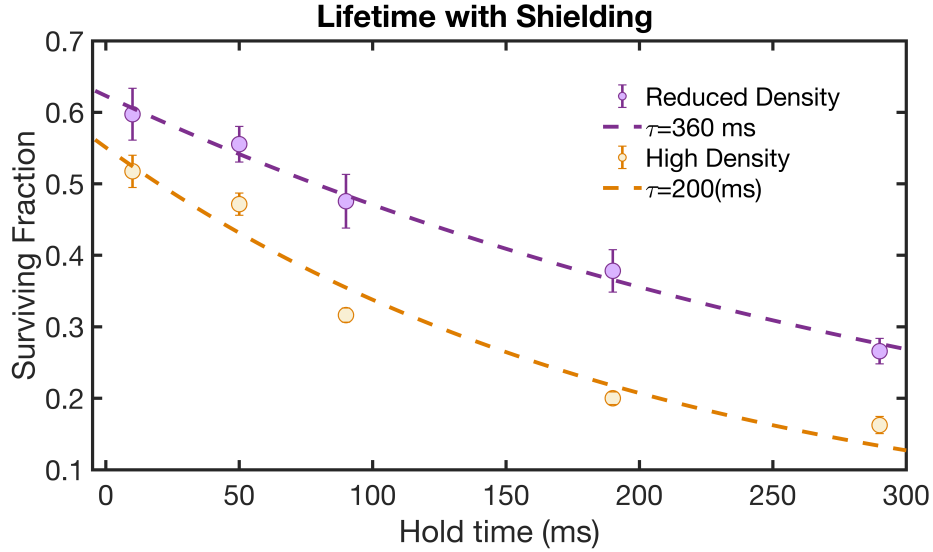


**Figure 5.6:** The two-body lifetime depends on the number density of molecules in the 780 nm ODT. We test that collisions are happening with shielding as expected by reducing the density and observing a subsequent reduction in the inelastic loss rate. The shielding scheme shows clear density dependence indicating the loss is collisional.

We don't have an estimate of the three-body recombination rate.

#### 5.4.1 SHIELDING STATE PREPARATION

The single molecule shielding state preparation process is the same as for the optical tweezer, however, in the larger trap the intensity is substantially lower and so are the effects of the tensor shifts. Even with 1 W of laser power generating the 780 nm ODT, the intensity is 14 times lower than the optical tweezer and in this case, the tensor shift strength ( $I\alpha_2$ ) is 1.2 MHz, barely discernable against the several MHz scale Zeeman splittings.

We measured the tensor shifts in the larger trap below and set the detuning for the

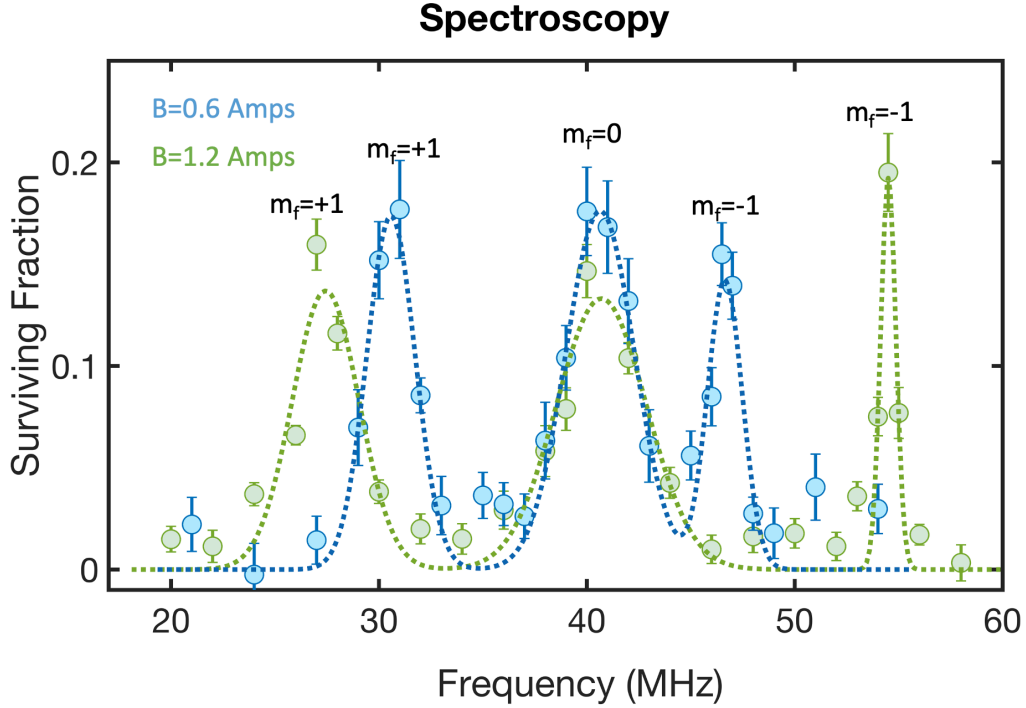


**Figure 5.7:** Microwave spectroscopy of the  $|N=0, F=0, m_f=0\rangle$  to  $|N=1, F=1^{-1}, m_f\rangle$  transition in the 780 nm ODT, split by a bias magnetic field along with the magnetic field and trap light polarization oriented parallel to each other. The trap light intensity is 14 times lower than the tweezer and the tensor stark shift is barely visible. We double the magnetic field and measure again to identify the  $|N=1, F=1^{-}, m_f=0\rangle$  transition. Recall in the optical tweezer, the tensor stark shift in the  $N=1$  manifold is large enough to flip the order of the  $m_f=0$  and  $m_f=-1$  states. By measuring the transitions at two different magnetic fields we can be certain the state are ordered in the “normal Zeeman ordering” for a system with a negative g-factor ( $m_f = +1, m_f = 0, m_f = -1$  from lowest to highest energy). This ensures we set the detuning correctly to dress the right states without level crossings playing a role in the dressed state preparation.

dressed state preparation to 2 MHz above the  $|N = 0, F = 0, m_f = 0\rangle$  to  $|N = 1, F = 1^-, m_f = -1\rangle$ , similar to before. The dressed state lifetime is more problematic for an evaporative cooling experiment than for our previous tweezer-based experiment. In the optical tweezer, the shielded inelastic lifetime was 60 ms however for evaporation, we need the shielding to last for several hundred milliseconds. While we achieved roughly 500 ms dressed state lifetimes in the optical tweezer, this is marginal for an evaporation experiment requiring around 200 ms to ramp the trap down, spilling the hot molecules. Without the use of a high finesse cavity, we were unable to improve the dressed state lifetimes and decided to move forward aware that we are working under a tighter time limitation than the single particle vacuum lifetime of 900 ms.

In contrast to the shielding experiment in the optical tweezer, we never observed a shielding factor greater than 2 (ratio of a shielded lifetime to bare ground state lifetime) in the bulk gas environment. This is likely due to the phase-noise-driven decay of the dressed state. To match a shielding factor of 6, the best we observed in the optical tweezer, would require a 2-second two-body lifetime which in turn requires a dressed state lifetime substantially longer than 2 seconds. The tweezer-based shielding experiment had a dressed state lifetime ten times longer than the 2-body lifetime. To match that, our microwave source would require a single sideband phase noise of less than  $-167$  dBc/Hz. Achieving that level of phase noise suppression would likely require a high finesse cavity which restricts our frequency tunability.

An important check on any collisional process, especially when we have multiple loss

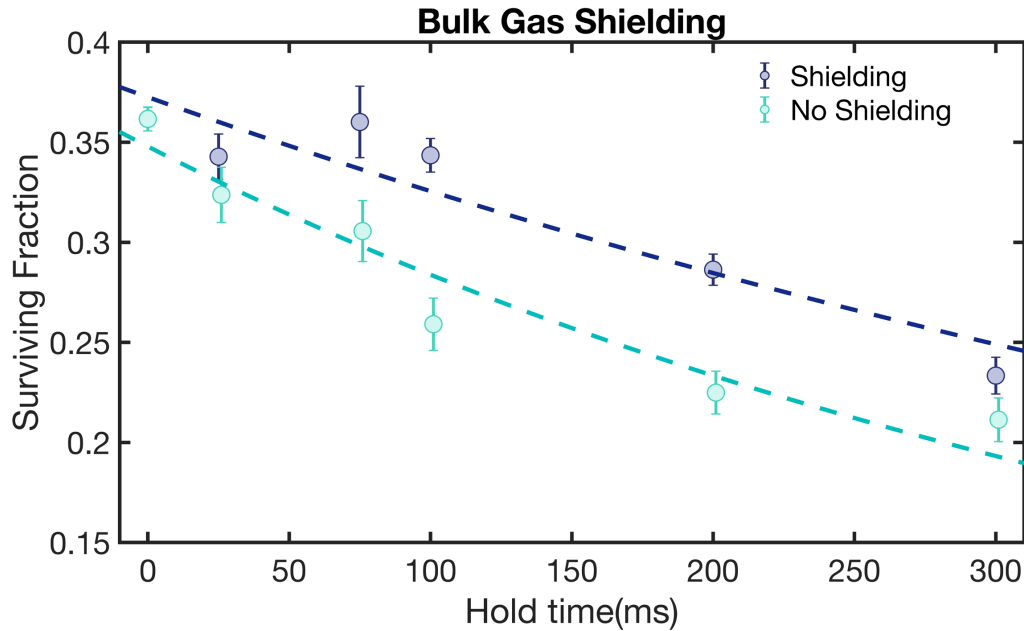


**Figure 5.8:** The shielding performance in the 780 nm ODT never matched the optical tweezer experiment lifetime. We saw shielding factors of roughly 2 in the bulk gas environment. One limitation was the dressed state lifetime, which was limited to around 500 ms. In the tweezer experiment, we never had a collision lifetime longer than 1/10 of the dressed state lifetime. In the bulk gas experiment, the dressed state lifetime is comparable if not shorter than the inelastic loss rate.

rates occurring on a similar time scale, is to check if the density dependence is correct. We do this by reducing the 1064 nm ODT loading and then leaving everything else constant. In practice, we can vary the density of the 780 nm ODT by roughly a factor of 3, maintaining collision rates high enough to observe. For measurements that don't benefit from collisions such as trap frequency measurements, we reduce the density by an order of magnitude to quench collisions and avoid confusion from collisional loss processes. See figures 5.5 and 5.6.

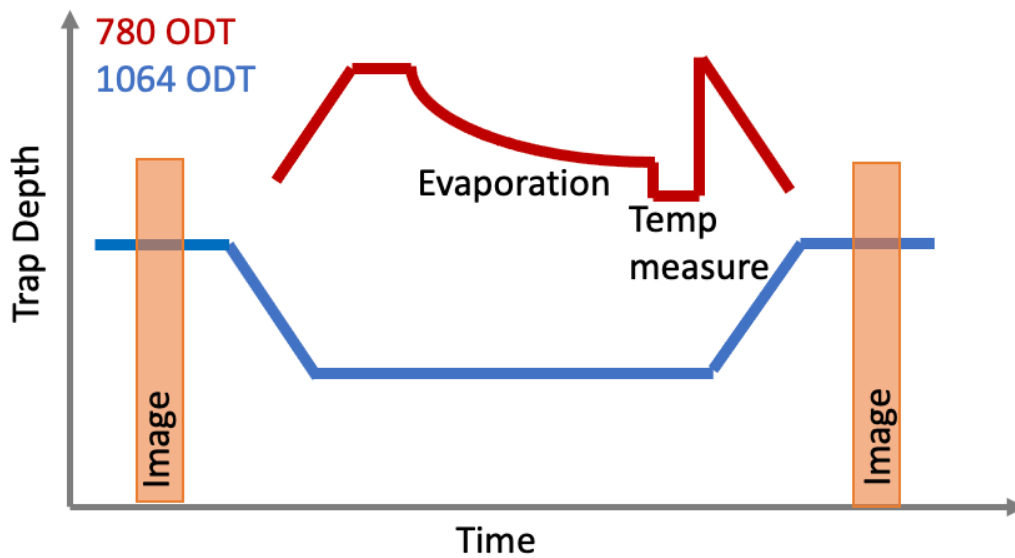


**Figure 5.9:** Trap ramp sequence for evaporative cooling. Molecules are transferred from the 1064 nm ODT to the 780 nm ODT, then the 1064 nm ODT is shut off. The 780 nm trap is ramped down exponentially during the forced evaporative cooling step. The temperature is measured after evaporative cooling by rapidly quenching to a shallower trap to “shave” the population. Surviving molecules are transferred back to the 1064 nm ODT for imaging.

## 5.5 EVAPORATIVE COOLING

With working shielding in place, we are ready to do forced evaporation. With a density of  $2.5 \times 10^{10} \text{ cm}^{-3}$  and a predicted elastic collision rate coefficient of  $\beta_{elastic} = 6 \times 10^{-9} \text{ cm}^3/\text{s}$ , we expect a 150 Hz elastic scattering rate at full trap depth. Following previous evaporative cooling experiments, we perform an exponential ramp down of the trap depth from  $650 \text{ } \mu\text{K}$  to  $65 \text{ } \mu\text{K}$ . Initially  $\eta = 11$  and in the case of adiabatic cooling only, we end with  $\eta = 3$ . The trap ramp sequence is shown in Figure 5.9. Our most successful demonstration of evaporative cooling involved an exponential ramp from  $650 \text{ } \mu\text{K}$  to  $65 \text{ } \mu\text{K}$  in 200 ms with  $\tau = 50 \text{ ms}$ . While it is difficult to directly measure the small amount of evaporative cooling on top of the adiabatic cooling from the trap ramp, we can compare the same trap ramp with and without shielding. In the absence of shielding, the elastic collision rate is estimated to be slow, 5 Hz. Roughly 3 collisions are needed to thermalize a mass-matched system, requiring 600 ms of thermalization time which we do not have in this experiment, therefore and we do not expect substantial evaporative cooling to take place. The unshielded evaporation provides a baseline comparison against which we can measure the effectiveness of evaporative cooling with shielding.

We measured the temperature of the cooled samples at the end of the evaporative cooling cycle without ramping the trap depth back to full depth. The temperature was measured by rapidly reducing the trap depth and waiting for molecules to spill out. At the low traps used for this measurement, there won't be any evaporative pro-

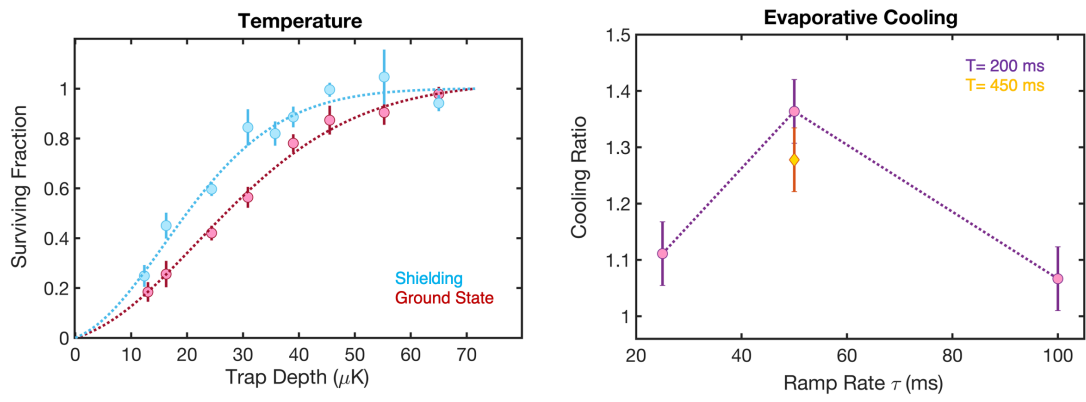


**Figure 5.10:** On the left is a temperature measurement produced by rapidly lowering the trap depth, holding for 30ms, and then measuring the surviving population after the evaporative cooling stage. The blue curve is the temperature of the shielded molecules after a 200ms evaporative cooling cycle and the red curve corresponds to ground state molecules after the same evaporation sequence. The rapid elastic collisions enabled by microwave dressing drive more evaporative cooling than the relatively low ground state collision rate for unshielded molecules. These temperatures were taken after a 200 ms forced evaporation period with an exponential ramp rate of 50 ms. On the right, we measured the temperature ratio of the shielded molecules to the unshielded molecules after cooling for 200 ms and 450 ms with different exponential ramp rates. Temperature ratios above 1 indicate the shielded sample is cooled more than the bare ground state sample.

cesses happening on the dynamical time scales of the trap. We modeled this process using the Gaussian-harmonic approximation to calculate the cut fraction following this reference<sup>144</sup>

For a gas with  $\eta = 3$ , the Gaussian-harmonic approximation is still valid but for initial values of  $\eta$  and lower, this approximation will become unreliable because a substantial fraction of molecules will be high enough in the trap to sample non-harmonic parts of the gaussian potential<sup>144</sup>. As a statistical test of the model, we fit our highest signal-to-noise ratio dataset, and found a  $\chi^2/\text{DOF}$  goodness of fit p-value of 0.78, indicating the model is consistent with the data and the measurement statistical error. This suggests the model isn't inconsistent with the Gaussian-harmonic approximation, since we do not see substantial deviations from the predicted shape of the curve within our measurement error.

From the fit values of the temperature, we calculated the cooling ratio as the temperature of the shielded sample divided by the temperature of the bare ground state for use as our metric against which to measure the success of evaporation with shielding. We don't expect evaporation to produce any significant cooling for the bare ground state molecules, thus a cooling ratio above 1 indicates evaporative cooling has occurred (see figure 5.10). We scanned several exponential cooling rates and evaporation duration only to find a weak maximum evaporative cooling effect for 200 ms of forced evaporation with an exponential time scale of  $\tau = 50$  ms.

## 5.6 ELASTIC COLLISION RATE

Previously we had based our evaporative cooling estimates on an elastic collision rate from a coupled channel calculation. We will now measure the elastic collision rate by rapidly cutting the trap depth and observing the loss dynamics. This differs from the evaporative cooling step because there is no adiabatic ramp of the trap, it is a sudden cut. Cutting the depth rapidly does not cool the molecules like an adiabatic ramp. We cut to a depth of  $120 \mu\text{K}$ , implying  $\eta = 2$  which leaves a substantial number of molecules in high-laying orbits in the trap. This lets us observe two loss processes: the escape of single particle trajectories with energy above the trap depth and evaporative losses due to elastic collisions redistributing energy to the untrapped tail of the Boltzmann distribution. This process occurs at the elastic scattering rate and we will use it to produce a measurement of the shielded elastic scattering rate.

Some of the molecule orbits are energetically unbounded however it can take many cycles of motion in the trap to eventually escape. We measured the escape time for untrapped trajectories by lowering the density in the 780 nm ODT to about  $2 \times 10^9 \text{ cm}^{-3}$ , quenching the collisions, and then observing the population decay as we cut the trap depth and held for a variable amount of time before ramping up again. We observed 20% losses on the 1 ms time scale followed by no further losses for longer hold times. This strongly indicates that all energetically untrapped orbits escape from the 780 nm ODT in less than 1 ms. At the cut depth, our trap frequencies are 3.6 kHz and 100 Hz along

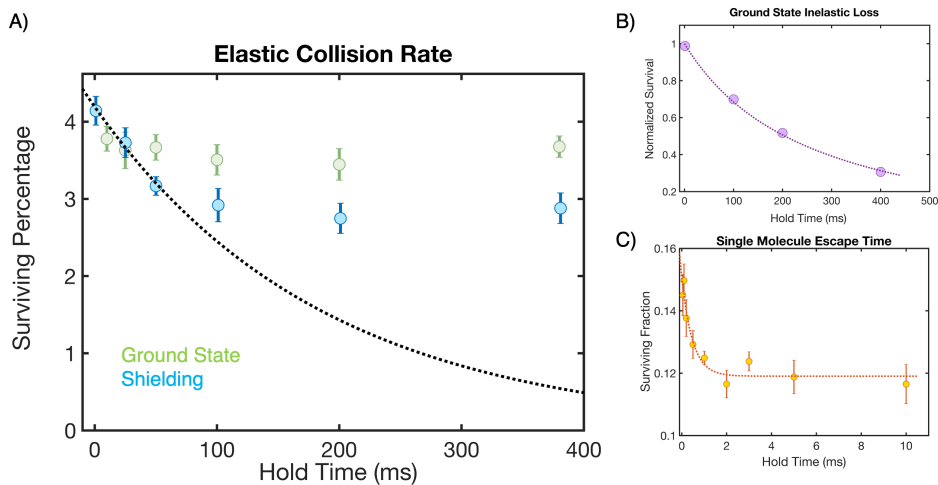


**Figure 5.11:** Figure A shows the survival of molecules after a rapid cut in trap depth. Ground state molecules (green points) experience no collisional redistribution due to the slow elastic collision rate and therefore no additional molecules are lost after the initial cut. Microwave-shielded molecules have an enhanced collision rate due to the dipolar interactions at play, resulting in a fast elastic collision rate and rethermalization of the population above the trap height, resulting in losses. The total hold time is constant, which cancels out inelastic losses. Figure B shows the ground state collision rate at the same trap depth used for the evaporative cooling elastic rate measurement. We use this time scale to get the density. Figure C shows the loss rate when the trap depth is cut at reduced density. No collisions occur and we have a probe of the single molecule unbounded-trajectory escape time. This time is much shorter than the evaporation time measured in figure A.

the radial and axial directions, respectively. The sub-millisecond escape time indicates most of the molecules are exiting via dynamics along the trap's radial directions.

In the case of elastic collision-driven evaporative losses, untrapped molecules are lost in the first 1 ms after the trap depth cut, however, these molecules are replenished from the bulk gas by elastic collisions. Energy is re-distributed in the ensemble, and some molecules are promoted to orbits above the escape energy, which will also be lost in less than 1 ms. We expect the elastic collision rate to be somewhat slow compared to the single molecule trap escape time.

With the microwave shielding enabled in figure 5.11, we observed an exponential decay rate of 50 ms for the first 50 ms before the collision process was quenched. In the case of pure evaporation, the loss should be deeper. After taking this data, we measured the dressed state lifetime to be 100 ms and believe that is the reason for the quench. Interpreting the first 50 ms decay as shielding-driven-evaporative loss, we estimate the elastic two-body rate to be  $\beta_{elastic} = 3 \times 10^{-9} \text{ cm}^3/\text{s}$ , similar to the coupled channel calculation prediction.

In the absence of shielding, the estimated two-body elastic rate is 15 times slow. We wouldn't expect to see losses under these conditions and indeed the bare ground state molecules do not appear to decay at all during the hold time at low trap depth.

Based on these measurements, we observed a ratio of elastic to inelastic loss rates of 15-50, which is a fair margin lower than the coupled channel calculation predicted. Most of the discrepancy comes from the reduced shielding performance, for reasons unknown.

## 5.7 SUMMARY

We demonstrated microwave shielding-driven evaporative cooling and measured the two-body elastic rate coefficient for microwave-dressed CaF molecules. This was also the first use of microwave shielding in a bulk gas environment. We understood several limitations to the depth of the evaporative cooling achieved in this experiment. The fundamental problem is one of the time scales. Our collision rates were not fast enough

to do evaporation within the dressed state lifetime and vacuum lifetime. Conversely, the dressed state lifetime and vacuum lifetime were too short to do evaporative cooling. Either way, the fix would be higher density from trapping more molecules or prolonging the dressed state lifetime by reducing the microwave phase noise.

It's notable that a different research group was able to achieve evaporative cooling to quantum degeneracy using microwave-shielded ultracold NaK molecules<sup>125</sup>. The NaK species used is a fermion and the starting temperature was already nearly Fermi degenerate. In addition, the microwave sources used for shielding generally have lower phase noise by virtue of the low frequency 2 GHz rotational gap in NaK. The NaK experiment also had roughly 100 times more molecules and an order of magnitude higher collision rate than our experiment, which is consistent with our assessment of the limitation in our own experiment.

Making the CaF experiment work better would require adding a high finesse cavity on the microwaves tuned to suppress the phase noise at 20 MHz. For efficient evaporation, a several-second dressed state lifetime will be needed. In addition to that, the vacuum lifetime will need to be longer too. This can be achieved in several ways, including transporting the molecules to an ultra-high vacuum environment, similar to what the CaF generation 2 experiment in our group does. Finally, a larger number of molecules would be needed which could be achieved by doing dynamic sweeps of the 1064 nm ODT to improve loading or replacing the 1064 nm ODT with a near-detuned 532 nm ODT (red detuned of the X-B transition) featuring a much larger trap volume at the

same depth and laser power.

## 5.8 PROSPECTIVES ON EVAPORATIVE COOLING OF CaF

The evaporative cooling outlook for CaF is not promising for realizing a Bose-Einstein condensate using our approach. If we were able to cool the molecules to 100 nK, a density of  $5 \times 10^{12} \text{ cm}^{-3}$  would be required for Bose condensation. At this density, the two-body lifetime would be 3 ms based on the loss rate measured in the tweezer shielding experiment. One could hope for a lower two-body loss rate in a shallow, low-intensity trap with small tensor stark shifts however the loss rate would have to be suppressed by several orders of magnitude to have a useable condensate.

At some point, three-body collisions will enter the picture and it's unlikely that microwave shielding will work in this situation. Having demonstrated evaporative cooling, understanding the limitations, and considering the prospects of this as a viable research path, we opted to abandon the study of collisions as a means to evaporatively cool CaF to quantum degeneracy.

# 6

## The Making of a Molecular Qubit

One promising prospective use for ultracold polar molecules is in quantum computing. A good qubit candidate must be addressable, strongly interacting with other qubits, and well isolated from the environment<sup>44,109,32,124</sup>. The first two criteria find themselves at odds with the third since generally, quantum systems rely on electric and magnetic fields to be addressable and to interact with other qubits. This means the

qubits will inherently have sensitivity to the lab environment. Ultracold polar molecules strike a balance with their strong dipolar interactions allowing coupling to neighboring molecules, microwave addressable transitions allowing addressability, and a rich internal structure providing options for reducing sensitivity to the lab environment.

In this chapter, we achieve the world record rotational coherence time for any ultracold polar molecular system by taking advantage of the exquisite control available over a single molecule in an optical tweezer trap. The rotational coherence time is the key starting point for any quantum computing platform. It is the length of time for which a qubit will hold the information; either a programmed configuration or the result of a computation. While there are tricks to undo the effects that ultimately limit the coherence time, an ideal system is pristine and has natural robustness. This is what we have demonstrated for a single trapped molecule in an optical tweezer.

To make this less abstract, in the case of the rotational coherence time, the question we seek to answer is how many times can we spin a molecule (without watching it) while it traverses the optical tweezer and still knows which direction it's pointing at any time. The direction it points is the quantum information. Once the experimenter has lost track of the pointing, the readout is meaningless and the information is either lost or uninterpretable. We'll begin by exploring the various effects that can cause dephasing and then throughout the chapter, we will discuss ways to mitigate these effects en route to measuring the longest rotational coherence time observed to date<sup>19,22,91,153,129,106</sup>.

## 6.1 CONSIDERATIONS

Many Factors can cause the rotation of the molecule to speed or slow down, resulting in the molecule either under-rotating or over-rotating in an uncontrolled way. This manifests itself when a changing field shifts the two qubit states relative to each other, causing the energy splitting to change<sup>121,78</sup>. Stray electric fields and changing magnetic fields in the lab must be suppressed by passive and active cancelations methods that we'll discuss in detail later.

The more interesting factors arise in the tweezer environment itself and have to do with the very nature of the molecules being anisotropic and how they interact with the polarization of the tweezer light. We develop a detailed, rigorous, understanding of the molecule-light interactions and combine that with the exquisite experimental control over the tweezer environment to achieve a coherence time limited only by the temperature floor of the most effective laser cooling scheme we know.

## 6.2 LIGHT SHIFTS IN AN OPTICAL TWEEZER

Inhomogeneous light shifts in the optical tweezer are the reason there is a trapping force but it's also one of the most substantial limitations to the coherence time. In a far-off resonant optical field such as a tweezer, the AC Stark shift can be described by three components; the scalar shift, the vector shift, and the tensor shift. The scalar shift is what supplies most of the trap depth. The trapping forces come from the

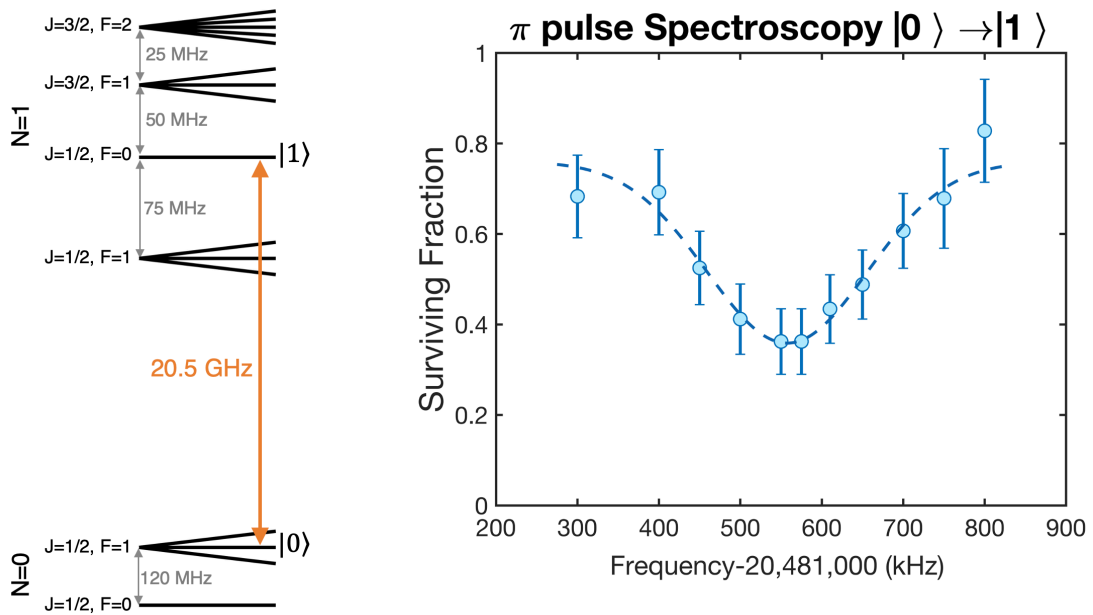


**Figure 6.1:** Left is a level diagram showing the  $N=0$  and  $N=1$  rotational levels in the electronic ground state of CaF. The orange arrow indicates the transition between the two states we will use as our qubit basis. The plot on the right is the spectroscopy of the qubit transition using a  $4.4 \mu\text{s}$   $\pi$ -pulse. The resonant  $\pi$  time is roughly known from previous data, and set to ensure spectroscopic resolution of the  $m_f$  levels split in a 1.5 Gauss magnetic field oriented perpendicular to the 780 nm optical tweezer polarization. The tweezer depth was at “full depth”,  $1800 \mu\text{K}$ . With shifts from both the magnetic field and optical tweezer included, the transition is located at 20481.55 MHz.

gradient of the Stark shift, requiring an inhomogeneous light field, like a tightly focused tweezer. A molecule will move around in an energetically allowed volume within the trap constrained by the trap parameters and the sample temperature. If the scalar light shift was the only shift present, it would have no impact on the coherence time because both of the qubit states are shifted by the same amount, independent of where the molecule traverses within the trap. On the other hand, the tensor and vector components of the light shift both have a dependence on the orientation of the molecule therefore they cause differential shifts between the qubit states. This means the energy splitting between the qubit states depends on the intensity of the trapped light, which varies as the molecules move on classical trajectories in the trap. The levels we used are indicated in Figure 6.1

The tensor stark shift is the anisotropic interaction of the molecule with linearly polarized light. The scale is set by the scalar stark shift and the matrix elements mimic shifts from a DC electric field. In Hund's case B basis, the matrix element below describes the tensor interaction.

$$\langle N_0, J_0, F_0, m_0 | T_Q^2 | N_1, J_1, F_1, m_1 \rangle = A \begin{pmatrix} F_0 & 2 & F_1 \\ -m_0 & Q & m_1 \end{pmatrix} \begin{Bmatrix} J_0 & F_0 & I \\ F_1 & J_1 & 2 \end{Bmatrix} \begin{Bmatrix} N_1 & J_0 & S \\ J_1 & N_0 & 2 \end{Bmatrix} \quad (6.1)$$

where

$$A = -6\sqrt{15/2}(-1)^{F_0-m_0+I+J_1+F_0+S+1+J_0+Q}\sqrt{(2F_0+1)(2F_1+1)(2J_0+1)(2J_1+1)} \quad (6.2)$$

The scale of the tensor shift is proportional to the scalar polarizability at the tweezer wavelength of 780 nm. It can be calculated, but we opted to measure the differential shift as a function of trap depth for the qubit transition to ensure our tensor stark shift energy calculation has the best predictive power (see figure 6.5)

Finally, the vector stark shift describes the interaction of the molecule with circularly polarized light. It mimics a magnetic field in the way that it splits the hyperfine levels. We discuss the vector shift at the end of the chapter since it is highly suppressed in our experiment.

### 6.3 STATE SELECTION

Picking the right set of qubit states is paramountly important, although the right choice is not obvious so let's carefully walk through the selection criteria. We plan to eventually use these qubit states for quantum computing, so they must allow direct dipolar coupling with a nearby molecule. This requires the two states to belong to different rotational manifolds, separated by 1 quantum of angular momentum since the dipolar interaction is nothing more than the effect of one molecule's internal electric field on the dipole moment of another molecule and vice versa. It's convenient to use the ground and first

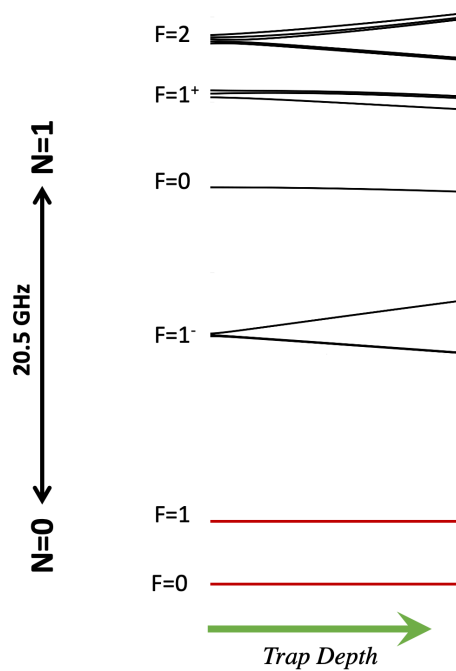


**Figure 6.2:** Relevant rotational and hyperfine levels with trap light shifts plotted. The  $N=0$  levels are not shifted at all whereas the  $N=1$  levels have differential AC-stark shifts.

excited states ( $|N = 0\rangle$  and  $|N = 1\rangle$ ). Figure 6.2 shows the available levels in the  $N=1$  rotational manifold.

Within the  $|N = 1\rangle$  manifold there are 12 states to choose from while the  $|N = 0\rangle$  manifold has 4. The next criterion, isolation from external magnetic and electric fields, eliminates most of the transitions which have roughly a full Bohr magneton of differential magnetic moment.

The transition between the spin stretched states  $|N = 1, F = 2, m_f = \pm 2\rangle$  and  $|N = 0, F = 1, m_f = \pm 1\rangle$  (all the angular momentum including rotation, electron spin, and nuclear spin is aligned on the same axis) seems promising because the ground and excited states have very nearly matched magnetic moments (within 5 Hz/Gauss<sup>29</sup>), however, the  $|N = 1, F = 2, m_f = \pm 2\rangle$  state has a significant light shift. There is a way to make this transition work, and we will return to the topic later, but we opted for the simple route using  $|0\rangle = |N = 0, F = 1, m_f = 0, \rangle$  and  $|1\rangle = |N = 1, F = 0, m_f = 0, \rangle$  as our qubit basis.

The  $|N = 1, F = 0, m_f = 0\rangle$  state is somewhat special because the electron spin and nuclear spin add up to cancel the rotational angular momentum. Unlike any other state in the  $N=1$  manifold, this state is isotropic and has no first-order Zeeman shift or light shift in the trap. Partnering it with the  $|N = 0, F = 1, m_f = 0, \rangle$  state, provides excellent robustness to external fields.

The price for this robustness is twofold. Owing to the 10's of MHz scale hyperfine interactions which couple the angular momentum to form the  $F=0$  state, the external

field insensitivity we want is only present in weak external fields. From a technical perspective, this is advantageous since it is generally easier to stabilize weak magnetic fields. The steepest price to be paid later is that this transition does not have the full molecule-frame dipole moment. It offers about 1 Debye, whereas the spin-stretched states offer the maximum dipole moment of  $3/\sqrt{3}$  Debye. When it comes time to observe dipole-dipole coupling, our qubit states will offer about 1/3 the maximum interaction strength. This point is not relevant to our work on the coherence time but it is important for working towards a functional quantum computer with this platform.

#### 6.4 EXPERIMENTAL SEQUENCE

To initially prepare the qubits for each experimental repetition, we generate a MOT of  $^{40}\text{Ca}^{19}\text{F}$  molecules<sup>5</sup>, use lambda-enhanced grey molasses cooling<sup>7</sup> to transfer the molecules into a 1064 nm optical dipole trap, and then load a single 780 nm tweezer<sup>7</sup> using a secondary lambda-cooling light pulse. Light-assisted collisions create a collisional blockade, resulting in single molecule loading as described previously in this thesis<sup>6</sup>. The single-loaded molecule is then optically pumped to the  $|1\rangle$  state, transferred to the  $|0\rangle$  state, and then any remaining population in the  $N=1$  manifold is blown away with resonant light. The tweezer depth  $U_i$  is then ramped from  $U_i = 1800 \mu\text{K}$  to  $U_f = 26 \mu\text{K}$ , which results in adiabatic cooling of the molecule from a temperature of  $T_i = 40 \mu\text{K}$  to  $T_f = 5 \mu\text{K}$ , while maintaining  $\eta = U/T > 5$ .

## 6.5 STABILIZING THE LAB ENVIRONMENT

Our choice of qubit states goes a long way towards passively reducing the impact of external electric and magnetic fields on the coherence time, however substantial experimental work would be necessary to actively stabilize the lab environment. We eliminated static electric fields, actively compensated slow DC magnetic field drifts in the room, and phase synchronized the experiment to the 60 Hz line phase. Figure 6.3 demonstrates the lab environment control.

### 6.5.1 QUBIT PERFORMANCE IN DC ELECTRIC FIELDS

In the case of slowly changing DC electric fields in the lab, all the electric dipole coupled sets of states in the  $N=0$  and  $N=1$  manifolds get similarly shifted, so our choice of qubit states doesn't offer much protection. However, the large rotational energy gap of 20.5 GHz in CaF offers a great deal of protection, resulting in a differential sensitivity of  $40 \text{ Hz}/(\text{V}/\text{cm})^2$  for the qubit transition. Static charges accumulate on insulating surfaces in the experiment and we saw during the shielding experiment, where the qubit transition was used for a different purpose, day-to-day shifts on the 100's of kHz scale. Using a DC electric field probe, we recorded fields of a few hundred volts/cm on the outside of the re-entrant window of the chamber. We added air ionizers directly over the re-entrant window at the top of the chamber and ensured that our in-vacuum MOT coils were tied to the ground immediately after the MOT stage of the experiment. With these

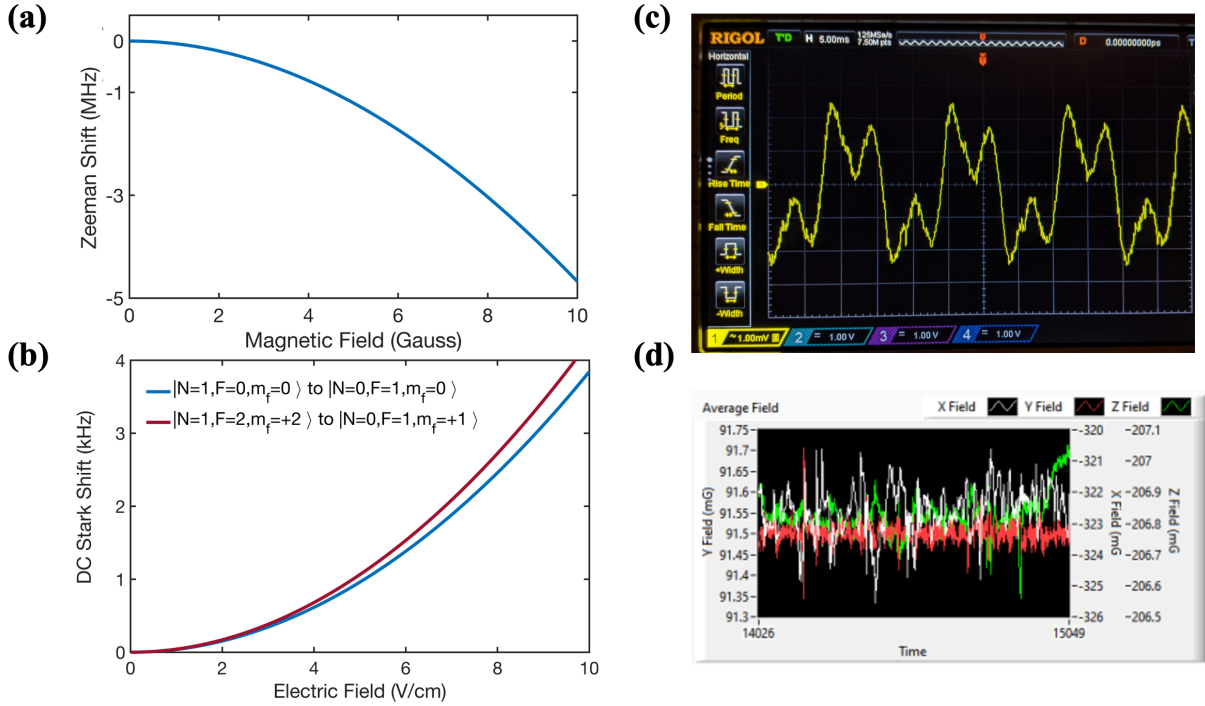


**Figure 6.3:** (a) The Zeeman sensitivity of the qubit transition computed by diagonalizing the ground electronic state Hamiltonian of CaF. For small fields, the quadratic Zeeman shift is  $-44 \text{ kHz/Gauss}^2$ . (b) The DC Stark shift sensitivity is calculated for the qubit transition and a transition between spin-stretched states. In the computation, the magnetic field is set to 14 Gauss and oriented parallel with the electric field. The magnetic field strength and orientation do not significantly change the DC Stark sensitivity in the low field regime. All the dipole transitions between the  $N=0$  and  $N=1$  manifolds have similar DC Stark shift sensitivity, all around  $40 \text{ Hz}/(\text{V/cm})^2$ . (c) The magnetic field was sampled on a Gauss probe placed near the top of the MOT chamber. The sensitivity of the Gauss probe is  $10 \text{ mV/mGauss}$ , indicating very large magnetic field oscillations. The primary components are the 60 Hz line frequency and it is associated with the 3rd harmonic at 180 Hz. The oscillations on top of the smooth waveform are from less correlated noise sources lacking an identifiable spectral decomposition. The magnetic field oscillating at the line frequency is very stable in terms of amplitude and phase, therefore we are able to make our experiment robust by triggering a set phase of the waveform. Part (d) shows a sample-and-hold magnetic field trace produced by subtracting off the average line phase waveform to uncover the non-deterministic noise. We actively cancel that noise using a PID loop feeding back on a set of 1-meter diameter coils. The Y and Z fields are stabilized while X is not. The X direction field, for reference, fluctuates by about 5 mGauss, whereas the stabilized Z and Y directions are on the  $200 \mu\text{Gauss}$  level and sub  $100 \mu\text{Gauss}$  levels, respectively. The Y field direction is parallel to the 1.5 gauss bias field used to establish the quantization axis, therefore this field stability is the most important. The other two directions are suppressed because they add in quadrature with the bias field.

precautions in place, we never again observed shifts in the qubit transition frequency due to DC electric field build-ups.

### 6.5.2 QUBIT PERFORMANCE IN DC MAGNETIC FIELDS

In a DC magnetic field, relative Zeeman shifts between the qubit states appear at second order as a result of decoupling the hyperfine interactions. For small magnetic fields, the differential sensitivity is  $-44 \text{ kHz/gauss}^2$ . The typical scale of DC magnetic field noise in our experiment was a few 10's of mGauss which would correspond to frequency fluctuations of about 40 Hz. To have phase coherence on the 100 ms time scale (accounting for the factor of  $2\pi$ ) would require frequency fluctuations to not exceed the 1 Hz scale corresponding to a magnetic field RMS stability of  $500 \mu\text{Gauss}$ . To achieve this, we monitored the magnetic field using a Bartington fluxgate magnetometer mounted on the top of the chamber about 10cm away from the molecules. It wasn't practical to put the sensor any closer, even though that would be desirable. Using a 3-axis set of PID-controlled compensation coils wrapped around the chamber with a diameter of about 1 meter, we actively canceled the DC fluctuations to the sub  $100 \mu\text{Gauss}$  level.

The DC field is not the whole story. We observed extremely large 10's of mGauss scale magnetic field components oscillating at 60 and 180 Hz from the AC power lines. We considered directly compensating the AC field by driving coils out of phase to cancel the line field, however, the phase of the line field in the lab varied on surprisingly small length scales. Our magnetometer mounted outside the chamber could not guide us to

cancel the field at the molecules, about 10 cm away. Our measurement showed the 60 Hz magnetic field was very stable, therefore we synchronized the experimental sequence to the wall by triggering Cicero on the rising slope of a signal produced by using a transformer plugged directly into the wall.

## 6.6 RAMSEY SPECTROSCOPY AND MICROWAVE SYSTEM PERFORMANCE

One way to measure the rotational coherence time is to coerce the molecule to rotate in a fixed orientation relative to a reference clock rotating at the same speed. After initializing the rotation, the clock and molecule separate but each continues to rotate (precess) on its own for a variable amount of time, without referencing each other. Finally, at the end of the precession time, we compare the molecule's orientation relative to the hands on the trusted clock. The coherence time is the maximum amount of time during which the molecule can precess and still remain aligned relative to the trusted reference clock.

This measurement technique is called Ramsey Interferometry. An initial microwave  $\pi/2$  pulse tuned to resonance creates a superposition of the two-qubit states, rotating the Bloch vector down from the pole onto the equator of the Bloch sphere. After the first pulse, the molecule undergoes free precession where the Bloch vector rotates around the equator of the Bloch sphere at a rate given by the energy splitting between the two qubit states. During this time, the microwave oscillator is still running in the background

but the amplifiers are switched off so no microwaves are present in the experiment. While the molecule precesses, we use a fast phase modulator to jump the phase of the microwaves. At the end of the free precession time (this could be arbitrarily long), another microwave  $\pi/2$  pulse is applied. In this sense, we are doing an interferometric experiment by comparing the microwave clock phase to the phase of the molecules after the free precession time. By scanning the microwave phase, we generate fringes with a contrast that we can fit for different precession times. The contrast of the fringe directly tells us how well the molecules have tracked the microwave oscillator during the free precession time. We extract the coherence time by measuring the contrast of the oscillation for different precession times and fitting the decay to a Gaussian model.

Once the Ramsey sequence ends, we use our Lambda imaging technique to image the molecules in the  $|1\rangle$  state. By imaging, we are measuring the projection of the wavefunction at the North pole of the Bloch sphere. Figure 6.6 shows the Ramsey fringes.

### 6.6.1 MICROWAVE SYSTEM DETAILS

The microwave system serves as the reference clock and the initiator of the Bloch vector rotation, therefore phase and power stability are very important. Figure 6.4 shows the microwave system used in our experiment. We generate the 20.6 GHz microwaves by mixing two sources; one at 18.6 GHz and one at 2 GHz. Both microwave sources were locked to the same 100 MHz low-phase noise reference oscillator. On the 2 GHz arm,

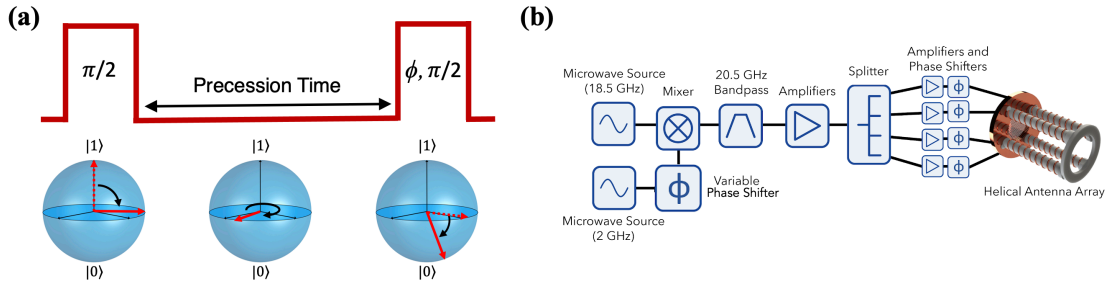


**Figure 6.4:** (a) Ramsey pulse sequence. A  $2.2 \mu\text{s}$   $\pi/2$  pulse is applied to create an equal superposition of the qubit states. Pictured below is the Bloch sphere representation of the qubit rotation, where the first  $\pi/2$  pulse initiates precession around the equator. The molecule is allowed to free precess for a variable amount of time before another  $\pi/2$  pulse with an adjustable phase is applied to rotate the molecule back to the measurement basis. By Lambda imaging the sample, we can measure the projection of the wave function along  $|1\rangle$ . (b) The microwaves are produced by mixing an 18.5 GHz Keysight E8257D with a 2 GHz Windfreak SynthHD Pro locked to a 100 MHz low-phase noise oscillator. A fast programmable phase shifter on the 2 GHz arm provides control over the phase of the second  $\pi/2$  pulse. Neither the high power amplifiers (Qorvo TGA4548-SM) nor the helical antenna array was strictly necessary for this experiment but both systems were functioning reliably after the microwave shielding experiment finished.

we use a fast phase modulator to jump the microwave phase during the free precession period. Next, the microwave sources are combined on a mixer and a bandpass filter selects the 20.6 GHz signal before it passes through two stacked microwave switches. The double switches are needed to suppress single switch -60 db leakage before the high power amplifiers which fed directly to the same helical antenna used for microwave shielding. Here, the polarization cleanliness of the microwaves is not critical and the helical antennas in their unoptimized configuration, combined with chamber reflections delivered some field in all polarizations. The key aspect of the microwave source for Ramsey spectroscopy is 1) power stability for consistent application of pulses and 2) an Allen deviation sufficiently low to be sure that loss of Ramsey phase contrast is due to dephasing of the molecules, and not phase diffusion of the microwave phase. Every

microwave source available to us far exceeded this criterion.

## 6.7 THE QUBIT STATES IN AN OPTICAL FIELD

Earlier we introduced the tensor stark shift as the anisotropic interaction between the polarization of the 780 nm tweezer light and the orientation of the molecule. It will not impact the  $|0\rangle$  state because  $|0\rangle$  belongs to the  $N=0$  manifold which doesn't have a tensor shift. The situation for the  $|1\rangle$  is more complicated. Since the  $F=0$  state is isotropic, it does not experience a first-order tensor shift. However, the tensor shift comes back at second order through mixing with the nearby  $F=2, m_f = 0$  hyperfine state. The light shift of the  $F=0$  state is quadratic in intensity ( $\Delta = \beta I^2$ ) and we measured the pre-factor, sometimes called the hyper-polarizability, to be  $-4.8 \text{ kHz}/(\text{kW}/\text{cm}^2)^2$  in the absence of magnetic field. This measurement was used to calibrate the strength of the tensor stark shift for all of our coherence time-related molecular structure simulations. See figure 6.5

This hyperpolarizability is how the light shift causes the energy gap between the two qubit states to change as the molecule experiences different intensity tweezer light over the course of its classical trajectory in the tweezer trap. In the next section, we will explore the role of magnetic fields as a tool to engineer the light shifts in a way favorable to reducing the intensity sensitivity of the qubit transition.

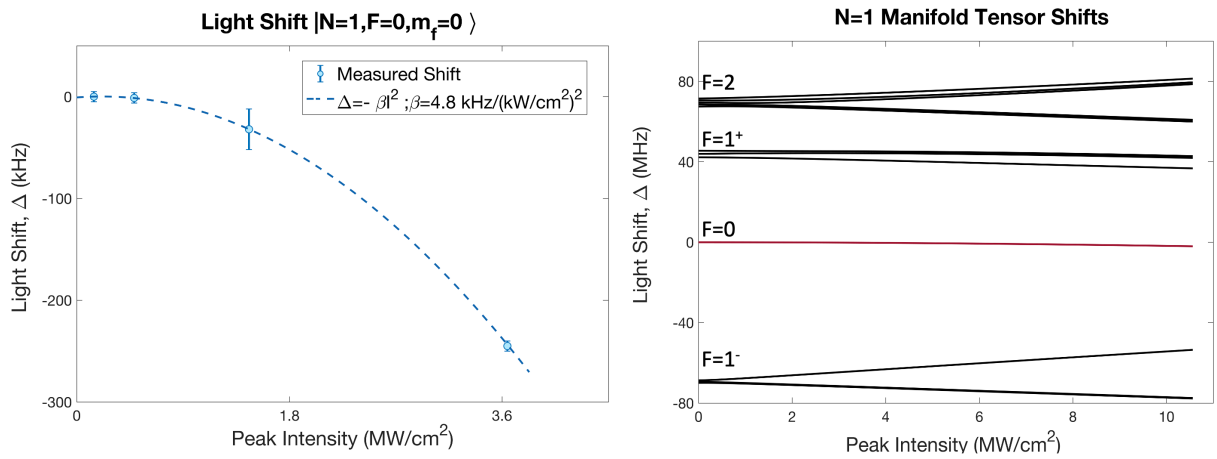


**Figure 6.5:** The left plot shows the qubit transition frequency shift as a function of optical tweezer depth. The data are fit to the function  $\Delta = -\beta I^2$  to model the quadratic nature of the Stark shift (hyperpolarizability) and the fit value for  $\beta$  is used to calibrate the Tensor stark shift strength used in all subsequent structure calculations. On the right is a plot showing the tensor shifts of all the hyperfine levels in the  $N=1$  rotational manifold in the presence of a 1.5 Gauss magnetic field oriented at  $77^\circ$  relative to the light polarization. The state highlighted in red is the uppermost qubit state (the lower qubit state in  $N=0$  does not experience a tensor shift). Notice it shifts the least of all the states in the  $N=1$  manifold.

### 6.7.1 “MAGIC” CONDITION

The problem becomes more interesting with the addition of another quantization axis; a magnetic field oriented at angle  $\theta$  relative to the tweezer light polarization. We can understand the interaction and how we will use it to improve the coherence time by considering the limiting cases. When the light intensity is low and the magnetic dominates, the light shift is linear. The Zeeman interaction maintains  $m_f$  as a good quantum number but not  $F$ , therefore our upper qubit state gets a first-order admixture of the neighboring  $F = 1, m_f = 0$  states. The  $F = 1$  states experience a linear light shift from a weak optical field and thus our upper qubit state now has a linear stark shift. The sign of the shift can be positive or negative and the sensitivity of the light shift is linear in the magnetic field strength.

In the other limit, the light shift is quadratic and negative as a function of intensity. The trick we can play is to set the magnetic field angle and magnitude such that at low intensity, the light shift is linear and positive, but at high intensity, it regains the negative curvature. This field configuration guarantees a flat region of the differential light shift vs. intensity where the intensity can change but the differential shift vanishes to first order. Following the literature precedent, we will refer to this as the “magic” condition; where we have optimized the fields such that the qubit transition has minimal sensitivity to changing light intensity. This “magic” condition depends sensitively on the intensity of the light, and both the direction and orientation of the magnetic field,

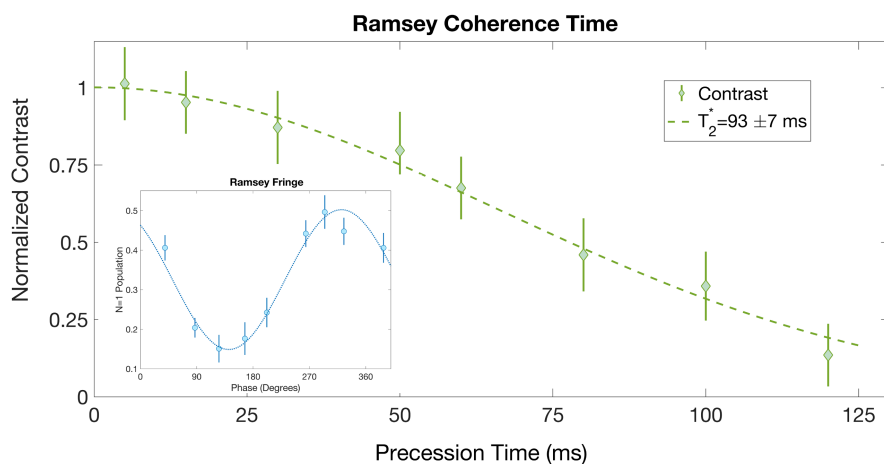


**Figure 6.6:** (a) Ramsey pulse sequence. A  $2.2 \mu\text{s}$   $\pi/2$  pulse is applied to create an even superposition of the qubit states (rotates onto the equator of the Bloch sphere). The molecule is allowed to free precess for some amount of time before another  $\pi/2$  pulse with an adjustable phase is applied to rotate the molecule back to the measurement basis. Next, we measure the component of the wave function pointing in the positive z-direction on the Bloch sphere by directly imaging molecules in the  $N=1$  upper qubit state. The projection oscillates with the phase shift, resulting in a fringe as seen in part (b). The contrast of the fringe carries information on how well the molecular system is maintaining the phase reference relative to the stable microwave oscillator. By measuring the contrast of the fringe for several different precession times, we can extract the coherence time by fitting it to a Gaussian decay model, pictured in part (c).

as seen in Figure 6.7.

The only part left to do is to tune the “magic” condition such that the flat region in the curve coincides with the peak intensity of the optical tweezer. There are a few subtleties to point out. The magic angle is not the usual  $\text{Acos}(1/\sqrt{3}) \approx 54.7^\circ$  dipolar nodal angle because we are relying on non-linear mixing in the Hamiltonian. This implies for weak magnetic fields the orientation of the quantization axes must be maximally different ( $90^\circ$ ) in order to allow a weak magnetic field to have as much impact as possible. Of course, if the B field is too small, there will be no such angle. As the magnetic field increases in strength, the magic angle will rotate down towards, and eventually asymptote to  $54.7^\circ$ .

## 6.8 “MAGIC” CONDITIONS IN THE EXPERIMENT

In the experiment, we choose to set the magic angle close to  $90^\circ$  because it allows us to work at the lowest magnetic field possible which reduces the impact of technical noise. The magnetic field was generated by a Tenma power supply running 1.2 amps through a 10 cm coil wrapped around the vacuum chamber producing a 1.5 Gauss magnetic field. Our process for finding the magic angle required rotating the linear polarization of the tweezer while holding the magnetic field constant in both angle and magnitude. We used a high extinction polarizer (better than  $10^{-7}$  linear extinction ratio) to first clean the polarization of the tweezer light after the very last optic, but just before the rotating wave plate used to set the angle of the polarization. The rotating wave

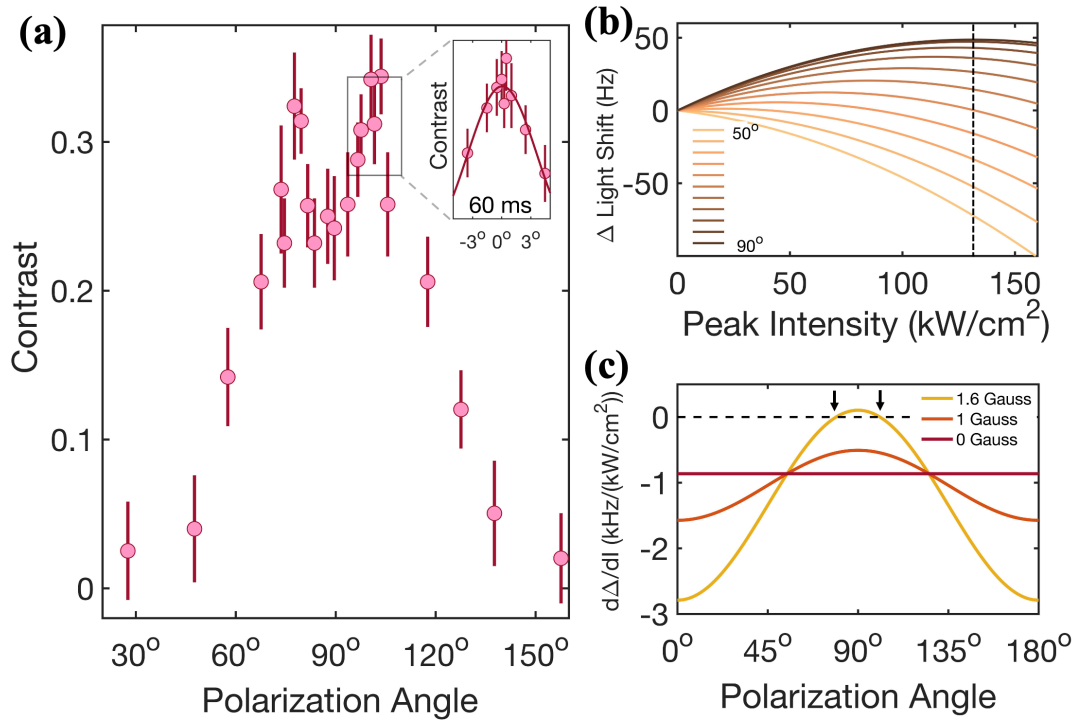


**Figure 6.7:** (a) Scan of the magic angle condition. At a fixed precession time of 30ms, we measured the phase contrast of the Ramsey fringes for a variety of different light polarization angles. Two magic conditions where the coherence time is maximized appeared on either side of 90°, as expected. To better locate the magic condition, we increased the precession time to 60 ms and performed a fine scan around the 103° magic condition. Part (b) shows the differential light shift between the two qubit states as a function of intensity for various orientations of a 1.5 Gauss magnetic field. As explained in subsection 6.7.1, the interplay between the magnetic field and light polarization leads to a flat region where the differential shift is very small with respect to a change in intensity. Part (c) shows the slope of the differential light shift at the peak tweezer intensity as a function of magnetic field orientation for different magnetic field strengths. The magic condition is at the zero crossing of this curve. A minimum magnetic field strength is required, determined by the tweezer peak intensity. We choose to operate with a relatively low magnetic field to mitigate technical issues.

plate was on a motorized Thorlabs mount for convenience, although the sensitivity of the magic condition nearly required the repeatability of a mechanized mount over an incremented hand-rotated optics mount. Half of a degree was the experimentally observed repeatability requirement-which is barely within the limit of a steady hand.

We found the most reliable and time-effective method for measuring the improvement in coherence time vs. polarization angle was to run a Ramsey sequence with a fixed precession time. Using the microwave phase shifter, we scanned the phase from 0-360 and measured the contrast of the Ramsey fringe as a stand-in for a complete measure of the coherence time which would have been prohibitively time-consuming. Our coarse scan with a precession time of 30 ms showed a clear signature of two magic angles, as expected by symmetry. We did a fine scan near one of the magic angles with a precession time of 60 ms to provide more resolving power for the exact location of the magic condition. Upon locating a magic angle at  $77^\circ$ , we measured the phase contrast at different precession times, fit to a Gaussian model for the decay of the contrast, and extracted a  $T_2^*$  time of 93 ms. The Gaussian model is the expected decay shape when the dephasing mechanism is inhomogeneous broadening which is the mechanism for un-canceled trap shifts.

### 6.8.1 IMPROVING THE COHERENCE TIME USING CORRECTIVE METHODS

The Ramsey coherence time is a bare measure of the isolation of the qubit transition from its local environment. While we want to push this time out by improving control

over the optical tweezer, there is another way to preserve the quantum information for longer. Adding additional microwave pulses during the precession time can help undo the dephasing that occurs in the system. the simplest thing is to add a single  $\pi$ -pulse in the middle of the precession time, depicted in Figure 6.8. This flips the qubit which means a perturbation causing phase accumulation in one direction for the first half of the precession time will naturally undo itself for the second half since the phase will be accumulated in the negative direction. This sequence is called a spin-echo and is a very powerful tool for canceling inhomogeneous broadening effects. We implemented a spin-echo pulse while at the “magic” condition and increased the coherence time by a factor of 5, to reach  $T_2 = 470 \text{ ms}$ . We do not know what limits the spin-echo time, as the  $T_2$  was the same very far away from the “magic” condition.

### 6.8.2 DYNAMICAL DECOUPLING

Adding even more pulses can help too. This is the basis of dynamical decoupling which is a general process of designing pulse sequences to cancel high-order dephasing effects while not interrupting the qubit system. Many pulse sequences exist and are optimized for different kinds of dephasing sources. We do not have detailed knowledge about the limitations of the spin-echo sequences so we somewhat arbitrarily choose to implement the Uhrig dynamical decoupling sequence, UDD(n) where n is the number of pulses applied.

The first time we tried implementing UDD was before we had phase locked the exper-

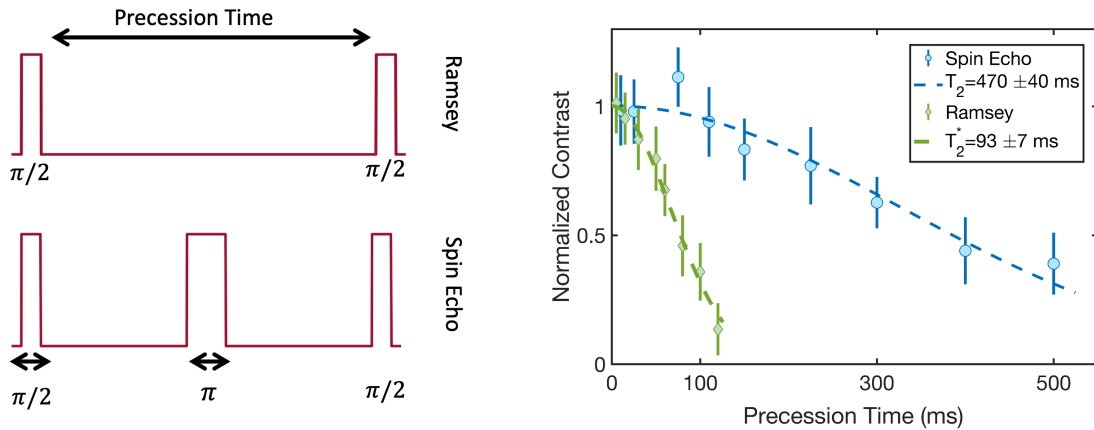


**Figure 6.8:** (a) Adding a  $\pi$ -pulse to the middle of the Ramsey sequence reflects the Bloch vector resulting in the accumulation of phase in the opposite direction. This will completely remove the phase accumulated from a static detuning and is effective in mitigating the impact of inhomogeneous broadening on the coherence time. In our experiment, the spin-echo improved the coherence time by a factor of 5, resulting in a 470 ms  $T_2$  time. The spin-echo coherence time appeared to be unaffected by the magic angle condition indicating that the spin-echo effectively removes trap-related decoherence.

iment trigger to the AC line phase, therefore the dominant noise was 60 Hz magnetic fields. We saw the coherence time steadily improved with the addition of more  $\pi$ -pulses, but was still orders of magnitude below our best result.

After stabilizing the lab environment and finding the magic angles, we implemented UDD again but found no real benefit over the spin echo, indicating several issues. The first possibility is the nature of the noise source is not compatible with the UDD sequence. The other possibility is that our microwave pulse stability might have been insufficient to drive many UDD pulse sequences with high enough fidelity to properly implement. This would cause our  $\pi$ -pulses to either over or under-rotate on the Bloch sphere and the errors would accumulate as more pulses are added to the sequence. We understand

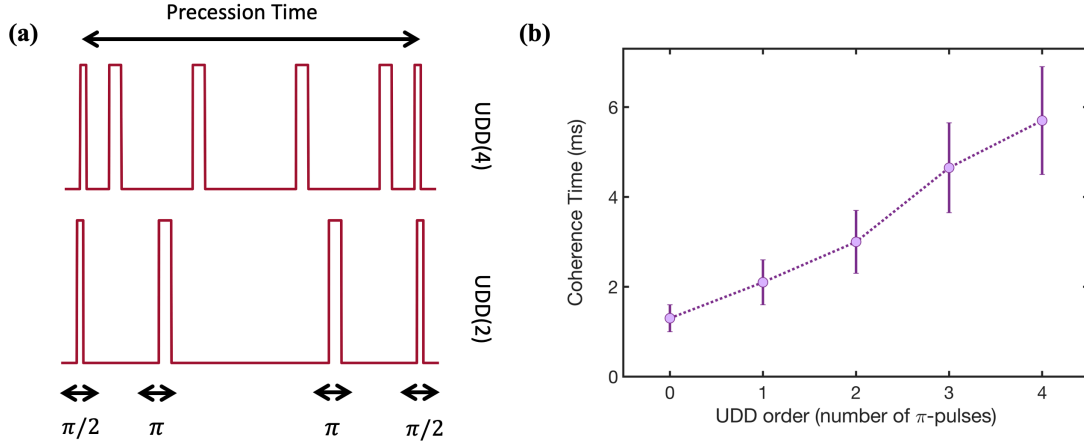


**Figure 6.9:** Dynamical decoupling pulse sequences. We implement UDD(N) where N is the number of  $\pi$ -pulses. The pulses are spaced according to the formula  $\pi_N(n) = \sin(n\pi/(2N + 2))^2$ . Before synchronizing the experiment to the AC line phase, we measured the coherence time for dynamical decoupling sequences with a variable number of  $\pi$ -pulses.

the technical limitation to our pulse fidelity is related to microwave sidebands appearing due to reflections off the vibrating turbo pump and stainless steel vacuum chamber. The results of the dynamical decoupling are shown in Figure 6.9.

## 6.9 WHAT LIMITS THE RAMSEY COHERENCE TIME?

We quickly ruled out technical limitations to the coherence time. At our operating magnetic field of 1.5 Gauss, the qubit transition has a differential sensitivity of less than  $\mu_B/10$ , therefore our sub 100  $\mu$ Gauss active field stabilization is adequate. The expected magnetic field limited coherence time under these conditions is a few hundred milliseconds.

Intensity noise on the tweezer light could be a factor however tuning to the magic

condition makes the qubit transition minimally sensitive to changes in intensity. Our tweezer PID stabilization loop reduced the RMS noise to the  $10^{-3}$  level relative to the total intensity. Based on the slope of the differential light shift at the magic condition, the RMS intensity noise corresponds to a coherence time limit longer than 1 second.

### 6.9.1 TEMPERATURE

We determined the temperature to be the effective limitation to the Ramsey coherence time. As the molecules move in the trap, they experience different light intensities over the course of their classical trajectory. The spread of the intensities sampled by the molecules is set by the temperature and it follows that the spread of the frequency shifts between qubit states is the spread of the intensity distribution convolved with the light shift sensitivity. Tuning to the magic condition only gives a flat light shift slope at exactly one intensity, therefore it does not remove all possible dephasing for a thermal sample traversing the trap.

During the Ramsey sequence, the trap is ramped down to a depth of  $25 \mu\text{K}$ , and the molecules adiabatically cool to  $5 \mu\text{K}$ . Under these conditions, the molecules are occupying 1000-10000 harmonic oscillator modes in the trap, therefore we can describe the motion classically.

We modeled this using a Monte Carlo simulation seeding a Gaussian trap with thermal molecules and tracing their trajectories. The simulation followed  $10^6$  molecules and built a distribution of light intensities sampled. Next, the light shift sensitivity was computed

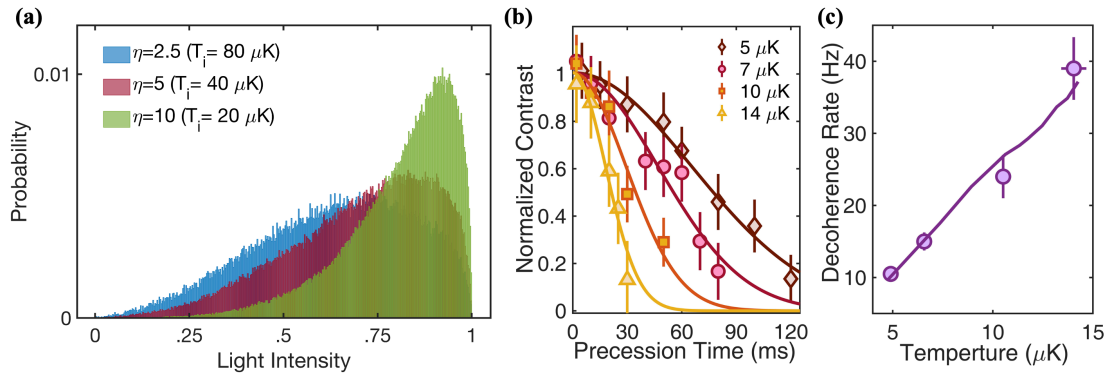


**Figure 6.10:** (a) Scan of the magic angle condition. At a fixed precession time of 30ms, we measured the phase contrast of the Ramsey fringes for a variety of different light polarization angles. Two magic conditions where the coherence time is maximized appeared on either side of  $90^\circ$ , as expected. To better locate the magic condition, we increased the precession time to 60 ms and performed a fine scan around the  $103^\circ$  magic condition. Part (b) shows the differential light shift between the two qubit states as a function of intensity for various orientations of a 1.5 Gauss magnetic field. As explained in subsection 6.7.1, the interplay between the magnetic field and light polarization leads to a flat region where the differential shift is very small with respect to a change in intensity. Part (c) shows the slope of the differential light shift at the peak tweezer intensity as a function of magnetic field orientation for different magnetic field strengths. The magic condition is at the zero crossing of this curve. A minimum magnetic field strength is required, determined by the tweezer peak intensity. We choose to operate with a relatively low magnetic field to mitigate technical issues.

for the tweezer power, magnetic field angle, and magnetic field strength. The width of the frequency distribution gives the coherence time. The Monte Carlo model captured the experiment very well, including the prediction of the temperature dependence and the magic angle data.

We measured the temperature dependence by changing the lambda cooling parameters prior to adiabatically ramping down the tweezer for the Ramsey measurements, as seen in Figure 6.10. This creates a thermal ensemble of molecules at an adjustable temperature. Repeating the microwave phase scans during the Ramsey sequence, we measured the coherence time. at several temperatures and observed a linear relationship

between temperature and decoherence rate ( $1/T_2^*$ ).

At lower temperatures, the optical tweezer trap is approximately harmonic. The Virial theorem tells us the average kinetic energy is equal to the potential energy which is proportional to the tweezer light intensity in an optical trap. In the case of an ideal gas, the variance in energy is  $T^2$  times the heat capacity, thus the width of the distribution of intensities experienced by the molecules scales linearly with temperature, as we measure. Combined with the quadratic nature of the differential light shift at the magic angle, the decoherence rate scales as  $T^2$ .

Longer rotational coherence times could be achieved by further cooling the sample beyond Lambda cooling. Single particle cooling techniques such as Raman sideband cooling might dramatically extend the rotational coherence times up to technical limitations.

## 6.10 LOOSE ENDS

At points in this chapter, several important but tangential aspects were briefly mentioned and will now be explained in some level of detail. Early in this chapter, we dismissed the vector stark shift as a potential source of decoherence. The vector shift requires circularly polarized light which is present in tightly focused traps<sup>28</sup>. It results from the bending of the linear polarization as the focused beam waist of  $1.4 \mu\text{m}$  is close to the 780 nm wavelength of the trap light (see Figure 6.11). This results in a polar-

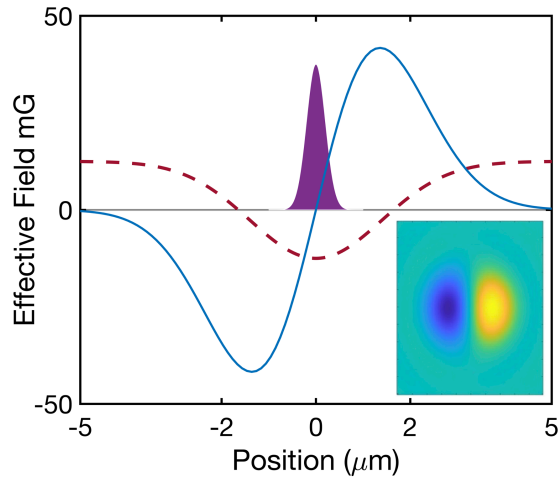


**Figure 6.11:** The blue trace is the radial effective magnetic field gradient along the tweezer light polarization direction at the focal plane calculated for a CaF molecule in a 780 nm tweezer with a beam waist of  $1.4 \mu\text{m}$  and depth of 2 mK. The dashed red curve is the intensity profile of the tweezer in the focal plane. The shaded purple curve is the region a CaF molecule at  $50 \mu\text{K}$  will explore. The inset figure shows the magnitude of the effective magnetic field in the focal plane. The tweezer polarization points along the x-axis in the inset.

ization gradient across the tweezer where left and right-handed circular polarizations appear on either side of the tweezer center. The tighter the focus, the more intense the polarization gradient.

The relative scale of the vector shift is set by the fine structure splitting (30 GHz) over the detuning of the tweezer light from the X-A transition (100 THz detuned). For our tweezer at a depth of  $1800 \mu\text{K}$  the effective magnetic field gradient is  $dB/dx = 25 \text{ mGauss}/\mu\text{m}$ . A sample temperature of  $50 \mu\text{K}$  would allow the molecule to experience variations in the effective magnetic field of  $1500 \mu\text{Gauss}$ . That's at "full" depth, however, at the tweezer depth used for the coherence time measurements, the expected spread in the field will be less than  $100 \mu\text{Gauss}$ . The direction of the effective field in the

tweezer is orthogonal to the direction of the 1.5 Gauss bias field we used to establish the magic condition, thus it adds in quadrature with a strong field, resulting in a  $\delta B \approx (100 \mu\text{Gauss})^2 / (1.5 \text{ Gauss})^2 \approx 10^{-9}$  Gauss level. The effective field from the vector stark shift is many orders of magnitude suppressed from being a major limitation, however, as a caveat to future experimenters, the scale of the gradient increases rapidly with tighter focused tweezers.

The second point is in regards to using the spin-stretched states as the qubit states. These states are the choice of previous coherence time experiments using bialkali molecules lacking the structure we used in this experiment<sup>107,141,115,103,57,122,27,159</sup>. It is possible to “tune” out substantial impacts of the light shift on the stretched state belonging to the N=1 manifold<sup>129</sup>. A strong magnetic field breaking the hyperfine interactions was used in previous work and probably would have also resulted in a long coherence time for us. We opted for the experimentally simple route given that low fields are often easier to stabilize and working with the F=0 transition is convenient for other reasons not limited to optical pumping performance.

## 6.11 FUTURE OUTLOOK

Demonstrating a 100 ms rotational coherence time and 500 ms spin-echo coherence time, more than a factor of 10 improvements over a previous system, is a major step towards leveraging the ultracold molecules in the optical tweezer platform for quantum

computing<sup>109,63</sup>. The figure of merit is how many gate operations can be completed per coherence time. A typical time scale for dipolar gates is a few milliseconds, and possibly as short as a few microseconds using a more clever scheme<sup>28</sup>. This allows several tens of gate operations per coherence time, providing a workable footing for future work on dipolar coupling.

Nothing we did was unique to the CaF molecule-including the selection of qubit states. The same structure we took advantage of will exist in molecules with a single unpaired electron and nuclear spin-1/2. Larger hyperfine spacing will help to reduce the hyper-polarizability but will never eliminate the need to tune the interaction using a magic condition. Many laser-coolable polyatomic molecules under consideration also offer similar hyperfine structures<sup>82,102,161</sup>.

Since this work, the second generation CaF experiment in the Doyle group under the leadership of Yicheng Bao and Scarlett Yu demonstrated dipolar coupling between neighboring CaF molecules<sup>15</sup> (also demonstrated at Princeton<sup>60</sup>). The ultracold polar molecule platform is rapidly maturing into a competitive platform for use in quantum computing.

# 7

## Aromatic Molecules for Laser Cooling

### 7.1 COLLECTING OUR BEARINGS

The CaF experiment demonstrated the utility of the optical tweezer platform for trapping and manipulating ultracold molecules with exquisite levels of control. We optimized an imaging system with better than 97% detection fidelity of a single CaF molecule in a tweezer. We added microwave control to drive rotational transitions and create pure

quantum states. Implementing fine control over the lab environment, combined with quantum state engineering, we reported the first useably long rotational coherence time. This was the first demonstration of a laser-cooled polar molecule for use in a quantum computing architecture.

With the dynamical control from the acoustic-optical deflector, we created an array of 5 molecules, rearranged the optical tweezers, and merged traps to study collisions. When we observed near-universal collisional losses, we designed a microwave shielding scheme to reduce the effect of lossy collisions while enhancing the rate of elastic collisions. Using the enhanced rate of elastic collisions we went on to demonstrate the forced evaporative cooling of CaF.

Where does this leave us?

The evaporative cooling was an important result and realizing a deep cooling method would be a key enabling development for the field as a whole however we cannot continue in that direction due to several serious limitations on our apparatus. The single-molecule coherence time result also shows promise we built a second-generation CaF experiment with quantum computing in mind and implemented design considerations from the lessons learned on the first-generation CaF experiment.

The apparatus was becoming cumbersome after several rounds of retrofitting. Originally the experiment was built to slow CaF and after that result, it quickly developed into a complicated experiment with no fewer than 11 subsystems built by different generations of students. Continuing to add complexity to the apparatus would put us into

the diminishing returns regime. With the second-generation experiment coming online soon, there wasn't a good reason to do a significant retrofit of the first-generation apparatus.

At this point, we decided to make a major direction change and re-fit the experiment to do an initial study of laser cooling on large aromatic molecules. The need for this is apparent: many "interesting" molecules are more complicated than diatomics. Larger molecules potentially offer more rotational, vibrational, and electronic energy level structures which are useful for precision measurement<sup>84,69,83,162</sup> to quantum computing<sup>64</sup>, simulation<sup>2</sup>, and especially quantum chemistry<sup>11</sup>. The catch is the platform is only useful if the added complexity can be controlled and the additional rotational and vibrational structure is not straightforward to control. Polyatomic species have many potential leakage channels, primarily vibrational, which need to be closed for laser cooling. A class of molecules with manageable vibrational branching, potentially requiring only a few repumping lasers, have been identified<sup>81,66,67</sup>, including some molecules with organic structures<sup>9,68,46,47</sup>. Laser cooling has been demonstrated to a limited capacity on polyatomic species including SrOH, YbOH, and CaOCH<sub>3</sub><sup>10,81,66,67</sup>. Much more substantial work has been done on CaOH molecules, which have been laser-cooled, optically trapped, and quantum-controlled using microwaves<sup>101</sup>. Our vision is to have large organic structures trapped in optical tweezers at ultracold temperatures. This is a challenging goal but we will lay the framework and discover some limitations in this chapter.

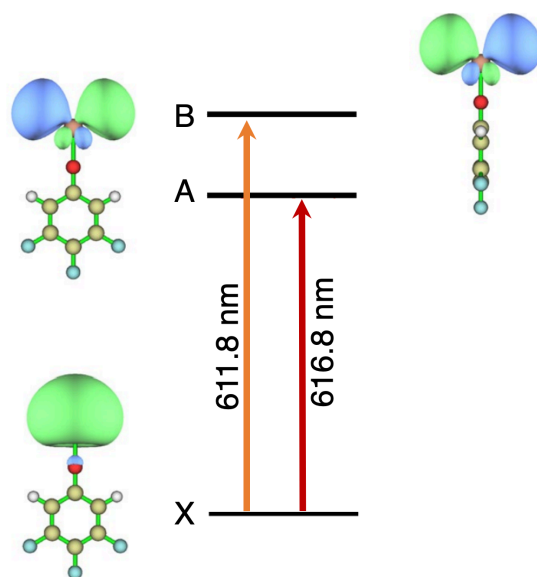


**Figure 7.1:** Schematic drawing of CaOPh-345F<sup>163</sup>. CaOPh molecules look exactly the same up to the three fluorine atoms replaced with three hydrogens. The electronic wave function of the valence electron is visualized for the X state ( $\tilde{X}^2A_1$ ) as well as the A ( $\tilde{A}^2B_2$ ) and B states ( $\tilde{B}^2B_1$ ). The wavelengths indicated in the figure are for CaOPh.

## 7.2 PHENOL DERIVED MOLECULES

The first criterion for laser cooling is “good” vibrational branching<sup>81,66,67</sup>. When the molecule is electronically excited, the vibrational potential is slightly different. As a result, when the molecule emits a photon it could decay to any of the vibrational states in the ground electronic state with a probability given by the wavefunction overlap. There is no rigorously enforced selection rule nor do we know a way to suppress the unwanted decays to numerous vibrationally excited levels in the electronic ground state. The best we can do is pick a molecule with favorable intrinsic branching ratios from the start. Carefully selected molecules can have potential energy surfaces that are similar in the ground and electronically excited states which means after the decay, the molecule will very likely return to the same vibrational level. The ones that don’t, leak to a handful of additional vibrational levels that we can repump with additional laser beams tuned to the repump wavelengths which are typically 10’s of nanometers red-shifted from the mainline. We call these “diagonal” molecules because they tend to not branch vibrationally after spontaneous emission decay events. For each possible vibrational decay, we will need a separate repump laser tuned to the specific frequency that re-excites molecules in the wrong vibrational state back up to the ground vibrational state by way of an electronic transition.

A recent study identified a class of molecules consisting of phenyl rings and a Ca-O optical cycling center bonded to the ring<sup>163</sup>. An optical cycling center is a functional

group, such as Ca-O, attached to the molecule which carries an optically active valence electron that is somewhat well isolated from the chemical bond (sometimes) leading to favorable Frank-Condon factors. This is not a general feature of molecular systems but it is a pattern for the species we use in this line of work. This phenyl structure is chemically interesting as a commonly occurring feature of organic molecules and it is potentially useful in quantum computing and quantum simulation because it has a large internal Hilbert space which makes it a good qudit (a “qubit” with more than two levels). The nuclear spins of the hydrogen atoms are also useful in this regard and this system resembles the molecules already in use for nuclear magnetic resonance quantum computing experiments.<sup>Jones</sup>

Remarkably these phenol-derivative molecules appeared to be diagonal as well as chemically interesting. We elected to focus our efforts on  $\text{CaOC}_5\text{H}_5$  (CaOPh) and CaOPh-345F which are phenol and fluoro-phenol derived molecules, respectively<sup>163</sup>. Figure 7.1 shows a ball and stick schematic of CaOPh-345F, indicating where the fluorine atoms replace hydrogen atoms on the number 3,4, and 5 carbons atoms along the ring. The layout of the atoms is mirror symmetric in the plane containing the phenyl ring. For both CaOPh-345F and CaOPh, the Ca-O optical cycling center is affixed to the number 1 carbon atom in the ring.

### 7.2.1 DISPERSED LASER-INDUCED FLUORESCENCE

A preliminary study done in the Doyle group in collaboration with the groups of Eric Hudson and Wes Cambell used a technique called dispersed laser-induced fluorescence (DLIF) to measure the vibrational branching ratios of different phenol derivatives<sup>163</sup>. This DLIF study involved using a pulsed laser to excite molecules in the ground electronic and vibrational level to the lowest energy excited electronic states (*A* and *B* states). The fluorescence emitted from the decaying molecules was collected and dispersed on a spectrometer grating. Molecules decaying to a vibrationally excited state in the ground electronic level emit fluorescence that is red-shifted relative to the excitation light. From the intensities of the red-shifted decays, one can determine the vibrational branching ratios. While we hope for a “diagonal” molecule, even the best photon-cycling molecules still have vibrational leakage. This measurement indicates the minimum number of vibrational decays which need to be repumped in order to reach a target number of photons. For slowing and generating a molecular MOT, one would need 3,000-10,000 photons. For simpler laser cooling schemes as few as 30-100 photons are sufficient to do transverse cooling of a molecular beam<sup>146</sup>.

The vibrational branching ratio measurements indicated that CaOPh and CaOPh-345F, have estimated Frank-Condon factors of 90% and 99% respectively. These molecules each have at least two strong electronic transitions with 60 ns lifetimes, short enough to have a fast scattering rate. They also have convenient transition wavelengths, around

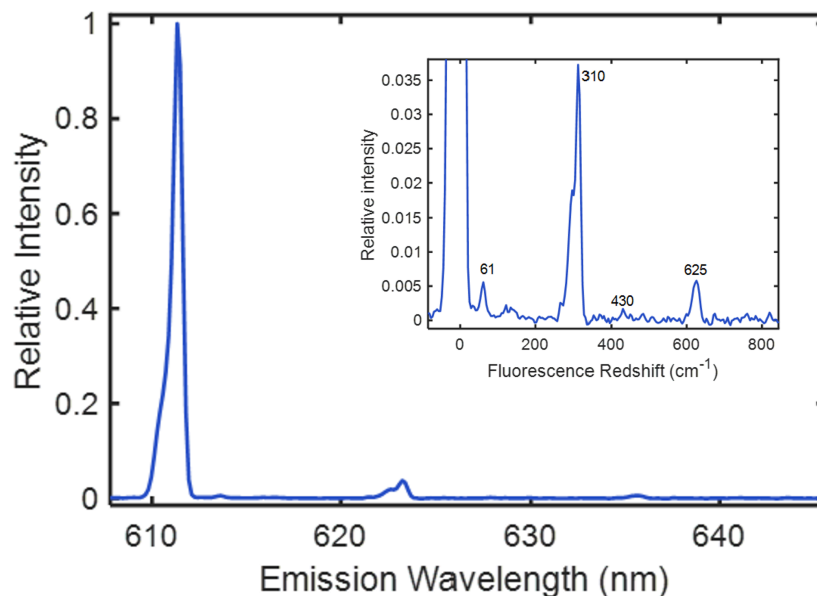


**Figure 7.2:** Dispersed laser-induced fluorescence (DLIF) spectroscopy of the CaOPh vibrational modes. CaOPh molecules are excited by a laser at 611.8 nm on the  $\tilde{B}^2B_1-\tilde{X}^2A_1$  transition in the vibrational ground state of each available mode. The additional peaks seen in the spectrum correspond to red-shifted fluorescence from decay to excited vibrational modes in the ground electronic state. The inset is a zoomed-in version of the same DLIF spectrum, with the y-axis normalized to the height of the diagonal decay from the larger plot. The decays are labeled by the red shift in units of wave numbers. The most prominent decay is to the 310  $\text{cm}^{-1}$  line which we believe is the Ca-O stretch mode. The 61  $\text{cm}^{-1}$  line corresponds to the in-plane and out-of-plane bending modes.

610-630 nm, for dye lasers using Rhodamine-based dyes. This makes both species promising laser cooling candidates.

### 7.3 PRODUCING THE PHENOL DERIVATIVES

We can make these molecules by reacting gas-phase phenol (or fluorinated phenol) with calcium metal vapor in a buffer gas cell. Calcium metal is ablated by a 20 mJ, 10 ns YAG pulse, frequency doubled to 532 nm. The calcium metal vapors react with the gaseous phenol in a background of helium atoms cooled to 4 K by our cryogenic system. The phenol vapor is introduced to the buffer gas cell in vapor form and fed in through a heated fill line that we will discuss in detail shortly. A slow (roughly 200 m/s) cold beam of CaOPh molecules exits the cell and the cryogenic beambox into a room temperature chamber where we conducted spectroscopic studies.

Phenol only has sufficient vapor pressure for temperatures above the melting point of 300 K. The buffer-gas cell needs to run at 4 K to produce a beam. At 4 K there is limited cooling power available, usually, around 1 Watt which means it doesn't require more than a few hundred milliwatts of heat load to raise the cell temperatures by a few degrees Kelvin. A warmer cell results in a faster beam and the higher temperature spreads the population over more rotational levels which reduces the per-quantum-state production yield.

We took an engineering approach to reduce heat loads on the buffer-gas cell which

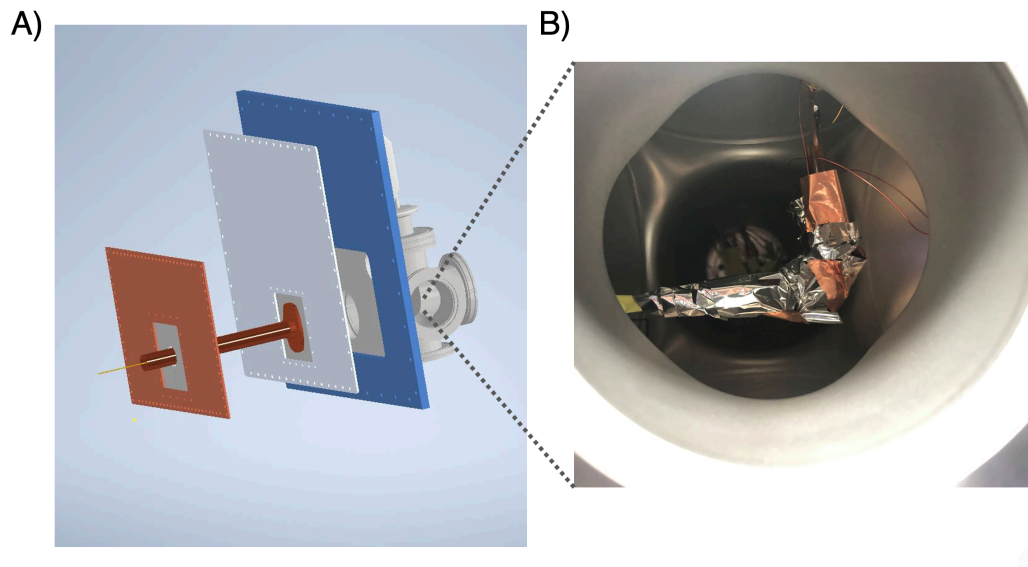


**Figure 7.3:** On the left is a 3D rendering of the fill line assembly as it passes through the vacuum chamber (beambox wall), 70 and 40-kelvin blackbody radiation shields. Note the larger diameter copper tube is only connected to the 70-Kelvin shield. At the back is a 6-way ISO-100 cross. This cross was useful for assembling the fill line but plays no role in daily operations. On the right an oriented image looking at the fill line 90° connection through the side port of the ISO-100 cross as indicated by the dotted lines. The vertical copper tube is where the elasticity needed to maintain the sliding degree of freedom for the fill line originates. The stainless steel elbow has its own separate heater attached, although we found the thermal conductivity along the line was sufficient to not need a separate heater element here. The mylar film wrap helps the fill line hold heat.

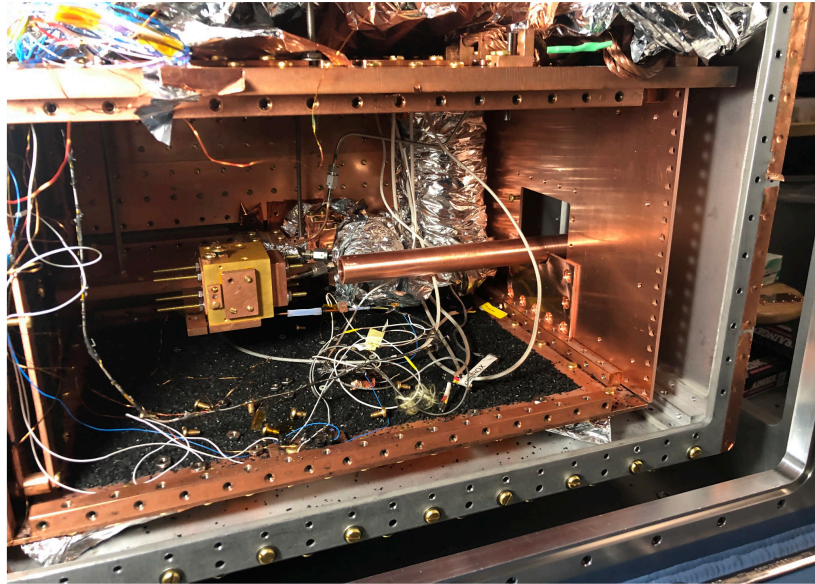


**Figure 7.4:** A full cutaway view with the 4-Kelvin shield side panel completely removed. The top 4-Kelvin panel above the heater fill line collar is also removed. The fill line positioning was set very carefully such that it auto-aligns with the cell. This makes cell changes very easy and thermal shorts due to the fill line tip touching a cold part of the cell are nearly impossible and have never happened in several 10's of cell change events. The liquid helium pot is in the back right corner of the 4-Kelvin box, wrapped in mylar film. Note the distance between the cell aperture and the 4-Kelvin shield aperture. This distance is critical to avoid the build-up of helium gas in the beam's path.

would otherwise degrade the performance of our beam source. The heat loads we are concerned with are 1) the blackbody heat load coming from the heated fill line and 2) the conductive heat load from the seal connecting the heated fill line to the cell itself. These are both engineering problems we worked hard to address.

The Cryomech pulse tubes we use (PT410) have about 1 Watt of cooling power on the 4 K stage and about 40 Watts of cooling power on the 40 Kelvin stage. In addition, our beambox has a liquid helium pot with a 1-liter liquid helium capacity, providing significant cooling power. While the cooling power of the liquid helium is very high,

the limited thermal conduction between the cell and pot will still lead to a rise in temperature when heat loads are added to the cell. Additional heat loads also reduce the run time of the experiment between helium pot refills by increasing the helium evaporation rate in the pot.

To maintain sufficient phenol vapor pressure (2-4 Torrs) and reduce the risk of fill line clogs from condensation points, we operate the fill line well above the 320 K melting point of phenol at 340 K. Since the blackbody heat load scales as  $T^4$ , the fill line operating temperature of 340 K will dump a lot of heat, emitted from the entire surface area of the heated fill line. We designed a copper sleeve to fit concentrically around the fill line. It attaches to the 40 K stage where we have ample cooling power. This protects the 4K components from the majority of the heat load, as shown in figure 7.4.

The fill line itself is a 1/16" copper tube with 300  $\Omega$  resistors glued every 5 cm along its length. The fill line temperature is measured by a Lakeshore diode affixed to the neck of the fill line where it exits the 40 Kelvin sleeve. To keep the gradient under 1 K between the thermistors, we would only need to place a heater every 60 cm but by over placing the heaters we can be sure to mitigate gradients. To maintain a temperature of 340 K measured at the fill line tip, we run about 600 mW of power through the chain of series-wired resistors glued to the fill line.

The heated fill line is supported by two G10 spacers along the length of the copper tube. These spacers are cut to minimize surface contact with the copper and they have cut-out regions to reduce the cross-section leading to lower thermal conductivity. The

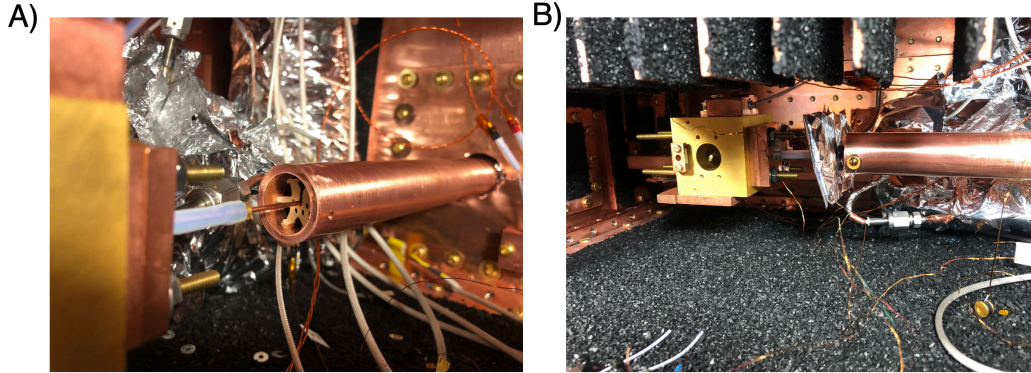


**Figure 7.5:** On the left (A), the G10 spacer holding the heated fill line concentrically inside the 70-Kelvin copper sleeve can be seen. The cross-section and feet of the spacer were designed to minimize thermal conductivity between the cold sleeve and the hot fill line. Note these parts were made from G10 sheets, not rods due to the weave pattern of the fiberglass. The Teflon spacer can be seen attaching the fill line neck to the back of the cell. On the right (B) is a more complete view of the fill line as it looks in use. A mylar blanket has been added around the fill line to block the line of sight from the back of the cell to the room-temperature 6-way ISO-100 cross at the back of the beambox. Without the blanket, there are a few square mm of room-temperature blackbody radiation directly illuminating the cell. Also visible is a lakeshore diode measuring the sleeve temperature right at the tip where it is the warmest.

contact feet of the spacers have an extrusion to prevent them from falling over when the fill line is sliding in the tube. We glued the spacers to the fill line, positioning each spacer about 1-inch inset from the leading and trailing end of the copper sleeve. The spacers conduct about 180 mW of combined heat load onto the copper sleeve whereas the blackbody radiation puts about 400 mW of heat on the sleeve. The connection to the cell is based on a Teflon sleeve coupling the copper nipple brazed to the back of the cell to an ultem ring placed concentrically around the fill line.

The external parts of the heated fill line, outside of the vacuum chamber, are also carefully designed. The vacuum-to-atmosphere interface happens in a 6-way ISO 100 cross-connected to the back of the beambox, shown in figure 7.6. The purpose of the

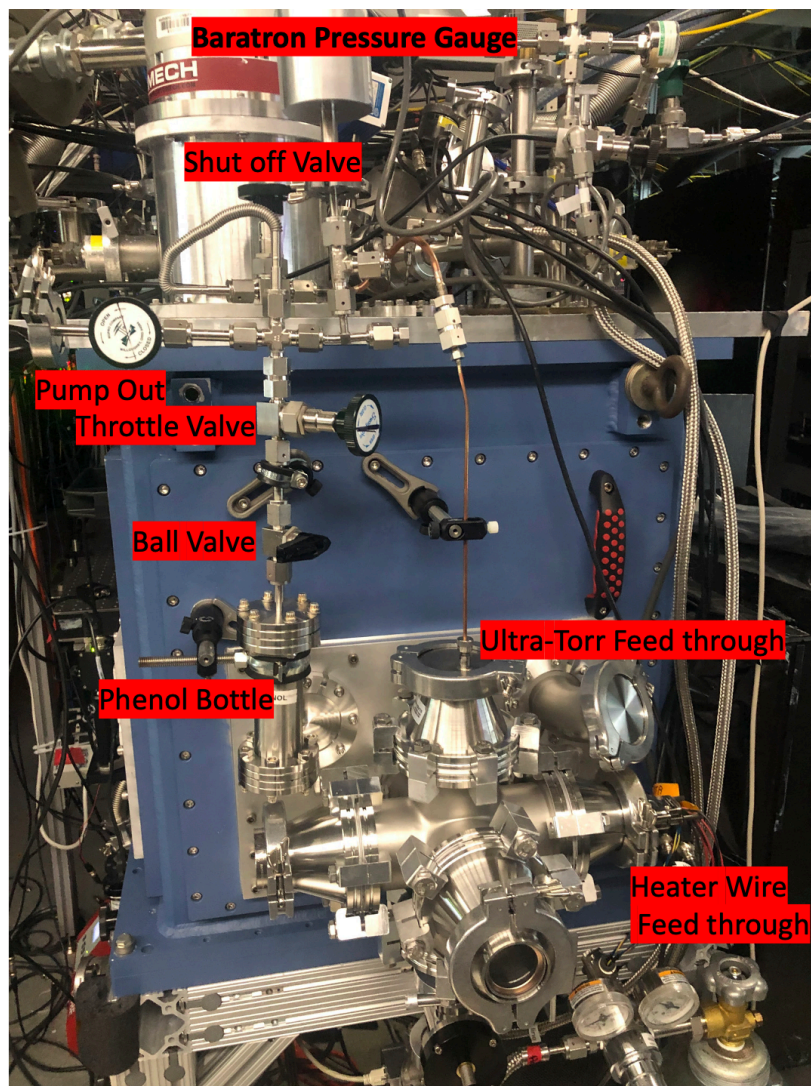


**Figure 7.6:** Atmosphere/room-temperature side of the fill line. Solid phenol is placed inside a CF 2.75" nipple which we heat to around 60° C, melting the phenol and generating vapor pressure. The ball valve is a binary shut-off valve used for replacing the bottle while controlling phenol exposure in the lab. The throttle valve is a stainless steel bellows-sealed valve that creates a variable impedance used to control the flow of phenol into the cell. We set this valve to a particular position based on the pressure reading from the baratron and the flow rate remains very stable. A separate pump-out port was added for utilities including leak checking the fill line. This is highly recommended. The fill line goes into the vacuum chamber via an Ultra-Torr gasket-sealed connector. The connector bezel is brazed directly into a KF-50 flange and the copper tube passes through a concentric O-ring. The only other functional arm of the ISO-100 is on the right where the feed-throughs for the fill line heaters pass through as well as a few additional lakeshore temperature diodes used to monitor parts of the fill line, including the stainless steel 90° elbow inside the ISO-100 6-way cross.

cross is to allow access to the 90° VCR-style connector between the vertical part of the fill line and the delivery line, going into the cell. This 90° VCR connector has its own independent heater circuit on it and we provide about 300 mW of heat to the elbow. See figure 7.3. Critically, the fill line has some elasticity which provides light, finger-push-scale, backing pressure forcing the tip into the cell. As the beambox thermocycles from room temperature to operating temperature everything contracts resulting in millimeter-scale displacements. The elasticity of the fill line is the mechanical buffer that absorbs the displacement due to thermal contraction.

Since the melting point of phenol is above room temperature the external parts of the fill line also need to be heated. This is accomplished by wrapping everything in heater tape and aluminum foil. We attached thermocouples every few centimeters to monitor for cold spots where phenol could condense and clog the line. The outside part of the fill line (see figure 7.6) consists of a CF 2.75" nipple filled with phenol, a baratron pressure gauge, and a throttle valve used to control the backing pressure (and flow rate) of the fill line. Typically we use flow controllers for this application however we did not have a high-temperature flow controller. Heating the phenol bottle to 55° C generates 4 Torr of vapor pressure behind the fill line. Based on measurements of the fill line's conductance, this corresponds to  $3 \times 10^{-4}$  Torr L/s or 0.02 standard cubic centimeters per minute. The flow of the phenol into the cell warms the cell by 30 mK.

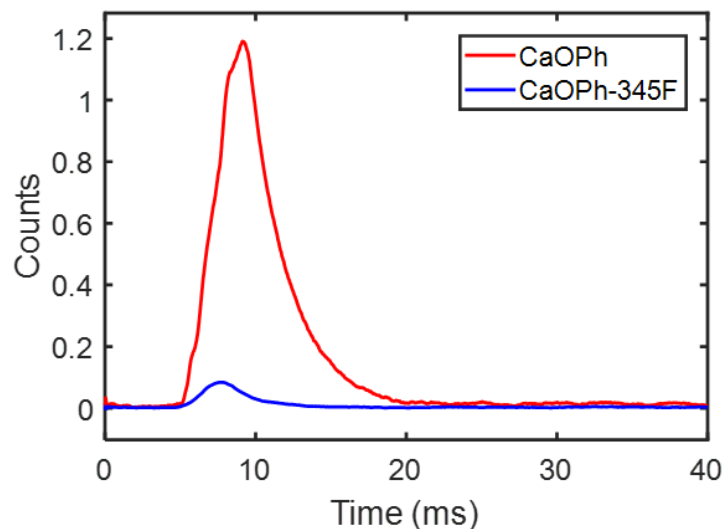


**Figure 7.7:** Time trace of a CaOPh beam vs. a CaOPh-345F fluorinated phenol beam. The beams were observed on a photon-multiplier tube and were driven by a laser illuminating strong transitions in both cases. The brightness of the beams provides an order unity production comparison between species. Evidently, the non-fluorinated phenol has a chemical reaction pathway more favorable for producing the molecule of choice.

### 7.3.1 PRODUCTION

Due to the optimistically large Frank-Condon factors of 99%, we opted to make the fluorinated CaOPh-345F molecule first. The production yield was low, less than 10% of the yield for non-fluorinated phenol. We compared the production of each species by observing the molecular beams seen as a time trace on a photomultiplier tube. While we did not yet know the quantum number assignments but the brightness of the lines in figure 7.7 allows an ordered unity direct comparison between the CaOPh and CaOPh-345F production yields. We make roughly an order of magnitude more CaOPh than CaOPh-345F.

We added “enhancement” light into the buffer gas cell in a similar spirit to some of the other laser cooling experiments. Chemical production in the buffer gas cell can be enhanced by exciting the calcium atoms to the metastable triplet P state ( $^3P_1$ ) where the chemical reaction pathway to form molecules such as CaOPh, CaOH, and YbOH is energetically open. The laser excitation significantly enhances the  $^3P_1$  population over the natural population excited from the ablation pulse. To excite the calcium atoms, we illuminate the cell with 300 mW of 657 nm light through the in-cell absorption window on the cell. The enhancement light is shuttered to reduce heat loads on the cell at all times other than a 3-millisecond window around when the ablation pulse is fired. For both the fluorinated and non-fluorinated phenol samples, we observed an enhancement factor of approximately 4, compared to an order of magnitude increase observed by YbOH and CaOH.

While the production of CaOPh greatly outmatched CaOPH-345F, there was another factor leading to our choice to pursue the non-fluorinated CaOPh. The DLIF predicted Frank-Condon factors for the CaOPH-345F are potentially skewed by a CaF background line falling right on the diagonal transition which would bias the Frank-Condon factor in the optimistic direction. Between the low production yield and the newly cast doubt on the Frank-Condon factors, we elected to stick with CaOPh for the remainder of the study.

CaOPh presented some peculiar production issues. We found no matter what we did the signal would start to fall off significantly after 24 hours of runtime while actively

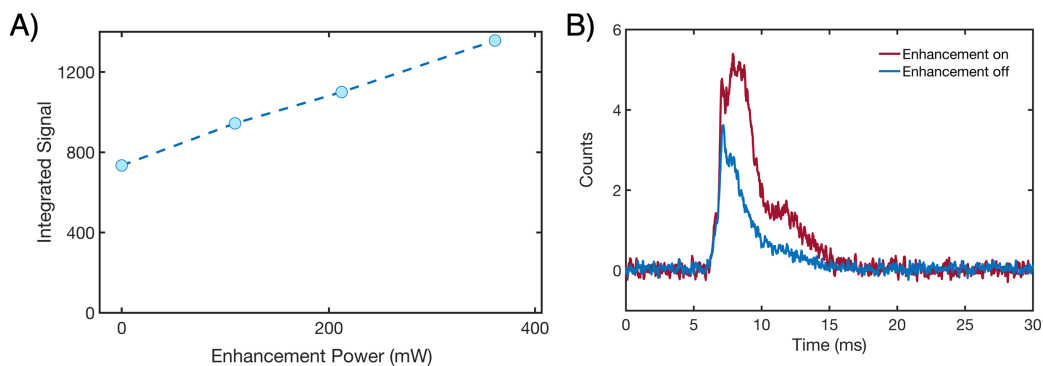


**Figure 7.8:** Exciting the calcium atoms to the metastable triplet P state in the buffer gas cell enhances the production of CaOPh. We optimized the alignment of the enhancement light through the in-cell window and then performed a power saturation scan. The window itself was covered in a layer of Kapton, however, the power on the horizontal axis takes into account the transmission of the light through the Kapton. On the right is a comparison of the molecular beams with and without the enhancement light. We typically observe production enhancement by a factor of 2-4.

ablating. This was the case for both the 1" and 2" long buffer gas cells we tried. In both cells, we often observed build-ups of phenol in the cell (see figure 7.9) and sometimes clinging to the tip of the fill line. This is the first time we have flowed a chemical that is solid at room temperature. It is possible that the buildups we observe are normal in other experiments but never observed because the flow chemicals vaporize during warmup whereas phenol remains solid. On the contrary, no experiment has such a limited run time. The flow rates in our experiment are similar to others in the group. When the source production drops after a few days of running, CaOPh production cannot be restored by warming up alone; a full cell cleaning was required. The 2" long cell was gold coated which appeared to make a substantial difference in the cell cleaning process in between runs. The copper cell showed surface oxidation requiring

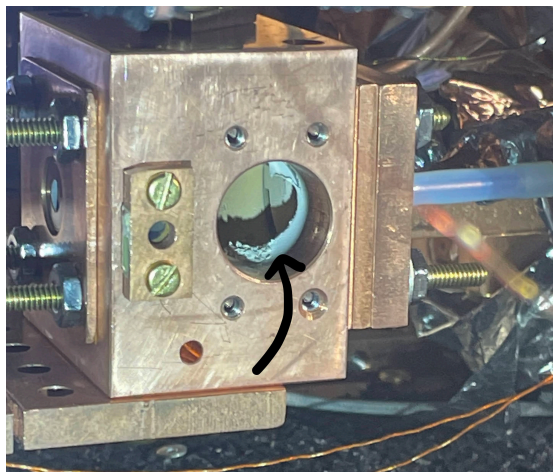


**Figure 7.9:** Deposits of phenol (indicated by the arrow) observed after 3 days of run time on the cell. The picture was taken through the calcium target mounting hole. Large build-ups like this were often seen but didn't correlate with fill line clogs. The rest of the cell had a nearly uniform coating of phenol over the surface. While the fill line does enter the cell near the target holder, it is not aimed directly at the calcium.

light sanding to restore the surface quality whereas the gold-coated cell could be cleaned with a tissue soaked in acetone.

We also found the calcium targets were not reusable, as they would become encased in a thick coating of phenol that was difficult to remove from the surface of the calcium. Even with the aforementioned production difficulties, we were able to run for 4 days per week, warming up on Thursday night for a Friday morning cell cleaning. This issue will require attention for future work on CaOPh.

#### 7.4 STRUCTURE OF ASYMMETRIC TOP MOLECULES

Now that we can produce CaOPh in our apparatus, we'll move on to describing the structure of asymmetric tops in general and then high-resolution spectroscopy of CaOPh.

An asymmetric top molecule is a molecule with three distinct moments of inertia<sup>9</sup>. Most molecules with more than two atoms are asymmetric tops. Generally, when we describe the rotational structure of a molecule, we refer to the angular momentum around the principal axes of rotation. For a general asymmetric top, the axes are labeled *A*, *B*, and *C* where *A* has the lowest moment of inertia (highest rotational frequency) and the *C* axis has the largest moment of inertia. In CaOPh, the rotational constants are  $A = 5.73$  GHz,  $B = 717$  MHz, and  $C = 638$  MHz. *B* and *C* are nearly the same, which indicates this asymmetric top molecule will only have a small asymmetry doubling due to rotations around the *B* and *C* axes being nearly degenerate. We specify the rotational state of the molecule with the quantum number  $J = N + S$  which includes the electron spin, the total rotational quantum number *N*, and the projections of the rotational angular momentum around the *A* and *C* axes with the quantum numbers  $K_a$  and  $K_c$ , respectively<sup>9</sup>.

These principal axes of rotation are the axes around which we define the angular momentum during an electronic transition. As such the selection rules for  $K_a$  and  $K_c$  depend on which axis the electronic dipole moment of the transition is oriented.

#### 7.4.1 SELECTION RULES

The A ( $\tilde{A}^2B_2$ ) and B ( $\tilde{B}^2B_1$ ) states of CaOPh have an electronic wave function reminiscent of an oriented P-orbital. The electron doesn't have orbital angular momentum around the A-axis because the carbon ring breaks the rotational symmetry. This in effect, freezes the p-orbital lobes.<sup>92</sup> The  $\tilde{A}^2B_2$  state has electron density lobes oriented in the

plane containing the carbon ring and the  $\tilde{B}^2B_1$  state is perpendicular to the plane and at slightly higher energy due to repulsion between the electron cloud and the nearby hydrogens. The orientations of the electronic wavefunctions in the  $\tilde{A}^2B_2$  and  $\tilde{B}^2B_1$  states also orient the electronic transition dipole moment for each transition. The  $\tilde{A}^2B_2$ - $\tilde{X}^2A_1$  transition drives rotations around the A-axis (A-type) which implies the selection rules are  $\Delta K_c = -1$  and  $\Delta K_a = \pm 0$  and the selection rules for the total angular momentum  $J$  are the usual dipole selection rules  $\Delta J = 0, \pm 1$ . The  $\tilde{B}^2B_1$ - $\tilde{X}^2A_1$  transition is C-type and the selection rules are  $\Delta K_c = 0$  and  $\Delta K_a = -1$ .

These selection rules can be violated in important ways that matter for laser cooling. Since the  $\tilde{A}^2B_2$  and  $\tilde{B}^2B_1$  states have different symmetry and different selection rules, any mixing between electronic states can make nominally forbidden decays such as  $\Delta N = 2$  and either  $K_a$  or  $K_c$  changing in a way consistent with a transition of a different symmetry become weakly allowed. This rotational leakage channel, if present, needs to be plugged.

## 7.5 HIGH RESOLUTION SPECTROSCOPY

The DLIF spectroscopy informs which molecules might be good laser cooling candidates based on vibrational branching, but it doesn't shed light on the rotational structure of the molecule. For this study, we will need to do high-resolution laser spectroscopy with narrow-band continuous wave laser light due to the small rotational constants

of a molecule with a large moment of inertia. CaOPh is expected to have a dense rotational spectrum compared to the smaller molecules we have observed in this group. Furthermore, many rotational levels in the electronic ground state will be populated at our source temperature of 4 K. We had a rough idea of where to begin our search from the DLIF data, and the larger number of thermally populated rotational states made it easier to find the initial signal.

The fluorescence from the molecules is detected on a photo-multiplier tube positioned perpendicular relative to the molecular beam. The photomultiplier tube provides time-resolved traces of the molecular beam as it moves through the illuminating laser beam. The typical fluorescence yield is 1-2 photons per molecule on all non-rotationally closed transitions due to branching to different rotational ground states. There is exactly one rotationally closed transition that does not branch which we will use for laser cooling. Furthermore, the natural population is distributed over many rotational states.

In light of that, we went to great effort to blacken the inside of our detection region as much as possible to reduce laser scatter. Since the excitation and emission wavelength are the same, we cannot selectively filter out laser scatter with an interference filter. The inside of the detection region has blackened baffles to absorb light. In the direction of the excitation laser beam, we use long blackened extension arms with anti-reflection coated windows on the top and bottom. Furthermore, we optimized the size of the laser beam to maximize the signal-to-noise ratio. Smaller laser beams scatter less but illuminate a small number of molecules over a centimeter-scale molecular beam. We

optimized the signal-to-noise ratio by adjusting the laser beam diameter. To capture more signal, directly across from the photomultiplier tube we installed a spherical mirror to provide a larger capture solid angle.

## 7.6 LASER INDUCED-FLOURESCENCE

Simply put, our goal is only to find the rotationally closed transition that is predicted to cycle photons. The  $\tilde{B}^2B_1$ - $\tilde{X}^2A_1$  transitions have C-type selection rules, meaning that  $\Delta K_a = -1$  thus the transition  $|\tilde{X}^2A_1, N = 1, K_a = 1, K_c = 0\rangle$  to  $|\tilde{B}^2B_1, N = 0, K_a = 0, K_c = 0\rangle$  is the rotationally closed photon cycling line. The excited state  $|\tilde{B}^2B_1, N = 0, K_a = 0, K_c = 0\rangle$  is the only rotational level in the  $\tilde{B}^2B_1$  state for which the spontaneous emission decay process will populate only one ground state,  $|\tilde{X}^2A_1, N = 1, K_a = 1, K_c = 0\rangle$ . On the  $\tilde{A}^2B_2$ - $\tilde{X}^2A_1$  transition, the same phenomena occur but with an A-type transition selection rule,  $\Delta K_c = -1$  implying that we need to use the  $|\tilde{X}^2A_1, N = 1, K_a = 0, K_c = 1\rangle$  to  $|\tilde{X}^2A_1, N = 0, K_a = 0, K_c = 0\rangle$  transition for rotationally closed photon cycling. To correctly identify either of these transitions, we need to know the quantum numbers and that requires assigning all of the transitions we observe with quantum numbers.

We resolved the rotational structure of the CaOPh molecules on the  $\tilde{A}^2B_2$ - $\tilde{X}^2A_1$  with a continuous-wave dye laser and the  $\tilde{B}^2B_1$ - $\tilde{X}^2A_1$  transitions using light from an optical parametric oscillator at 616.8 nm and 611.8 nm, respectively. The dense spectrum had lines appearing roughly every 100-300 MHz over a total range of about 90 GHz.

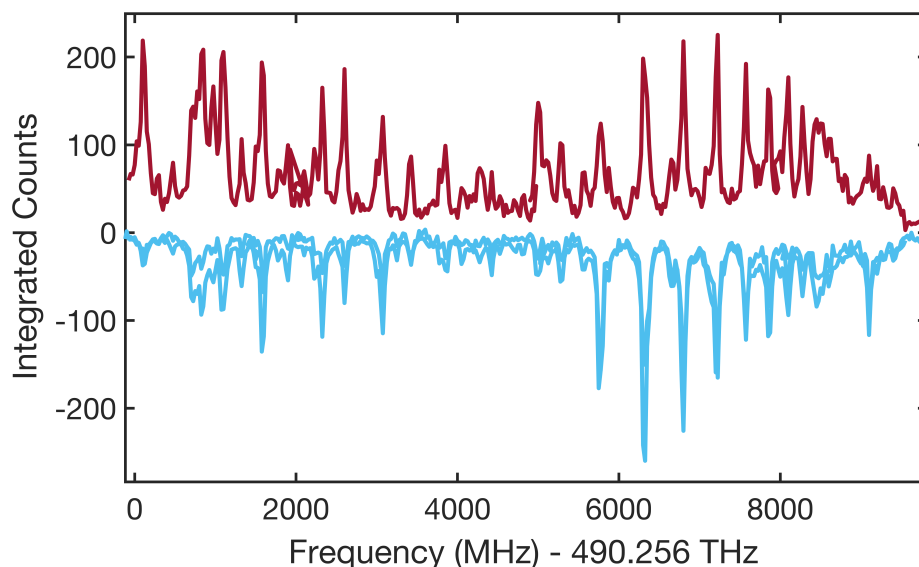


**Figure 7.10:** The  $A$ ,  $B$ , and  $C$  rotational constants in CaOPh have values in temperature units of roughly 300 mK for the  $A$ -axis and 40 mK for the  $B$  and  $C$  axes, indicating the rotational ground state populations will be temperature sensitive. We can vary the temperature of the buffer gas source by pumping on the helium pot which cools the cell from a base temperature of 4 K to 2 K. We looked at a region of the spectrum at 4-Kelvin (red trace) and again at 2.5 K (inverted blue trace), observing several lines changing relative intensities or disappearing altogether. The temperature dependence provides a clue about the rotational ground state in the transition and whether or not it is a high energy rotational state (will be depleted at a lower temperature) or a low laying rotational level (gains population at a lower temperature). Ultimately, we found better ways to assign the spectrum but the temperature dependence is a useful sanity check.

Finding the first transitions proved to be easy and we observed around 500 lines before attempting to fit the spectrum.

### 7.6.1 LINE ASSIGNMENTS

Our general strategy was to try to identify any kind of recognizable structure in the spectrum and make a preliminary line assignment based on that from which we can then

fit molecular constants and thus assign the rest of the lines. We managed to identify a pattern of asymmetry splittings. An approximate formula for the asymmetry splitting as a function of  $K_a$  can be written down for near prolate-asymmetric top molecules such as CaOPh, following this reference<sup>147</sup>. Using our estimates for the three rotational constants, we computed the curves in 7.11 which match the data well for the case of the  $K_a = 2$  to  $K_a = 3$  transition family.

The asymmetry splitting alone doesn't indicate if the transition corresponds to  $K_a = 2$  in the excited or ground electronic state. We associated the  $K_a = 2$  levels with the ground electronic state due to the measured transition frequencies. Using that we made educated guesses for the fit parameters in the PGopher model<sup>148</sup> to compute the spectrum. We assigned around 10 lines based on what we thought was the  $K=2$  family of lines. PGopher then fits 11 molecular structure parameters and 1 external parameter, the sample temperature. From the fit, we extrapolate the quantum numbers for all of the 500 lines we observed. We need a way to test the extrapolated line assignments, which we can do by identifying sets of coupled lines, which requires finding transitions that share either an excited or ground state.

We performed an optical-optical double resonance measurement to figure out which lines were connected via a common ground or excited state. A laser upstream was tuned to resonance with a particular transition. A second laser downstream was used to detect the result of the optical pumping provided by the first laser. Initially, we set both pump and probe lasers to the same transition and observed depletion of the

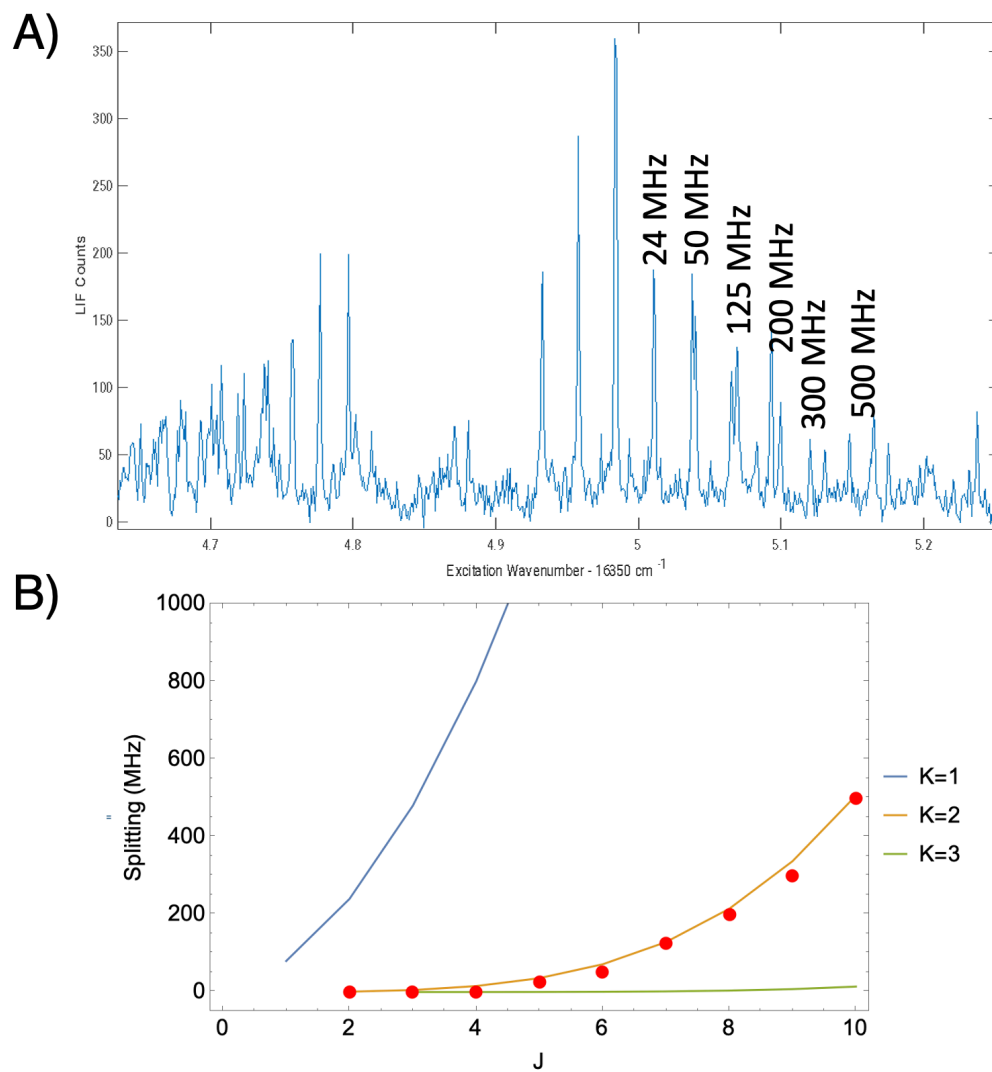


**Figure 7.11:** We identified a recognizable pattern of line doublings that we attributed to the asymmetry splitting of the electronic ground state  $K_a = 2$  to excited state  $K_a = 3$  transitions. Figure A shows the pattern of asymmetry splittings in the fluorescence spectrum as we observed them. Figure B shows the model for different  $K_a$  combinations. The only parameters we put into the model were the approximate values of the  $A$ ,  $B$ , and  $C$  rotational constants.

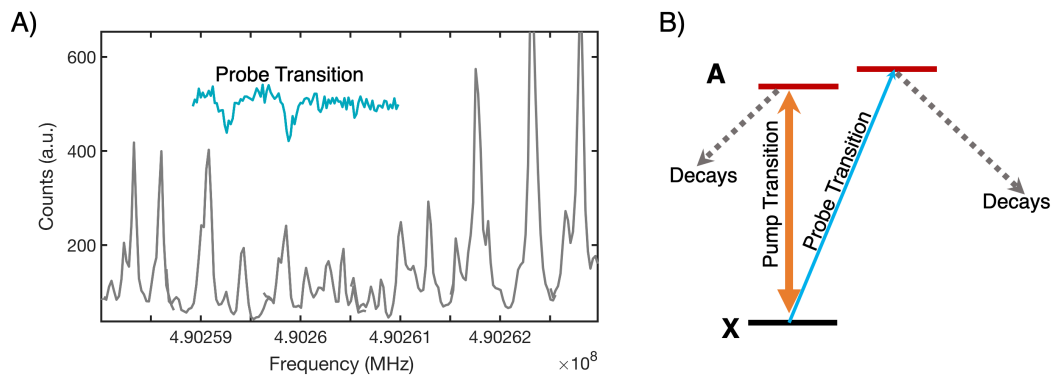


**Figure 7.12:** On the left (A) in grey is a part of the fluorescence spectrum of CaOPh. In teal is an optical double resonance spectrum where the pump laser is parked on a particular transition (not shown in this spectrum) and the probe laser (teal trace) is scanned. Dips in the signal indicate the pump and probe transitions share a ground state. (B) The pump transition laser excites the population and pumps it out of the ground state, resulting in the suppression of the probe signal when the two transitions share a ground state.

ground state population. The pump laser excites the population which scatters photons until it decays to a different ground state at which point it is dark to the laser. The downstream probe laser sees a sharp decrease in signal when the upstream laser is depleting the population in the ground state. We use this pump-probe setup with both lasers tuned to the same frequency to optimize the pumping region laser for maximum depletion. This guarantees sufficiently long interaction regions and high enough power to scatter several photons pumping out the ground state population. We found depletion was typically 60–90% complete, depending on the laser beam size. Maximum depletion was observed when the pump beam was large (1 cm) and the probe beam located 30 cm downstream was small (1-3 mm).

Next, we tune the downstream probe laser to a transition we suspect is connected

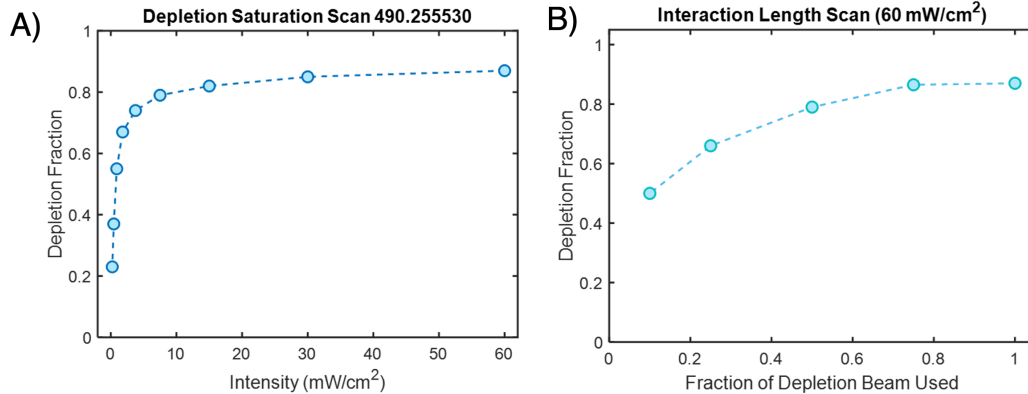


**Figure 7.13:** Characterization of the depletion of the photon cycling transition using a 1 cm diameter beam with a peak intensity of  $60 \text{ mW/cm}^2$ . The power saturation on the left showed we have significant overhead. The plot on the right shows the clipping of the pump beam to measure how much interaction length is needed for full depletion. These two measurements indicate significant power saturation but barely enough interaction length over a 1 cm beam.

to the transition driven in the pumping region. If the two transitions share the same ground state, then the probe laser will observe a drop in signal as a result of the shared ground state becoming depleted. If the two transitions share the same excited state but come from different ground states, then an increase in signal on the probe is expected because the pump beam will excite the population to the shared excited state from which it can decay to the other connected ground state on the probe transition. Figure 7.12 shows the results of the double resonance measurements.

This technique doesn't tell us the quantum numbers of the transitions directly, however, it guarantees that the states involved in coupled transitions differ by two quanta of angular momentum at most since they are coupled by two photons. Using this to piece together the spectrum, we can hop from one rotational manifold to another in a rational way that both informs and tests the quantum number assignments. Once

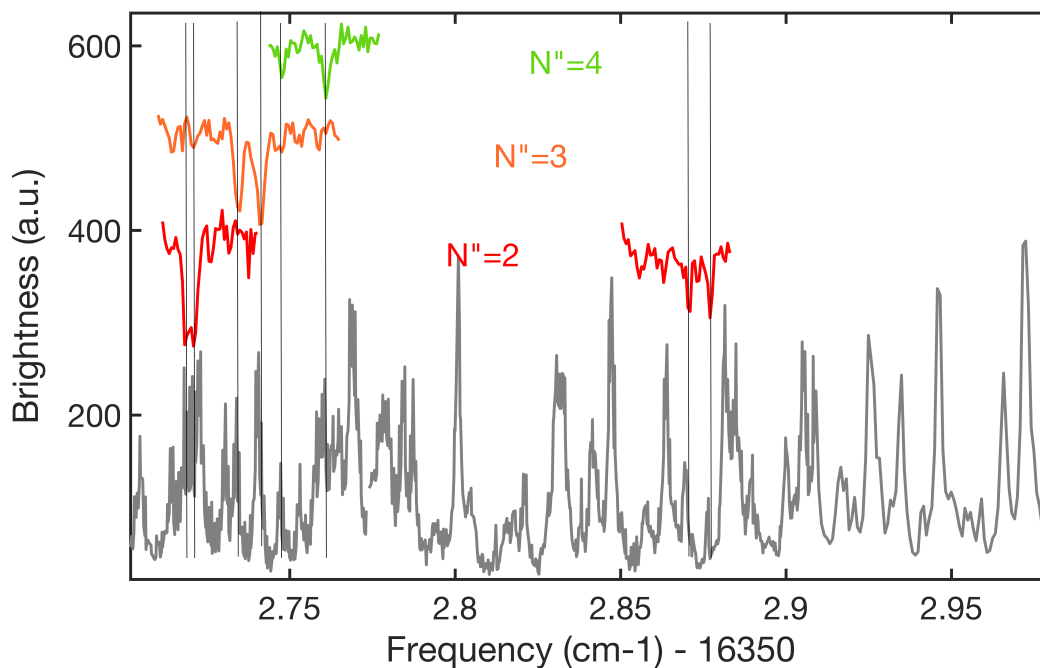


**Figure 7.14:** Representative double resonance scans for a variety of lines. This was done to verify the quantum number assignments to the spectral lines by confirming that selected transitions share either a ground or excited state. Optical double resonance does not guarantee the quantum number assignment is correct but it guarantees the angular momentum of the states involved in coupled transitions cannot differ by more than two quanta since they are coupled by at most two photons. We never observed disagreement between the predicted coupled lines and observed coupled lines, instilling confidence in the fit.

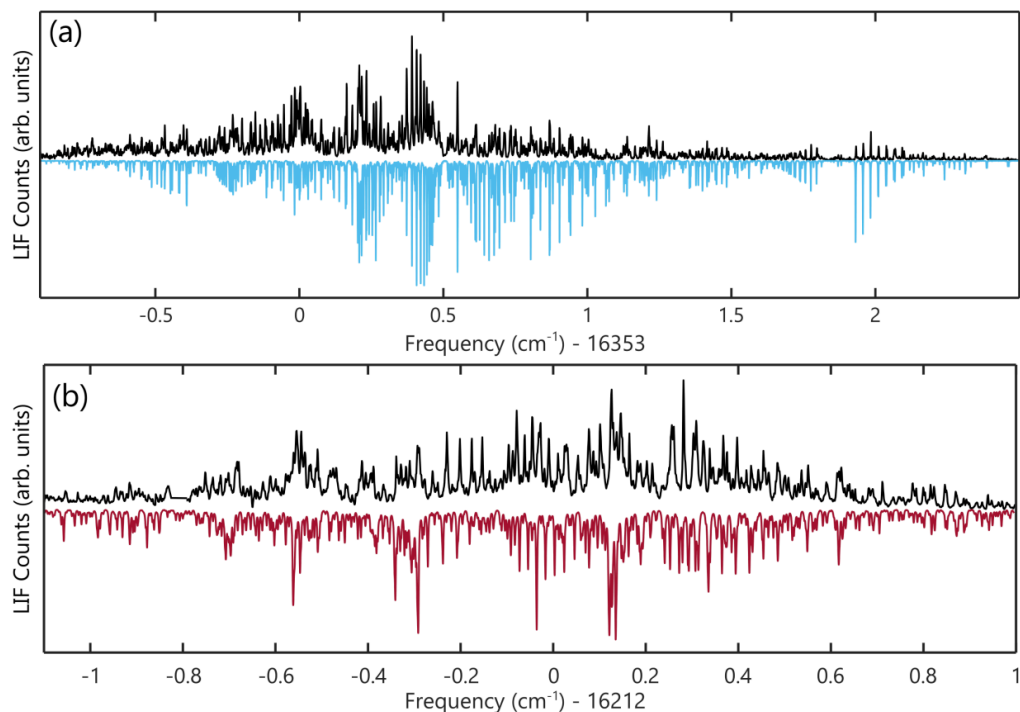


**Figure 7.15:** High-resolution rotationally resolved fluorescence spectrum of CaOPh. The top plot shows the  $\tilde{B}^2B_1-\tilde{X}^2A_1$  transition with the data in black and the PgoPher fit in blue underneath. In the lower box is the data for the  $\tilde{A}^2B_2-\tilde{X}^2A_1$  transition with the experimental data in black and the fit in red.

we had fit the spectrum, we tested many predicted double resonance features including some high  $N$  states and never once observed the wrong behavior. Repeated agreement instilled confidence in the quantum number assignments.

The observed line intensities are sensitive to temperature. The simulated spectrum best resembles the data when the simulated rotational temperature is set to 1.8 K, which indicates there is some adiabatic expansion cooling from 4.5 K to 1.8 K as the beam exits the cell and expands into the vacuum.

### 7.6.2 SPIN-ROTATION STRUCTURE OF CAOPH

Additional structure in the rotational spectrum was observed due to the spin-rotation effect. Coupling between the spin of the electron and the rotation of the molecule leads to a doubling of the rotational lines which scales linearly with  $N$ . We don't have an accurate prediction of the ground electronic state spin-rotational constant for CaOPh because the state spin-rotation splitting was not observed. This implies the spin-rotation splitting is smaller than the 10 MHz natural linewidth of the electronic transition. However, the spin-rotation structure in the excited states is much larger than in the ground state and we readily observe this splitting. The lack of resolved ground state spin-rotation splitting is new territory for a photon-cycling molecular system. In every other case, laser-cooled molecules require spin-rotation sidebands to couple both spin-rotation components. A small, unresolved, spin-rotation splitting could lead to a long-lived dark state that precesses slowly back to a bright state, limiting the scattering rate significantly.

### 7.7 INITIAL ATTEMPTS TO PHOTON CYCLE

The goal of fitting the CaOPh rotational spectrum was to identify the rotationally closed photon cycling transition ( $|\tilde{X}^2A_1, N=1, K_a=1, K_c=0\rangle$  to  $|\tilde{B}^2B_1, N=0, K_a=0, K_c=0\rangle$ ), which we found near 490.255 THz. To confirm the quantum number assignment and to rule out any possible rotational leakage channels, we did careful pump/probe

Parameter	$\tilde{X}^2A_1$	$\tilde{A}^2B_2$	$\tilde{B}^2B_1$
$T_0$		16211.8763(4)	16353.3787(2)
$A$	0.19153(4)	0.19099(14)	0.19197(6)
$(B + C)/2$	0.02261(1)	0.022739(9)	0.022751(10)
$B - C$	0.00263(1)	0.00274(2)	0.00270(2)
$\Delta_K \times 10^5$		5.1(7)	4.5(2)
$\Delta_{JK} \times 10^8$		1.1(9)	0.19(4)
$\Delta_J \times 10^7$		-1.9(6)	-1.2(4)
$\epsilon_{aa}$		0.3791(6)	-0.3833(2)
$\epsilon_{bb}$		0.0102(2)	0.0097(1)
$\epsilon_{cc}$		0.0074(2)	0.00698(9)
$\Delta_K^S \times 10^4$		2(1.5)	-0.06(2)

**Figure 7.16:** Hamiltonian fit constants from the Pgopher simulation, reproduced from reference<sup>8</sup>. All fit values are in units of wavenumbers ( $\text{cm}^{-1}$ ).

double resonance spectroscopy on the suspected photon cycling transition, leading to no detectable leakage to any other rotational levels, including the  $N=2$  levels.

We also checked the depletion of the suspected photon cycling transition by tuning the pump and probe lasers to the same frequency. We increased the power of the pump laser and the beam size to provide more interaction length, observing the depletion change from 50% to nearly 85%, indicating that most molecules had scattered a sufficient number of photons to fall into what we hope is the  $V = 1$  Ca-O stretch vibrational level ( $|\tilde{X}^2A_1, V = 1, N = 1, K_a = 1, K_c = 0\rangle$ ), which we are not repumping yet. Optimizing the depletion of the beam verifies that we are not limited by interaction length or power.

Satisfied that repeated photon scattering was occurring, we looked for an increase in fluorescence detected by the photomultiplier tube in the pump region. Based on the Frank-Condon factors, we expected to see up to 20 photons, yielding a nearly 20-fold increase in fluorescence over all other rotational transitions we had observed. This was

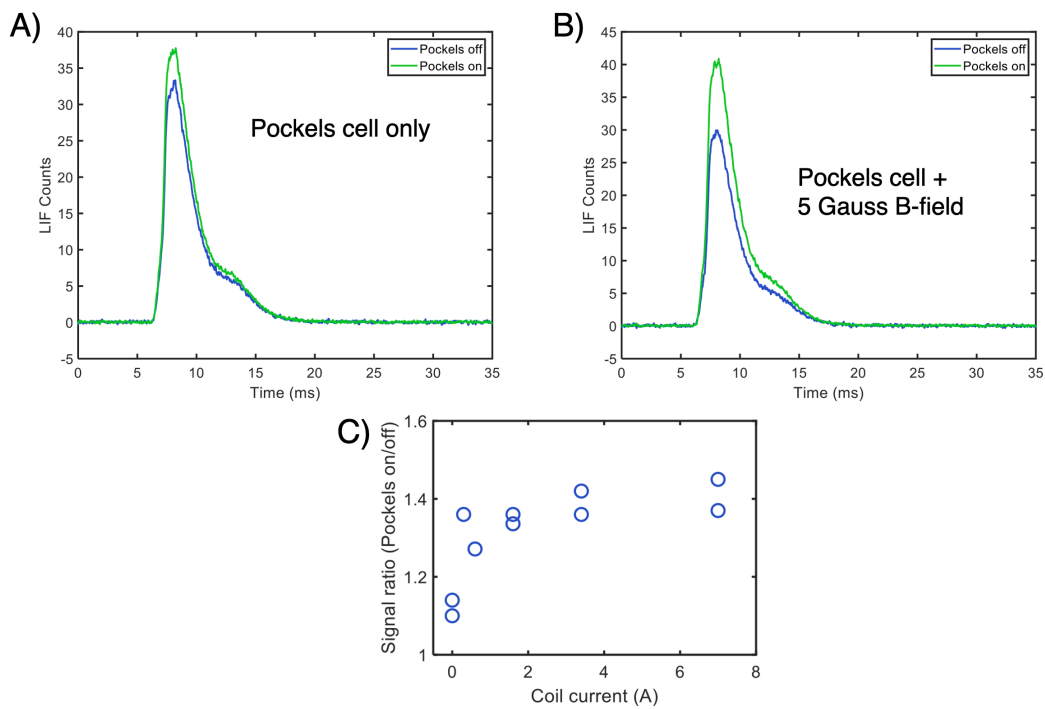


**Figure 7.17:** We attempted to cycle photons on the  $\tilde{A}^2B_2-\tilde{X}^2A_1$  transition by using a Pockels cell and a remixing magnetic field to destabilize any potential dark states limiting the scattering rate. We detected the molecular beam on a photo-multiplier tube, looking for an increase in fluorescence, but observing 10's-of-percent-level increases in fluorescence. For reference, other strong transitions that are not expected to photon-cycle show similar levels of fluorescence. The calibration on the x-axis in figure c is 8 amps  $\rightarrow$  15 Gauss.

not seen. We suspected the existence of long-lived states, dark to the laser polarization, which can slow down the effective scattering rate. A photon cannot be scattered while the molecules are in a dark state and thus for long-lived dark states, the scattering is limited by the rate at which the dark states mix with bright states to once again allow photon scattering. We added a Pockels cell to rapidly switch the excitation light polarization to destabilize any dark states that are not coupled to the polarization of the laser light. After scanning the switching frequency over a broad range from 100 kHz to 2 MHz, we observed a small increase in fluorescence. A remixing magnetic field at  $45^\circ$  was added, resulting in no increase in fluorescence. At this point it was unclear what the limitation was, so we opted for a more revealing diagnostic.

## 7.8 FLOURENCE IMAGING

We implemented a different technique to measure the photon scattering rate directly by imaging the decay of the molecular fluorescence on an EMCCD camera. The imaging system is set to look perpendicular to the molecule beam while a spatially uniform laser beam illuminates the molecules in the direction perpendicular to both the molecular beam and the imaging axis. The uniform excitation beam was generated using two cylindrical lenses in a telescope configuration to create a beam roughly 3 cm long with a Gaussian profile in the transverse direction and a roughly uniform intensity profile in the longitudinal direction, along which the molecular beam will propagate.

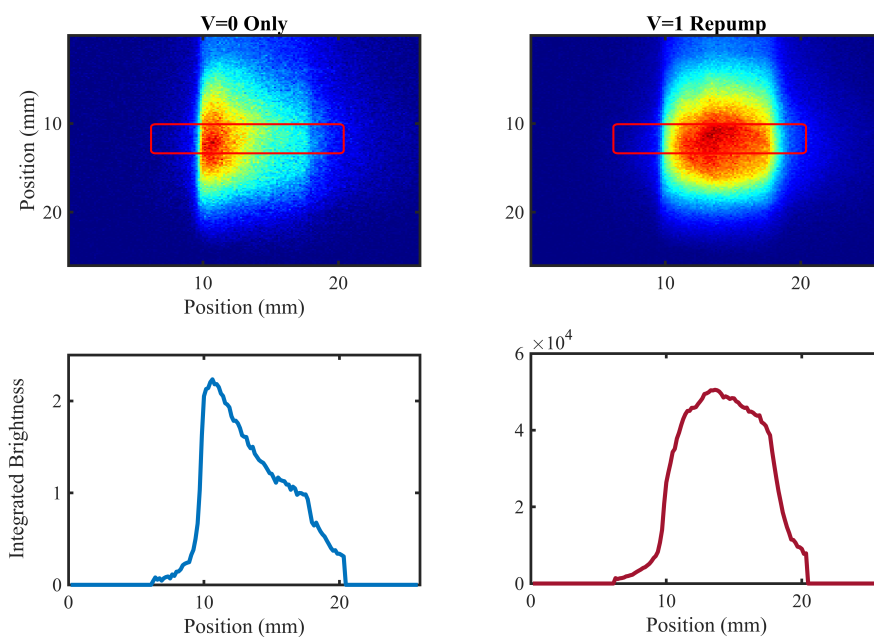


**Figure 7.18:** Fluorescence streak imaging of a CaOH beam illuminated by a uniform laser beam propagating downward in the image frame. The CaOH molecular beam moves from the left to the right with a sharp scattering onset created by masking the excitation laser beam with a razor blade. We expect 20 photons at approximately 1 MHz scattering rate with both spin-rotation side bands on the main line light. We measured a scattering rate of 880 kHz by fitting the vertical integral of the fluorescence in the ROI marked on the image (shown in the plots on the bottom row). With the addition of the V=1 repump light, we expect over 100 photons. Our interaction region is not long enough to resolve an exponential decay on this length scale but the fluorescence looks qualitatively different from the V=0 light-only data. Using the same setup for CaOPh, we expect to easily distinguish photon cycling.

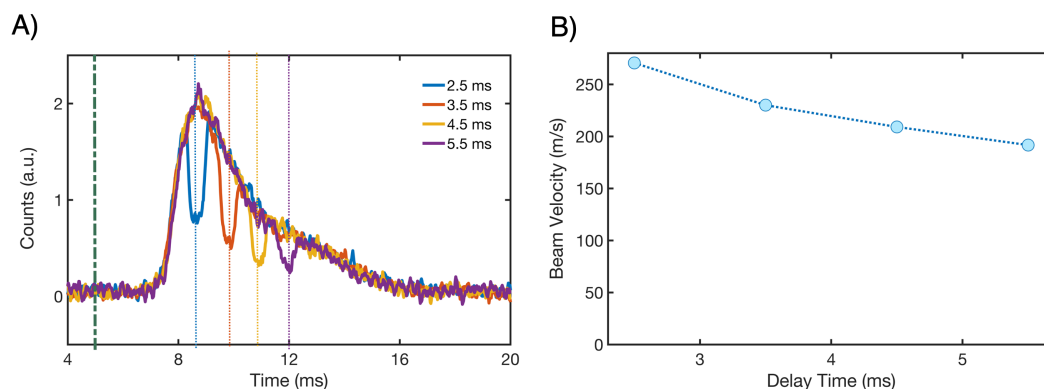


**Figure 7.19:** Calibrating the scattering rate requires knowing the forward velocity of the molecular beam. We installed an acousto-optic modulator on the depletion beam to allow fast switching. Illuminating the molecular beam for  $500 \mu\text{s}$  in the upstream region will deplete a small portion of the beam leaving a marker that we can use for a time of flight measurement between the depletion region and the detection region. By scanning the delay time (the vertical green line in Figure A denotes the time at which the YAG fires) for the short depletion pulse we can also measure the velocity dispersion in the molecular beam. The average velocity is 220 m/s which we will use to calibrate the scattering rates from the fluorescence streak images. The forward velocity of all the species we create will be similar because at 7 sccm the molecular beam is nearly fully boosted. This means the velocity of the helium is what sets the beam velocity, not the thermal velocity of the much heavier entrained gas.

When the molecules enter the laser beam, they begin to fluoresce, ideally emitting light at some scattering rate until they fall into a dark state at an exponential rate set by the branching ratio and the scattering rate. The camera sees this as a streak of fluorescence with a sharp onset generated by masking the excitation laser beam with a razor blade resulting in a slow exponential decay of the molecular beam brightness across the imaging field of view. The length of the spatial streak on the camera is set by the scattering rate, the branching ratio of the transition, and the speed of the molecular beam.

We measured the mean velocity of the molecular beam under our nominal operating conditions of 4 K and 7 sccm of buffer gas flow in the cell. We made the measurement by

rapidly switching on an upstream depletion laser beam using an acousto-optic modulator to carve out a narrow section of the beam which we used as a marker. We then measured the time of flight between the depletion beam and the detection photo-multiplier tube in the detection region, 10 cm downstream. This allows us to measure the beam’s forward velocity, which peaked at approximately 220 m/s.

We did an initial calibration using CaOH, which is expected to scatter 20 photons at 1 MHz, shown in figure 7.18. We observed a fluorescence streak consistent with a scattering rate of 820 kHz, indicating our setup works as well as the original CaOH experiment where this method was also used<sup>18</sup>

In the case of CaOPh, we want to calibrate using a transition that will scatter a known number of photons to avoid confusion between the scattering rate and the number of photons scattered. We used a well-isolated R-branch transition, located near 490.267 THz, which can act as a “pseudo-single-photon” source. Furthermore, this R-branch transition,  $|\tilde{A}^2B_2, N = 3, K_a = 1, K_c = 2\rangle$  to  $|\tilde{X}^2A_1, N = 2, K_a = 0, K_c = 2\rangle$  is isolated by nearly 500 MHz on either side to avoid confusion from the next nearest transition, reducing the off-resonant scatter background.

The length of the fluorescence streak on the R-branch transition indicated a scattering rate of 13.7 kHz, which is 60 times slower than CaOH. There are other transitions within 1 GHz of the R-branch we are driving. These transitions will be slowly driven at the off-resonant rate determined by the detuning and saturation parameter of the drive laser, set to resonantly drive the R-branch. We lowered the laser power to check if the single

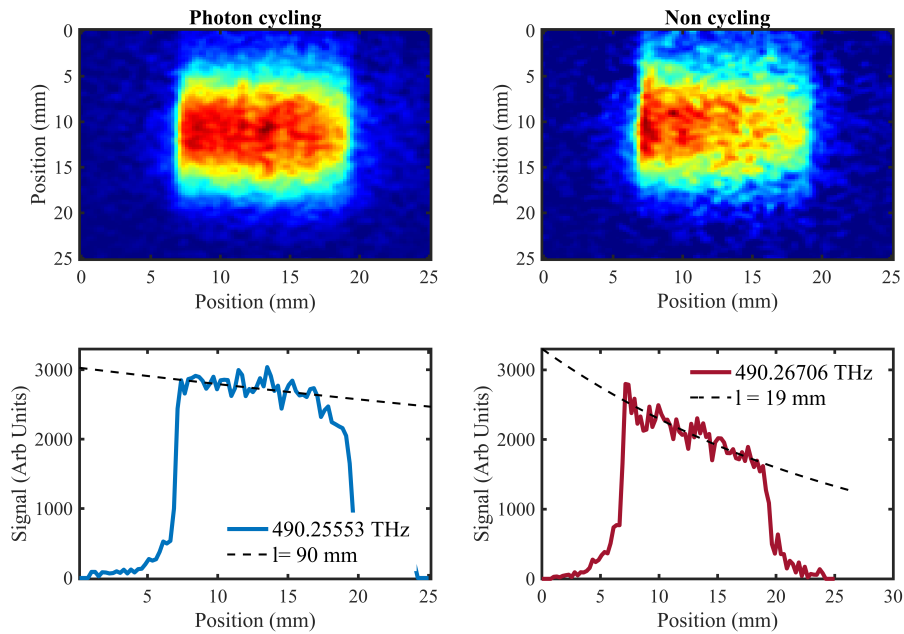


**Figure 7.20:** On the left is a fluorescence streak image of CaOPh on the 490.255530 THz photon cycling line. The vertical integration of the image region of interest plotted below is consistent with no fluorescence decay over the 15 mm excitation beam. On the right, we compare to a “pseudo-single-photon” source to calibrate the scattering rate separately from the number of photons cycled. The “pseudo-single-photon” source is an R-branch transition at 490.267060 THz. The decay length of 19 mm at a beam velocity of 220 m/s suggests a scattering rate of 13.7 kHz. While the photon cycling transition clearly has a different character than the R-branch, we cannot conclude how many photons were scattered, and the scattering rate measurement on the R-branch indicates there might be a significant issue that we are unaware of.

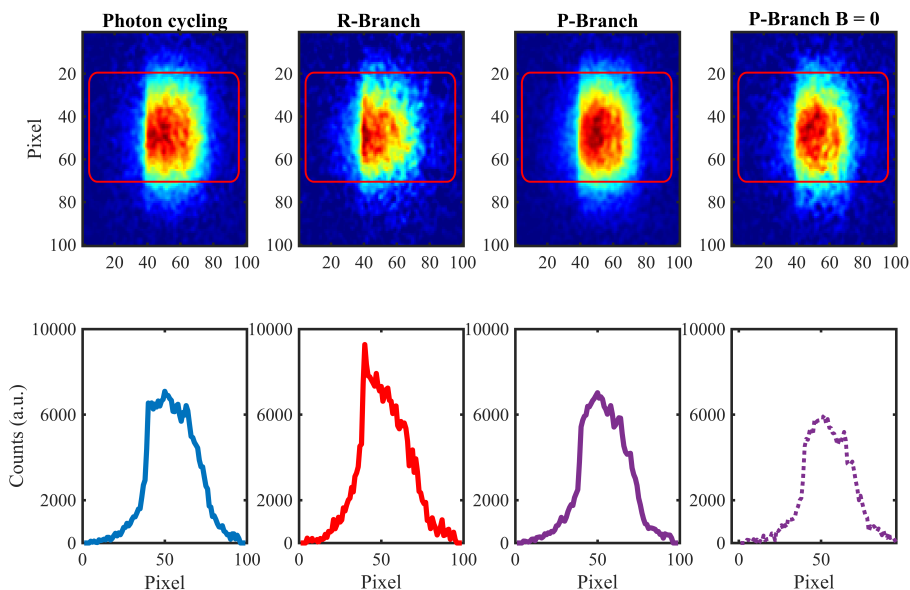


**Figure 7.21:** An additional comparison between different types of transitions in CaOPh. The photon cycling and R-branch transitions are the same as in the last figure. Comparing to a P-branch is useful because P-branches can cycle several photons before the population leaks to a different ground state. The P-branch also looks different, indicating some photon cycling. We also toggled the magnetic field (usually around 2 Gauss at the location of the molecules) to see if this impacted the scattering rate. It did not.

photon fluorescence was obscured by a slowly-driven off-resonant scattering background. This is not what we saw when we reduced the power, the fluorescence streak remained the same at lower power, indicating all the light is coming from transitions driven on resonance.

We then moved to the photon cycling transition to repeat the same measurement shown in figure 7.20 and figure 7.21. The result looked qualitatively different from the R-branch, indicating we were scattering more than 1 photon. The slope of the fits suggests 5 photons were scattered on the cycling transition, however, the fit decay

length isn't well constrained because the fluorescence scattering exited the field of view before undergoing measurable decay at a slow scattering rate.

We were once again concerned about off-resonant scattering given that the photon-cycling transition is an even more congested region of the spectrum than the R-branch, with several other rotational transitions in the 100-300 MHz range. None of these nearby transitions are coupled to the photon-cycling transition and all of them have  $N > 3$ . These states will pump out eventually and are not problematic for anything other than determining the scattering rate. With more laser frequencies, one could pre-pump these states to do a background-free scattering rate measurement but this wasn't a practical solution for us. Our way to distinguish off-resonant scatter is limited to measuring power-broadening behavior as we lower the laser power, where the off-resonant scatter will diminish, leaving a relatively sharp feature from the photon-cycling line driven on resonance. We did not see a sharper feature emerge from the background, indicating there is no issue with off-resonant scattering.

## 7.9 REPUMP TRANSITION

At this point, we opted to find the  $V = 1$  Ca-O stretching mode repump transition to increase the number of photons scattered through vibrational repumping. We searched for the transition by driving the  $\tilde{B}^2B_1-\tilde{X}^2A_1$  photon cycling transition to pump population into  $V=1$ , which we planned to repump through the same  $\tilde{B}^2B_1-\tilde{X}^2A_1$  electronic

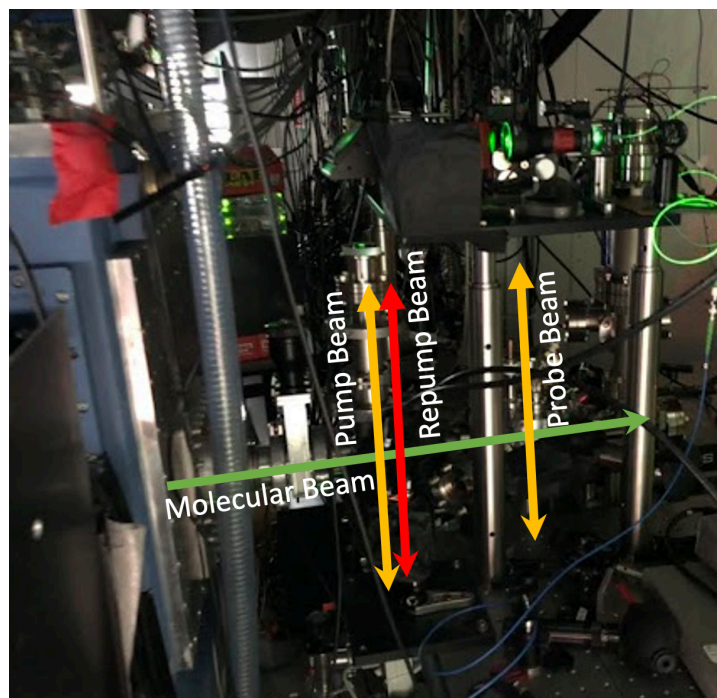


**Figure 7.22:** Picture of the experimental apparatus for spectroscopy with the molecular beam and laser beams denoted. The first photomultiplier tube is located in the pump region and the secondary detection photomultiplier tube is downstream in the probe region. The setup is the same for double resonance spectroscopy but without the repump beam.

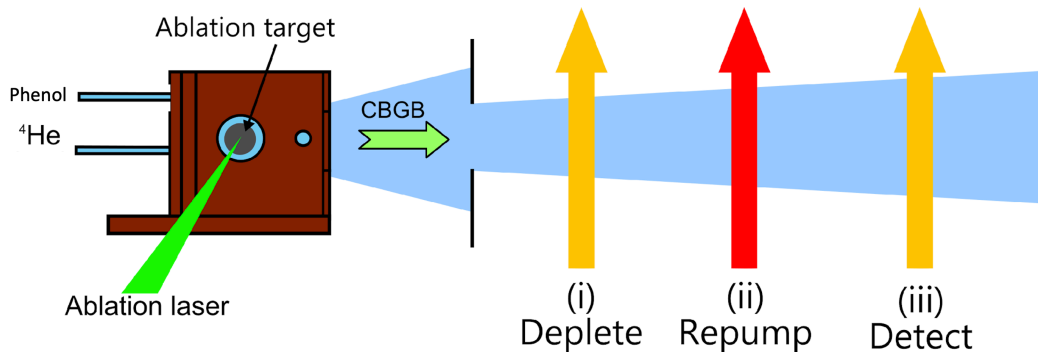


**Figure 7.23:** Configuration used for the pump-repump-detect measurements. All three beams are spatially separated. The signal is detected on the photo-multiplier tube in Region (iii), while an additional photo-multiplier tube in Region (i) monitors the buffer gas beam production. The three cascading laser beams, in Regions (i), (ii), and (iii) include (Region (i)) a large beam (1 cm) depleting the mainline transition in the upstream region, (Region (ii)) a slightly smaller (7 mm) repump beam just downstream of the depletion beam, and finally, (Region (iii)) an even smaller (3 mm) detection beam tuned to the mainline transition in the far downstream region.

transition. While most experiments would opt to utilize the  $\tilde{A}^2B_2$  to  $\tilde{X}^2A_1$  transitions for repumping to optimize the scattering rate, we elect to use the same electronic state for photon cycling and repumping because, in asymmetric top molecules, these electronic transitions have different rotational selection rules which means repumping using the  $\tilde{A}^2B_2$ - $\tilde{X}^2A_1$  transition would not repopulate the correct rotational level for laser cooling on the  $\tilde{B}^2B_1$ - $\tilde{X}^2A_1$ - transition<sup>9</sup>.

We scanned the frequency of the  $V = 1$  repump laser positioned downstream looking for an off-diagonal excitation where the population is excited by the repump wavelength but decays at the main line diagonal wavelength. Narrowband interference filters make this type of spectroscopic search almost completely background free, resulting in a very high detection fidelity.

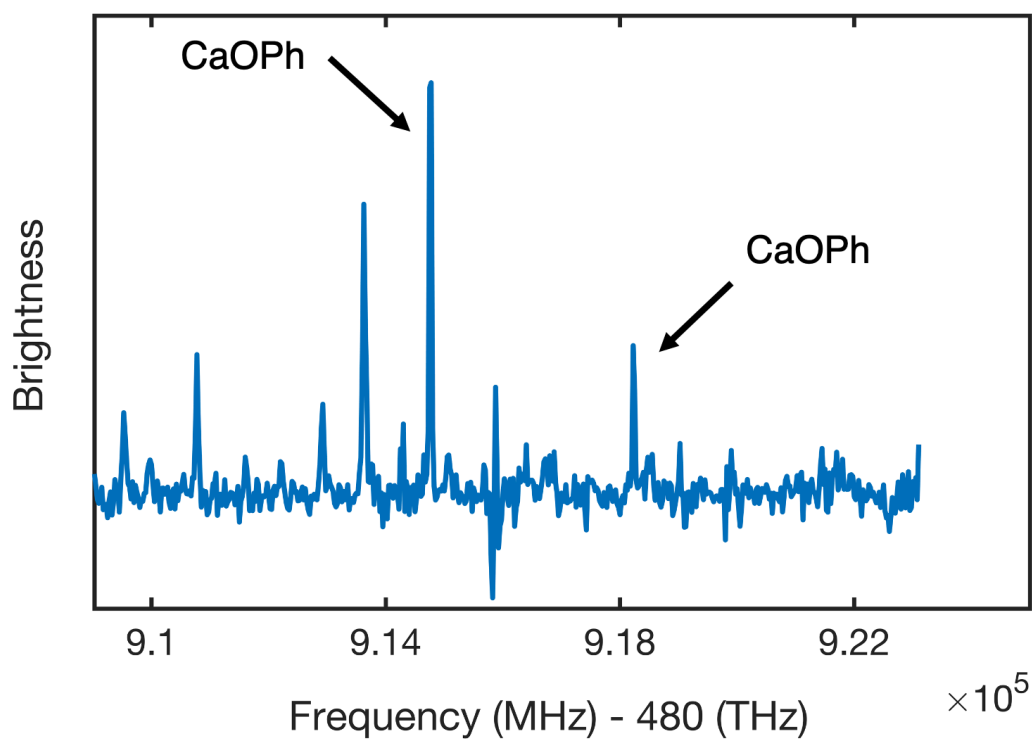


**Figure 7.24:** Detection of the repump transition. The population is pumped in the upstream region on the photon cycling transition to populate  $V=1$ . In the detection region, the molecules are illuminated by the 624 nm repump light and we detect fluorescence around 611 nm on a photomultiplier tube with an interference filter. There is a CaOH background that is excited at 624 nm and decays at nearly 611 nm which explains the extra lines we observe. It's easy to determine which lines are the CaOPh repump transitions by blocking the upstream pumping region and observing the lines disappear in the downstream region.

Unfortunately, CaOH, which is also produced in some quantity during the ablation, happens to have a line that is excited by the CaOPh  $V = 1$  repump wavelength and decays within 1 nm of the CaOPh diagonal transition wavelength, which is still detectable on the photo-multiplier tube. This creates a false background of line appearing every few GHz during the scan. It is easy to distinguish the CaOPh lines because we are pumping into the  $|\tilde{X}^2A_1, V = 1, N = 1, K_a = 1, K_c = 0\rangle$  state with the upstream pump laser and as a result, the brightness of the CaOPh repump line will respond to shuttering the pump light. We quickly identified two repump transitions corresponding to CaOPh at approximately 480.914 THz and 480.918 THz, respectively. One is the correct repumping line  $|\tilde{X}^2A_1, V = 1, N = 1, K_a = 1, K_c = 0\rangle \rightarrow |\tilde{B}^2B_1, V = 0, N = 0, K_a = 0, K_c = 0\rangle$ , and the other line is  $|\tilde{X}^2A_1, V = 1, N = 1, K_a = 1, K_c = 0\rangle \rightarrow |\tilde{B}^2B_1, V = 0, N = 2, K_a = 2, K_c = 0\rangle$ . Of course, the  $N=2$  ( $|\tilde{B}^2B_1, V = 0, N = 2, K_a = 2, K_c = 0\rangle$ ) level will have some repumping effect but it is incomplete because some of the molecules will decay into the  $N=3$  manifold. The splitting between the  $|\tilde{B}^2B_1, V = 0, N = 0, K_a = 0, K_c = 0\rangle$  and  $|\tilde{B}^2B_1, V = 0, N = 2, K_a = 2, K_c = 0\rangle$  excited states should exactly match the splitting observed in the high-resolution spectroscopy taken earlier because the repump transition uses exactly the same excited states, however, the excited state splitting on the repump transition did not match the rotation splitting measured on the diagonal transition by about 300 MHz. We performed another set of optical double resonance measurements to confirm these are the correct repump states despite the mismatched splittings we observed.

Another peculiarity was that no natural population existed in the  $|\tilde{X}^2A_1, V = 1, N =$

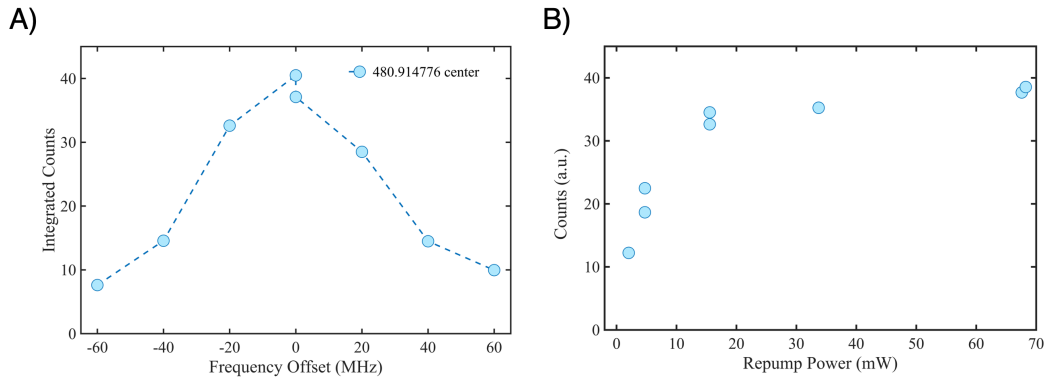


**Figure 7.25:** We characterized the  $V=1$  repump transition by depleting the photon cycling transition with an upstream beam, repumping downstream of the depletion beam, and then detecting on the photon cycling transition further downstream. The signal is the repumped population on the photon cycling transition. The repump transition is both power-broadened and power saturated.

$1, K_a = 1, K_c = 0$ ) state in the absence of the mainline pump laser. This seems to indicate that the helium buffer gas collisions can thermalize the Ca-O stretch vibrational degree of freedom. We do not see this behavior in CaF or CaOH which have similar energy scales associated with the Ca-X stretch mode.

## 7.10 PUMP AND REPUMP MEASUREMENT

With the repump frequency known, we did a pump-repump measurement to determine how much population can be repumped. The first beam is a high-power and spatially large (1 cm) depletion beam driving the diagonal laser cooling transition to maximum depletion, around 75%. Downstream of that is the  $V = 1$  repump beam which is slightly smaller (7 mm) than the first pump beam. The final beam in the detection region is a low-power (10 mW) and small (3 mm) laser beam detecting population on the photon

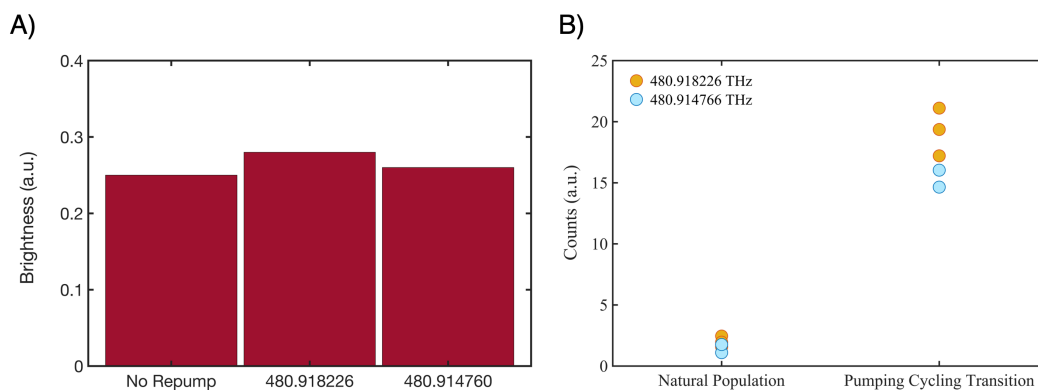


**Figure 7.26:** After optimizing the repump power, beam size, and alignment for maximum repumping, we made a measure of total repumping efficiency. The “no repump” bar represents the residue population that was not depleted in Region (i) depicted in figure 8.2. The next two bars represent the signal detected on the photo-multiplier tube in Region (iii) with the repump laser in Region (ii) tuned to the noted frequency. The correct repump transition should recover most of the population and become very bright in this region. Both lines showed some amount of repumping but neither line brought back a significant population fraction, indicating a serious issue with the repumping scheme or an unknown loss channel. On the right is a plot of the repump signal only (detecting with the repump). Both transitions should be similar in brightness because only a single photon can be scattered when the repump transition is driven at the repump wavelength but detected on the mainline wavelength. The natural population in the  $V=1$  state is consistent with zero for both rotational lines.

cycling transition. With the repump beam blocked, we optimize the alignment of the pump and detection beams by depleting the molecules as much as possible, indicating sufficient photon scattering in the pump region and good spatial alignment for the molecules to pass into the smaller detection beam.

Finally, we turn on the repump beam and attempt to bring the depleted population back. After several iterations of optimization, we were only able to recover about 7% of the population with the repump, shown in figure 7.26. Furthermore, we scanned the power of the repump beam and determined we are saturating the transition.

## 7.11 ASSESING THE SITUATION

Our photon scattering fluorescence streak images indicate that we scattered about 2 photons on the photon cycling transition at a scattering rate of 14 kHz which is very slow. Adding remixing magnetic fields and polarization switching Pockels cells failed to improve the scattering rate. We found the  $V=1$  repump transition but observed no additional photons scattered when we added the repump light in the fluorescence streak imaging region. Furthermore, we could not recover a significant fraction of the population by repumping the only vibrational transition we observed in DLIF to be a major loss channel. This is concerning and potentially indicates additional loss channels at the order unity level.

We probed nearby rotational levels (nearby in angular momentum) but did not detect a rotational leakage channel. We confirmed in a very broad DLIF measurement that no lines were to the blue of what we identified as the diagonal transition. That serves as a check against misidentifying  $V = 1$  as  $V = 0$ . It's also concerning that the  $N = 0$  to  $N = 2$  excited state splitting measured for the  $V = 1$  repump transition is 300 MHz larger than measured on the diagonal transition. It should be identical. This potentially indicates an incorrect quantum number assignment, however, our double resonance measurements suggest these are the correct states.

As a final yet highly speculative check, we probed for  $\text{Ca}^+$  ion fluorescence which would indicate the molecule is ionizing. The Ca-O potential well depth in the ground

electronic state is less than two 611 nm  $\tilde{B}^2B_1-\tilde{X}^2A_1$  photons which could lead to ionization, although we do not expect this to happen. We looked for  $Ca^+$  ion fluorescence on a UV-photomultiplier tube but did not observe any signal. It's also possible the molecule has a different dissociation channel that doesn't emit a free calcium ion for us to detect.

There are more exotic possibilities such as an internal conversion process. One way an internal conversion process could be imagined is that energy from the photo-excitation gets distributed over many internal vibrational modes which can live for a long time and decay in the deep infrared where we cannot detect emission in the DLIF spectroscopy. This would go undetected in our Frank-Condon factor estimate because the branching calculated from DLIF only carries information about the radiative decay processes. The only hint the other decay processes could be at play would be a reduced fluorescence yield which is hard to quantify unless it is several orders of magnitude suppressed because it would require a detailed understanding of the chemical production yield.

We have circumstantial evidence that internal conversion processes do not happen for CaOPh given that the fluorescence yield is high enough to observe CaOPh. In this case, the internal conversion rate would have to be roughly matched to the radiative lifetime of the excited state, which in turn requires fine-tuning parameters. This is unlikely. Also, internal conversion rates seem to scale strongly with system size and fluorescence from  $CaOC_7H_{10}$  which are roughly twice the size of CaOPh, have been observed by our group. A general internal conversion model would suggest if CaOPh is an edge case then  $CaOC_7H_{10}$  should not emit any fluorescence light.

Another possibility is that the selection rules for an asymmetric top are less well-defined than we thought. This is also unlikely because we did not observe rotational leakage, let alone large enough leakage channels to compete with photon cycling on the order unity level.

With no clear direction to continue CaOPh, we decided to switch to CaNH<sub>2</sub>, which is also an asymmetric top with a similar symmetry to CaOPh. This will help us understand if the limited photon scattering we saw was related to the low symmetry of asymmetric tops or if it is instead a fundamental issue with either CaOPh in particular or larger molecules in general.



# Laser Cooling of an Asymmetric Top

Molecule

## 8.1 A SIMPLER ASYMMETRIC TOP

The study of CaOPh in the previous chapter made clear the need to understand how to photon cycle and laser cool a more “manageable” asymmetric top molecule, meaning

one where the possible branching channels are easier to understand. To that end, we will focus our efforts on understanding, photon cycling, and laser cooling  $\text{CaNH}_2$  molecules, smaller than  $\text{CaOCH}_3$ , which has already been laser-cooled<sup>101</sup>, therefore it should not be hampered by “large molecule” types of issues such as internal conversion processes.  $\text{CaNH}_2$  has the same spatial symmetry as  $\text{CaOPh}$ , with the two hydrogens playing the role of the planar carbon ring in  $\text{CaOPh}$ <sup>9</sup>. By moving to this simpler molecule, we hope to isolate the mechanisms related to laser cooling large molecules from the peculiarities of asymmetric top molecules.

## 8.2 PRODUCTION

$\text{CaNH}_2$  production involves flowing ammonia gas into the buffer gas cell and reacting it with calcium atoms ablated from a solid metal target. Compared to phenol, ammonia has a much colder liquefaction point of around 240 K at a pressure of a few Torr, which allows us to run the fill line at a cooler temperature (260 K, vs 340 K for phenol). Lower temperature reduced the heat load by a factor of 3, improving the helium pot run time to around 3 hours. We also removed the heater tape needed for phenol from the atmosphere side of the fill line to add a flow controller in place of the throttle valve. We used an MKS flow controller built for corrosive gases and set the flow rate to 0.4 sccm.

Similar to other calcium-containing radicals we’ve studied in the group,  $\text{CaNH}_2$  pro-

duction can be enhanced by optically exciting the calcium atoms in the ablation plumb to the meta-stable  $^3P_1$  state. This enhances the production of  $\text{CaNH}_2$  by a factor of 4.

The overall cell performance is much better with ammonia as the reactant gas compared to phenol. We can run for several weeks without needing to warm up the beambox. A warm-up without cleaning the cell accomplishes two things: it refreshes the sorbs by releasing captured helium and it also clears out the ammonia that has frozen in the cell. We do not observe degraded molecular beam signals even many weeks after the last warm-up, in stark comparison to CaOPh. Full cell cleanings are rarely needed and we have run for up to four months without a drop-off in the signal. To keep the calcium target fresh and production reliable, we raster the ablation spot over a large fraction of the calcium target.

We have longevity concerns with the charcoal sorbs. After moving away from CaF, we flowed fluorinated phenol for several weeks and observed poor source performance although we could not definitively tie it to the sorbs. When we switched to CaOPh (non-fluorinated) we replaced all of the protected sorbs out of an abundance of caution. We had additional concerns that ammonia would degrade the sorbs too, but after 6 months of run time with ammonia flow, we have not observed any adverse effects. The ammonia does not appear to be degrading anything in the beambox although viton (the fluoro-elastomer that most of the beambox O-ring gaskets are made from) has long-term compatibility issues with ammonia. For this reason, we always pump on the beambox when it is at room temperature to mitigate contact with the O-rings. At cryogenic

temperatures, there should be no ammonia contact with the O-rings due to the fast cryo-pumping rate of the ammonia onto all of the cold surfaces.

### 8.3 VIBRATIONAL STRUCTURE

We took dispersed laser-induced fluorescence data on  $\text{CaNH}_2$  to estimate the Frank-Condon factors and locate the largest vibrational leakage channels. The mainline alone will provide about 20 photons and with one additional repump laser, we expect 70 photons. A second repump laser is predicted to increase the number of photons to a few hundred. The largest vibrational decay is the first excited state of the Ca-N stretch mode and the second largest contribution is decay to the second excitation of the out-of-plane bending mode, shown in figure 8.1. The first excitation of this bending mode appears to be highly suppressed. Both of these repump transitions are around 650 nm and easily addressable with rhodamine-based dye lasers. We performed additional, extended, DLIF measurements to rule out contributions from the  $V = 2$  excitation of the Ca-N stretch mode. There were no visible decays anywhere near where this line was predicted to occur.

### 8.4 $\text{CANH}_2$ SPECTROSCOPY

Following the same trajectory as CaOPh, we moved from understanding the vibrational decays to characterizing the rotational structure with high-resolution continuous wave

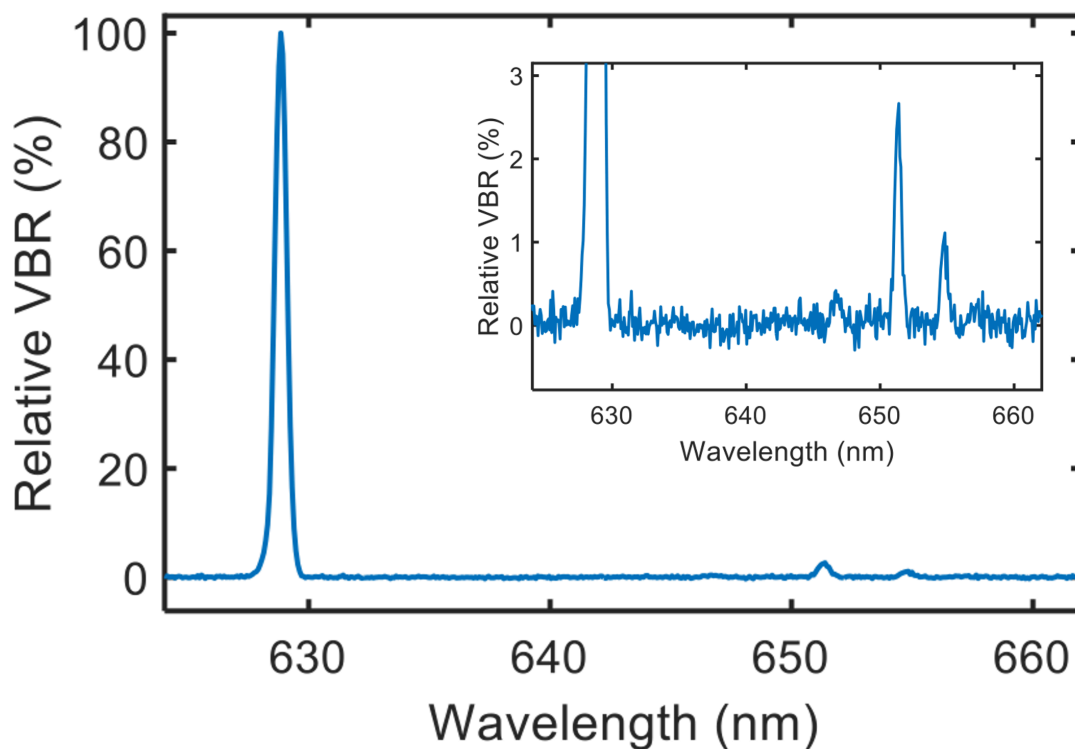


**Figure 8.1:** Dispersed laser-induced fluorescence (DLIF) spectroscopy of the  $\text{CaNH}_2$  vibrational modes.  $\text{CaNH}_2$  molecules are excited by a laser at 629 nm on the  $\tilde{B}^2B_1-\tilde{X}^2A_1$  transition in the vibrational ground state of each mode. The additional peaks seen in the spectrum correspond to red-shifted fluorescence from decay to excited vibrational modes in the ground electronic state. The inset is a zoomed-in version of the same DLIF spectrum, with the y-axis normalized to the height of the diagonal decay from the larger plot. The 653 nm decay is the Ca-N stretching mode and the 656 nm decay is the second excitation of the in-plane bending mode. These are the only two decay channels we are repumping.

laser spectroscopy.  $\text{CaNH}_2$  has larger rotational constants (small moments of inertia) than  $\text{CaOPh}$  making the rotationally resolved spectrum sparse by comparison. Using the molecular constants from reference<sup>165</sup>, we fit the rotational transitions between the  $\tilde{A}^2B_2$  and  $\tilde{B}^2B_1$  states very accurately and found each line was within a few 10's of MHz of the predicted frequency. The photon cycling transition  $|\tilde{X}^2B_2, N=1, K_a=1, K_c=0\rangle$  to  $|\tilde{B}^2B_1, N=0, K_a=0, K_c=0\rangle$  was easily identified.

The one notable exception to the agreement between the model and data was the  $\tilde{C}^2A_1$  state which we could not match well using the numbers from this reference<sup>104</sup>. We fit our own data to the model Hamiltonian in reference<sup>104</sup> yet still could not match the spectrum well. We confirmed the state identified as the  $\tilde{C}^2A_1$  state photon cycling transition ( $|\tilde{X}^2B_2, N=1, K_a=0, K_c=1\rangle$  to  $|\tilde{C}^2A_1, N=0, K_a=0, K_c=0\rangle$ ) is depleted by driving the  $\tilde{B}^2B_1$  state photon cycling line in an upstream region of the beamline. This is good evidence that this assignment (of the main line, at least) is correct. Understanding the  $\tilde{C}^2A_1$  state is not critical for our laser cooling agenda because the  $\tilde{C}^2A_1$  state is much less diagonal than the  $\tilde{A}^2B_2$  and  $\tilde{B}^2B_1$  states so it was never in contention for direct use in laser cooling for anything other than a repumper. We elect to use the  $\tilde{B}^2B_1$  state, centered around 630 nm due to dye lasers available at this wavelength and at the corresponding wavelengths of 652 nm and 656 nm for the two most important repumps.

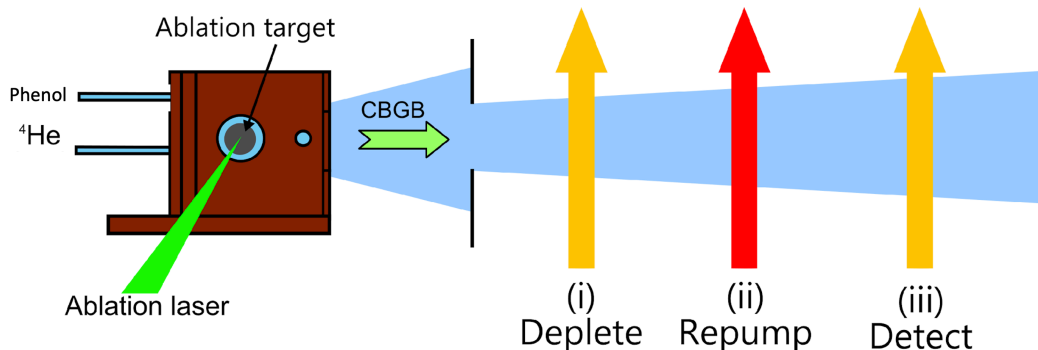


**Figure 8.2:** Configuration used for the pump-repump-detect measurements. All three beams are spatially separated. The signal is detected on the photo-multiplier tube in Region (iii), while an additional photo-multiplier tube in Region (i) monitors the buffer gas beam production. The three cascading laser beams, in Regions (i), (ii), and (iii) include (Region (i)) a large beam (1 cm) depleting the mainline transition in the upstream region, (Region (ii)) a slightly smaller (7 mm) repump beam just downstream of the depletion beam, and finally, (Region (iii)) an even smaller (3 mm) detection beam tuned to the mainline transition in the far downstream region. In the experiment, beam (i) and beam (ii) share a 2.75" viewport which places them very close together. This is not ideal and is likely the cause of the unfavorable vibrational repumping in figure 8.4

## 8.5 VIBRATIONAL REPUMP TRANSITIONS

Next, went to search out the correct rotational transitions involved in the  $V = 1$  and  $V = 2$  repump transitions at high resolution. The search for the vibrational repumpers was aided by a new calibration scheme for the spectrometer used in the DLIF measurements. We illuminated the spectrometer with laser light from a dye laser that was also referenced to the wavemeter. We fit the center of the scattered laser light and correlated it with the wavemeter reading. Repeating this process for several wavelengths, both above and below the location of the repump transition, allowed us to come up with a very accurate calibration for the spectrometer. We found both the  $V = 1$  Ca-N stretch mode (Figure 8.3) and the  $V = 2$  bending mode within a few GHz of the DLIF fit center using this

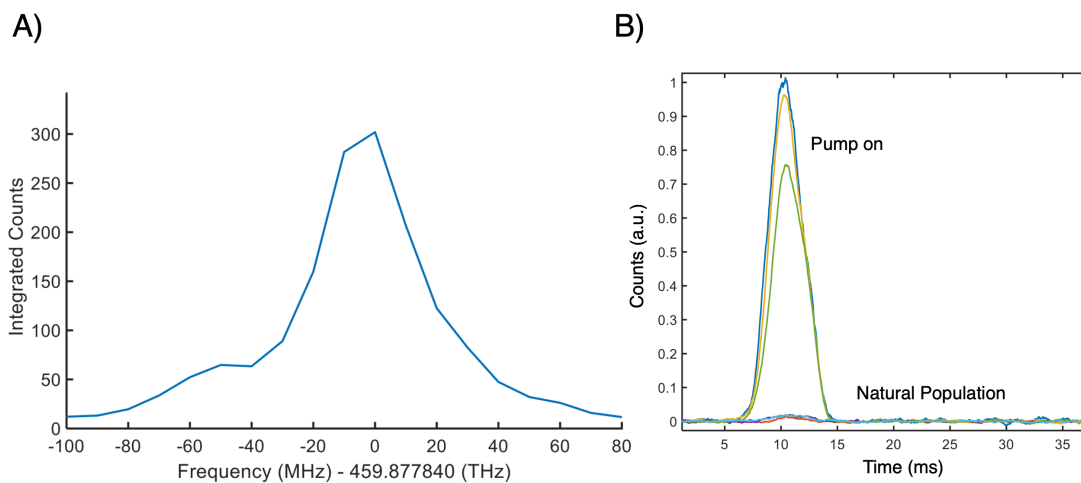


**Figure 8.3:** High resolution spectroscopy of the  $V = 1$  repump transition. We pump the photon cycling transition upstream, then repump it at 653 nm in the detection region, where a photomultiplier tube with an interference filter detects off-diagonal decays back to the  $V = 0$  ground state at 629 nm. B) Time traces of the molecular beam taken with and without the upstream pumping on the photon cycling transition. A comparatively small amount of natural population exists in the  $V = 1$  excited state in the absence of optical pumping.

calibration technique. Figure 8.4 characterizes the two repump transitions.

Similar to CaOPh, we saw almost no natural population in the excited vibrational states. While we do not have a working theory explaining how the asymmetric top nature of the molecule affects the buffer gas cooling collisions with helium, we have seen two species of asymmetric tops without any natural population in the excited vibrational levels but we did see a strong CaOH background while hunting CaOPh vibrational repumpers, indicating the CaOH molecules produced have a significant natural population in the excited vibrational states.

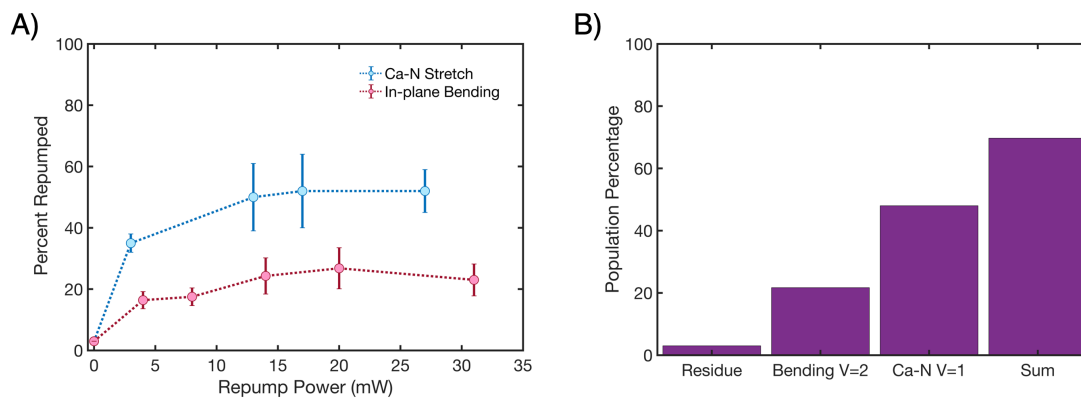


**Figure 8.4:** A) Power saturation curves for the  $V = 1$  and  $V = 2$  repump transitions were measured independently. The three beams (pump, repump, detection) are described in figure 8.2. Both saturation curves are normalized to the “full” beam signal measured with the upstream pump beam blocked. This value is the maximum amount that can be repumped since the vibrationally excited states have no appreciable natural population. The unfavorable vibrational repumping is likely a result of the beam placement. In the experiment, beam (i) and beam (ii) from figure 8.2 share a 2.75” viewport which places them very close together. Ideally, the three beams should be in three separate chambers to remove systematic effects which can bias the repumping fraction lower, as we see. B) Total molecule budget is broken down per category. The residue is the fraction of molecules that are not depleted by the mainline pumping light, (repump light is off, of course). The next two bars show the normalized repump fraction with the  $V = 2$  and  $V = 1$  repump beams, taken one at a time, respectively. The final bar is the sum of the repumps, indicating that 30 % of the population is “missing”. The reality is better than this measurement indicates, based on the number of photons scattered in figure 8.10.

### 8.5.1 SPIN-ROTATION STRUCTURE

Unlike CaOPh, CaNH<sub>2</sub> has spectroscopically resolved spin rotation splittings in the electronic ground state, several times bigger than the linewidth of the electronic transition. We measured the spin-rotation splitting between the  $J = 1/2$  and  $J = 3/1$  states and then used an acousto-optic modulator to produce a mainline beam with sidebands matching the 40 MHz spin-rotation splitting (Spin-rotation structure shown in Figure 8.5). We also observed spin-rotation structure on both of the vibrational repump transitions, however, the ground electronic state spin-rotation splitting was 60 MHz for both  $V = 1$  (Ca-N stretch) and  $V = 2$  (in-plane bending mode). Typically the spin-rotation splitting is the same in the ground and excited vibrational levels within the electronic ground state. This unusual behavior was also observed in YbOH and is attributed to the presence of f-shell electrons, which of course do not exist in CaNH<sub>2</sub>. We added two additional acousto-optic modulator sideband setups to cover the 60 MHz spin-rotation side bands on the  $V = 1$  transition for CaNH<sub>2</sub>.

### 8.6 PHOTON CYCLING AND ROTATIONAL LEAKAGE

Using the photo-multiplier tube to detect the fluorescence of the molecular beam outside the beambox, we attempted to photon cycle CaNH<sub>2</sub> by comparing the fluorescence with and without the spin-rotation sidebands on the mainline (no vibrational repumps). With the limited interaction length in our spectroscopy-specific setup, we observed a factor

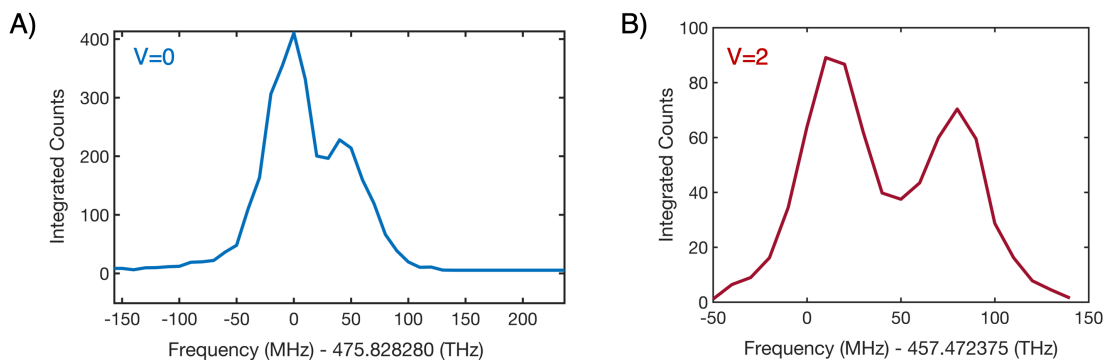


**Figure 8.5:** High-resolution spectroscopy of the spin-rotation structure in the vibrational ground state (figure A) and the  $V = 2$  bending mode (figure B). The ground state spin-rotation splitting of the photon cycling transition is about 40 MHz whereas the spin-rotation splitting in the vibrationally excited states, both Ca-N and the in-plane bending mode, is closer to 60 MHz.

of 8 increase in fluorescence with the sidebands on, indicating some amount of photon cycling. In the absence of the spin-rotation sidebands, the population gets pumped into the J state (either  $J=1/2$  or  $J=3/2$ ) that isn't illuminated, however, given the 40 MHz splitting and 10 MHz linewidth, some off-resonant scattering will repump the “dark” J-state leading to photon cycling with a slow scattering rate. This makes extracting the number of photons scattered by comparing fluorescence captured on a photomultiplier tube with and without sidebands difficult however we have definitive evidence of photon cycling.

## 8.7 ROTATIONAL LEAKAGE

A major concern for asymmetric top molecules is rotational leakage due to the different selection rules associated with electronic transitions of different symmetries. In  $\text{CaNH}_2$ ,

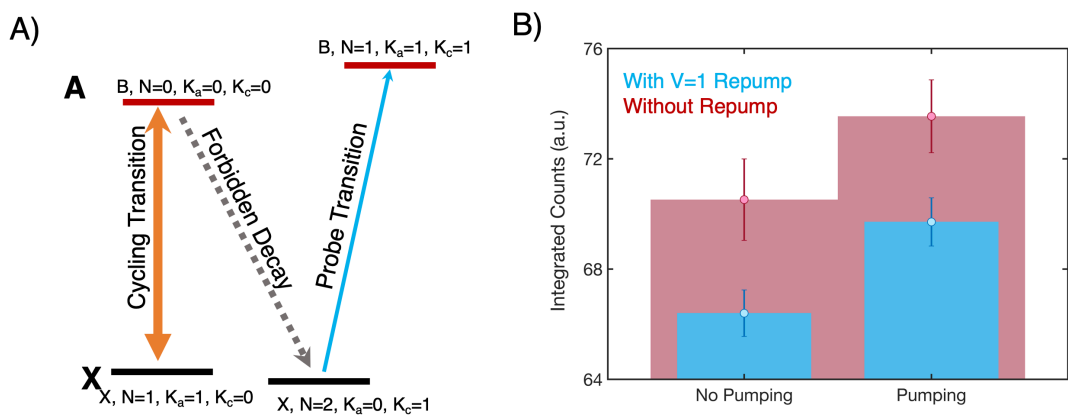


**Figure 8.6:** Due to the structure of asymmetric top molecules, there are possible rotational leakage channels. To test this, we drive the photon cycling transition to depletion in the upstream region, then observe the population decaying to the most likely leakage channel,  $|\tilde{B}^2B_1, N=0, K_a=0, K_c=0\rangle$  to  $|\tilde{X}^2A_1, N=2, K_a=0, K_c=1\rangle$  which is nominally forbidden. A) The detection scheme involves monitoring the population in the  $|X, N=2, K_a=0, K_c=1\rangle$  ground state, detected on the  $|\tilde{X}^2A_1, N=2, K_a=0, K_c=1\rangle$  to  $|\tilde{B}^2B_1, N=1, K_a=1, K_c=1\rangle$  transition and comparing that population with and without upstream pumping on the mainline. We did this with and without the  $V=1$  repump in the upstream pumping region but observed the same leakage both times. See the red and blue bars in Figure B). Extracting the branching ratio without knowing exactly how many photons were scattered is not possible, as the number of chances to branch to the  $N=2$  ground state from the photon cycling transition increases linearly with the number of photons scattered.

the  $\tilde{A}^2B_2$  and  $\tilde{B}^2B_1$  states are type-a and type-c transitions respectively. We expect a small mixing fraction of 5% which is enough to open rotational leakage channels that we should be able to observe after cycling several photons. The main concern is the excited electronic state used for photon cycling  $|\tilde{B}^2B_1, J = 1/2, N = 0, K_a = 0, K_c = 0\rangle$  will decay to  $|\tilde{X}^2A_1, J = 3/2, N = 2, K_a = 0, K_c = 0\rangle$ . We can check for this  $\Delta N = 2$  decay by pumping the photon cycling transition in the upstream region (see Figure 8.14 of the apparatus and then observing a probe transition such as  $|\tilde{X}^2A_1, J = 3/2, N = 2, K_a = 0, K_c = 0\rangle$  to  $|\tilde{B}^2B_1, J = 1/2, N = 1, K_a = 0, K_c = 1\rangle$  where the ground state of the probe transition is the state to which we suspect decays out of the rotationally “closed” photon cycling transition will accumulate. We carefully compare the fluorescence observed downstream on the probe transition with and without the upstream pump laser beam in resonance with the photon cycling transition. We switch the pump beam on and off every other shot using a shutter. The rapid toggling helps to mitigate biases in the data from ablation drifts. In addition, we raster the ablation automatically and average for several thousand shots to reduce the statistical effects of source fluctuations since we are looking for a small increase in signal on top of an already bright line. We saw a 6% percent increase in fluorescence which appeared reliably when the pump laser addressing the photon cycling transition was on. We also added the  $V = 1$  repump light to the pumping region which should lead to 50% accumulation in the  $|\tilde{X}^2A_1, J = 3/2, N = 2, K_a = 0, K_c = 0\rangle$  state since additional photon scattering provided by the vibrational repump increases the chances of the  $\Delta N = 2$  decay we are measuring. The actual branching ratio is hard

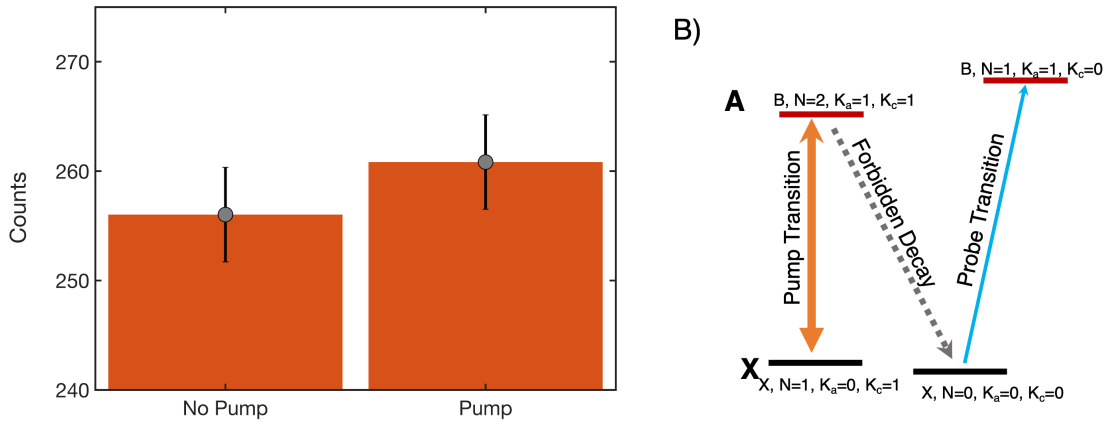


**Figure 8.7:** As a means to estimate the rotational branching ratio, we drove an R-branch transition which should cycle on average about 1 photon. This transition is the opposite of the  $\Delta N = 2$  decay from the photon cycling transition, which means the branching ratio from  $N=0$  to  $N=2$  should be similar. We started by pumping the  $|X, N = 1, K_a = 0, K_c = 1\rangle$  to  $|\tilde{B}^2B_1, N = 2, K_a = 1, K_c = 1\rangle$  transition and looking for the forbidden decay from  $|B, N = 2, K_a = 1, K_c = 1\rangle$  to  $|X, N = 0, K_a = 0, K_c = 0\rangle$ . As shown in Figure B), we monitored the  $\Delta N = 2$  rotational leakage by comparing the  $|\tilde{X}^2A_1, N = 0, K_a = 0, K_c = 0\rangle$  to  $|\tilde{B}^2B_1, N = 1, K_a = 1, K_c = 0\rangle$  transition with and without pumping upstream on the transition indicated by the orange arrow in figure B). The leakage detected was within the statistical error bars after 4000 shots. This is not unexpected given the pump transition will cycle less than 2 photons whereas in figure 8.6 the photon cycling transition has 10 times more opportunity for the  $\Delta N = 2$  decay to occur due to the prolonged photon cycling.

to estimate because we do not know exactly how many photons were cycled in the pumping region. Assuming we cycled between 1 and 20 photons (without the repump), the actual branching ratio is between 6% at worst, to 0.3% at best. We attempted to calibrate the leak rate in Figure 8.7 by driving the same loss channel on an R-branch transition which cycles approximately 1 photon.

### 8.7.1 OPPOSITE PARITY DECAYS

We also probed opposite parity decays from  $|\tilde{B}^2B_1, J = 1/2, N = 0, K_a = 0, K_c\rangle$  to  $|\tilde{X}^2A_1, J = 1/2, N = 1, K_a = 0, K_c = 1\rangle$  by observing the  $|\tilde{X}^2A_1, J = 1/2, N = 1, K_a = 0, K_c = 1\rangle$  to  $|\tilde{B}^2B_1, J = 3/2, N = 2, K_a = 0, K_c = 2\rangle$  transition at 475.846878 THz, illustrated in Figure 8.8. This probes the electric field in the region where the molecules are illuminated. The small opposite parity splitting of approximately 40 MHz makes the molecules susceptible to mixing from electric fields which causes opposite parity decay. We observed no leakage here. This is also verification that the leakage we measured previously for the  $\Delta N = 2$  channel is not a result of leaked light from the pumping region being detected downstream or any other technical systematic effect which could bias the signal up in the detection region while the pumping light is on.

### 8.7.2 ROTATIONAL REPUMPING

The  $N = 2$  rotational repumping needs to be done by driving the decay path exactly backward. Unfortunately, it cannot be repumped through the  $\tilde{A}^2B_2\text{-}\tilde{X}^2A_1$  transition because the  $\Delta K_c$  and  $\Delta K_a$  selection rules are different. This also means the rotational repumper cannot be driven through any other rotational states in the  $\tilde{B}^2B_1\text{-}\tilde{X}^2A_1$  manifold. The only option is to drive the forbidden transition  $|\tilde{X}^2A_1, J = 3/2, N = 2, K_a = 0, K_c = 0\rangle$  to  $|\tilde{B}^2B_1, J = 1/2, N = 0, K_a = 0, K_c = 0\rangle$  at 475.792510 THz, which we predicted using the PgoPher model. We never saw an effect on the photon scattering by adding this

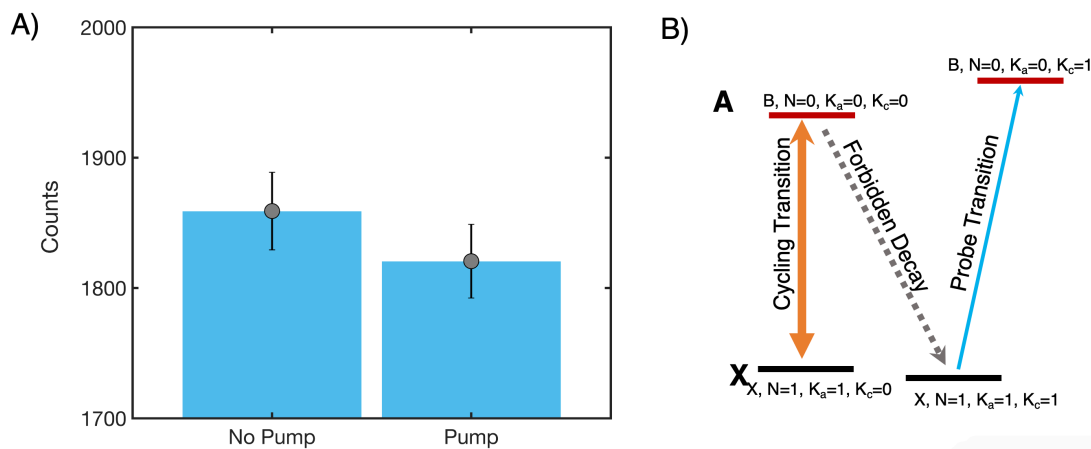


**Figure 8.8:** The final rotational leakage channel we checked using this method was for opposite parity decays, indicating the presence of an electric field in the photon cycling region where the upstream pump laser beam is located. We started by pumping the photon cycling transition and looking for the parity-forbidden decay from  $|\tilde{B}^2B_1, N=0, K_a=0, K_c=0\rangle$  to  $|\tilde{X}^2A_1, N=1, K_a=1, K_c=1\rangle$ . As shown in Figure B), we monitored the parity-forbidden rotational leakage by comparing the  $|\tilde{X}^2A_1, N=1, K_a=1, K_c=1\rangle$  to  $|\tilde{B}^2B_1, N=0, K_a=0, K_c=1\rangle$  transition with and without pumping upstream on the transition indicated by the orange arrow in Figure B). The leakage detected was within the statistical error bars after 4000 shots, indicating the electric field in the optical pumping region is sufficiently small to not mix opposite parity levels across the roughly 40 MHz asymmetry splitting gap.

repump, despite doing a careful frequency scan around the predicted frequency.

## 8.8 FLUORESCENCE STREAK IMAGING

In a similar spirit to the CaOPh experiment, we used fluorescence streak imaging to measure the scattering rate and calibrate the number of photons cycled on the photon cycling transition in  $\text{CaNH}_2$ . First, we looked at two R-branches at 457.564261 THz and another one at 457.590300 THz which we used as a “pseudo-single photon” source to calibrate the scattering rate separately from the number of photons cycled on the rotationally closed photon cycling transition. Figure 8.9 shows the “pseudo-single photon” calibration data and Figure 8.11 shows additional comparisons. The fluorescence from both R-branch transitions decayed with two characteristic timescales, a faster one corresponding to a 250 kHz scattering rate and a slower decay in the tail. The excitation time, on the rising edge of the fluorescence streak, is exactly the same as the fast decay time indicating that the transition is saturated and that the faster decay timescale is the correct one for the case of resonant scattering. The slower exponential decay is attributed to the geometry of the molecular beam and the nearly-uniform excitation laser beam. Since the excitation laser beam is elongated via a cylindrical lens telescope, the orientation of the long direction of the laser beam relative to the molecular beam propagation direction is important. When the beams are slightly off-parallel, the slow fluorescence decay in the “pseudo-single photon” case changes shape dramatically, indi-

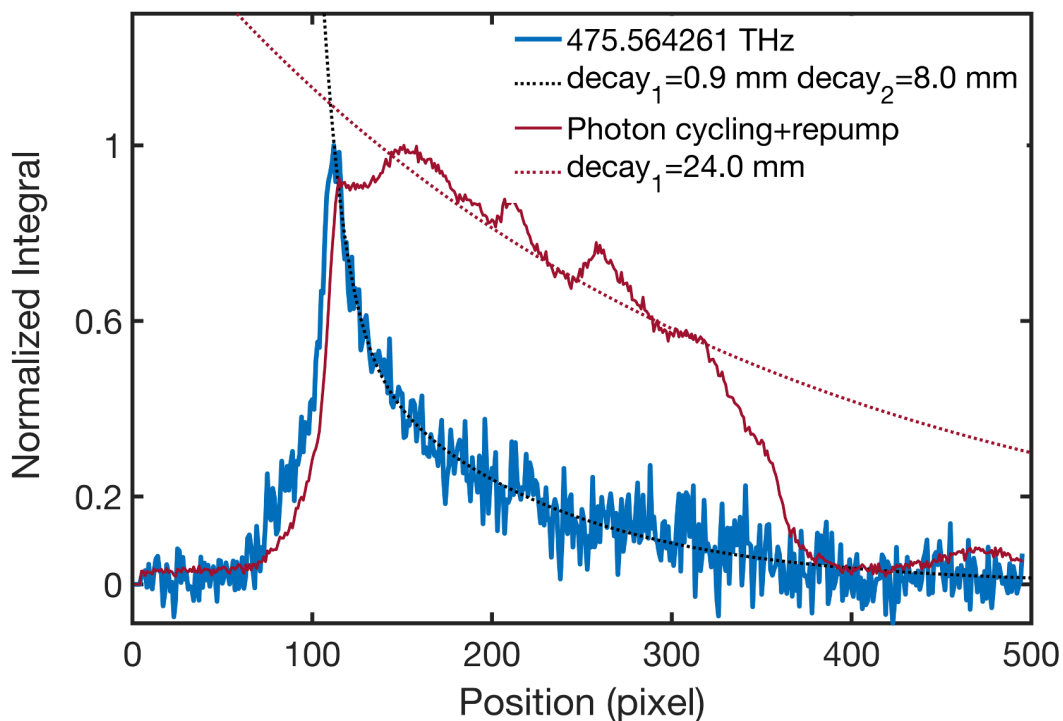


**Figure 8.9:** Similar to the CaOPh scattering rate measurements made by imaging the uniformly illuminated molecular beam on an EMCCD camera, we measured the scattering rate on  $\text{CaNH}_2$ . The blue trace is an R-branch at 457.564261 THz which we used as a “pseudo-single photon” source to calibrate the scattering rate separately from the number of photons cycled on the rotationally closed cycling transition. The decay of fluorescence is fit by a double exponential curve where the first decay is the resonantly driven R-branch transitions and the secondary, much slower time scale is the decay of off-resonantly driven nearby transitions. The faster decay corresponds to a scattering rate of about 250 kHz. The curve in red is the photon cycling transition with the  $V=1$  repump, giving a decay length 27 times longer than the R-branch. The scattering abruptly stops at the edge of the laser beam, cleanly masked by a razor blade just shy of the camera’s full field of view. The structure on top of the red curve is real and indicates non-uniformities in the imaging beam. Both transitions have the same scattering rate, therefore we conclude that we scattered 27 photons on the photon cycling transition with the  $V=1$  repump. The signal-to-noise of these two curves looks significantly different because the cycling transition is about 20 times brighter than the R-branch.

cating this is a geometric effect related to molecules entering the excitation laser beam downstream of the razor blade.

When we compared the “pseudo-single photon” transition to the photon cycling transition, the decay length measured on the camera for the cycling transition is 20 times longer. The two transitions have the same scattering rate, thus the prolonged spatial decay indicates that the photon cycling transition is scattering 20 times more photons. We added a Pockels cell to potentially improve the scattering rate by destabilizing dark states with polarization switching. The Pockels cell had a repeatable roughly 5% effect on the scattering rate, but we could not find an optimal switching frequency. The scattering rate looked identical for square wave switching frequencies between 200 kHz and 2 MHz.

Next, we added the  $V = 1$  repumper which increased the average number of photons scattered to 27. We use an acousto-optical modulator to generate 60 MHz side bands, resonant with the  $V = 1$  spin-rotation splittings. We then added the  $V = 2$  (in-plane bending mode) repump and observed no further increase in the number of photons scattered. The  $V = 2$  repump light did not have spin rotation sidebands for that test, although there should still be some amount of repumping. We tested the  $V = 2$  repump in isolation by borrowing the sideband setup from  $V = 1$  to measure photon scattering with the mainline light and  $V = 2$  without  $V = 1$ , as shown in figure 8.12. There was a reliable effect of the  $V = 2$  repumper but we still had an unknown loss channel. The fluorescence streak results with the repumpers included are consistent with the pump

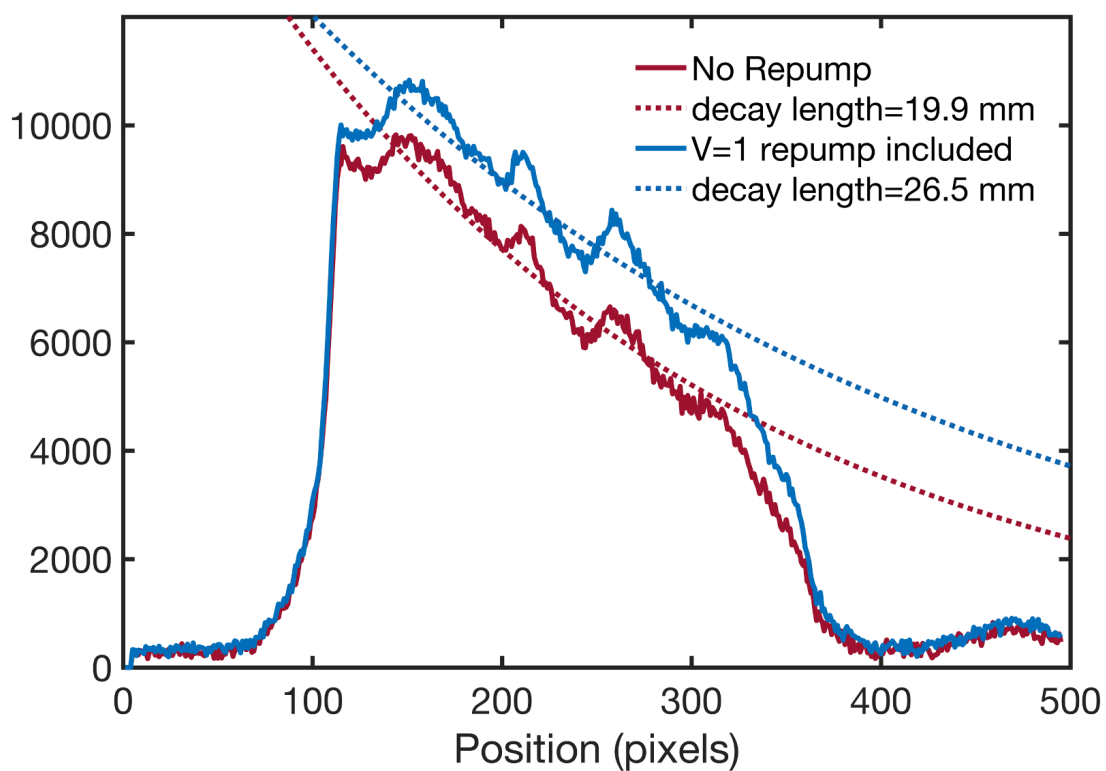


**Figure 8.10:** Fluorescence streak comparison of the photon cycling transition with and without the  $V = 1$  vibrational repump. The ratio of the decay lengths reflects the number of photons scattered (at the same scattering rate) in both cases. The  $V = 1$  repump adds about 40% more photons. Compared to the “single” photon reference in figure 8.9, the mainline scatters about 20 photons, matching the Frank-Condon factor prediction very well, and with the addition of the  $V = 1$  repump, the number of photons goes up to 27.

and repump data in figure 8.4. This is a strong indication of an additional loss channel. The two lowest-level loss channels we know are  $V = 2$  and  $N = 2$ . When we photon cycle with both the mainline and  $V = 1$  repump light, only an insignificant amount of population accumulates in either  $V = 2$  or the  $N = 2$  rotational leakage channel.

Our previous measurements indicate there is a  $\Delta N = 2$  rotational leakage channel out of the photon cycling transition, but we do not have an accurate estimate for the branching ratio. In light of the apparent loss issues, we added the  $N = 2$  rotational repump light which directly drives the “forbidden” decay channel back to the photon cycling transition. While we do not expect to see an effect given our measurements of the branching ratios to the  $N = 2$  loss channel, we tried to photon cycle with the  $N = 2$  repump present to rule out the possibility of an error in the branching ratio measurement.

From the PGopher model, we calculated the rotational repump frequency to be 475.792510 THz, which corresponds to driving  $|\tilde{X}^2A_1, N = 2, K_a = 1, K_c = 1\rangle$  to  $|\tilde{B}^2B_1, N = 0, K_a = 0, K_c = 0\rangle$ . We then tried photon cycling with the mainline laser,  $V = 1$  repump laser, and the  $N = 2$  rotational repump laser. We scanned the  $N = 2$  repump frequency over 100 MHz in 10 MHz steps but saw no additional scattering. The PGopher model predicts the  $\tilde{B}^2B_1-\tilde{X}^2A_1$  transitions in  $\text{CaNH}_2$  to 20 MHz or better, making it unlikely that we missed the  $N = 2$  rotational repump transition. It’s worth noting that due to limited dye laser resources, we were never able to run the experiment with the mainline light,  $V = 1$ ,  $V = 2$  and the  $N = 2$  repump lasers all at the same time. This is potentially

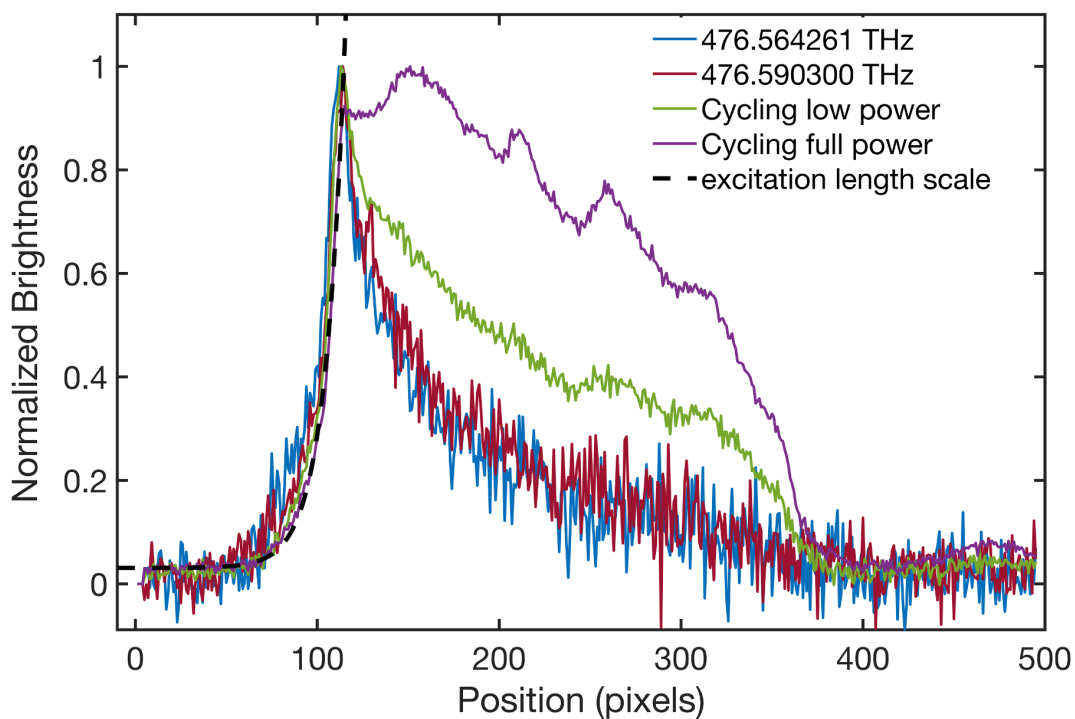


**Figure 8.11:** Fluorescence streaks for several transitions are plotted here. In all cases, the excitation rate is the same, indicating saturation. The excitation rate is also the same as the decay rate of the “pseudo-single photon” sources, in blue and red. The green and purple are both driving the photon cycling transition. The purple is driven at full power of 60 mW with both spin-rotation side bands on. The green is driven at about 15 mW with one spin-rotation sideband off. There is an initial fast decay peak with a slope matching the “pseudo-single photon” sources followed by a long slow off-resonant decay corresponding to the spin-rotation sideband 40 MHz away. This is instructive to the CaOPh measurements where we could not isolate the photon cycling transition well due to other nearby transitions.

important because the  $V = 2$  and  $N = 2$  could enter at roughly the same level, however, that means both loss channels should collectively contain nearly 100% of the population and our measurements indicate less than 30% of the population accumulates in these two states. There is very likely another loss channel that we have not found.

## 8.9 DEFLECTION

Our goal is to demonstrate 1D Sisyphus cooling/heating of  $\text{CaNH}_2$ . A previous experiment in the Doyle group using  $\text{CaOCH}_3$  was able to observe an unambiguous laser cooling feature with only 30 photons on hand. They saw very clear laser cooling with 120 photons, accomplished by adding another repump laser. In light of this, we decided to press forward with our 30 photon budget for the known repumper transitions on  $\text{CaNH}_2$ .

We modified the apparatus to accommodate a new laser cooling region. The original top plate on the chamber was replaced by a 6" CF viewport, giving maximum optical access for multi-passing the laser cooling beams over a large interaction length. The next improvement was to add a molecular beam collimating aperture at the entrance to the MOT chamber. The aperture is 3 mm tall by 9 mm wide. The vertical direction is the direction in which we will cool the molecules. The 3 mm aperture spatially filters the molecular beam resulting in a transverse temperature of 1 mK. In the horizontal direction, the 9 mm aperture length was chosen as a compromise between laser beam

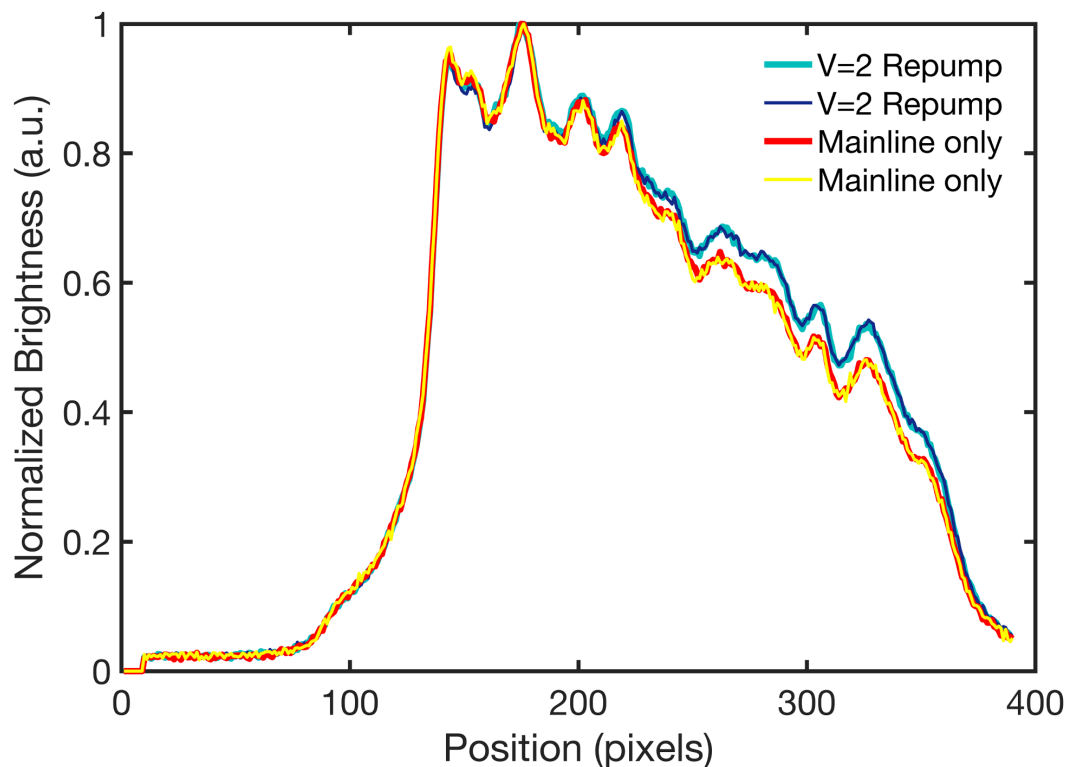


**Figure 8.12:** We attempted photon cycling using the photon cycling transition with both spin-rotation sidebands, the  $V = 1$  repump with both spin-rotation side bands and the  $V = 2$  repump without spin-rotation side bands. We did not observe any additional photon scattering in this configuration. We then swapped the spin-rotation sidebands onto the  $V = 2$  repump and tried photon cycling with the photon cycling and  $V = 2$  repump lasers only. That reliably resulted in more photons being scattered. The two blue traces represent repeated measurements with both the photon cycling laser and the  $V = 2$  laser, whereas the red and yellow traces are repeated measurements of the fluorescence with the photon cycling laser only. The measurements are reproducible and show some prolonged photon scattering when the  $V = 2$  repump is added.

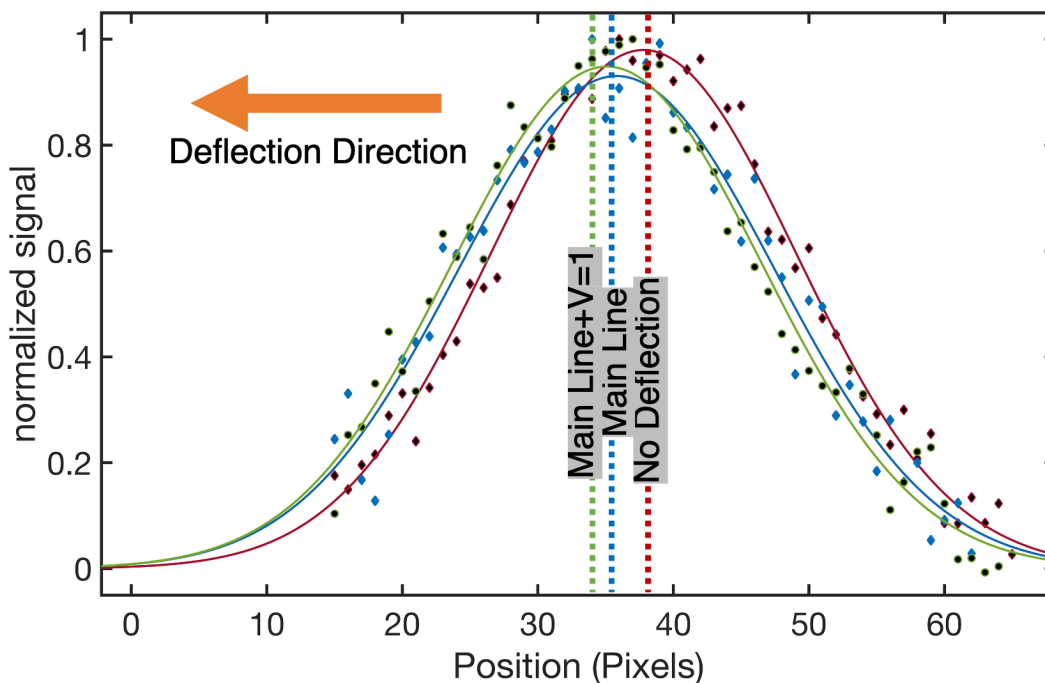


**Figure 8.13:** Using a single-pass laser beam in the upstream region, we deflected the molecular beam and measured the displacement. Compared to the reference molecular beam with no deflection light, we were able to observe a deflection consistent with 20 photon recoils worth of transverse momentum with the mainline laser only. Adding the repump, the deflection displacement improved and we calculated that 30 photons were scattered.

size and passing as many molecules as possible. A wider slit would require larger laser beams to illuminate the entirety of the molecular beam.

60 cm downstream of the aperture and laser cooling region is a new detection region. This consists of a blackened 6-way cross with an imaging beam propagating vertically and an EMCCD camera with a 2x de-magnifying telescope positioned in the horizontal direction, to observe the cooling or heating of the beam in the vertical direction.

Initially, we illuminated the molecular beam with a single-pass vertical laser beam

on the photon cycling transition. As the molecules scatter light, they accumulate an average transverse momentum which results in a downward deflection of the molecular beam as it propagates the 60 cm beamline into the imaging region where the downward deflection is measured on the camera. We used this as a secondary confirmation tool to measure the number of photons scattered. The downward deflection of the beam when illuminated by the photon cycling laser beam alone was consistent with 19 photons scattered using a molecular beam velocity of 225 m/s. Figure 8.13 shows the deflection data. Adding the  $V = 1$  repump improved the deflection, consistent with scattering 30 photons. This set of measurements is fully consistent with the fluorescence streak imaging technique.

## 8.10 SISYPHUS HEATING AND COOLING

To demonstrate 1D laser cooling on  $\text{CaNH}_2$  with 30 photons in the budget, we will use an efficient cooling process to remove a large amount of kinetic energy per photon scattered. This process also needs to have a sufficiently large capture velocity to effectively cool a sample with an initial temperature of 1 mK. Magnetically assisted Sisyphus cooling accomplishes both. The Sisyphus process involves the molecular beam traversing a near-resonant standing wave of linearly polarized light propagating perpendicular to the molecular beam, to generate cooling in the transverse direction along the laser cooling beam propagation axis. The molecules moving along the propagation axis of the laser

cooling beam climb an AC-Stark shift-generated potential hill formed by the interference between the forward and retro-reflected laser cooling beams. For blue detuned light, the molecules move up the hill, then through a combination of optical pumping and magnetic field remixing, return to the minimum of the potential hill while dissipating the difference in potential energy from the top to the bottom of the hill as a frequency shift in the emitted photon. The magnetic remixing is important to the process, as it ensures rapid remixing due to the Zeeman precession, and works best when the remixing magnetic field is oriented at  $45^\circ$  relative to the laser light polarization. Figure 8.14 shows the experimental apparatus.

There is another effect at work here and that is Doppler cooling/heating. Doppler cooling happens when the counter-propagating laser beams are red-detuned relative to the molecular transition. As the molecule moves along the laser beam, the Doppler shift moves the counter-propagating beam closer to resonance resulting in a proclivity to absorb photons coming from the direction against the motion of the molecule which on average cools the molecule. Blue detuning has the opposite effect.

The Doppler cooling/heat and Sisyphus heating/cooling have opposite dependences on the detuning, thus these two processes compete. The Sisyphus process has a smaller capture velocity but the amount of energy removed per photon is related to the AC-Stark shift and can be much larger than an equivalent heating event from the Doppler processes happening simultaneously. In the case of Sisyphus heating, this competition generates a molecular beam with two spatial lobes at approximately  $\pm V_{capture}$ , where the

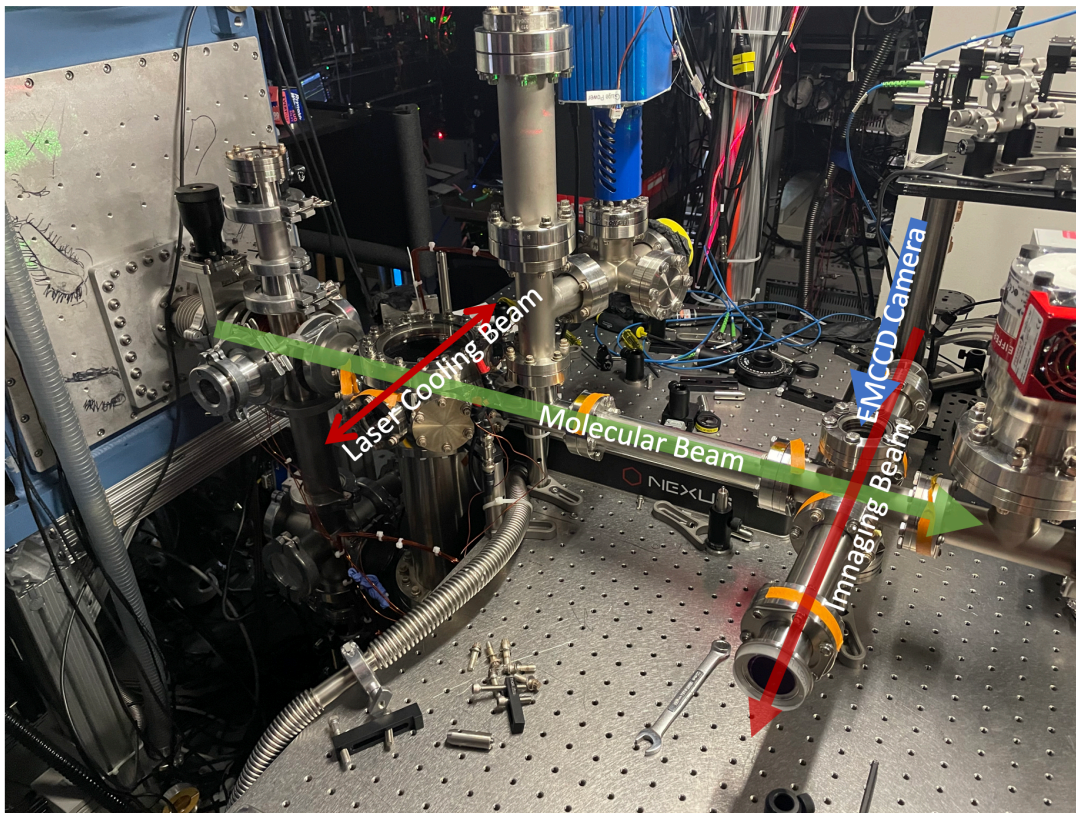


**Figure 8.14:** Schematic overview of the laser cooling setup. The laser cooling beams are retro-reflected in the first region (old CaF MOT chamber), after the collimating aperture. The  $V = 1$  repump light is combined with the mainline in this region. 70 cm downstream, a vertical beam acts as the detection beam and an EMCCD camera in the horizontal plane images the compression or heating of the molecular beam along the direction of the cooling laser beam propagation axis.

Sisyphus mechanism is heating the beam to  $\pm V_{capture}$  and the doppler process is cooling beam, but less effectively than Sisyphus heating in the temperature range corresponding to mean thermal velocities above  $V_{capture}$ .

We optimized the laser cooling beams by maximizing the depletion of the molecular beam on the photon cycling transition in the cooling region. This ensures good overlap between the cooling beam, imaging beam, and molecular beam. Next, we generated a 2 Gauss magnetic field and set the crossed polarizations of the two spin-rotation components of the cooling beam at  $45^\circ$  relative to the magnetic field. Based on the laser power available and the minimum 9 mm cooling laser beam size, we illuminated the molecules with roughly  $20 \text{ mW/cm}^2$  of mainline light. This was enough to see a definitive Sisyphus heating feature and a measurable cooling of the molecular beam with a photon budget of only 20 photons. See figure 8.16. The Sisyphus heating feature appeared with a laser intensity of roughly  $20 \text{ mW/cm}^2$  and at a detuning of -15 MHz. We also observed a small amount of Sisyphus cooling, shown in Figure 8.16. We were unable to make the cooling feature any more pronounced, leading us to wonder if the small spin-rotation splitting in  $\text{CaNH}_2$  is an issue. At a detuning of -15 MHz, the light is nearly in between the spin-rotation components which could result in competing Sisyphus heating and cooling effects.  $\text{CaOCH}_3$  has a small spin-rotation splitting and in that case, a single laser frequency was used and detuned to the blue/red of both spin-rotation lines, however in  $\text{CaNH}_2$  the spin-rotation splitting is too large to off-resonantly drive in the same way.

We attempted to remedy the problem by increasing the spin-rotation sideband spacing from 40 MHz to 50 MHz and then set the detuning to +5 MHz. The idea is that the sideband at +15 MHz relative to one spin-rotation component will drive Sisyphus cooling while the other sideband +5 MHz detuned from its associated spin-rotation branch acts as a repump beam, but it is too far detuned from the other spin-rotation component to drive a competing Sisyphus process. We saw no sign of Sisyphus heating or cooling from this configuration, so the spin-rotation side band frequency was returned to 40 MHz.

#### 8.10.1 SUM FREQUENCY LASER SOURCE

The available laser power for the mainline beam, generated by a dye laser, was marginal at best. Using the dye lasers, we had roughly 100 mW of light available at the molecules, whereas CaOH, CaOCH<sub>3</sub>, and YbOH all used 1-Watt-scale solid-state laser sources for cooling. We made significant improvements to the apparatus by building a sum-frequency solid-state laser system to replace the dye laser still in use for the mainline light. Using a 10 Watt 1549 nm beam and a 10 Watt 1062 nm beam combined on a periodically poled crystal, we generated 5 Watts of mainline light. The light is fiber coupled to an acousto-optical modulator used to generate the 40 MHz spin-rotation sidebands for the mainline.

The new source delivered 1 Watt of mainline light to the experiment. The molecular beam depletion improved from roughly 90% to 100%, where we could not see any detectable molecular signal in the detection chamber after averaging the signal for 1000

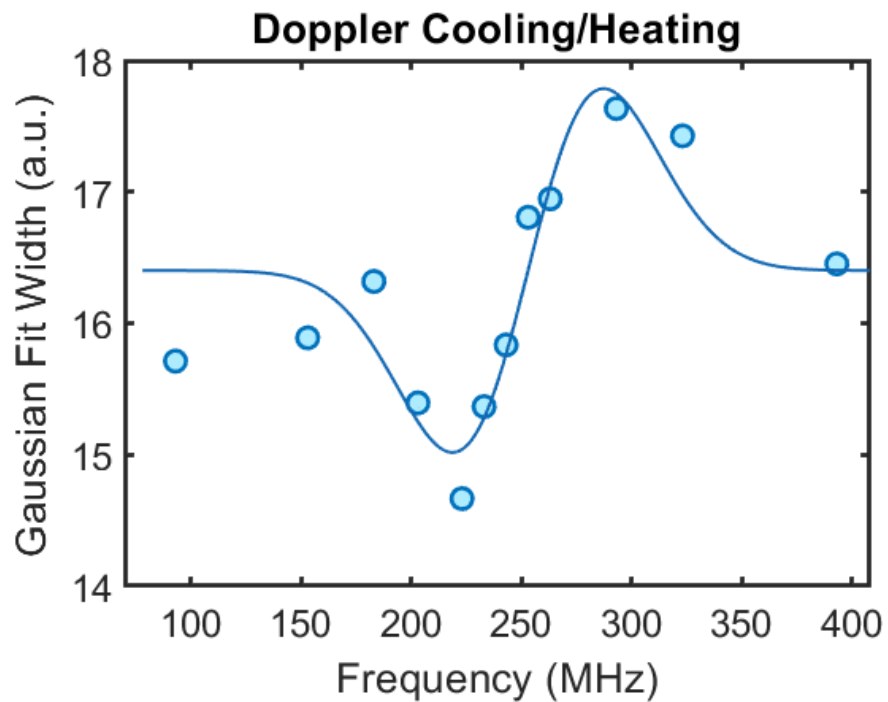


**Figure 8.15:** Doppler cooling is observed when the cooling beams are retro-reflected without forming a standing wave. The y-axis is the width of the molecular beam after 70 cm of propagation, which is a direct measurement of the transverse temperature. Compression of the cloud indicates cooling while expansion corresponds to heating. Cooling is observed when the detuning is red of the transition (283 MHz on this plot) and heating is observed on the blue detuned side. This is the opposite of Sisyphus cooling/heating. Both spin-rotation sideband components are present.

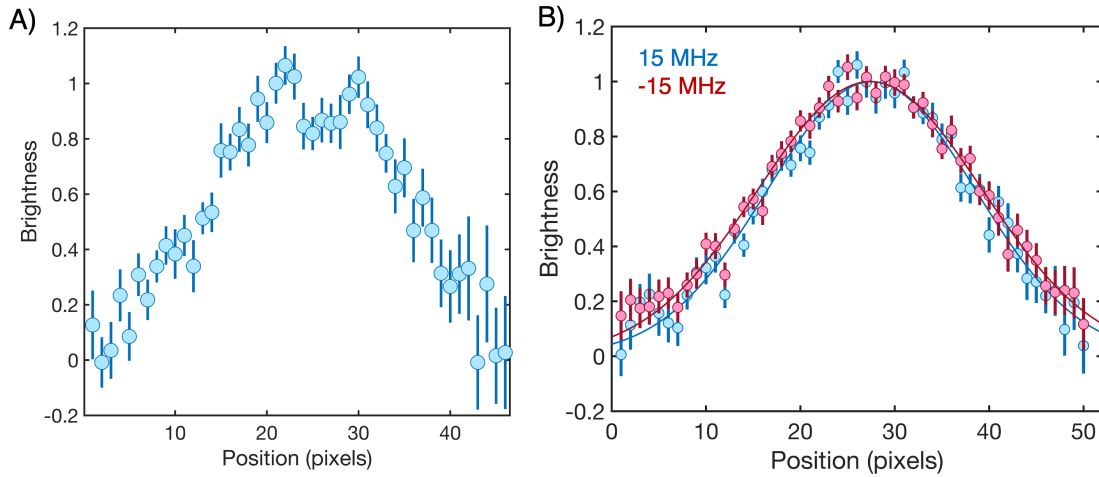


**Figure 8.16:** Sisyphus heating and cooling features. In Figure A, we observed a clear Sisyphus heating feature with the signature double peaks indicating population build-up near the capture velocity for Sisyphus heating/cooling. In Figure B, we compared the width of the imaged molecular beam at  $\pm 15$  MHz detuning. No clear Sisyphus heating feature was observed, however, the Sisyphus heating configuration resulted in a molecular beam with a width of  $16.8 \pm 0.2$  pixels while the blue detuned cooling configuration fit to a width of  $15.6 \pm 0.2$  pixels, indicating a small amount of Sisyphus cooling.

shots on the EMCCD camera. We added the  $V = 1$  repump light to the detection region which vastly improved the signal.

With the new sum-frequency laser source, we tried to observe Sisyphus cooling and heating. We saw a signature of Doppler cooling (Figure 8.15) when the retro-beam was slightly misaligned, interrupting the Sisyphus mechanism. Next, we added both  $V = 1$  and  $V = 2$  repumps to the laser cooling beam path in hopes that cycling a few additional photons would make the laser cooling signal more observable.

## 8.11 SUMMARY

We understood the structure of a simple asymmetric top molecule,  $\text{CaNH}_2$ , chosen as a symmetry-related stand-in for  $\text{CaOPh}$ . The goal was to establish that photon cycling and laser cooling on a near prolate asymmetric top molecule is possible. We cycled 30 photons, found two vibrational repump transitions, and discovered a rotational leakage channel that will need to be repumped as well, although we did not observe additional photon scattering when the  $N = 2$  rotational repump was added. Despite our efforts, we have evidence of another loss channel entering at the 3% level that we were unable to find. It's not clear what this loss channel is. Our DLIF measurements do not show any other substantial losses to any vibrational modes we observed. The measured rotational leakage rate is likely too small to explain the losses. Regardless, we demonstrated 1D Sisyphus laser cooling of an asymmetric top molecule.

# 9

## Conclusion

In this thesis, we explored the properties of CaF molecules in optical tweezers and optical dipole traps and laid the foundation for laser cooling of organic-inspired asymmetric top molecules.

Starting with a diatomic molecule, calcium monofluoride, we developed an optical tweezer platform for use in quantum computing and demonstrated rotational coherence

times significantly longer than measured dipole-enabled gate times. Our 100 ms Ramsey coherence time and 500 ms spin-echo coherence time exceed the previous record-long rotational coherence time of molecules in an optical trap by an order of magnitude. This was also the first measurement of the rotational coherence time of a trapped polar molecule in an optical tweezer. We identified residual tensor stark shifts as the limiting factor, which can be reduced by further cooling. Raman side-band cooling would be the ideal method for further cooling the molecules in an optical tweezer trap. Raman side-band cooling is currently under investigation in the second-generation CaF experiment. The combination of the long rotational coherence time reported here with the strong dipolar interactions recently observed in the CaF second-generation experiment indicates significant progress of the platform for future uses in quantum computing.

Using the Tweezer platform, we studied ultracold collisions of exactly two molecules and exerted full quantum control over the internal structure of the molecules. The collisions resulted in a rapid loss from the tweezers, leading us to develop a microwave shield to prevent these lossy collisions, suppressing the loss rate by a factor of 6. The shielding was limited by a simple anisotropic interaction between the molecules and the optical tweezer light which can be mitigated in a bulk gas sample by using a larger trap with significantly lower peak intensity. The shielding scheme enhanced the rate of elastic collisions enabling the demonstration of forced evaporative cooling. Our evaporative cooling scheme was heavily limited by the low number and density of molecules, which slowed down the rate of elastic collisions to the point at which the finite dressed state

lifetime was a severe problem. High-density samples and lower phase noise microwave sources are predicted to improve the situation.

We explored the possible use of larger molecules for quantum science, by studying the rotational structure of an asymmetric top and aromatic molecule, calcium monophenoxide, to identify a path toward laser cooling and trapping. We cycled several photons, but theory predicted many more. After eliminating several decay paths, the key loss remained unknown. Applying the same methods to  $\text{CaNH}_2$ , a smaller asymmetric top molecule with similar spatial symmetry, we performed laser cooling. Using  $\text{CaNH}_2$ , we demonstrated photon cycling, and then observed Doppler as well as Sisyphus cooling and heating features for the first time using an asymmetric top molecule. This work lays the foundation for future laser-cooling of organic-inspired molecules in an optical tweezer array for applications ranging from quantum computing to quantum chemistry, and precision measurement.

The path forward for the CaOPh experiment will require finding and hopefully repumping the unknown loss channel. Depending on the nature of the loss, a repumping pathway is not guaranteed. It is our hope that the leakage channel can be closed well enough to cycle several 10,000's of photons, enough to do laser slowing, load a MOT, transfer to an optical tweezer, and then do high-fidelity detection of the tweezer-trapped sample. A large organic-inspired molecule that can be fully controlled in an optical tweezer is an exciting prospect that we hope is attainable. The outlook for CaF as a good qubit is bright and we hope a digital quantum computer based on trapped

ultracold laser-cooled molecules in optical tweezers will be available in the foreseeable future.

# References

- [1] ACME Collaboration (2014). Order of magnitude smaller limit on the electric dipole moment of the electron. *Science*, 343(6168), 269–272.
- [2] Albert, V. V., Covey, J. P., & Preskill, J. (2020). Robust encoding of a qubit in a molecule. *Phys. Rev. X*, 10(3), 031050.
- [3] Anderegg, L., Augenbraun, B. L., Bao, Y., Burchesky, S., Cheuk, L. W., Ketterle, W., & Doyle, J. M. (2018a). Laser cooling of optically trapped molecules. *Nature Physics*, 14(9), 890–893.
- [4] Anderegg, L., Augenbraun, B. L., Bao, Y., Burchesky, S., Cheuk, L. W., Ketterle, W., & Doyle, J. M. (2018b). Laser cooling of optically trapped molecules. *arXiv:1803.04571*.
- [5] Anderegg, L., Augenbraun, B. L., Chae, E., Hemmerling, B., Hutzler, N. R., Ravi, A., Collopy, A., Ye, J., Ketterle, W., & Doyle, J. M. (2017). Radio frequency magneto-optical trapping of CaF with high density. *Physical Review Letters*, 119(10).
- [6] Anderegg, L., Cheuk, L. W., Bao, Y., Burchesky, S., Ketterle, W., Ni, K.-K., & Doyle, J. M. (2019). An optical tweezer array of ultracold molecules. *Science*, 365(6458), 1156.
- [7] Aspect, A., Arimondo, E., Kaiser, R., Vansteenkiste, N., & Cohen-Tannoudji, C. (1988). Laser cooling below the one-photon recoil energy by velocity-selective coherent population trapping. *Phys. Rev. Lett.*, 61, 826–829.
- [8] Augenbraun, B. L., Burchesky, S., Winnicki, A., & Doyle, J. M. (2022). High-resolution laser spectroscopy of a functionalized aromatic molecule. *The Journal of Physical Chemistry Letters*, 13(46), 10771–10777. PMID: 36374523.

- [9] Augenbraun, B. L., Doyle, J. M., Zelevinsky, T., & Kozyryev, I. (2020a). Molecular asymmetry and optical cycling: Laser cooling asymmetric top molecules. *Phys. Rev. X*, 10(3), 031022.
- [10] Augenbraun, B. L., Lasner, Z. D., Frenett, A., Sawaoka, H., Miller, C., Steimle, T. C., & Doyle, J. M. (2020b). Laser-cooled polyatomic molecules for improved electron electric dipole moment searches. *New J. Phys.*, 22(2), 022003.
- [11] Augustovičová, L. D. & Bohn, J. L. (2019). Ultracold collisions of polyatomic molecules: CaOH. *New J. Phys.*, 21(10), 103022.
- [12] Bakr, W. S., Gillen, J. I., Peng, A., Fölling, S., & Greiner, M. (2009). A quantum gas microscope for detecting single atoms in a hubbard-regime optical lattice. *Nature*, 462, 74.
- [13] Balakrishnan, N. (2016). Perspective: Ultracold molecules and the dawn of cold controlled chemistry. *The Journal of Chemical Physics*, 145(15), 150901.
- [14] Bali, S., Hoffmann, D., & Walker, T. (1994). Novel intensity dependence of ultracold collisions involving repulsive states. *Europhysics Letters (EPL)*, 27(4), 273–277.
- [15] Bao, Y., Yu, S. S., Anderegg, L., Chae, E., Ketterle, W., Ni, K.-K., & Doyle, J. M. (2022). Dipolar spin-exchange and entanglement between molecules in an optical tweezer array.
- [16] Barredo, D., de Léséleuc, S., Lienhard, V., Lahaye, T., & Browaeys, A. (2016). An atom-by-atom assembler of defect-free arbitrary two-dimensional atomic arrays. *Science*, 354(6315), 1021–1023.
- [17] Barry, J. F., McCarron, D. J., Norrgard, E. B., Steinecker, M. H., & DeMille, D. (2014). Magneto-optical trapping of a diatomic molecule. *Nature*, 512(7514), 286–289.
- [18] Baum, L. (2020). *Laser Cooling and 1D Magneto-Optical Trapping of Calcium Monohydroxide*. PhD thesis, Cambridge MA.
- [19] Bause, R., Li, M., Schindewolf, A., Chen, X.-Y., Duda, M., Kotochigova, S., Bloch, I., & Luo, X.-Y. (2020). Tune-out and magic wavelengths for ground-state  $^{23}\text{Na}^{40}\text{K}$  molecules. *Phys. Rev. Lett.*, 125, 023201.

- [20] Bernien, H., Schwartz, S., Keesling, A., Levine, H., Omran, A., Pichler, H., Choi, S., Zibrov, A. S., Endres, M., Greiner, M., Vuletić, V., & Lukin, M. D. (2017). Probing many-body dynamics on a 51-atom quantum simulator. *Nature*, 551, 579.
- [21] Blackmore, J. A., Caldwell, L., Gregory, P. D., Bridge, E. M., Sawant, R., Aldegunde, J., Mur-Petit, J., Jaksch, D., Hutson, J. M., Sauer, B. E., Tarbutt, M. R., & Cornish, S. L. (2018). Ultracold molecules for quantum simulation: rotational coherences in CaF and RbCs. *Quantum Science and Technology*, 4(1), 014010.
- [22] Blackmore, J. A., Sawant, R., Gregory, P. D., Bromley, S. L., Aldegunde, J., Hutson, J. M., & Cornish, S. L. (2020). Controlling the ac stark effect of rbc's with dc electric and magnetic fields. *Phys. Rev. A*, 102, 053316.
- [23] Bourgain, R., Pellegrino, J., Fuhrmanek, A., Sortais, Y. R. P., & Browaeys, A. (2013). Evaporative cooling of a small number of atoms in a single-beam microscopic dipole trap. *Phys. Rev. A*, 88, 023428.
- [24] Brown, M. O., Thiele, T., Kiehl, C., Hsu, T.-W., & Regal, C. A. (2019). Gray-molasses optical-tweezer loading: Controlling collisions for scaling atom-array assembly. *Phys. Rev. X*, 9, 011057.
- [25] Burchianti, A., Valtolina, G., Seman, J. A., Pace, E., Pas, M. D., Inguscio, M., Zaccanti, M., & Roati, G. (2014). Efficient all-optical production of large Li6 quantum gases using D1 gray-molasses cooling. *Physical Review A*, 90(4).
- [26] Büchler, H. P., Micheli, A., & Zoller, P. (2007). Three-body interactions with cold polar molecules. *Nature Physics*, 3(10), 726–731.
- [27] Cairncross, W. B., Zhang, J. T., Picard, L. R. B., Yu, Y., Wang, K., & Ni, K.-K. (2021). Assembly of a rovibrational ground state molecule in an optical tweezer. *Arxiv*.
- [28] Caldwell, L. & Tarbutt, M. (2020). Enhancing dipolar interactions between molecules using state-dependent optical tweezer traps. *Physical Review Letters*, 125(24), 243201.
- [29] Caldwell, L., Williams, H., Fitch, N., Aldegunde, J., Hutson, J. M., Sauer, B., & Tarbutt, M. (2020). Long rotational coherence times of molecules in a magnetic trap. *Physical Review Letters*, 124(6), 063001.

- [30] Carr, L. D., DeMille, D., Krems, R. V., & Ye, J. (2009a). Cold and ultracold molecules: science, technology and applications. *New Journal of Physics*, 11(5), 055049.
- [31] Carr, L. D., DeMille, D., Krems, R. V., & Ye, J. (2009b). Cold and Ultracold Molecules: Science, Technology and Applications. *New J. Phys.*, 11(5).
- [32] Chae, E. (2021). Entanglement via rotational blockade of mgf molecules in a magic potential. *Phys. Chem. Chem. Phys.*, 23, 1215–1220.
- [33] Chen, Z., Bohnet, J. G., Weiner, J. M., & Thompson, J. K. (2012). General formalism for evaluating the impact of phase noise on bloch vector rotations. *Phys. Rev. A*, 86, 032313.
- [34] Cheuk, L. W., Anderegg, L., Augenbraun, B. L., Bao, Y., Burchesky, S., Ketterle, W., & Doyle, J. M. (2018).  $\Lambda$ -enhanced imaging of molecules in an optical trap. *Physical Review Letters*, 121(8), 083201.
- [35] Cheuk, L. W., Anderegg, L., Bao, Y., Burchesky, S., Yu, S. S., Ketterle, W., Ni, K.-K., & Doyle, J. M. (2020). Observation of collisions between two ultracold ground-state CaF molecules. *Phys. Rev. Lett.*, 125(4).
- [36] Cheuk, L. W., Nichols, M. A., Okan, M., Gersdorf, T., Ramasesh, V. V., Bakr, W. S., Lompe, T., & Zwierlein, M. W. (2015). Quantum-gas microscope for fermionic atoms. *Phys. Rev. Lett.*, 114, 193001.
- [37] Christianen, A., Karman, T., & Groenenboom, G. C. (2019a). Quasiclassical method for calculating the density of states of ultracold collision complexes. *Phys. Rev. A*, 100, 032708.
- [38] Christianen, A., Zwierlein, M. W., Groenenboom, G. C., & Karman, T. (2019b). Photoinduced two-body loss of ultracold molecules. *Phys. Rev. Lett.*, 123, 123402.
- [39] Collopy, A. L., Ding, S., Wu, Y., Finneran, I. A., Anderegg, L., Augenbraun, B. L., Doyle, J. M., & Ye, J. (2018). 3d magneto-optical trap of yttrium monoxide. *Physical Review Letters*, 121(21).
- [40] Colzi, G., Durastante, G., Fava, E., Serafini, S., Lamporesi, G., & Ferrari, G. (2016). Sub-doppler cooling of sodium atoms in gray molasses. *Phys. Rev. A*, 93(2), 023421.

- [41] Cooper, A., Covey, J. P., Madjarov, I. S., Porsev, S. G., Safronova, M. S., & Endres, M. (2018). Alkaline-earth atoms in optical tweezers. *Physical Review X*, 8(4).
- [42] Czuba, K. & Sikora, D. (2010). Phase drift versus temperature measurements of coaxial cables. In *18-th INTERNATIONAL CONFERENCE ON MICROWAVES, RADAR AND WIRELESS COMMUNICATIONS* (pp. 1–3).
- [43] de Miranda, M. H. G., Chotia, A., Neyenhuis, B., Wang, D., Quéméner, G., Ospelkaus, S., Bohn, J. L., Ye, J., & Jin, D. S. (2011). Controlling the quantum stereodynamics of ultracold bimolecular reactions. *Nature Physics*, 7(6), 502–507.
- [44] DeMille, D. (2002). Quantum computation with trapped polar molecules. *Physical Review Letters*, 88(6), 067901.
- [45] Devlin, J. A. & Tarbutt, M. R. (2016). Three-dimensional doppler, polarization-gradient, and magneto-optical forces for atoms and molecules with dark states. *New J. Phys.*, 18(12), 123017.
- [46] Dickerson, C. E., Guo, H., Shin, A. J., Augenbraun, B. L., Caram, J. R., Campbell, W. C., & Alexandrova, A. N. (2021a). Franck-condon tuning of optical cycling centers by organic functionalization. *Phys. Rev. Lett.*, 126(12).
- [47] Dickerson, C. E., Guo, H., Zhu, G.-Z., Hudson, E. R., Caram, J. R., Campbell, W. C., & Alexandrova, A. N. (2021b). Optical cycling functionalization of arenes. *J. Phys. Chem. Lett.*, 12(16), 3989–3995.
- [48] Endres, M., Bernien, H., Keesling, A., Levine, H., Anschuetz, E. R., Krajenbrink, A., Senko, C., Vuletic, V., Greiner, M., & Lukin, M. D. (2016). Atom-by-atom assembly of defect-free one-dimensional cold atom arrays. *Science*, 354(6315), 1024–1027.
- [49] Frye, M. D., Julienne, P. S., & Hutson, J. M. (2015). Cold atomic and molecular collisions: approaching the universal loss regime. *New Journal of Physics*, 17(4), 045019.
- [50] González-Martínez, M. L., Bohn, J. L., & Quéméner, G. (2017). Adimensional theory of shielding in ultracold collisions of dipolar rotors. *Phys. Rev. A*, 96(3), 032718.

- [51] Gorshkov, A. V., Rabl, P., Pupillo, G., Micheli, A., Zoller, P., Lukin, M. D., & Büchler, H. P. (2008). Suppression of inelastic collisions between polar molecules with a repulsive shield. *Phys. Rev. Lett.*, 101, 073201.
- [52] Gregory, P. D., Aldegunde, J., Hutson, J. M., & Cornish, S. L. (2016). Controlling the rotational and hyperfine state of ultracold  $^{87}\text{Rb}^{133}\text{Cs}$  molecules. *Phys. Rev. A*, 94(4), 041403.
- [53] Gregory, P. D., Frye, M. D., Blackmore, J. A., Bridge, E. M., Sawant, R., Hutson, J. M., & Cornish, S. L. (2019). Sticky collisions of ultracold rbc molecules. *Nature Communications*, 10(1), 3104.
- [54] Gribakin, G. F. & Flambaum, V. V. (1993). Calculation of the scattering length in atomic collisions using the semiclassical approximation. *Phys. Rev. A*, 48, 546–553.
- [55] Grier, A. T., Ferrier-Barbut, I., Rem, B. S., Delehay, M., Khaykovich, L., Chevy, F., & Salomon, C. (2013).  $\Lambda$ -enhanced sub-doppler cooling of lithium atoms in  $D_1$  gray molasses. *Phys. Rev. A*, 87, 063411.
- [56] Grynberg, G. & Courtois, J.-Y. (1994). Proposal for a magneto-optical lattice for trapping atoms in nearly-dark states. *Europhysics Letters (EPL)*, 27(1), 41–46.
- [57] Guo, M., Zhu, B., Lu, B., Ye, X., Wang, F., Vexiau, R., Bouloufa-Maafa, N., Quémener, G., Dulieu, O., & Wang, D. (2016). Creation of an ultracold gas of ground-state dipolar  $^{23}\text{Na}^{87}\text{Rb}$  molecules. *Phys. Rev. Lett.*, 116, 205303.
- [58] H R Sadeghpour, J L Bohn, M. J. C. B. D. E. I. I. F. J. H. M. & Rau, A. R. P. (2000). Collisions near threshold in atomic and molecular physics. *Journal of Physics B: Atomic, Molecular and Optical Physics*, 33, 051403.
- [59] Haller, E., Hudson, J., Kelly, A., Cotta, D. A., Peaudecerf, B., Bruce, G. D., & Kuhr, S. (2015). Single-atom imaging of fermions in a quantum-gas microscope. *Nature Physics*, 11, 738.
- [60] Holland, C. M., Lu, Y., & Cheuk, L. W. (2022). On-demand entanglement of molecules in a reconfigurable optical tweezer array.

- [61] Hood, J. D., Yu, Y., Lin, Y.-W., Zhang, J. T., Wang, K., Liu, L. R., Gao, B., & Ni, K.-K. (2019). Multichannel interactions of two atoms in an optical tweezer. *arXiv:1907.11226v1*.
- [62] Hu, M.-G., Liu, Y., Grimes, D. D., Lin, Y.-W., Gheorghe, A. H., Vexiau, R., Bouloufa-Maafa, N., Dulieu, O., Rosenband, T., & Ni, K.-K. (2019). Direct observation of bimolecular reactions of ultracold krb molecules. *Science*, 366(6469), 1111–1115.
- [63] Hughes, M., Frye, M. D., Sawant, R., Bhole, G., Jones, J. A., Cornish, S. L., Tarbutt, M. R., Hutson, J. M., Jaksch, D., & Mur-Petit, J. (2020). Robust entangling gate for polar molecules using magnetic and microwave fields. *Physical Review A*, 101(6), 062308.
- [64] Hutzler, N. R. (2020). Polyatomic molecules as quantum sensors for fundamental physics. *Quantum Sci. Technol.*, 5(4), 044011.
- [65] Idziaszek, Z. & Julienne, P. S. (2010). Universal rate constants for reactive collisions of ultracold molecules. *Phys. Rev. Lett.*, 104, 113202.
- [66] Isaev, T. & Berger, R. (2016). Polyatomic candidates for cooling of molecules with lasers from simple theoretical concepts. *Phys. Rev. Lett.*, 116(6), 063006.
- [67] Isaev, T., Zaitsevskii, A., & Eliav, E. (2017). Laser-coolable polyatomic molecules with heavy nuclei. *J. Phys. B*, 50(22), 225101.
- [68] Ivanov, M. V., Bangerter, F. H., Wójcik, P., & Krylov, A. I. (2020). Toward ultracold organic chemistry: Prospects of laser cooling large organic molecules. *J. Phys. Chem. Lett.*, 11(16), 6670–6676.
- [69] Jansen, P., Bethlem, H. L., & Ubachs, W. (2014). Tipping the scales: Search for drifting constants from molecular spectra. *J. Chem. Phys.*, 140(1), 010901.
- [Jones] Jones, J. A. Implementation of a quantum algorithm on a nuclear magnetic resonance quantum computer. *The Journal of Chemical Physics*, 109, 1648.
- [71] Julienne, P. (1996). Cold binary atomic collisions in a light field. *Journal of Research of the National Institute of Standards and Technology*, 101(4), 487.

- [72] Kara, D. M., Smallman, I. J., Hudson, J. J., Sauer, B. E., Tarbutt, M. R., & Hinds, E. A. (2012). Measurement of the electron's electric dipole moment using YbF molecules: methods and data analysis. *New Journal of Physics*, 14(10), 103051.
- [73] Karman, T. (2020). Microwave shielding with far-from-circular polarization. *Physical Review A*, 101(4), 042702.
- [74] Karman, T. & Hutson, J. M. (2018). Microwave shielding of ultracold polar molecules. *Phys. Rev. Lett.*, 121, 163401.
- [75] Karman, T. & Hutson, J. M. (2019). Microwave shielding of ultracold polar molecules with imperfectly circular polarization. *Physical Review A*, 100(5), 052704.
- [76] Karra, M., Sharma, K., Friedrich, B., Kais, S., & Herschbach, D. (2016). Prospects for quantum computing with an array of ultracold polar paramagnetic molecules. *The Journal of Chemical Physics*, 144(9), 094301.
- [77] Kaufman, A. M., Lester, B. J., & Regal, C. A. (2012). Cooling a single atom in an optical tweezer to its quantum ground state. *Physical Review X*, 2(4).
- [78] Kotochigova, S. & DeMille, D. (2010). Electric-field-dependent dynamic polarizability and state-insensitive conditions for optical trapping of diatomic polar molecules. *Phys. Rev. A*, 82, 063421.
- [79] Kozyryev, I., Baum, L., Matsuda, K., Augenbraun, B. L., Anderegg, L., Sedlack, A. P., & Doyle, J. M. (2017). Sisyphus laser cooling of a polyatomic molecule. *Phys. Rev. Lett.*, 118, 173201.
- [80] Kozyryev, I., Baum, L., Matsuda, K., & Doyle, J. M. (2016a). Proposal for laser cooling of complex polyatomic molecules. *ChemPhysChem*, 17(22), 3641–3648.
- [81] Kozyryev, I., Baum, L., Matsuda, K., & Doyle, J. M. (2016b). Proposal for laser cooling of complex polyatomic molecules. *ChemPhysChem*, 17, 3641.
- [82] Kozyryev, I. & Hutzler, N. R. (2017a). Precision measurement of time-reversal symmetry violation with laser-cooled polyatomic molecules. *Physical Review Letters*, 119(13).

- [83] Kozyryev, I. & Hutzler, N. R. (2017b). Precision measurement of time-reversal symmetry violation with laser-cooled polyatomic molecules. *Phys. Rev. Lett.*, 119, 133002.
- [84] Kozyryev, I., Lasner, Z., & Doyle, J. M. (2021). Enhanced sensitivity to ultralight bosonic dark matter in the spectra of the linear radical SrOH. *Phys. Rev. A*, 103(4).
- [85] Kraft, U. (1996). Main-beam polarization properties of four-element sequential-rotation arrays with arbitrary radiators. *IEEE Transactions on Antennas and Propagation*, 44(4), 515–522.
- [86] Krems, R. V. (2008a). Cold controlled chemistry. *Phys. Chem. Chem. Phys.*, 10(28), 4079–4092.
- [87] Krems, R. V. (2008b). Cold controlled chemistry. *Physical Chemistry Chemical Physics*, 10(28), 4079.
- [88] Lawall, J., Bardou, F., Saubamea, B., Shimizu, K., Leduc, M., Aspect, A., & Cohen-Tannoudji, C. (1994). Two-dimensional subrecoil laser cooling. *Phys. Rev. Lett.*, 73, 1915–1918.
- [89] Lawall, J., Kulin, S., Saubamea, B., Bigelow, N., Leduc, M., & Cohen-Tannoudji, C. (1995). Three-dimensional laser cooling of helium beyond the single-photon recoil limit. *Phys. Rev. Lett.*, 75, 4194–4197.
- [90] Lim, J., Almond, J. R., Tarbutt, M., Nguyen, D. T., & Steimle, T. C. (2017). The [557]-X<sup>2</sup>Σ and [561]-X<sup>2</sup>Σ bands of ytterbium fluoride, <sup>174</sup>YbF. *J. Mol. Spec.*, 338, 81–90.
- [91] Lin, J., He, J., Ye, X., & Wang, D. (2021). Anisotropic polarizability of ultracold ground-state <sup>23</sup>Na<sup>87</sup>Rb molecules. *Phys. Rev. A*, 103, 023332.
- [92] Liu, J. (2018). Rotational and fine structure of open-shell molecules in nearly degenerate electronic states. *J. Chem. Phys.*, 148(12), 124112.
- [93] Liu, L. R., Hood, J. D., Yu, Y., Zhang, J. T., Hutzler, N. R., Rosenband, T., & Ni, K.-K. (2018a). Building one molecule from a reservoir of two atoms. *Science*, 360(6391), 900–903.

- [94] Liu, L. R., Hood, J. D., Yu, Y., Zhang, J. T., Hutzler, N. R., Rosenband, T., & Ni, K.-K. (2018b). Building one molecule from a reservoir of two atoms. *Science*, 360(6391), 900.
- [95] Mayle, M., Quéméner, G., Ruzic, B. P., & Bohn, J. L. (2013). Scattering of ultracold molecules in the highly resonant regime. *Phys. Rev. A*, 87, 012709.
- [96] Mayle, M., Ruzic, B. P., & Bohn, J. L. (2012). Statistical aspects of ultracold resonant scattering. *Phys. Rev. A*, 85, 062712.
- [97] McCarron, D., Steinecker, M., Zhu, Y., & DeMille, D. (2018). Magnetic trapping of an ultracold gas of polar molecules. *Physical Review Letters*, 121(1).
- [98] McCarron, D. J., Steinecker, M. H., Zhu, Y., & DeMille, D. (2017). Magnetically-trapped molecules efficiently loaded from a molecular mot. *ArXiv e-prints*.
- [99] Micheli, A., Brennen, G. K., & Zoller, P. (2006). A toolbox for lattice-spin models with polar molecules. *Nature Physics*, 2(5), 341–347.
- [100] Migdall, A. L., Prodan, J. V., Phillips, W. D., Bergeman, T. H., & Metcalf, H. J. (1985). First observation of magnetically trapped neutral atoms. *Phys. Rev. Lett.*, 54, 2596–2599.
- [101] Mitra, D., Vilas, N. B., Hallas, C., Anderegg, L., Augenbraun, B. L., Baum, L., Miller, C., Raval, S., & Doyle, J. M. (2020a). Direct laser cooling of a symmetric top molecule. *Science*, 369(6509), 1366–1369.
- [102] Mitra, D., Vilas, N. B., Hallas, C., Anderegg, L., Augenbraun, B. L., Baum, L., Miller, C., Raval, S., & Doyle, J. M. (2020b). Direct laser cooling of a symmetric top molecule. *Science*, 369(6509), 1366–1369.
- [103] Molony, P. K., Gregory, P. D., Ji, Z., Lu, B., Köppinger, M. P., Le Sueur, C. R., Blackley, C. L., Hutson, J. M., & Cornish, S. L. (2014). Creation of ultracold  $\text{Rb}^{87}\text{Cs}^{133}$  molecules in the rovibrational ground state. *Phys. Rev. Lett.*, 113(25), 255301.
- [104] Morbi, Zhao, B. (1997). A high resolution analysis of the transition pure precession in polyatomic molecules. *The Journal of Chemical Physics*, 106, 4860.

- [105] Napolitano, R., Weiner, J., & Julienne, P. S. (1997). Theory of optical suppression of ultracold-collision rates by polarized light. *Physical Review A*, 55(2), 1191–1207.
- [106] Neyenhuis, B., Yan, B., Moses, S. A., Covey, J. P., Chotia, A., Petrov, A., Kotochigova, S., Ye, J., & Jin, D. S. (2012). Anisotropic polarizability of ultracold PolarK40rb87molecules. *Physical Review Letters*, 109(23).
- [107] Ni, K.-K., Ospelkaus, S., de Miranda, M. H. G., Pe’er, A., Neyenhuis, B., Zirbel, J. J., Kotochigova, S., Julienne, P. S., Jin, D. S., & Ye, J. (2008). A high phase-space-density gas of polar molecules. *Science*, 322(5899), 231.
- [108] Ni, K.-K., Rosenband, T., & Grimes, D. D. (2018a). Dipolar exchange quantum logic gate with polar molecules. *Chemical Science*, 9(33), 6830–6838.
- [109] Ni, K.-K., Rosenband, T., & Grimes, D. D. (2018b). Dipolar exchange quantum logic gate with polar molecules. *Chem. Sci.*, 9(33), 6830–6838.
- [110] Nichols, M. A., Liu, Y.-X., Zhu, L., Hu, M.-G., Liu, Y., & Ni, K.-K. (2022). Detection of long-lived complexes in ultracold atom-molecule collisions. *Phys. Rev. X*, 12, 011049.
- [111] Norcia, M., Young, A., & Kaufman, A. (2018). Microscopic control and detection of ultracold strontium in optical-tweezer arrays. *Physical Review X*, 8(4).
- [112] Norrgard, E., McCarron, D., Steinecker, M., Tarbutt, M., & DeMille, D. (2016). Sub-millikelvin dipolar molecules in a radio-frequency magneto-optical trap. *Phys. Rev. Lett.*, 116(6), 063004.
- [113] O’Hara, K. M., Gehm, M. E., Granade, S. R., & Thomas, J. E. (2001). Scaling laws for evaporative cooling in time-dependent optical traps. *Phys. Rev. A*, 64, 051403.
- [114] Ospelkaus, S., Ni, K.-K., Wang, D., de Miranda, M. H. G., Neyenhuis, B., Quemener, G., Julienne, P. S., Bohn, J. L., Jin, D. S., & Ye, J. (2010). Quantum-state controlled chemical reactions of ultracold potassium-rubidium molecules. *Science*, 327(5967), 853–857.
- [115] Park, J. W., Will, S. A., & Zwierlein, M. W. (2015). Ultracold dipolar gas of fermionic  $^{23}\text{Na}^{40}\text{K}$  molecules in their absolute ground state. *Phys. Rev. Lett.*, 114(20), 205302.

- [116] Parsons, M. F., Huber, F., Mazurenko, A., Chiu, C. S., Setiawan, W., Wooley-Brown, K., Blatt, S., & Greiner, M. (2015). Site-resolved imaging of fermionic  ${}^6\text{Li}$  in an optical lattice. *Phys. Rev. Lett.*, 114, 213002.
- [117] Prehn, A., Ibrügger, M., Glöckner, R., Rempe, G., & Zeppenfeld, M. (2016). Optoelectrical cooling of polar molecules to submillikelvin temperatures. *Phys. Rev. Lett.*, 116(6), 063005.
- [118] Pupillo, G., Griessner, A., Micheli, A., Ortner, M., Wang, D.-W., & Zoller, P. (2008). Cold atoms and molecules in self-assembled dipolar lattices. *Physical Review Letters*, 100(5), 050402.
- [119] Quémener, G. & Bohn, J. L. (2016). Shielding  ${}^2\Sigma$  ultracold dipolar molecular collisions with electric fields. *Phys. Rev. A*, 93, 012704.
- [120] Rosa, M. D. (2004). Laser-cooling molecules. *The European Physical Journal D*, 31(2), 395–402.
- [121] Rosenband, T., Grimes, D. D., & Ni, K.-K. (2018). Elliptical polarization for molecular stark shift compensation in deep optical traps. *Opt. Express*, 26(16), 19821–19825.
- [122] Rvachov, T. M., Son, H., Sommer, A. T., Ebadi, S., Park, J. J., Zwierlein, M. W., Ketterle, W., & Jamison, A. O. (2017). Long-lived ultracold molecules with electric and magnetic dipole moments. *Phys. Rev. Lett.*, 119(14), 143001.
- [123] Saskin, S., Wilson, J. T., Grinkemeyer, B., & Thompson, J. D. (2019). Narrow-line cooling and imaging of ytterbium atoms in an optical tweezer array. *Phys. Rev. Lett.*, 122, 143002.
- [124] Sawant, R., Blackmore, J. A., Gregory, P. D., Mur-Petit, J., Jaksch, D., Aldegunde, J., Hutson, J. M., Tarbutt, M. R., & Cornish, S. L. (2020). Ultracold polar molecules as qudits. *New Journal of Physics*, 22(1), 013027.
- [125] Schindewolf (2022). Evaporation of microwave-shielded polar molecules to quantum degeneracy. *Nature*, 607, 677–681.
- [126] Schlosser, N., Reymond, G., & Grangier, P. (2002a). Collisional blockade in microscopic optical dipole traps. *Physical Review Letters*, 89(2).

- [127] Schlosser, N., Reymond, G., & Grangier, P. (2002b). Collisional blockade in microscopic optical dipole traps. *Phys. Rev. Lett.*, 89, 023005.
- [128] Schlosser, N., Reymond, G., Protsenko, I., & Grangier, P. (2001). Sub-poissonian loading of single atoms in a microscopic dipole trap. *Nature*, 411(6841), 1024–1027.
- [129] Seeßelberg, F., Luo, X.-Y., Li, M., Bause, R., Kotochigova, S., Bloch, I., & Gohle, C. (2018). Extending rotational coherence of interacting polar molecules in a spin-decoupled magic trap. *Phys. Rev. Lett.*, 121, 253401.
- [130] Sherson, J. F., Weitenberg, C., Endres, M., Cheneau, M., Bloch, I., & Kuhr, S. (2010). Single-atom-resolved fluorescence imaging of an atomic Mott insulator. *Nature*, 467, 68.
- [131] Shuman, E. S., Barry, J. F., Glenn, D. R., & DeMille, D. (2009). Radiative force from optical cycling on a diatomic molecule. *Phys. Rev. Lett.*, 103(22), 223001.
- [132] Sievers, F., Kretzschmar, N., Fernandes, D. R., Suchet, D., Rabinovic, M., Wu, S., Parker, C. V., Khaykovich, L., Salomon, C., & Chevy, F. (2015). Simultaneous sub-doppler laser cooling of fermionic  $\text{Li}^6$  and  $\text{K}^{40}$  on the D1 line: Theory and experiment. *Physical Review A*, 91(2).
- [133] Sompet, P., Szigeti, S. S., Schwartz, E., Bradley, A. S., & Andersen, M. F. (2019). Thermally robust spin correlations between two  $(85)\text{Rb}$  atoms in an optical micro-trap. *Nature communications*, 10(1), 1889–1889.
- [134] Son, H., Park, J. J., Ketterle, W., & Jamison, A. O. (2019). Observation of collisional cooling of ultracold molecules. *arXiv:1907.09630v1*.
- [135] Son, H., Park, J. J., Ketterle, W., & Jamison, A. O. (2020). Collisional cooling of ultracold molecules. *Nature*, 580(7802), 197–200.
- [136] Steinecker, M. H., McCarron, D. J., Zhu, Y., & DeMille, D. (2016). Improved radio-frequency magneto-optical trap of  $\text{SrF}$  molecules. *ChemPhysChem*, 17(22), 3664–3669.
- [137] Stuhl, B. K., Hummon, M. T., Yeo, M., Quéméner, G., Bohn, J. L., & Ye, J. (2012). Evaporative cooling of the dipolar hydroxyl radical. *Nature*, 492(7429), 396–400.

- [138] Stuhl, B. K., H. M. T. Y. M. Q. G. B. J. L. . Y. J. (2012). Evaporative cooling of the dipolar hydroxyl radical. *Nature*, 492, 396–400.
- [139] Suominen, K.-A., Holland, M. J., Burnett, K., & Julienne, P. (1995). Optical shielding of cold collisions. *Physical Review A*, 51(2), 1446–1457.
- [140] Takekoshi, T., Patterson, B. M., & Knize, R. J. (1998). Observation of optically trapped cold cesium molecules. *Physical Review Letters*, 81(23), 5105–5108.
- [141] Takekoshi, T., Reichsöllner, L., Schindewolf, A., Hutson, J. M., Le Sueur, C. R., Dulieu, O., Ferlaino, F., Grimm, R., & Nägerl, H.-C. (2014). Ultracold dense samples of dipolar rbc molecules in the rovibrational and hyperfine ground state. *Phys. Rev. Lett.*, 113(20), 205301.
- [142] Truppe, S., Williams, H. J., Hambach, M., Caldwell, L., Fitch, N. J., Hinds, E. A., Sauer, B. E., & Tarbutt, M. R. (2017a). Molecules cooled below the doppler limit. *Nature Physics*, 13(12), 1173–1176.
- [143] Truppe, S., Williams, H. J., Hambach, M., Caldwell, L., Fitch, N. J., Hinds, E. A., Sauer, B. E., & Tarbutt, M. R. (2017b). Molecules cooled below the doppler limit. *Nature Physics*, 13, 1173.
- [144] Tuchendler, C., Lance, A. M., Browaeys, A., Sortais, Y. R. P., & Grangier, P. (2008). Energy distribution and cooling of a single atom in an optical tweezer. *Phys. Rev. A*, 78, 033425.
- [145] Valtolina, G., Matsuda, K., Tobias, W. G., Li, J.-R., De Marco, L., & Ye, J. (2020). Dipolar evaporation of reactive molecules to below the fermi temperature. *Nature*, 588(7837), 239–243.
- [146] Vilas, N. B., Hallas, C., Anderegg, L., Robichaud, P., Winnicki, A., Mitra, D., & Doyle, J. M. (2022). Magneto-optical trapping and sub-Doppler cooling of a polyatomic molecule. *Nature*, 606(7912), 70–74.
- [147] WALTER GORDY, R. L. C. (1984). *MICROWAVE MOLECULAR SPECTRA*. New York NY: JOHN WILEY and SONS, 5 edition.

- [148] Western, C. M. (2017). Pgopher: A program for simulating rotational, vibrational and electronic spectra. *Journal of Quantitative Spectroscopy and Radiative Transfer*, 186, 221–242. Satellite Remote Sensing and Spectroscopy: Joint ACE-Odin Meeting, October 2015.
- [149] Williams, H., Caldwell, L., Fitch, N., Truppe, S., Rodewald, J., Hinds, E., Sauer, B., & Tarbutt, M. (2018). Magnetic trapping and coherent control of laser-cooled molecules. *Physical Review Letters*, 120(16).
- [150] Williams, H. J., Truppe, S., Hambach, M., Caldwell, L., Fitch, N. J., Hinds, E. A., Sauer, B. E., & Tarbutt, M. R. (2017). Characteristics of a magneto-optical trap of molecules. *New J. Phys.*, 19(11), 113035.
- [151] Xu, P., Yang, J., Liu, M., He, X., Zeng, Y., Wang, K., Wang, J., Papoular, D. J., Shlyapnikov, G. V., & Zhan, M. (2015). Interaction-induced decay of a heteronuclear two-atom system. *Nature Communications*, 6(1), 7803.
- [152] Yan, B., Moses, S. A., Gadway, B., Covey, J. P., Hazzard, K. R. A., Rey, A. M., Jin, D. S., & Ye, J. (2013a). Observation of dipolar spin-exchange interactions with lattice-confined polar molecules. *Nature*, 501(7468), 521–525.
- [153] Yan, B., Moses, S. A., Gadway, B., Covey, J. P., Hazzard, K. R. A., Rey, A. M., Jin, D. S., & Ye, J. (2013b). Observation of dipolar spin-exchange interactions with lattice-confined polar molecules. *Nature*, 501(7468), 521–525.
- [154] Yan, Z. Z., Park, J. W., Ni, Y., Loh, H., Will, S., Karman, T., & Zwierlein, M. (2020). Resonant dipolar collisions of ultracold molecules induced by microwave dressing. *Physical Review Letters*, 125(6).
- [155] Yavuz, D. D., Kulatunga, P. B., Urban, E., Johnson, T. A., Proite, N., Henage, T., Walker, T. G., & Saffman, M. (2006a). Fast ground state manipulation of neutral atoms in microscopic optical traps. *Physical Review Letters*, 96(6).
- [156] Yavuz, D. D., Kulatunga, P. B., Urban, E., Johnson, T. A., Proite, N., Henage, T., Walker, T. G., & Saffman, M. (2006b). Fast ground state manipulation of neutral atoms in microscopic optical traps. *Phys. Rev. Lett.*, 96, 063001.
- [157] Ye, J., Blatt, S., Boyd, M. M., Foreman, S. M., Hudson, E. R., Ido, T., Lev, B., Ludlow, A. D., Sawyer, B. C., Stuhl, B., & Zelevinsky, T. (2006). Precision

- measurement based on ultracold atoms and cold molecules. In *AIP Conference Proceedings*: AIP.
- [158] Ye, X., Guo, M., González-Martínez, M. L., Quéméner, G., & Wang, D. (2018a). Collisions of ultracold  $^{23}\text{Na}$  molecules with controlled chemical reactivities. *Science Advances*, 4(1), eaaq0083.
- [159] Ye, X., Guo, M., González-Martínez, M. L., Quéméner, G., & Wang, D. (2018b). Collisions of ultracold  $^{23}\text{Na}$  molecules with controlled chemical reactivities. *Sci Adv*, 4(1), eaaq0083.
- [160] Yelin, S. F., Kirby, K., & Côté, R. (2006). Schemes for robust quantum computation with polar molecules. *Physical Review A*, 74(5), 050301.
- [161] Yu, P., Cheuk, L. W., Kozyryev, I., & Doyle, J. M. (2019). A scalable quantum computing platform using symmetric-top molecules. *New J. Phys.*, 21, 093049.
- [162] Yu, P. & Hutzler, N. R. (2021). Probing fundamental symmetries of deformed nuclei in symmetric top molecules. *Phys. Rev. Lett.*, 126(2).
- [163] Zhu, G.-Z., Mitra, D., Augenbraun, B. L., Dickerson, C. E., Frim, M. J., Lao, G., Lasner, Z. D., Alexandrova, A. N., Campbell, W. C., Caram, J. R., Doyle, J. M., & Hudson, E. R. (2022). Functionalizing aromatic compounds with optical cycling centers. *Nat. Chem.*, 14, 995.
- [164] Zilio, S. C., Marcassa, L., Muniz, S., Horowicz, R., Bagnato, V., Napolitano, R., Weiner, J., & Julienne, P. S. (1996). Polarization dependence of optical suppression in photoassociative ionization collisions in a sodium magneto-optic trap. *Phys. Rev. Lett.*, 76, 2033–2036.
- [165] Zulfikar Morbi, C. Z. & Bernath, P. F. (1990). A high resolution analysis of the transition pure precession in polyatomic molecules. *The Journal of Chemical Physics*, 93, 1001.